MATHEMATICAL MODELING OF CIRCULATION IN TWO-DIMENSIONAL PLANE FLOW

FINAL REPORT TO THE

NATIONAL SCIENCE FOUNDATION

GRANT NO. CME-7805458

Prepared by

Civil Engineering Department
Engineering Research Center
Colorado State University
Fort Collins, Colorado 80523

V. M. Ponce
S. B. Yabusaki

June 1980

CER79-80VMP-SBY59

ABSTRACT

MATHEMATICAL MODELING OF CIRCULATION IN OPEN CHANNELS

An investigation of depth-averaged open channel flow is performed to determine the physical processes which contribute to the occurrence of circulating currents. To this end, a mathematical model capable of resolving secondary flow is derived by integrating the three-dimensional turbulent flow equations over flow depth. An important feature of the model is the numerical representation of the closure term for the effective stresses. The finite difference solution procedure is multi-operational, i.e., consisting of explicit computational schemes used in conjunction with the alternating-direction implicit (ADI) method. Two problem configurations are tested in this study: (1) a channel-pool system; and (2) a channel expansion. Results from the numerical experiments appear to be reasonable. In this study, the mechanisms of the effective stresses, convective inertia, and friction are found to be important factors in the circulation phenomenon. Additionally, the numerical specification of the modeled problem is shown to be a major consideration in the simulation of circulating flow.

PREFACE

The clarification of the physical nature of circulation in a free surface flow context has eluded the engineering profession. Herein, a numerical model is used as the tool to investigate the interaction of the various contributing forces, i.e., convective inertia, effective stresses, and bottom friction. The study seeks answers to fundamental questions, and therefore, is within the realm of basic research. Its findings will hopefully pave the way for a better understanding of circulating flow in particular, and of two-dimensional numerical models in general.

This study was made possible by a grant from the National Science Foundation, grant No. CME-7805458. The support of this institution is gratefully acknowledged.

V. M. Ponce

S. B. Yabusaki

TABLE OF CONTENTS

TABLE OF CONTENTS (continued)

LIST OF TABLES

LIST OF FIGURES

LIST OF FIGURES (continued)

LIST OF FIGURES (continued)

LIST OF FIGURES (continued)

LIST OF FIGURES (continued)

LIST OF SYMBOLS

b = subscript for bottom

C = Chézy resistance coefficient

F = any dependent variable

f = Coriolis parameter

f_r = dimensionless friction factor

g = gravitational acceleration

h = flow depth

j = x-coordinate nodal index

k = y-coordinate nodal index

k_1 = turbulent motion kinetic energy

L = turbulent motion length scale

N = total number of grid points in a computational sweep

n = t-coordinate nodal index

P = internal solution vector

P_b = pressure at the bed

P_s = pressure at the surface

p = average pressure

Q = internal solution vector

R = internal solution vector

S = internal solution vector

s = subscript for surface

T = effective stress

t = time

Δt = time increment

U = channel velocity

u = velocity component in the x-direction

u' = temporal velocity fluctuation in the x-direction

LIST OF SYMBOLS (continued)

$\bar{u}$ = depth-averaged velocity

$\bar{u}^*$ = spatially-averaged velocity

v = velocity component in the y-direction

$\bar{v}$ = depth-averaged velocity

$\bar{v}^*$ = spatially-averaged velocity

w = velocity component in the z-direction

x = coordinate direction

Δx = space increment in the x-direction

y = coordinate direction

Δy = space increment in the y-direction

z = coordinate direction

z_b = bottom elevation

α = weighting factor

ε = eddy diffusivity

ε_1 = kinetic energy dissipation rate of turbulent motion

η = water surface elevation

ν = kinematic viscosity

ξ = Courant number criterion

ρ = fluid density

τ = surface stress

ϕ = geographical lattitude

ω = angular velocity of earth's rotation

CHAPTER 1

INTRODUCTION

The study of depth-averaged open channel flow is essential for the solution of contemporary problems which face those who manage the utilization of waterways, harbors, and estuaries. Potential changes in boundary geometry or discharge will undoubtedly disturb the established pattern of currents relied upon for navigation. Localized effects of sediment deposition and degradation are of primary concern in the development of alluvial channels. The siting of cooling facilities will have a significant effect upon the biological community in the area. Dilution of industrial wastes depends on the dispersion provided by currents at the point of injection. All the above are problems which lend themselves to the application of two-dimensional mathematical modeling.

Mathematical models have been developed in response to the absence of analytical solutions for the turbulent fluid flow equations. Previous to the development of efficient high-speed computer hardware, physical models were used exclusively where complex flow phenomena was to be investigated. However, as advances were made in computer technology, economies in time and effort soon made computer modeling a viable alternative. Presently, mathematical models of various levels of sophistication are available.

Two-dimensional plane flow models have existed since the mid 1960's. These models offer a compromise between the simple one-dimensional routing of water and the cumbersome and expensive three-dimensional formulation. An important consideration in the selection of a two-dimensional model is the ability of the model to simulate secondary flow, i.e., circulation. Although such models do exist, a comprehensive analysis of the individual mechanisms which interact to produce circulation has not been attempted with a numerical model.

The objectives of this study are twofold: (1) the clarification of the physical processes leading to the generation of circulation; and (2) the identification of important factors in the numerical specification of circulation problems. Of particular interest in the physical process investigation are the actions of the effective shear stresses, convective inertia, and bed resistance. Earlier studies have pointed out the probable links between these terms and the occurrence of secondary flow. In a discrete representation of a continuum problem, a variety of computational procedures and boundary conditions are available. This study seeks to identify the behavioral differences caused by a particular selection of discretization parameters and boundary conditions.

In accordance with the outlined objectives, a review of research efforts prior to this study is presented in Chapter 2. The governing equations of depth-averaged turbulent fluid flow are derived in Chapter 3. By integrating the general three-dimensional Navier-Stokes equations over the flow depth, the resulting mathematical model consists of two momentum equations and one continuity equation. In Chapter 4, the three equations are expressed in a finite difference formulation amenable to numerical solution. A multi-operational procedure utilizing both implicit and explicit computational schemes is selected to solve for the dependent variables. Specific application of the numerical model to several geometric configurations and boundary conditions is described in Chapter 5. An extensive testing program designed to isolate individual processes of the circulation phenomena is performed on two configurations: (1) a channel-pool system; and (2) a sudden channel expansion. Results of these experiments are analyzed and evaluated in Chapter 6. Chapter 7 summarizes the contributions of this study and recommends areas of future research. A listing of the FORTRAN computer code is given in Appendix IV.

CHAPTER 2

REVIEW OF LITERATURE

2.1 INTRODUCTION

The mathematical modeling of open channel flow is a relatively recent development in the field of hydraulic engineering. Before the computer became available, extensive use was made of physical models since analytical methods could only handle the highly simplified cases. These physical hydraulic models provided engineers with reasonably good answers to complex problems, but required large amounts of effort and time. In addition, the finished models were inflexible, and costly modifications were needed if different conditions were to be tested. As developments in the technology of high speed digital computers increased the computational efficiency and memory storage space, there was a parallel advance in mathematical models and a stronger research effort in the refinement of such models. Mathematical models require smaller development and operating costs while offering almost unlimited flexibility in the simulation of alternatives. Certain specialized problems still remain within the realm of physical modeling, but the use of mathematical models continues to grow.

The mathematical description of open channel flow is best accomplished in a three-dimensional spatial framework. However, the complexity of a formulation in three dimensions and the associated effort in constructing and operating a numerical model may be tremendous, and therefore, the cost prohibitive. Thus, simplifications in the model specification which are reasonably valid for the prototype situation are continuously being sought. Often, a considerable reduction in complexity and cost can be achieved by removing a spatial dimension from consideration. Fortunately, many instances exist in which less complex two- and one-dimensional models are sufficient to properly describe the problem under consideration.

Early success in the mathematical modeling of open channel flows occurred in the one-dimensional flood routing in rivers. The objective of these models was the calculation of flood stages in stream channels. Initially, flood routing models were based on lumped parameters and simplified forms of the Saint Venant equations of unsteady open channel flow. Thus, these simulations were limited not only to the accuracy with which a one-dimensional formulation could describe a three-dimensional phenomena, but also to the specific range of applicability dictated by the simplifying assumptions to the Saint Venant equations.

Hydrologic (or storage) routing is a lumped parameter approach to the flood routing problem. In this method of routing, a simple algebraic relationship between flow and storage is used in lieu of the more complex governing partial differential equations. In the case of flood waves passing through reservoirs, the dominance of storage effects over the resistance and inertia forces allows the use of the water continuity equation alone. This is the basis of the level pool routing procedure.

In the case of flood waves through stream channels, the reach storage is shown to depend not only on the outflow as in the reservoir case, but also on the inflow. Therefore, in stream channel routing, both the equations of water continuity and motion need to be included in the formulation of a one-dimensional unsteady flow model. In this case, it is often advantageous from the practical standpoint to omit terms of negligible magnitude in the equation of motion. This gives rise to several approximate wave models, each possessing a range of applicability associated with the omitted terms. The kinematic wave model is the simplest of these approximate models, describing flood wave travel by a balance of friction and gravity forces, neglecting all other forces.

Another approximate model widely used in practice is the diffusive wave model. By including the pressure force in addition to the friction and gravity forces, this model is capable of simulating both flood wave travel and attenuation. A general treatment of one-dimensional open channel flow is given by the dynamic wave model in which all terms of the Saint Venant equation are included in the analysis.

2.2 TWO-DIMENSIONAL MODELS

Many open channel flow problems cannot be adequately described in one space dimension. Among these are flow in estuaries, lakes, and embayments. Two-dimensional modeling is, in many instances, appropriate to describe some of the important features of these flows. In general, a two-dimensional model can be either of the plan-view or vertical-view type. In a plan-view model, the flow properties are averaged in the vertical direction, while in a vertical-view model they are averaged in one of the horizontal directions. In the context of this work, a two-dimensional model will be understood to refer to a plan-view model, unless specifically stated otherwise. Models of the plan-view type are used in the cases where the channel width is several times the average flow depth, enabling the bottom roughness to effectively generate a uniform velocity distribution in the vertical direction.

Two-dimensional numerical models of open channel flow are relatively recent developments, and thus, most of the work in this field dates back to the last two decades. In essence, two-dimensional models are formulated by integrating the three-dimensional equations of fluid dynamics over the flow depth. The two-dimensional depth-integrated system of equations is not without its pitfalls: there is a closure problem associated with the effective shear stresses which act tangentially on vertical sides of a fluid element. No rigorous relation between these stresses and the depth-averaged variables is currently available. In addition, some other terms of the depth-integrated equation set are often omitted for reasons of mathematical expediency.

Two-dimensional modeling of flow in lakes is sometimes accomplished without some of the terms included in the depth-integrated equation set. By nature, lake circulation is driven primarily by the surface wind stresses and the geostrophic Coriolis acceleration. Thus, it is not uncommon for modelers to neglect the convective inertia, friction, or effective shear stresses, although the basis for these deletions is sometimes open to question. A further simplification which appears fully justified for lake circulation models is the assumption of a planar water surface, referred to in the literature as the "rigid lid" approximation.

The early research on depth-averaged two-dimensional mathematical models was in connection with studies of the ocean environment. Hansen (9) is widely credited for being the first to outline the depth-averaged two-dimensional formulation as it is known today. Later, several other researchers, most notably Leendertse (13,14), followed Hansen in applying two-dimensional modeling concepts to the study of estuarine and coastal hydrodynamics. Using a depth-averaged two-dimensional model, Leendertse (13) satisfactorily calibrated a simulation of currents and water depths in several estuaries. Particular emphasis was given in Leendertse's work to the numerical properties of the two-dimensional model, as evidenced by the linear analysis of stability and convergence following the von Neumann technique (17).

In the last decade, an increased awareness of environmental aspects has led to the inclusion of pollutant, sediment and thermal transport in the numerical modeling of two-dimensional flows. An important feature of these models is the accurate description of secondary currents. It is often these currents that carry heat and pollutants away from coasts, and influence the natural morphologic processes of erosion and accretion. Accordingly, it is necessary that the physical processes governing these currents be correctly understood and properly accounted for in the numerical model.

Kuipers and Vreugdenhil (10) extended Leendertse's model to accomodate steady circulating flow by considering the physical mechanism responsible for vorticity generation. A salient feature of the Kuipers and Vreugdenhil model is that the turbulent diffusion necessary to transfer energy from the main flow to the secondary flow is not explicitly included in the finite difference equations. Rather, it appears as a byproduct of the spatial smoothing which is necessary to control nonlinear instability. In a companion report, Flokstra (6) emphasized the need to explicitly account for the effective shear stresses in modeling circulating flow. The specification of a no-slip condition at closed boundaries was deemed necessary by Flokstra, reasoning that the wall shear was more important than bottom shear in generating and maintaining vorticity in the flow. Abbott and Rasmussen

(2) verified Kuipers and Vreugdenhil's finding that convective inertia is absolutely necessary for the generation of secondary flow, and acknowledged that "pseudo-circulation" in some models could be due to the effect of numerical diffusion inherent in first order finite difference approximations.

More recently, attention has been focused on ways of improving the representation of the effective shear stresses in two-dimensional models. In the past, if these stresses were included at all, a constant turbulent diffusivity (23) was used as a way of closing the equation set. McGuirk and Rodi (16) have recently cast doubts on the validity of such an approximation for the case of jet flows in which the turbulent diffusion processes become very important. Following Launder and Spalding (11), they used a turbulence model in which the transport properties were expressed as a function of the mean flow variables. Lean and Weare (12) have identified two turbulent contributions to the dominant effective shear stress: (1) bed-generated turbulence, and (2) shear layer turbulence. Each of these contributions can be expressed in terms of an eddy viscosity dependent on flow conditions. Criteria was then established by which a simplified analysis, using just one type of eddy viscosity, could be applied.

2.3 THREE-DIMENSIONAL MODELS

For certain applications, a two-dimensional representation of open channel flow may not be adequate to describe the flow in question. This is the case, for instance, of stratified flows and flows with vertical secondary currents. In order to properly describe such three-dimensional features, it is necessary to resort to a three-dimensional model. Several of these models have been developed over the last few years, but the attendant complexity and low cost effectiveness has hindered their further use.

Examples of three-dimensional models of free surface flows are those of Leendertse and Liu (15) and Rastogi and Rodi (22). Leendertse and Liu (15) extended the two-dimensional modeling concept to three-dimensions, by layering planes of two-dimensional models to provide a reasonable description of the variation of flow properties in the vertical direction. Their formulation was fully explicit, and therefore, limited in the grid size by the Courant criterion.

Rastogi and Rodi (22) developed a model for three-dimensional free surface flow by expressing the Navier-Stokes equations for flows that are parabolic in the longitudinal direction. Therefore, in the Rastogi and Rodi model, downstream effects cannot influence the upstream flow. Such parabolic-type equations are amenable to the particularly economic solution method of marching forward integration developed by Patankar and Spalding (18). However, the solution can proceed in the downstream direction only when the longitudinal distribution of the flow depth is known a priori, since the latter is normally controlled by downstream events. A particular feature of the Rastogi and Rodi model is the use of a turbulence model originally due to Launder and Spalding (11). In this model, the local state of turbulence is characterized by two-parameters: the kinetic energy k_1 of the turbulent motion, and its rate of dissipation ε_1. The parameter k_1 is a measure of the intensity of the turbulent fluctuations, while ε_1 is closely related to a length scale L characterizing the turbulent motion. The variation of k_1 and ε_1 over the flow field is determined by semi-empirical transport models based on the Navier-Stokes equations.

2.4 DEPTH-AVERAGED TWO-DIMENSIONAL MODELS

In a comprehensive analysis of free surface flow in two horizontal directions, Leendertse (13) developed a computational model for long period wave propagation in well-mixed estuaries and coastal seas. With this application in mind, the effect of flow nonuniformity was not significant, rendering the effective stresses negligible when compared with bottom friction. Therefore, a reasonably accurate representation was possible without including the effective stresses in the governing equations. The numerical properties of the computational model were determined through a linear analysis of the finite difference equations. The nonlinear resistance and convective terms were omitted and studied separately. The scheme was classified as second order accurate with good convergence characteristics. In an effort to find a stable and accurate difference scheme, the von Neumann linear stability criteria was applied to several discrete representations of the partial differential equations, resulting in the selection of a multi-operational solution scheme, with alternating-direction and mixed explicit-implicit formulation. An amplitude and phase error analysis associated with the complex propagation technique used to assess numerical stability, found that while large time increments were satisfactory with respect to stability, computed wave velocities under these conditions were smaller than physical wave velocities. A similar dispersive numerical effect occurred when too few discrete grid points were used to resolve the continuum problem. The forward difference implicit method was identified as strongly diffusive, damping out both physical and error waves in the computational process. The difficulty in analyzing the nonlinear terms, as mentioned above, led to a separate treatment. Energy transfer from long waves to short waves is interrupted when the size of the physical wave is twice that of the spatial grid increment, i.e., at the minimum grid resolution. Nonlinear terms feed these accumulating short waves back into the system until the computation becomes unstable. Thus, some dissipation function, physical or otherwise, must be used in the calculation in order to arrest the explosive growth of energy. Instabilities also occurred when an off-centered finite difference representation of the convective terms was used at the closed boundaries of the model. For this reason, the convective inertia terms were eliminated from calculations adjacent to boundary points. The magnitude of these terms was considered to be small and therefore, their neglect justified for the sake of improved model stability.

Kuipers and Vreugdenhil (10) extended Leendertse's 1967 model to the realm of secondary flows. By imposing a steady condition at the open boundaries, they were able to use the unsteady character of Leendertse's model as an iterative technique to approach steady circulating flow in certain specified boundary configurations. A theoretical analysis of the vorticity-generating mechanisms was performed in order to throw additional light onto the causes of circulating flow in depth-averaged two-dimensional models. Excluding wind stresses, vorticity can be created either by the convective term, interacting with converging or diverging flow; or through the effective shear stresses. The importance of these two mechanisms was found to be dependent on the distance over which changes in the velocity profile took place. If that distance is less than "a few hundred times the water depth," the effective stresses and convective inertia are significant. Three components of effective shear stresses were identified: (1) viscous stresses; (2) turbulent stresses; and (3) large-scale momentum transfer due to the departure of the local velocity from the depth-averaged velocity. This last contribution is considered to be the most important, arising primarily as a byproduct of the depth-integration of the original three-dimensional equations. Numerical experiments showed the necessity of including the convective inertia terms in order to model two-dimensional circulating flow. Oscillations of a numerical nature are attributed to nonlinear interaction, and are filtered out using artificial viscosity to dissipate the energy piled up at the subgrid scale. The observed circulation in the model is attributed to the combined effect of the convective inertia terms and the artificial viscosity, since no explicit account of the effective stresses was made. In fact, the artificial viscosity is used in lieu of the effective stresses, in an extension to two-dimensions of the well-known one-dimensional numerical diffusion effect (4). An analog of the eddy diffusivity associated with the effective stresses is identified, but apparently there is no physical basis with which to select its magnitude.

In a companion report to Kuipers and Vreugdenhil (10), Flokstra (6) directed attention to the importance of correctly modeling the effective shear stresses. Without actually resolving the closure problem associated with the modeling of these stresses, Flokstra made a detailed study of the relevant physical mechanisms in generating circulating flow. Building on the factors identified by Kuipers and Vreugdenhil as important to secondary flow, Flokstra made use of a vorticity balance to further investigate the combined effect of these factors. According to this analysis, it is theoretically impossible to generate circulating flows without modeling the effective shear stresses. Additionally, the cross term was singled out as the most important of the three effective stresses, since the turbulent part of these terms can be shown to transfer energy into the eddies, while the convective part transfers energy out. Although both Leendertse and Kuipers and Vreugdenhil eliminate the effective shear stresses from the respective equation set, circulation occurs in the latter model as a direct consequence of spatial smoothing. In free shear layers, the effective shear stresses dominate the vorticity-dissipating effects of bottom friction. In such cases where a single type of turbulence mechanism is prevalent, a simplified turbulence model of the effective shear stresses is recommended. In addition, Flokstra's analysis leads to the conclusion that a no-slip condition at the closed boundaries is essential to the generation of eddy circulating patterns.

Abbott and Rasmussen (2) described circulation in rapidly expanding and contracting flow using a depth-averaged model where convected momenta and bottom friction were the primary considerations. They verified Kuipers and Vreugdenhil's conclusion that the convective inertia terms are necessary for the generation of circulation. However, in contradiction with the previous authors, Abbott and Rasmussen concluded that the resistance effects are important in the generation of circulation. Using physical reasoning, they attributed the circulatory patterns to a direct consequence of the resistance effects dominating the inertial effects. The use of two separate dispersion coefficients to handle momentum transfers that are resolvable with the grid and those that are not, is recommended. These coefficients are related to the amount of bottom friction. When the convective terms are modeled accurately, strong dispersion smooths the effects of a rough grid while leaving the flow field virtually unaffected. Abbott and Rasmussen concluded that "pseudo-circulations," occurring strictly due to the truncation errors of the first order difference schemes were possible in depth-averaged two-dimensional models.

Flokstra (7) studied the closure problem in depth-averaged two-dimensional flow, and concluded that the mechanism of energy transfer in two-dimensional models is significantly different from that found in the real three-dimensional world. According to Flokstra, the three-dimensional energy transfer is from larger scales to smaller scales, while the opposite is true for two-dimensional flow. Thus, the use of three-dimensional turbulence models to simulate the effective shear stresses in depth-averaged two-dimensional flow is not justified. The problem is complicated by the presence of three-dimensional components in the depth-averaged effective shear stresses. More research remains to be carried out in order to clarify the importance of this problem.

The occurrence of nonlinear instability in two-dimensional numerical models was also studied by Flokstra. Three approaches were cited to handle this problem: (1) a spatial smoothing process similar to that used by Kuipers and Vreugdenhil; (2) the explicit introduction of an eddy viscosity term in the equations of motion; and (3) the use of a difference scheme that generates numerical viscosity. Considerable care must be exercised in order to prevent the dissipative mechanisms from masking the accuracy of the overall computation.

Rastogi and Rodi (22), emphasizing the importance of an accurate portrayal of turbulent flow in mathematical models, presented two- and three-dimensional open channel flow models that contained turbulent transport parameters coupled with the main flow. In each case, a law-of-the-wall was used in conjunction with the two-parameter turbulent transport model of Launder and Spalding (11). Empirical transport constants, not problem-specific, were used in order to evaluate the transport terms. Due to the strict two-dimensional representation used, circulation is not described by the Rastogi and Rodi model.

McGuirk and Rodi (16), upon the same lines of Rastogi and Rodi (22), developed a depth-averaged velocity and contaminant distribution model of open channel flow. They considered the problem of a recirculation region immediately downstream of a side discharge into a flowing river. The model idealized the free surface with the "rigid lid" approximation, neglecting the variation of flow depth. This assumption is valid provided water level variations are small compared with the flow depth, and is not justified for long stretches of gradually varied flow in which large variations in flow depth can occur in the streamwise direction. However, the effects of a lateral surface slope are accounted for by allowing the pressure to vary at the water surface. Considering the constant turbulent diffusion coefficient and nonexplicit representations of the turbulent structure too crude for the side jet phenomena, McGuirk and Rodi (16) utilized an extension of Launder and Spalding's (11) two-dimensional turbulence model. A closure analysis indicated that the amount of numerical diffusion introduced by an upwind differencing scheme for the convective terms, was significantly smaller than the turbulent diffusion in regions in which diffusion was important.

Lean and Weare (12) tested Flokstra's theoretically-based conclusions using a depth-averaged circulation model of flows past a breakwater. The effective stresses are shown to have contributions from shear layer turbulence and turbulence generated at the bed. Criteria is presented to delimit the conditions under which the shear layer turbulence will predominate. Since only bed-generated turbulence can be represented in terms of mean flow variables, a turbulence model is required to model the effective stresses. An observation of numerical circulation (8) similar to that experienced by Abbott and Rasmussen (2) but caused by a coarse computational grid, is used to dispute Flokstra's argument that the effective stresses are necessary for circulating flow to occur. Numerical experiments of secondary flow generation verified the importance of the convective inertia terms and the no-slip condition at closed boundaries.

2.5 SUMMARY

At present, many uncertainties exist in the mathematical modeling of depth-averaged two-dimensional open channel flow. Clearly, the main obstacle to reliable modeling in two-dimensions is the accurate, physical description of the effective shear stresses. Although indisputably tied to the vorticity phenomena, these stresses have been represented by a wide variety of approaches, ranging from total neglect to sophisticated three-dimensional turbulence models. However successful each of these methods purports to be, until the physical nature of the effective stress terms is further clarified, the modeling will have to rely strongly on the calibration phase.

Convective inertia is also important to the vorticity-generating mechanism. Apparently, these terms interact with the effective stresses to produce circulation in two-dimensional flow. While the structure of the convective inertia terms is readily identified in the governing equations, their nonlinearity complicates the formulation and often leads to numerical stability problems. The control of nonlinear instability requires the use of some artifice to smooth out error growth. Unfortunately, the additional viscosity created by the smoothing procedure can sometimes cause the numerical solution to deviate from the physical solution.

There is an apparent confusion regarding the effect of bed resistance in two-dimensional circulation. The opposing views expressed in the literature may reflect the manner in which the effective stresses were defined in these models. Similarly, Flokstra's conclusion regarding the need for a no-slip condition at closed boundaries may be suspect in view of the circulation under a partial-slip velocity profile observed in the Kuipers and Vreugdenhil model.

The occurrence of numerical circulation (1,8,20) should temper hasty interpretations regarding the success of modeling circulating flow. Unless a complete closure analysis is performed, the effect of truncation error will tend to mask the physical problem. The problems associated with this aspect of two-dimensional modeling are indeed complex. The objective of current research in this area is to contribute to the understanding of the model behavior and its relation to the physical problem, i.e., the closure of two-dimensional numerical diffusion in a manner similar to the closure of one-dimensional numerical diffusion (4).

CHAPTER 3

GOVERNING EQUATIONS

3.1 INTRODUCTION

This chapter describes the derivation of equations applicable to the mathematical modeling of depth-averaged two-dimensional open channel flow. Essentially, the turbulent flow phenomena is described only in the horizontal plane, with all fluid and flow properties invariant along a vertical line. Beginning with a presentation of the general three-dimensional equations of turbulent flow in section 3.2, the analysis proceeds in section 3.3 to detail the integration process leading to the special case of depth-averaged two-dimensional flow (10,21,24). The assumptions and limitations inherent in the derivation are clearly noted in order to ensure proper application of the model. Closure problems associated with the representation of the effective shear stresses and the bottom stresses are discussed in section 3.4. Finally, various terms in the momentum equation are reviewed in section 3.5, with the aim of clarifying their physical contribution to the circulation phenomenon.

3.2 GENERAL EQUATIONS OF TURBULENT FLOW

In describing general three-dimensional flow, basic principles of mass and momentum conservation are used to derive the governing equations that relate the flow variables. For the case of mass conservation, the net mass flux through a control volume is balanced by a changing fluid density as illustrated by the following equation:

$$\frac{\partial \rho}{\partial t} + \frac{\partial(\rho u)}{\partial x} + \frac{\partial(\rho v)}{\partial y} + \frac{\partial(\rho w)}{\partial z} = 0 \qquad (3.1)$$

in which ρ = fluid density; u, v, w = velocity components; x, y, z = coordinate system; and t = time. This equation is valid provided there is an absence of internal mass sources and the fluid is continuous in space.

If instead of a mass flux balance, a momentum flux balance is performed on the control volume, the following equations can be determined:

$$\frac{\partial(\rho u)}{\partial t} + \frac{\partial(\rho u^2)}{\partial x} + \frac{\partial(\rho uv)}{\partial y} + \frac{\partial(\rho uw)}{\partial z} + \rho fw - \rho fv$$

$$= - \frac{\partial p}{\partial x} + \frac{\partial \tau_{xx}}{\partial x} + \frac{\partial \tau_{yx}}{\partial y} + \frac{\partial \tau_{zx}}{\partial z} \qquad (3.2)$$

$$\frac{\partial(\rho v)}{\partial t} + \frac{\partial(\rho uv)}{\partial x} + \frac{\partial(\rho v^2)}{\partial y} + \frac{\partial(\rho vw)}{\partial z} + \rho fu - \rho fw$$

$$= - \frac{\partial p}{\partial y} + \frac{\partial \tau_{xy}}{\partial x} + \frac{\partial \tau_{yy}}{\partial y} + \frac{\partial \tau_{zy}}{\partial z} \qquad (3.3)$$

$$\frac{\partial(\rho w)}{\partial t} + \frac{\partial(\rho uw)}{\partial x} + \frac{\partial(\rho vw)}{\partial y} + \frac{\partial(\rho w^2)}{\partial z} + \rho fv - \rho fu$$

$$= - \frac{\partial p}{\partial z} - \rho g + \frac{\partial \tau_{xz}}{\partial x} + \frac{\partial \tau_{yz}}{\partial y} + \frac{\partial \tau_{zz}}{\partial z} \qquad (3.4)$$

in which f = Coriolis parameter, ($f = 2\ \omega \sin\phi$); ω = angular velocity of the earth's rotation; ϕ = geographical latitude; p = average pressure; and g = gravitational acceleration.

The surface stress τ_{xy} is defined as:

$$\tau_{xy} = \rho\nu\left(\frac{\partial u}{\partial y} + \frac{\partial v}{\partial x}\right) - \overline{\rho u'v'} \qquad (3.5)$$

in which ν = kinematic viscosity; and $\overline{u'v'}$ = average correlation of turbulent velocity fluctuations. Other surface stresses are defined similarly. The components of the surface stress represent contributions from molecular viscosity and turbulent momentum transfer (Reynolds stress), respectively. In addition to the foregoing assumptions, internal sources of momentum have been excluded from the equations. The presence of the gravitational body force in the z-component of the momentum equation implies the selection of the z-coordinate to be positive extending perpendicularly outward from the earth's surface.

A basic assumption of the flow considered in this study is that vertical accelerations and velocities are negligible compared to that of gravity; therefore, the assumption of hydrostatic pressure distribution in the vertical is valid. As a result of this, Coriolis terms containing the vertical velocity become negligible compared to the remaining Coriolis terms. The magnitude of the gravitational body force in the z-component momentum equation is many times larger than the remaining terms except for the vertical pressure gradient. Therefore, this reduces the conservation of momentum in the z-direction to an expression of hydrostatic pressure distribution in the vertical. The resulting momentum equations are expressed as follows:

$$\frac{\partial(\rho u)}{\partial t} + \frac{\partial(\rho u^2)}{\partial x} + \frac{\partial(\rho uv)}{\partial y} + \frac{\partial(\rho uw)}{\partial z} - \rho f v = -\frac{\partial p}{\partial x} + \frac{\partial \tau_{xx}}{\partial x} + \frac{\partial \tau_{yx}}{\partial y} + \frac{\partial \tau_{zx}}{\partial z} \tag{3.6}$$

$$\frac{\partial(\rho v)}{\partial t} + \frac{\partial(\rho uv)}{\partial x} + \frac{\partial(\rho v^2)}{\partial y} + \frac{\partial(\rho vw)}{\partial z} + \rho f u = -\frac{\partial p}{\partial y} + \frac{\partial \tau_{xy}}{\partial x} + \frac{\partial \tau_{yy}}{\partial y} + \frac{\partial \tau_{zy}}{\partial z} \tag{3.7}$$

$$\frac{\partial p}{\partial z} = -\rho g \tag{3.8}$$

The kinematic and dynamic boundary conditions are useful in the formulation of the depth-integrated form of the governing equations.

These two sets of conditions constitute a statement of mass and momentum principles applied to surface and bottom control volumes Figure 3.1 illustrates the equilibrium of mass fluxes at the water surface under the assumption of incompressible flow. Similarly, the bottom element is shown in Figure 3.2.

If small terms are neglected, the mass flux balance generates the kinematic boundary conditions:

$$u\Big|_{\eta}\frac{\partial\eta}{\partial x} + v\Big|_{\eta}\frac{\partial\eta}{\partial y} - w\Big|_{\eta} + \frac{\partial\eta}{\partial t} = 0 \tag{3.9}$$

$$u\Big|_{z_b}\frac{\partial z_b}{\partial x} + v\Big|_{z_b}\frac{\partial z_b}{\partial y} - w\Big|_{z_b} = 0 \tag{3.10}$$

in which η = water surface elevation, ($\eta = z_b + h$); z_b = bottom elevation; and h = flow depth. Inherent in these two equations are the assumptions of negligible precipitation and evaporation at the water surface, while at the bottom, the bed is considered to be fixed and impermeable.

Using a similar procedure that enabled the kinematic boundary conditions to be determined, a stress balance is performed on the surface and bottom control volumes as shown in Figures 3.3 and 3.4, yielding the dynamic boundary conditions:

<u>at the surface</u>

$$P_s\frac{\partial\eta}{\partial x} + \tau_{sx} = p\Big|_{\eta}\frac{\partial\eta}{\partial x} - \tau_{xx}\Big|_{\eta}\frac{\partial\eta}{\partial x} - \tau_{yx}\Big|_{\eta}\frac{\partial\eta}{\partial y} + \tau_{zx}\Big|_{\eta} \tag{3.11}$$

$$P_s\frac{\partial\eta}{\partial y} + \tau_{sy} = p\Big|_{\eta}\frac{\partial\eta}{\partial y} - \tau_{xy}\Big|_{\eta}\frac{\partial\eta}{\partial x} - \tau_{yy}\Big|_{\eta}\frac{\partial\eta}{\partial y} + \tau_{zy}\Big|_{\eta} \tag{3.12}$$

$$-P_s + \tau_{sx}\frac{\partial\eta}{\partial x} + \tau_{sy}\frac{\partial\eta}{\partial y} = -p\Big|_{\eta} - \tau_{xz}\Big|_{\eta}\frac{\partial\eta}{\partial x} - \tau_{yz}\Big|_{\eta}\frac{\partial\eta}{\partial y} + \tau_{zz}\Big|_{\eta} \tag{3.13}$$

<u>at the bottom</u>

$$P_b\frac{\partial z_b}{\partial x} + \tau_{bx} = p\Big|_{z_b}\frac{\partial z_b}{\partial x} - \tau_{xx}\Big|_{z_b}\frac{\partial z_b}{\partial x} - \tau_{yx}\Big|_{z_b}\frac{\partial z_b}{\partial y} + \tau_{zx}\Big|_{z_b} \tag{3.14}$$

$$P_b \frac{\partial z_b}{\partial y} + \tau_{by} = p\bigg|_{z_b} \frac{\partial z_b}{\partial y} - \tau_{yy}\bigg|_{z_b} \frac{\partial z_b}{\partial y} - \tau_{xy}\bigg|_{z_b} \frac{\partial z_b}{\partial x} + \tau_{zy}\bigg|_{z_b} \qquad (3.15)$$

$$- P_b + \tau_{bx} \frac{\partial z_b}{\partial x} + \tau_{by} \frac{\partial z_b}{\partial y} = - p\bigg|_{z_b} - \tau_{xz}\bigg|_{z_b} \frac{\partial z_b}{\partial x} - \tau_{yz}\bigg|_{z_b} \frac{\partial z_b}{\partial y} + \tau_{zz}\bigg|_{z_b} \qquad (3.16)$$

in which P_s = pressure on water surface; P_b = pressure from bed; τ_{sx}, τ_{sy} = surface shear stresses; and τ_{bx}, τ_{by} = bottom shear stresses. Equations 3.11 to 3.16 are based on the assumption that the direction of action of surface and bottom shear stresses deviates very little from the coordinate directions.

3.3 VERTICAL INTEGRATION

The assumptions made so far have not seriously impaired the general applicability of the two-dimensional formulation. Integrating the governing equations over the flow depth, however, places a severe limitation on the applicability of the model because in so doing, the information on the vertical distribution of velocities is partially lost. Fortunately, the shallow water levels found in most rivers and estuaries often do not require such detailed information for a satisfactory representation. Several successful estuarine models reported in the literature operate under the constraint of a depth-integrated formulation. On the other hand, three dimensional phenomena such as stratified flows and buoyancy effects cannot be accurately described under these conditions.

At this point, it may be instructive to clarify the difference between a two-dimensional idealization of flow and the depth-averaged formulation used in this study. A strictly two-dimensional flow idealization does not account for the variation of the horizontal velocities over the flow depth, thus relying solely on turbulence as the energy transfer mechanism. Integrating the three-dimensional equations over the flow depth results in terms which do consider the nonuniform velocity distribution in the vertical. These three-dimensional characteristics are found in the effective shear stress terms which occur as a byproduct of the vertical integration of the convective inertia and surface stress terms in the momentum equations. Further details of the nature of these effective shear stresses are presented in the following section.

The depth-averaging process begins with the integration of the mass conservation equation, leading to the following equation:

$$\int_{z_b}^{\eta} \frac{\partial \rho}{\partial t}\, dz + \int_{z_b}^{\eta} \frac{\partial(\rho u)}{\partial x}\, dz + \int_{z_b}^{\eta} \frac{\partial(\rho v)}{\partial y}\, dz + \int_{z_b}^{\eta} \frac{\partial(\rho w)}{\partial z}\, dz = 0 \qquad (3.17)$$

Using Liebnitz's rule, the order of integration and differentiation are reversed, yielding:

$$\frac{\partial}{\partial t}\int_{z_b}^{\eta} \rho\, dz - \rho\Big|_{\eta}\frac{\partial \eta}{\partial t} + \rho\Big|_{z_b}\frac{\partial z_b}{\partial t} + \frac{\partial}{\partial x}\int_{z_b}^{\eta} \rho u\, dz - \rho u\Big|_{\eta}\frac{\partial \eta}{\partial x} + \rho u\Big|_{z_b}\frac{\partial z_b}{\partial x}$$

$$+ \frac{\partial}{\partial y}\int_{z_b}^{\eta} \rho v\, dz - \rho v\Big|_{\eta}\frac{\partial \eta}{\partial y} + \rho v\Big|_{z_b}\frac{\partial z_b}{\partial y} + \rho w\Big|_{\eta} - \rho w\Big|_{z_b} = 0 \qquad (3.18)$$

The kinematic boundary conditions, the assumption of incompressibility and a fixed bed, allow Equation 3.18 to be simplified to:

$$\frac{\partial \eta}{\partial t} + \frac{\partial(h\bar{u})}{\partial x} + \frac{\partial(h\bar{v})}{\partial y} = 0 \qquad (3.19)$$

in which $\bar{F} = \frac{1}{h}\int F\, dz$; F = any property; and $\bar{F}$ = any average property. Physically speaking, this depth-averaged form of the mass conservation equation balances the net outflux of water from a control volume by a decrease in storage volume, i.e., a falling water surface.

Similarly, the equations of conservation of momentum in integrated form are given below:

$$\frac{\partial}{\partial t}\int_{z_b}^{\eta}\rho u\,dz - \rho u\Big|_{\eta}\frac{\partial\eta}{\partial t} + \rho u\Big|_{z_b}\frac{\partial z_b}{\partial t} + \frac{\partial}{\partial x}\int_{z_b}^{\eta}\rho u^2\,dz - \rho u^2\Big|_{\eta}\frac{\partial\eta}{\partial x} + \rho u^2\Big|_{z_b}\frac{\partial z_b}{\partial x}$$

$$+ \frac{\partial}{\partial y}\int_{z_b}^{\eta}\rho uv\,dz - \rho uv\Big|_{\eta}\frac{\partial\eta}{\partial y} + \rho uv\Big|_{z_b}\frac{\partial z_b}{\partial y} + \rho uw\Big|_{\eta} - \rho uw\Big|_{z_b} - f\int_{z_b}^{\eta}\rho v\,dz$$

$$+ \frac{\partial}{\partial x}\int_{z_b}^{\eta} p\,dz - p\Big|_{\eta}\frac{\partial\eta}{\partial x} + p\Big|_{z_b}\frac{\partial z_b}{\partial x} - \frac{\partial}{\partial x}\int_{z_b}^{\eta}\tau_{xx}dz + \tau_{xx}\Big|_{\eta}\frac{\partial\eta}{\partial x} - \tau_{xx}\Big|_{z_b}\frac{\partial z_b}{\partial x}$$

$$- \frac{\partial}{\partial y}\int_{z_b}^{\eta}\tau_{yx}\,dz + \tau_{yx}\Big|_{\eta}\frac{\partial\eta}{\partial y} - \tau_{yx}\Big|_{z_b}\frac{\partial z_b}{\partial y} - \tau_{zx}\Big|_{\eta} + \tau_{zx}\Big|_{z_b} = 0 \quad (3.20)$$

$$\frac{\partial}{\partial t}\int_{z_b}^{\eta}\rho v\,dz - \rho v\Big|_{\eta}\frac{\partial\eta}{\partial t} + \rho v\Big|_{z_b}\frac{\partial z_b}{\partial t} + \frac{\partial}{\partial x}\int_{z_b}^{\eta}\rho uv\,dz - \rho uv\Big|_{\eta}\frac{\partial\eta}{\partial x} + \rho uv\Big|_{z_b}\frac{\partial z_b}{\partial x}$$

$$+ \frac{\partial}{\partial y}\int_{z_b}^{\eta}\rho v^2 dz - \rho v^2\Big|_{\eta}\frac{\partial\eta}{\partial y} + \rho v^2\Big|_{z_b}\frac{\partial z_b}{\partial y} + \rho vw\Big|_{\eta} - \rho vw\Big|_{z_b} + f\int_{z_b}^{\eta}\rho u\,dz$$

$$+ \frac{\partial}{\partial y}\int_{z_b}^{\eta} p\,dz - p\Big|_{\eta}\frac{\partial\eta}{\partial y} + p\Big|_{z_b}\frac{\partial z_b}{\partial y} - \frac{\partial}{\partial x}\int_{z_b}^{\eta}\tau_{xy}dz + \tau_{xy}\Big|_{\eta}\frac{\partial\eta}{\partial x} - \tau_{xy}\Big|_{z_b}\frac{\partial z_b}{\partial x}$$

$$- \frac{\partial}{\partial y}\int_{z_b}^{\eta}\tau_{yy}dz + \tau_{yy}\Big|_{\eta}\frac{\partial\eta}{\partial y} - \tau_{yy}\Big|_{z_b}\frac{\partial z_b}{\partial y} - \tau_{zy}\Big|_{\eta} + \tau_{zy}\Big|_{z_b} = 0 \quad (3.21)$$

In addition to the kinematic boundary conditions and the assumptions used previously, the dynamic boundary conditions are also employed here, resulting in the following equations:

$$\frac{\partial}{\partial t}(\bar{u}h) + \frac{\partial}{\partial x}\int_{z_b}^{\eta} u^2 dz + \frac{\partial}{\partial y}\int_{z_b}^{\eta} uv dz - f\bar{v}h + \frac{1}{\rho}\frac{\partial}{\partial x}\int_{z_b}^{\eta} p dz$$

$$- \frac{1}{\rho}\frac{\partial}{\partial x}\int_{z_b}^{\eta} \tau_{xx}\, dz - \frac{1}{\rho}\frac{\partial}{\partial y}\int_{z_b}^{\eta} \tau_{yx}\, dz - \frac{1}{\rho}(\tau_{sx} - \tau_{bx})$$

$$+ \frac{1}{\rho} P_b \frac{\partial z_b}{\partial x} - \frac{1}{\rho} P_s \frac{\partial \eta}{\partial x} = 0 \qquad (3.22)$$

$$\frac{\partial}{\partial t}(\bar{v}h) + \frac{\partial}{\partial x}\int_{z_b}^{\eta} uv dz + \frac{\partial}{\partial y}\int_{z_b}^{\eta} v^2 dz + f\bar{u}h + \frac{1}{\rho}\frac{\partial}{\partial y}\int_{z_b}^{\eta} p\, dz$$

$$- \frac{1}{\rho}\frac{\partial}{\partial x}\int_{z_b}^{\eta} \tau_{xy} dz - \frac{1}{\rho}\frac{\partial}{\partial y}\int_{z_b}^{\eta} \tau_{yy} dz - \frac{1}{\rho}(\tau_{sy} - \tau_{by})$$

$$+ \frac{1}{\rho} P_b \frac{\partial z_b}{\partial y} - \frac{1}{\rho} P_s \frac{\partial \eta}{\partial y} = 0 \qquad (3.23)$$

Further simplification is possible as a consequence of earlier approximations. The air pressure at the water surface, P_s, is zero since the water pressure is gage-referenced. The assumption of hydrostatic pressure distribution enables the following expressions:

$$\frac{1}{\rho}\ \frac{\partial}{\partial x}\int_{z_b}^{\eta} pdz = gh\ \frac{\partial h}{\partial x} \qquad (3.24)$$

$$\frac{1}{\rho}\ \frac{\partial}{\partial y}\int_{z_b}^{\eta} pdz = gh\ \frac{\partial h}{\partial y} \qquad (3.25)$$

$$P_b = \rho g h \qquad (3.26)$$

If the convective inertia terms are manipulated using the algebraic relations:

$$u^2 = (u-\bar{u})^2 + 2u\bar{u} - \bar{u}^2 \tag{3.27}$$

$$uv = (u-\bar{u})(v-\bar{v}) + u\bar{v} + \bar{u}v - \bar{u}\bar{v} \tag{3.28}$$

$$v^2 = (v-\bar{v})^2 + 2v\bar{v} - \bar{v}^2 \tag{3.29}$$

the momentum equations can be written as follows:

$$\frac{\partial}{\partial t}(\bar{u}h) + \frac{\partial}{\partial x}\int_{z_b}^{\eta}(u-\bar{u})^2 dz + \frac{\partial}{\partial x}(\bar{u}^2 h) + \frac{\partial}{\partial y}\int_{z_b}^{\eta}(u-\bar{u})(v-\bar{v})dz$$

$$+ \frac{\partial}{\partial y}(\bar{u}\bar{v}h) - f\bar{v}h + gh\frac{\partial\eta}{\partial x} - \frac{1}{\rho}\frac{\partial}{\partial x}\int_{z_b}^{\eta}\tau_{xx}\, dz$$

$$- \frac{1}{\rho}\frac{\partial}{\partial y}\int_{z_b}^{\eta}\tau_{yx} dz - \frac{1}{\rho}(\tau_{sx}-\tau_{bx}) = 0 \tag{3.30}$$

$$\frac{\partial}{\partial t}(\bar{v}h) + \frac{\partial}{\partial x}\int_{z_b}^{\eta}(u-\bar{u})(v-\bar{v})dz + \frac{\partial}{\partial x}(\bar{u}\bar{v}h) + \frac{\partial}{\partial y}\int_{z_b}^{\eta}(v-\bar{v})^2 dz$$

$$+ \frac{\partial}{\partial y}(\bar{v}^2 h) + f\bar{u}h + gh\frac{\partial\eta}{\partial y} - \frac{1}{\rho}\frac{\partial}{\partial x}\int_{z_b}^{\eta}\tau_{xy}\, dz$$

$$- \frac{1}{\rho}\frac{\partial}{\partial y}\int_{z_b}^{\eta}\tau_{yy} dz - \frac{1}{\rho}(\tau_{sy} - \tau_{by}) = 0 \tag{3.31}$$

The notation can be shortened by defining the effective stresses as follows:

$$T_{xx} = \frac{1}{h}\int_{z_b}^{\eta}[\tau_{xx} - \rho(u-\bar{u})^2]dz \tag{3.32}$$

$$T_{xy} = T_{yx} = \frac{1}{h}\int_{z_b}^{\eta}[\tau_{yx} - \rho(u-\bar{u})(v-\bar{v})]dz \tag{3.33}$$

$$T_{yy} = \frac{1}{h}\int_{z_b}^{\eta}[\tau_{yy} - \rho(v-\bar{v})^2]dz \tag{3.34}$$

Therefore, the resulting equations are:

$$\frac{\partial}{\partial t}(\bar{u}h) + \frac{\partial}{\partial x}(\bar{u}^2 h) + \frac{\partial}{\partial y}(\bar{u}\bar{v}h) - f\bar{v}h + gh\frac{\partial \eta}{\partial x}$$

$$-\frac{1}{\rho}(\tau_{sx}-\tau_{bx}) - \frac{1}{\rho}\frac{\partial}{\partial x}(hT_{xx}) - \frac{1}{\rho}\frac{\partial}{\partial y}(hT_{xy}) = 0 \qquad (3.35)$$

$$\frac{\partial}{\partial t}(\bar{v}h) + \frac{\partial}{\partial x}(\bar{u}\bar{v}h) + \frac{\partial}{\partial y}(\bar{v}^2 h) + f\bar{u}h + gh\frac{\partial \eta}{\partial y}$$

$$-\frac{1}{\rho}(\tau_{sy}-\tau_{by}) - \frac{1}{\rho}\frac{\partial}{\partial x}(hT_{xy}) - \frac{1}{\rho}\frac{\partial}{\partial y}(hT_{yy}) = 0 \qquad (3.36)$$

If the derivatives of the first three terms in each equation are expanded, terms found in the equation of mass conservation appear, and can, therefore, be canceled. The final form of the momentum equations is determined by dividing through by the water depth, h, to give:

$$\frac{\partial \bar{u}}{\partial t} + \bar{u}\frac{\partial \bar{u}}{\partial x} + \bar{v}\frac{\partial \bar{u}}{\partial y} - f\bar{v} + g\frac{\partial \eta}{\partial x} - \frac{1}{\rho h}(\tau_{sx}-\tau_{bx})$$

$$-\frac{1}{\rho h}\frac{\partial}{\partial x}(hT_{xx}) - \frac{1}{\rho h}\frac{\partial}{\partial y}(hT_{xy}) = 0 \qquad (3.37)$$

$$\frac{\partial \bar{v}}{\partial t} + \bar{u}\frac{\partial \bar{v}}{\partial x} + \bar{v}\frac{\partial \bar{v}}{\partial y} + f\bar{u} + g\frac{\partial \eta}{\partial y} - \frac{1}{\rho h}(\tau_{sy}-\tau_{by})$$

$$-\frac{1}{\rho h}\frac{\partial}{\partial x}(hT_{xy}) - \frac{1}{\rho h}\frac{\partial}{\partial y}(hT_{yy}) = 0 \qquad (3.38)$$

3.4 SIGNIFICANCE OF THE VARIOUS TERMS IN THE MOMENTUM EQUATIONS

Certain features of the equations derived in section 3.3 can be dispensed with in order to clarify the nature of the mechanisms being tested. For the purposes of this study, the wind stress and geostrophic effects will be removed from the analysis. Flokstra (6) has pointed out that these terms are, in part, responsible for the generation of vorticity in the flow. Thus, an explanation is necessary in order to justify the formal neglect of these terms. For the type of flow under consideration, i.e., open channel flow, the magnitude of wind and geostrophic effects is insignificant as compared to the driving forces found in the mean flow currents. These two terms can be easily incorporated into the model if desired, and their absence does not detract from the generality of the conclusions of this study.

The present equation set, although containing many approximations and simplifications, is not closed. Historically, turbulent flow theory has suffered from an incomplete physical representation of the turbulent momentum transfer (Reynolds stresses), i.e., those stresses due to the correlations of turbulent velocity fluctuations. Depth-averaging the formulation further complicates the problem by creating an additional stress due to the nonuniform velocity distribution in the vertical. These two stresses and the viscous shear stress combine into the term previously identified as the effective stress. The three components of the effective stress (viscous, turbulent, and velocity nonuniformity) each apply a lateral tangential stress on fluid elements and are inherently tied to the three-dimensional character of the flow. The viscous shear stress is significant only near walls in the laminar sublayer and does not generally affect the large scale eddy flow. The Reynolds stress provides the momentum transfer necessary to drive the secondary flow, and, according to Flokstra, the nonuniformity component of the effective stress dissipates energy, removing momentum from secondary flow. Lean and Weare (12) include bed-generated turbulence as a contribution to the effective stress and determine the criteria under which bed-generated turbulence will dominate shear layer turbulence.

Representing the effective stresses in terms of the main flow variables is by far the largest impediment to the accurate modeling of circulating flow. Since this problem remains to be solved, the use of empirical parameters and calibration techniques is unavoidable. Methods currently used in the literature range from the assumption of a constant turbulent diffusion coefficient, to "field models" which include an uncoupled turbulence model to calculate turbulent transport terms at each computational node (22).

In this study, the procedure developed by Kuipers and Vreugdenhil (10) will be adopted. They used a numerical eddy diffusivity, ε, to account for the effective stresses in their model, such that:

$$\frac{1}{\rho h}\left[\frac{\partial}{\partial x}(hT_{xx}) + \frac{\partial}{\partial y}(hT_{xy})\right] = \varepsilon\left(\frac{\partial^2 \bar{u}}{\partial x^2} + \frac{\partial^2 \bar{u}}{\partial y^2}\right) \tag{3.39}$$

$$\frac{1}{\rho h}\left[\frac{\partial}{\partial x}(hT_{xy}) + \frac{\partial}{\partial y}(hT_{yy})\right] = \varepsilon\left(\frac{\partial^2 \bar{v}}{\partial x^2} + \frac{\partial^2 \bar{v}}{\partial y^2}\right) \tag{3.40}$$

in which $\varepsilon = \alpha \frac{(\Delta x)^2}{2\,\Delta t}$; α = weighting factor used in the spatial smoothing by velocity-averaging; Δx = spatial increment; and Δt = temporal increment.

The selection of the value of α is not physically-based, and the need for flow calibration is apparent. This particular technique does not explicitly contain the effective shear stresses in the equations used, but introduces them in a velocity-averaging routine which simulates the contribution of the effective stresses. In this routine, an averaging procedure occurs after each set of new dependent variables has been computed, as follows:

$$\bar{u}^*_{j,k} = \bar{u}_{j,k}(1-\alpha) + \frac{\alpha}{4}(\bar{u}_{j-1,k} + \bar{u}_{j,k-1} + \bar{u}_{j,k+1} + \bar{u}_{j+1,k}) \tag{3.41}$$

$$\bar{v}^*_{j,k} = \bar{v}_{j,k}(1-\alpha) + \frac{\alpha}{4}(\bar{v}_{j-1,k} + \bar{v}_{j,k-1} + \bar{v}_{j,k+1} + \bar{v}_{j+1,k}) \tag{3.42}$$

in which $\bar{u}^*_{j,k}$ = new $\bar{u}_{j,k}$; $\bar{v}^*_{j,k}$ = new $v_{j,k}$; and j,k = spatial indices. When these substitutions are made in the governing equations, the extra diffusivity terms appear.

The bottom shear stress, like the effective stress, has not been rigorously related to flow properties. However, years of experimentation has resulted in the availability of several satisfactory empirical resistance equations. Any of the applicable resistance equations can be used to relate the bottom shear stress to the flow velocity, assuming the validity of a steady uniform flow roughness. The Chézy expression is preferred for simplicity, due to the dimensionless friction factor, f_r, associated with it, as follows:

$$\tau_{bx} = \rho f_r \, \bar{u}(\bar{u}^2+\bar{v}^2)^{\frac{1}{2}} \tag{3.43}$$

$$\tau_{by} = \rho f_r \, \bar{v}(\bar{u}^2+\bar{v}^2)^{\frac{1}{2}} \tag{3.44}$$

in which $f_r = \frac{g}{C^2}$; and C = Chézy coefficient.

3.5 FACTORS INFLUENCING CIRCULATING FLOW

This section will discuss the significance of various terms in the momentum equation with respect to the generation and maintenance of circulating flow. Previous modeling attempts have sometimes resorted to the omission of the effective stress, convective inertia, or friction terms, due, in part, to the uncertainty or nonlinearity associated with these terms. The physical reasoning to justify these approximations was often not very clear.

Flokstra (7), in an analytical evaluation of the vorticity phenomenon, concluded that the presence of the effective stresses in a two-dimensional model formulation was a necessary but not sufficient condition for the occurrence of secondary flow. These stresses were considered to be the primary mechanism of momentum exchange between the shear flow and the circulating flow. Leendertse (13) neglected the effective stress term, reasoning that it was very small compared to the bottom stress effects associated with long-period wave behavior in estuaries. The absence of circulation in Leendertse's model tends to support the findings of Flokstra. Kuipers and Vreugdenhil (10) were not conclusive with their experimental testing of the importance of effective stresses, but claimed that an order of magnitude argument shows these stresses to be relatively unimportant.

The convective acceleration terms in the momentum equation are often omitted in numerical modeling because of the nonlinearity introduced into the partial differential equation system. Leendertse included convective accelerations in his 1967 model but was forced to remove the nonlinear terms to perform the von Neumann linear stability analysis. Kuipers and Vreugdenhil theoretically and empirically established the need to include the convective acceleration in the analysis of secondary flow. Essentially, the convective acceleration supplies the mechanism necessary to transport vorticity in the mean flow. Flokstra (6), with theoretical arguments, and Abbott and Rasmussen (2), in experiments, have concurred in these findings.

The importance of bottom and closed boundary friction has not been clearly established in the literature. As noted earlier, Leendertse believed that the bottom stress effects dominated other stress contributions for long period waves. Abbott and Rasmussen (2) described the circulation phenomenon as a competition between inertial and resistance forces. Flokstra (6) found both the effective stresses and the wall stresses to be of more significant influence on vorticity generation than the bottom shear stress. Thus, a no-slip condition at the wall was considered to be a necessary requirement for circulation to occur. Lean and Weare (12) discovered that each of the various shear stresses could be dominant under different flow conditions. The latter appears to be the most cogent analysis available when considering the relative importance of the various shear stresses in generating circulating flow in depth-averaged two-dimensional models.

CHAPTER 4

NUMERICAL MODELING

4.1 INTRODUCTION

This chapter describes the development of a mathematical model of open channel flow based on the equation set derived in the previous chapter. An explanation of the difficulties found in the analytical treatment of the problem as well as the conversion to a numerical formulation is presented in section 4.2. Basic concepts and definitions are introduced in section 4.3 to help the reader become familiar with the notation of the finite difference method. Section 4.4 provides an overview of the operational procedure used in the model. In section 4.5, the equations derived in Chapter 3 are replaced with finite difference analogs, while section 4.6 describes the algorithm used to solve the numerical representation. Boundary types and their treatment are discussed in section 4.7. Section 4.8 is devoted to a discussion of the numerical properties of the model.

4.2 MATHEMATICAL MODELING

Depending on the manner in which the effective stresses are expressed, the partial differential equations derived in Chapter 3 comprise either a hyperbolic or parabolic set. In each case, initial and boundary conditions are required to fully specify the problem, assuming that the various empirical parameters have already been determined. As happens in every instance in which turbulent open channel flow is considered, no closed form solution exists for the analytical equation set. This leads to a search for a numerical technique that can overcome the intractable nature of the analytical problem posed. Among the various mathematical approaches available, the finite difference and the finite element methods are the most widely used. This study utilizes the finite difference approximation to the partial differential equation set in the solution procedure.

The conversion of an analytical statement to a numerical statement begins with the application of a difference scheme to the differential equations. Calculus operations then become algebraic relations of dependent variables defined at discretely spaced locations in the independent variable domain. Although providing solutions to problems that could not be otherwise solved, mathematical models are hampered by certain limitations not encountered in calculus. The discrete nature of the variable domain acts in such a way as to control the stability and accuracy of the model. Often the discretized form of the differential equations does not represent the original problem due to the inadvertent creation of artificial terms. Conversely, increased accuracy in the specification of the finite difference scheme does not guarantee a stable solution.

The difficulties associated with the finite difference method are not insurmountable, as shown by the large number of successful modeling efforts documented in the literature. Mathematical modeling is now firmly established as an indispensable tool, and the parallel advancements in numerical analysis and computer technology can only increase the present range of application.

4.3 FINITE DIFFERENCE PRELIMINARIES

The basis of the finite difference method is the substitution of a computational grid for the continuous domain of the independent variables. Since the present problem has been specified in three independent variables (x, y, and t), a three-dimensional solution network results, with dependent variables defined at the nodal points. In order to visualize the computational structure used in this model, the reader must imagine levels of horizontal x-y spatial grid domains layered in the vertical time dimension. Conceptually, the four variables, u, v, η, and z_b, should all be defined at every node location. However, practical limitations in the computational procedure make it more convenient to define a separate grid system for each of these variables. These four grid systems are staggered in space in a form originally due to Platzman (19), as shown in Fig. 4.1.

By definition, the distance between adjacent nodes is controlled by the space and time increments Δx, Δy, and Δt. It is not necessary for Δx to be equal to Δy. However, the representation of the effective stresses used in this model does depend on this assumption. Specifying the location of a dependent variable is based on the following notation: $F^n_{j,k}$; in which F = a dependent variable; j = x-coordinate, $(j\Delta x)$; k = y-coordinate, $(k\Delta y)$; and n = t-coordinate, $(n\Delta t)$. A typical time level n would then have the appearance shown in Fig. 4.1. As can be seen from this figure, the interlocking nature of the grid system reduces the distance between adjacent nodes to one half the spatial increment, although identical variables remain one spatial increment apart. Since each dependent variable location is unique, it is not necessary to use half increments when subscripting, i.e., the same subscripts imply different locations for different dependent variables.

Among the several types of finite difference schemes available, the central difference approximations provide second order accuracy. For this reason, central differences are used wherever possible in the computational representation of the derivatives. Examples of central difference schemes are:

$$\left.\frac{\partial F}{\partial x}\right|_{F_{j,k}} = \frac{F_{j+1,k} - F_{j-1,k}}{2\Delta x} \tag{4.1}$$

$$\left.\frac{\partial F}{\partial y}\right|_{F_{j,k}} = \frac{F_{j,k+1} - F_{j,k-1}}{2\Delta y} \tag{4.2}$$

$$\left.\frac{\partial F}{\partial t}\right|_{F^{n+\frac{1}{2}}_{j,k}} = \frac{F^{n+1}_{j,k} - F^{n}_{j,k}}{\Delta t} \tag{4.3}$$

Generally speaking, spatial derivatives can always be expressed in terms of a central difference as shown above. However, temporal derivatives cannot be represented in this fashion unless iterations are performed, because both the $n+\frac{1}{2}$ and $n+1$ time levels are unknown. The additional computational effort required by an iterative formulation is usually not warranted. Consequently, a less accurate but more expedient backward difference scheme:

$$\left.\frac{\partial F}{\partial t}\right|_{F^{n+\frac{1}{2}}_{j,k}} = \frac{F^{n+\frac{1}{2}}_{j,k} - F^{n}_{j,k}}{\frac{1}{2}\Delta t} \tag{4.4}$$

is used for all temporal derivatives.

Two types of solution schemes exist for problems expressed in terms of finite differences: (1) explicit; and (2) implicit. Explicit schemes propagate a direct solution for unknown dependent variables from one grid point to the next by calculating new values exclusively in terms of known neighboring values. The explicit scheme requires a simple formulation but is generally subject to a strict numerical stability criterion, which effectively places an upper limit on the magnitude of the time step, Δt, that can be used in practice.

An implicit scheme is characterized by the presence of more than one unknown variable in the difference equation, requiring the solution of a set of simultaneous equations in order to generate an array of new values. No stability conditions are usually imposed on the time step size in implicit solutions, and therefore, considerable economies in computer time are possible. However, implicit schemes are difficult to formulate and, in the case of nonlinear equations, suffer from problems of iterative convergence.

4.4 OVERVIEW OF THE COMPUTATIONAL PROCEDURE

The computational procedure used in this model is a multi-operational mode solution based on the division of each time step, Δt, into two stages of a half-time step each. Leendertse (13) modified the well-known "alternating-direction implicit" or ADI method, by including two explicit schemes in such a way that each stage contained an implicit scheme followed by an explicit scheme. The advantage of the ADI method, in addition to those attributable to implicit schemes, lies in the solution procedure which solves the x-momentum equation separately from the y-momentum equation, permitting the two-dimensional problem to be solved as a sequence of two one-dimensional problems. After each implicit step, a single dependent variable remains unknown and can be efficiently solved for by an explicit method. Thus, the multi-operational solution procedure enables an optimum exploitation of the best features of both implicit and explicit schemes.

The introduction of the effective stress terms is accomplished by the spatial smoothing performed at the conclusion of each stage. A summary of the general operations in sequential order follows.

First Stage

1. Implicit solution of $u^{n+\frac{1}{2}}$ and $\eta^{n+\frac{1}{2}}$ using the continuity and x-momentum equations.
2. Explicit solution of $v^{n+\frac{1}{2}}$ using the y-momentum equation.
3. Spatial smoothing of $u^{n+\frac{1}{2}}$ and $v^{n+\frac{1}{2}}$ using a velocity-averaging scheme.

Second Stage

1. Implicit solution of v^{n+1} and η^{n+1} using the continuity and y-momentum equations.
2. Explicit solution of u^{n+1} using the x-momentum equation.
3. Spatial smoothing of u^{n+1} and v^{n+1} using a velocity-averaging scheme.

4.5 FINITE DIFFERENCE EQUATIONS

The numerical model is based on the set of governing equations derived in Chapter 3 (throughout this chapter, the overbars denoting depth-integrated variables have been omitted for simplicity):

$$\frac{\partial u}{\partial t} + u\,\frac{\partial u}{\partial x} + v\,\frac{\partial u}{\partial y} + g\,\frac{\partial \eta}{\partial x} + f_r u\,\frac{(u^2+v^2)^{\frac{1}{2}}}{(\eta - z_b)} = 0 \qquad (4.5)$$

$$\frac{\partial v}{\partial t} + u\,\frac{\partial v}{\partial x} + v\,\frac{\partial v}{\partial y} + g\,\frac{\partial \eta}{\partial y} + f_r v\,\frac{(u^2+v^2)^{\frac{1}{2}}}{(\eta - z_b)} = 0 \qquad (4.6)$$

$$\frac{\partial \eta}{\partial t} + \frac{\partial}{\partial x}\,[(\eta - z_b)u] + \frac{\partial}{\partial y}\,[(\eta - z_b)v] = 0 \qquad (4.7)$$

The first two equations express the conservation of momentum, while the third equation expresses the conservation of mass.

The finite difference method replaces the partial differential operators with algebraic operations defined at the nodal grid points. Each of the three equations has a difference scheme centered about a unique location on the grid system. The x-momentum equation is referenced to the node occupied by $u_{j,k}$ while the y-momentum equation is centered about node location $v_{j,k}$; $\eta_{j,k}$ is the reference location for the continuity equation. As mentioned in section 4.3, a second-order accurate representation of a differential equation is possible by the use of central differences. Applying this scheme to the x-momentum and continuity equations yields:

X-Momentum Equation (Nonlinear Implicit)

$$\left.\frac{\partial u}{\partial t}\right|_{u^{n+\frac{1}{2}}_{j,k}} = \frac{u^{n+1}_{j,k} - u^{n}_{j,k}}{\Delta t} \tag{4.7}$$

$$\left. u\,\frac{\partial u}{\partial x}\right|_{u^{n+\frac{1}{2}}_{j,k}} = u^{n+\frac{1}{2}}_{j,k}\left[\frac{u^{n+\frac{1}{2}}_{j+1,k} - u^{n+\frac{1}{2}}_{j-1,k}}{2\Delta x}\right] \tag{4.8}$$

$$\left. v\,\frac{\partial u}{\partial y}\right|_{u^{n+\frac{1}{2}}_{j,k}} = \frac{1}{4}\left(v^{n+\frac{1}{2}}_{j,k} + v^{n+\frac{1}{2}}_{j,k-1} + v^{n+\frac{1}{2}}_{j+1,k} + v^{n+\frac{1}{2}}_{j+1,k-1}\right)\left[\frac{u^{n+\frac{1}{2}}_{j,k+1} - u^{n+\frac{1}{2}}_{j,k-1}}{2\Delta y}\right] \tag{4.9}$$

$$\left. g\,\frac{\partial \eta}{\partial x}\right|_{u^{n+\frac{1}{2}}_{j,k}} = g\left[\frac{\eta^{n+\frac{1}{2}}_{j+1,k} - \eta^{n+\frac{1}{2}}_{j,k}}{\Delta x}\right] \tag{4.10}$$

$$\left. f_r\, u\,\frac{(u^2+v^2)^{\frac{1}{2}}}{(\eta - z_b)}\right|_{u^{n+\frac{1}{2}}_{j,k}} =$$

$$\frac{1}{2}\left(f_{r_{j,k}} + f_{r_{j+1,k}}\right) u^{n+\frac{1}{2}}_{j,k}\,\frac{\left[\left(u^{n+\frac{1}{2}}_{j,k}\right)^2 + \left(\dfrac{v^{n+\frac{1}{2}}_{j,k} + v^{n+\frac{1}{2}}_{j,k-1} + v^{n+\frac{1}{2}}_{j+1,k} + v^{n+\frac{1}{2}}_{j+1,k-1}}{4}\right)^2\right]^{\frac{1}{2}}}{\frac{1}{2}\left(\eta^{n+\frac{1}{2}}_{j,k} + \eta^{n+\frac{1}{2}}_{j+1,k}\right) - \frac{1}{2}\left(z_{b_{j,k}} + z_{b_{j,k-1}}\right)} \tag{4.11}$$

Continuity Equation (Nonlinear Implicit)

$$\left.\frac{\partial \eta}{\partial t}\right|_{\eta^{n+\frac{1}{2}}_{j,k}} = \frac{\eta^{n+1}_{j,k} - \eta^{n}_{j,k}}{\Delta t} \tag{4.12}$$

$$\left.\frac{\partial}{\partial x}[(\eta - z_b)u]\right|_{\eta^{n+\frac{1}{2}}_{j,k}} = \left[\frac{\frac{1}{2}(\eta^{n+\frac{1}{2}}_{j+1,k} + \eta^{n+\frac{1}{2}}_{j,k}) - \frac{1}{2}(z_{b_{j,k-1}} + z_{b_{j,k}})}{\Delta x}\right] u^{n+\frac{1}{2}}_{j,k}$$

$$- \left[\frac{\frac{1}{2}(\eta^{n+\frac{1}{2}}_{j-1,k} + \eta^{n+\frac{1}{2}}_{j,k}) - \frac{1}{2}(z_{b_{j-1,k-1}} + z_{b_{j-1,k}})}{\Delta x}\right] u^{n+\frac{1}{2}}_{j-1,k} \tag{4.13}$$

$$\left.\frac{\partial}{\partial y}[(\eta - z_b)v]\right|_{\eta^{n+\frac{1}{2}}_{j,k}} = \left[\frac{\frac{1}{2}(\eta^{n+\frac{1}{2}}_{j,k+1} + \eta^{n+\frac{1}{2}}_{j,k}) - \frac{1}{2}(z_{b_{j,k}} + z_{b_{j-1,k}})}{\Delta y}\right] v^{n+\frac{1}{2}}_{j,k}$$

$$- \left[\frac{\frac{1}{2}(\eta^{n+\frac{1}{2}}_{j,k-1} + \eta^{n+\frac{1}{2}}_{j,k}) - \frac{1}{2}(z_{b_{j,k-1}} + z_{b_{j-1,k-1}})}{\Delta y}\right] v^{n+\frac{1}{2}}_{j,k-1} \tag{4.14}$$

Each of the finite difference representations given by Eqs. 4.7 to 4.14 is a centered approximation. Apart from the stability problems usually associated with centered differences, the presence of nonlinear terms renders numerical solutions unmanageable. Nonlinear equations can only be solved by using iterative methods, which can often be plagued by convergence problems. On the other hand, linear equations enable a direct computation, and are, therefore, capable of economical solution schemes. By the judicious specification of known and unknown values in the finite difference equations, a representation that is linear in the unknowns is possible. The particular way in which the equations are linearized is not rigid, depending to some degree on the algorithm chosen to solve the equations. It should be noted that a certain amount of error is introduced into the analysis by the linearization process, because the temporal derivatives are replaced by off-centered difference approximations. The difference equations used in the linearized model corresponding to the first stage-implicit computation are the following:

X-Momentum (Linear Implicit)

$$\left.\frac{\partial u}{\partial t}\right|_{u_{j,k}^{n+\frac{1}{2}}} = \frac{u_{j,k}^{n+\frac{1}{2}} - u_{j,k}^{n}}{\frac{1}{2}\Delta t} \tag{4.15}$$

$$\left. u\frac{\partial u}{\partial x}\right|_{u_{j,k}^{n+\frac{1}{2}}} = u_{j,k}^{n+\frac{1}{2}}\left[\frac{u_{j+1,k}^{n} - u_{j-1,k}^{n}}{2\Delta x}\right] \tag{4.16}$$

$$\left. v\frac{\partial u}{\partial y}\right|_{u_{j,k}^{n+\frac{1}{2}}} = \left[\frac{v_{j,k-1}^{n} + v_{j+1,k-1}^{n} + v_{j,k}^{n} + v_{j+1,k}^{n}}{4}\right]\left[\frac{u_{j,k+1}^{n} - u_{j,k-1}^{n}}{2\Delta y}\right] \tag{4.17}$$

$$\left. g\frac{\partial \eta}{\partial x}\right|_{u_{j,k}^{n+\frac{1}{2}}} = g\left[\frac{\eta_{j+1,k}^{n+\frac{1}{2}} - \eta_{j,k}^{n+\frac{1}{2}}}{\Delta x}\right] \tag{4.18}$$

$$\left. f_r\, u\,\frac{(u^2+v^2)^{\frac{1}{2}}}{(\eta - z)}\right|_{u_{j,k}^{n+\frac{1}{2}}} =$$

$$\left[\frac{f_{r_{j,k}} + f_{r_{j+1,k}}}{2}\right]\left[\frac{u_{j,k}^{n+\frac{1}{2}}\left[(u_{j,k}^{n})^2 + \left(\frac{v_{j,k-1}^{n} + v_{j+1,k-1}^{n} + v_{j,k}^{n} + v_{j+1,k}^{n}}{4}\right)^2\right]^{\frac{1}{2}}}{\left[\frac{\eta_{j+1,k}^{n} + \eta_{j,k}^{n}}{2} - \frac{z_{b_{j,k}} + z_{b_{j,k-1}}}{2}\right]}\right] \tag{4.19}$$

Continuity (Linear Implicit)

$$\left.\frac{\partial \eta}{\partial t}\right|_{\eta_{j,k}^{n+\frac{1}{2}}} = \frac{\eta_{j,k}^{n+\frac{1}{2}} - \eta_{j,k}^{n}}{\frac{1}{2}\Delta t} \tag{4.20}$$

$$\frac{\partial}{\partial x}[(\eta - z_b)u]\Big|_{\eta^{n+\frac{1}{2}}_{j,k}} = \frac{\left[\frac{\eta^n_{j+1,k}+\eta^n_{j,k}}{2} - \frac{z_{b_{j,k}}+z_{b_{j,k-1}}}{2}\right] u^{n+\frac{1}{2}}_{j,k}}{\Delta x}$$

$$- \frac{\left[\frac{\eta^n_{j,k}+\eta^n_{j-1,k}}{2} - \frac{z_{b_{j-1,k}}+z_{b_{j-1,k-1}}}{2}\right] u^{n+\frac{1}{2}}_{j-1,k}}{\Delta x} \qquad (4.21)$$

$$\frac{\partial}{\partial y}[(\eta - z_b)v]\Big|_{\eta^{n+\frac{1}{2}}_{j,k}} = \frac{\left[\frac{\eta^n_{j,k+1}+\eta^n_{j,k}}{2} - \frac{z_{b_{j,k}}+z_{b_{j-1,k}}}{2}\right] v^n_{j,k}}{\Delta y}$$

$$- \frac{\left[\frac{\eta^n_{j,k}+\eta^n_{j,k-1}}{2} - \frac{z_{b_{j,k-1}}+z_{b_{j-1,k-1}}}{2}\right] v^n_{j,k-1}}{\Delta y} \qquad (4.22)$$

A simplified notation collecting known and unknown values will assist in the construction of the solution algorithm. Thus, the first-stage implicit step equations become:

X-Momentum (Implicit)

$$\frac{\partial u}{\partial t}\Big|_{u^{n+\frac{1}{2}}_{j,k}} = \frac{u^{n+\frac{1}{2}}_{j,k} - (UC)}{\frac{1}{2}\Delta t} \qquad (4.23)$$

$$u\frac{\partial u}{\partial x}\Big|_{u^{n+\frac{1}{2}}_{j,k}} = u^{n+\frac{1}{2}}_{j,k}\,(DCT) \qquad (4.24)$$

$$v\frac{\partial u}{\partial y}\Big|_{u^{n+\frac{1}{2}}_{j,k}} = (VAV)(CCT) \qquad (4.25)$$

$$g\frac{\partial \eta}{\partial x}\Big|_{u^{n+\frac{1}{2}}_{j,k}} = g\left[\frac{\eta^{n+\frac{1}{2}}_{j+1,k} - \eta^{n+\frac{1}{2}}_{j,k}}{\Delta x}\right] \qquad (4.26)$$

$$f_r\, u\,\frac{(u^2+v^2)^{\frac{1}{2}}}{(\eta - z_b)}\Big|_{u^{n+\frac{1}{2}}_{j,k}} = (FR)\,(FRT)\,u^{n+\frac{1}{2}}_{j,k} \qquad (4.27)$$

in which

$$UC = u^n_{j,k} \tag{4.28}$$

$$DCT = \frac{u^n_{j+1,k} - u^n_{j-1,k}}{2\Delta x} \tag{4.29}$$

$$VAV = \frac{1}{4}\left(v^n_{j,k-1} + v^n_{j+1,k-1} + v^n_{j,k} + v^n_{j+1,k}\right) \tag{4.30}$$

$$CCT = \frac{u^n_{j,k+1} - u^n_{j,k-1}}{2\Delta y} \tag{4.31}$$

$$FR = \frac{1}{2}\left(f_{r_{j,k}} + f_{r_{j+1,k}}\right) \tag{4.32}$$

$$FRT = \frac{[(UC)^2 + (VAV)^2]^{\frac{1}{2}}}{\left[\frac{\eta^n_{j+1,k} + \eta^n_{j,k}}{2} - \frac{z_{b_{j,k}} + z_{b_{j,k-1}}}{2}\right]} \tag{4.33}$$

Continuity (Implicit)

$$\left.\frac{\partial \eta}{\partial t}\right|_{\eta^{n+\frac{1}{2}}_{j,k}} = \frac{\eta^{n+\frac{1}{2}}_{j,k} - WL}{\frac{1}{2}\Delta t} \tag{4.34}$$

$$\left.\frac{\partial}{\partial x}[(\eta - z_b)u]\right|_{\eta^{n+\frac{1}{2}}_{j,k}} = \frac{DE}{\Delta x}\, u^{n+\frac{1}{2}}_{j,k} - \frac{DW}{\Delta x}\, u^{n+\frac{1}{2}}_{j-1,k} \tag{4.35}$$

$$\left.\frac{\partial}{\partial y}[(\eta - z_b)v]\right|_{\eta^{n+\frac{1}{2}}_{j,k}} = DDV \tag{4.36}$$

in which

$$WL = \eta^n_{j,k} \tag{4.37}$$

$$DE = \frac{1}{2}\left(\eta_{j+1,k} + \eta_{j,k} - z_{b_{j,k}} - z_{b_{j,k-1}}\right) \tag{4.38}$$

$$DW = \frac{1}{2}\left(\eta^n_{j,k} + \eta^n_{j-1,k} - z_{b_{j-1,k}} - z_{b_{j-1,k-1}}\right) \tag{4.39}$$

$$\mathrm{DDV} = \frac{\left[\frac{\eta^n_{j,k+1}+\eta^n_{j,k}}{2} - \frac{z_{b_{j,k}}+z_{b_{j-1,k}}}{2}\right] v^n_{j,k}}{\Delta y}$$

$$- \frac{\left[\frac{\eta^n_{j,k}+\eta^n_{j,k-1}}{2} - \frac{z_{b_{j,k-1}}+z_{b_{j-1,k-1}}}{2}\right] v^n_{j,k-1}}{\Delta y} \tag{4.40}$$

The presence of three unknown variables in the formulation of the x-momentum and continuity equations verifies the implicit nature of this representation. The linearization of the y-momentum equation is straightforward, since all the $u^{n+\frac{1}{2}}$ and $\eta^{n+\frac{1}{2}}$ values are known from the previous implicit half-stage.

<u>Y-Momentum (Explicit)</u>

$$\left.\frac{\partial v}{\partial t}\right|_{v^{n+\frac{1}{2}}_{j,k}} = \frac{v^{n+\frac{1}{2}}_{j,k}-v^n_{j,k}}{\frac{1}{2}\Delta t} \tag{4.41}$$

$$u\left.\frac{\partial v}{\partial x}\right|_{v^{n+\frac{1}{2}}_{j,k}} = \left(\frac{u^{n+\frac{1}{2}}_{j,k}+u^{n+\frac{1}{2}}_{j,k+1}+u^{n+\frac{1}{2}}_{j-1,k+1}+u^{n+\frac{1}{2}}_{j-1,k}}{4}\right)\left(\frac{v^n_{j+1,k}-v^n_{j-1,k}}{2\Delta x}\right) \tag{4.42}$$

$$v\left.\frac{\partial v}{\partial y}\right|_{v^{n+\frac{1}{2}}_{j,k}} = v^{n+\frac{1}{2}}_{j,k}\left[\frac{v^n_{j,k+1}-v^n_{j,k-1}}{2\Delta y}\right] \tag{4.43}$$

$$g\left.\frac{\partial \eta}{\partial y}\right|_{v^{n+\frac{1}{2}}_{j,k}} = g\left[\frac{\eta^{n+\frac{1}{2}}_{j,k+1}-\eta^{n+\frac{1}{2}}_{j,k}}{\Delta y}\right] \tag{4.44}$$

$$f_r\, v\left.\frac{(u^2+v^2)^{\frac{1}{2}}}{(\eta-z_b)}\right|_{v^{n+\frac{1}{2}}_{j,k}} =$$

$$\left(\frac{f_{j,k}+f_{j,k+1}}{2}\right)\left[\frac{v^{n+\frac{1}{2}}_{j,k}\left[(v^n_{j,k})^2+\left(\frac{u^n_{j,k}+u^n_{j,k+1}+u^n_{j-1,k}+u^n_{j-1,k+1}}{4}\right)^2\right]^{\frac{1}{2}}}{\left(\frac{\eta^{n+\frac{1}{2}}_{j,k+1}+\eta^{n+\frac{1}{2}}_{j,k}}{2} - \frac{z_{b_{j,k}}+z_{b_{j-1,k}}}{2}\right)}\right] \tag{4.45}$$

Known and unknown variables can be expressed in a simplified notation similar to that of the implicit step:

Y-Momentum (Explicit)

$$\left.\frac{\partial v}{\partial t}\right|_{v_{j,k}^{n+\frac{1}{2}}} = \frac{v_{j,k}^{n+\frac{1}{2}}-(VC)}{\frac{1}{2}\Delta t} \tag{4.46}$$

$$\left.u\,\frac{\partial v}{\partial x}\right|_{v_{j,k}^{n+\frac{1}{2}}} = CCT \tag{4.47}$$

$$\left.v\,\frac{\partial v}{\partial y}\right|_{v_{j,k}^{n+\frac{1}{2}}} = v_{j,k}^{n+\frac{1}{2}}\,(DCT) \tag{4.48}$$

$$\left.g\,\frac{\partial \eta}{\partial y}\right|_{v_{j,k}^{n+\frac{1}{2}}} = PRT \tag{4.49}$$

$$\left.f_r v\,\frac{(u^2+v^2)^{\frac{1}{2}}}{(\eta-z_b)}\right|_{v_{j,k}^{n+\frac{1}{2}}} = v_{j,k}^{n+\frac{1}{2}}\,(FRT) \tag{4.50}$$

in which

$$VC = v_{j,k}^{n} \tag{4.51}$$

$$CCT = \left(\frac{u_{j,k}^{n+\frac{1}{2}}+u_{j,k+1}^{n+\frac{1}{2}}+u_{j-1,k+1}^{n+\frac{1}{2}}+u_{j-1,k}^{n+\frac{1}{2}}}{4}\right)\left(\frac{v_{j+1,k}^{n}-v_{j-1,k}^{n}}{2\Delta x}\right) \tag{4.52}$$

$$DCT = \frac{v_{j,k+1}^{n}-v_{j,k-1}^{n}}{2\Delta y} \tag{4.53}$$

$$PRT = g\left[\frac{\eta_{j,k+1}^{n+\frac{1}{2}}-\eta_{j,k}^{n+\frac{1}{2}}}{\Delta y}\right] \tag{4.54}$$

$$FRT = \left(\frac{f_{r_{j,k}}+f_{r_{j,k+1}}}{2}\right)\frac{\left[(VC)^2+\left(\frac{u_{j,k}^{n}+u_{j,k+1}^{n}+u_{j-1,k}^{n}+u_{j-1,k+1}^{n}}{4}\right)^2\right]^{\frac{1}{2}}}{\left(\frac{\eta_{j,k+1}^{n+\frac{1}{2}}+\eta_{j,k}^{n+\frac{1}{2}}}{2}-\frac{z_{b_{j,k}}+z_{b_{j-1,k}}}{2}\right)} \tag{4.55}$$

Due to this selection of variables, the y-momentum equation is expressed in terms of a single unknown and can easily be solved by an explicit solution procedure. Applying the same techniques to the second-stage operations results in the following expressions:

Y-Momentum (Implicit)

$$\left.\frac{\partial v}{\partial t}\right|_{v_{j,k}^{n+1}} = \frac{v_{j,k}^{n+1}-(VC)}{\frac{1}{2}\Delta t} \tag{4.56}$$

$$\left.u\,\frac{\partial v}{\partial x}\right|_{v_{j,k}^{n+1}} = (UAV)(CCT) \tag{4.57}$$

$$\left.v\,\frac{\partial v}{\partial y}\right|_{v_{j,k}^{n+1}} = v_{j,k}^{n+1}\,(DCT) \tag{4.58}$$

$$\left.g\,\frac{\partial \eta}{\partial y}\right|_{v_{j,k}^{n+1}} = g\left[\frac{\eta_{j,k+1}^{n+1}-\eta_{j,k}^{n+1}}{\Delta y}\right] \tag{4.59}$$

$$\left.f_r v\,\frac{(u^2+v^2)^{\frac{1}{2}}}{(\eta-z_b)}\right|_{v_{j,k}^{n+1}} = (FR)\,(FRT)\,v_{j,k}^{n+1} \tag{4.60}$$

in which

$$VC = v_{j,k}^{n+\frac{1}{2}} \tag{4.61}$$

$$UAV = \frac{1}{4}\left(u_{j-1,k}^{n+\frac{1}{2}} + u_{j,k}^{n+\frac{1}{2}} + u_{j-1,k+1}^{n+\frac{1}{2}} + u_{j,k+1}^{n+\frac{1}{2}}\right) \tag{4.62}$$

$$CCT = \frac{v_{j+1,k}^{n+\frac{1}{2}}-v_{j-1,k}^{n+\frac{1}{2}}}{2\Delta x} \tag{4.63}$$

$$DCT = \frac{v_{j,k+1}^{n+\frac{1}{2}}-v_{j,k-1}^{n+\frac{1}{2}}}{2\Delta y} \tag{4.64}$$

$$FR = \tfrac{1}{2}\,(f_{r_{j,k}} + f_{r_{j,k+1}}) \tag{4.65}$$

$$FRT = \frac{[(VC)^2+(UAV)^2]^{\frac{1}{2}}}{\left[\dfrac{\eta_{j,k+1}^{n+\frac{1}{2}} + \eta_{j,k}^{n+\frac{1}{2}}}{2} - \dfrac{z_{b_{j,k}} + z_{b_{j-1,k}}}{2}\right]} \tag{4.66}$$

<u>Continuity (Implicit)</u>

$$\left.\frac{\partial\eta}{\partial t}\right|_{\eta_{j,k}^{n+1}} = \frac{\eta_{j,k}^{n+1} - WL}{\frac{1}{2}\Delta t} \tag{4.67}$$

$$\left.\frac{\partial}{\partial x}\,[(\eta - z_b)u]\right|_{\eta_{j,k}^{n+1}} = DDU \tag{4.68}$$

$$\left.\frac{\partial}{\partial y}\,[(\eta - z_b)v]\right|_{\eta_{j,k}^{n+1}} = \frac{DN}{\Delta y}\, v_{j,k}^{n+1} - \frac{DS}{\Delta y}\, v_{j,k-1}^{n+1} \tag{4.69}$$

in which

$$WL = \eta_{j,k}^{n+\frac{1}{2}} \tag{4.70}$$

$$DDU = \frac{\left[\dfrac{\eta_{j+1,k}^{n+\frac{1}{2}} + \eta_{j,k}^{n+\frac{1}{2}}}{2} - \dfrac{z_{b_{j,k}} + z_{b_{j,k-1}}}{2}\right] u_{j,k}^{n+\frac{1}{2}}}{\Delta x} - \frac{\left[\dfrac{\eta_{j,k}^{n+\frac{1}{2}} + \eta_{j-1,k}^{n+\frac{1}{2}}}{2} - \dfrac{z_{b_{j-1,k}} + z_{b_{j-1,k-1}}}{2}\right] u_{j-1,k}^{n+\frac{1}{2}}}{\Delta x} \tag{4.71}$$

$$DN = \left[\frac{\eta_{j,k+1}^{n+\frac{1}{2}} + \eta_{j,k}^{n+\frac{1}{2}}}{2} - \frac{z_{b_{j,k}} + z_{b_{j-1,k}}}{2}\right] \tag{4.72}$$

$$DS = \left[\frac{\eta_{j,k-1}^{n+\frac{1}{2}} + \eta_{j,k}^{n+\frac{1}{2}}}{2} - \frac{z_{b_{j,k-1}} + z_{b_{j-1,k-1}}}{2}\right] \tag{4.73}$$

<u>X-Momentum (Explicit)</u>

$$\left.\frac{\partial u}{\partial t}\right|_{u^{n+1}_{j,k}} = \frac{u^{n+1}_{j,k}-(UC)}{\frac{1}{2}\Delta t} \tag{4.74}$$

$$\left.u\,\frac{\partial u}{\partial x}\right|_{u^{n+1}_{j,k}} = u^{n+1}_{j,k}\,(DCT) \tag{4.75}$$

$$\left.v\,\frac{\partial u}{\partial y}\right|_{u^{n+1}_{j,k}} = CCT \tag{4.76}$$

$$\left.g\,\frac{\partial \eta}{\partial x}\right|_{u^{n+1}_{j,k}} = PRT \tag{4.77}$$

$$\left.f_r\,u\,\frac{(u^2+v^2)^{\frac{1}{2}}}{(\eta-z_b)}\right|_{u^{n+1}_{j,k}} = u^{n+1}_{j,k}\,(FRT) \tag{4.78}$$

in which

$$UC = u^{n+\frac{1}{2}}_{j,k} \tag{4.79}$$

$$DCT = \frac{u^{n+\frac{1}{2}}_{j+1,k}-u^{n+\frac{1}{2}}_{j-1,k}}{2\Delta x} \tag{4.80}$$

$$CCT = \left(\frac{v^{n+1}_{j,k}+v^{n+1}_{j+1,k}+v^{n+1}_{j+1,k-1}+v^{n+1}_{j,k-1}}{4}\right)\left(\frac{u^{n+\frac{1}{2}}_{j,k+1}-u^{n+\frac{1}{2}}_{j,k-1}}{2\Delta y}\right) \tag{4.81}$$

$$PRT = g\left[\frac{\eta^{n+1}_{j+1,k}-\eta^{n+1}_{j,k}}{\Delta x}\right] \tag{4.82}$$

$$FRT = \frac{\left(\frac{f_{r_{j+1,k}}+f_{r_{j,k}}}{2}\right)\left\{(UC)^2+\left[\frac{v^{n+\frac{1}{2}}_{j,k}+v^{n+\frac{1}{2}}_{j+1,k}+v^{n+\frac{1}{2}}_{j+1,k-1}+v^{n+\frac{1}{2}}_{j,k-1}}{4}\right]^2\right\}^{\frac{1}{2}}}{\left(\frac{\eta^{n+1}_{j+1,k}+\eta^{n+1}_{j,k}}{2}-\frac{z_{b_{j,k}}+z_{b_{j,k-1}}}{2}\right)} \tag{4.83}$$

4.6 SOLUTION ALGORITHMS

In the first-stage, the x-momentum and continuity equations as derived in section 4.5 are the following:

X-Momentum

$$\frac{u_{j,k}^{n+\frac{1}{2}}-(UC)}{\frac{1}{2}\Delta t} + u_{j,k}^{n+\frac{1}{2}}(DCT) + (VAV)(CCT) \tag{4.84}$$

$$+ g\left[\frac{\eta_{j+1,k}^{n+\frac{1}{2}}-\eta_{j,k}^{n+\frac{1}{2}}}{\Delta x}\right] + (FR)(FRT)\,u_{j,k}^{n+\frac{1}{2}} = 0 \tag{4.85}$$

Continuity

$$\frac{\eta_{j,k}^{n+\frac{1}{2}}-WL}{\frac{1}{2}\Delta t} + \frac{DE}{\Delta x}u_{j,k}^{n+\frac{1}{2}} - \frac{DW}{\Delta x}u_{j-1,k}^{n+\frac{1}{2}} + DDV = 0 \tag{4.86}$$

These equations can be rearranged and simplified to the following form:

X-Momentum

$$T\,\eta_{j,k}^{n+\frac{1}{2}} + A_j u_{j,k}^{n+\frac{1}{2}} - T\,\eta_{j+1,k}^{n+\frac{1}{2}} = B_j \tag{4.87}$$

in which

$$T = -\frac{g\Delta t}{2\Delta x} \tag{4.88}$$

$$A_j = 1 + \tfrac{1}{2}\Delta t\,[(FR)(FRT)+(DCT)] \tag{4.89}$$

$$B_j = UC - \tfrac{1}{2}\Delta t\,(VAV)(CCT) \tag{4.90}$$

Continuity

$$C_j\,u_{j-1,k}^{n+\frac{1}{2}} + \eta_{j,k}^{n+\frac{1}{2}} + D_j\,u_{j,k}^{n+\frac{1}{2}} = E_j \tag{4.91}$$

in which

$$C_j = -\frac{\Delta t}{2\Delta x}(DW) \tag{4.92}$$

$$D_j = \frac{\Delta t}{2\Delta x}(DE) \tag{4.93}$$

$$E_j = WL - \tfrac{1}{2}\Delta t\,(DDV) \tag{4.94}$$

The subscript j on the coefficients A, B, C, D, and E, indicates that a single line solution procedure is to be used, i.e., unknowns will be solved along one x-grid line at a time. Additionally, all variables are specified at the $(n+\frac{1}{2})\Delta t$ time level. Placing both equations into one matrix produces:

$$
\begin{array}{cccccccccccccc}
\eta_1 & u_1 & \eta_2 & u_2 & \cdot\cdot & \cdot\cdot & \cdot\cdot & \cdot\cdot & \eta_{N-1} & u_{N-1} & \eta_N & u_N & & \\
T & A_1 & -T & & & & & & & & & & = & B_1 \\
 & C_1 & 1 & D_1 & & & & & & & & & = & E_1 \\
 & & T & A_2 & -T & & & & & & & & = & B_2 \\
 & & & C_2 & 1 & D_2 & & & & & & & = & E_2 \\
 & & & & & & & & & & & & & \\
 & & & & & & & & T & A_{N-1} & -T & & = & B_{N-1} \\
 & & & & & & & & & C_{N-1} & 1 & D_{N-1} & = & E_{N-1}
\end{array}
$$

in which N is the number of grid points along the x-direction.

Two characteristics of this matrix are essential to its successful inversion. The first is the availability of 2(N-1) equations to solve for 2N unknowns. Thus, in order to adequately specify the problem before inversion of the matrix, two boundary conditions must be provided, one at the beginning of the line of unknowns and another at the end.

The second important characteristic of this matrix is the tridiagonal structure of its nonzero entries. This enables the use of the efficient tridiagonal algorithm to invert the matrix. Two manipulative "sweeps" through the tridiagonal matrix are required to determine the solution. After the specification of the "upstream" boundary condition, the first sweep generates four internal arrays as it moves through the matrix. The last sweep proceeds in the opposite direction using the arrays from the first sweep to calculate the unknown velocities and surface elevations. A detailed account of the tridiagonal algorithm is given below.

The linear nature of Eqs. 4.87 and 4.91 permit the following assumptions to be made:

$$\eta_j = P_j u_j + Q_j \tag{4.95}$$

$$u_j = R_j \eta_{j+1} + S_j \tag{4.96}$$

in which P_j, Q_j, R_j and S_j are internal solution vectors. These solution vectors are derived by substituting the above expressions into the indicial equations of continuity and momentum. If $u_{j-1,k}$ in Eq. 4.91 is replaced with a representation of the type in Eq. 4.96, the following equation results:

$$C_j (R_{j-1} \eta_j + S_{j-1}) + \eta_j + D_j u_j = E_j \tag{4.97}$$

rearranging,

$$\eta_j = - \frac{D_j}{C_j R_{j-1} + 1} u_j + \frac{E_j - C_j S_{j-1}}{C_j R_{j-1} + 1} \tag{4.98}$$

Comparing Eq. 4.98 with Eq. 4.95, P_j and Q_j are defined as follows:

$$P_j = - \frac{D_j}{C_j R_{j-1} + 1} \tag{4.99}$$

$$Q_j = \frac{E_j - C_j S_{j-1}}{C_j R_{j-1} + 1} \tag{4.100}$$

Similarly, if η_j from Eq. 4.95 is substituted into Eq. 4.87, R_j and S_j are defined:

$$R_j = \frac{T}{T P_j + A_j} \tag{4.101}$$

$$S_j = \frac{B_j - T\,Q_j}{T\,P_j + A_j} \tag{4.102}$$

The recursive formulas, Eqs. 4.99 to 4.102, interact in such a way that all the elements of each vector can be determined if a pair of values, either P_j and Q_j or R_j and S_j, are known. Fortunately, one of these two pairs is always defined when the "upstream" boundary condition is specified. Once arrays P, Q, R, and S are computed, the "downstream" boundary condition is substituted into the appropriate equation, Eq. 4.95 or 4.96, depending on whether a velocity or surface elevation condition is being used as a "downstream" boundary specification. Coordinating this pair of equations allows the remaining unknowns to be calculated. An example will serve to demonstrate the mechanics of the tridiagonal algorithm.

Let u_1 be the initial boundary condition so that Eq. 4.96 becomes

$$u_1 = R_1\,\eta_2 + S_1 \tag{4.103}$$

With η_2 unknown, the only known possible combination of R_1 and S_1 is: $R_1 = 0$ and $S_1 = u_1$. Therefore, P_2 can be determined from Eq. 4.99:

$$P_2 = -\frac{D_2}{C_2 R_1 + 1} = -D_2 \tag{4.104}$$

while Q_2 can be found by Eq. 4.100:

$$Q_2 = \frac{E_2 - C_2 S_1}{C_2 R_1 + 1} = E_2 - C_2\,(u_1) \tag{4.105}$$

From R_1, S_1, P_2, and Q_2, all other values can be found by repeated applications of the four recursive formulas. It should be noted that P_1 and Q_1 are necessary only to calculate η_1, a value which lies outside the boundary configuration. Since η_1 is not relevant to the tridiagonal algorithm, P_1 and Q_1 are not computed.

If the "downstream" boundary condition is η_N, Eqs. 4.95 and 4.96 can be used recursively to calculate the remaining unknowns, as follows:

$$u_{N-j} = R_{N-j}\,\eta_{N-j+1} + S_{N-j} \tag{4.106}$$

$$\eta_{N-j} = P_{N-j}\,u_{N-j} + Q_{N-j} \tag{4.107}$$

in which $\quad j = 1,2,\ldots,(N-1).$

Proceeding from row to row with the repeated use of the tridiagonal algorithm will identify all unknown velocities, $u^{n+\frac{1}{2}}_{j,k}$, and water surface elevations, $\eta^{n+\frac{1}{2}}_{j,k}$, in the first half-time step. The solution for each velocity, $v^{n+\frac{1}{2}}_{j,k}$, in the first-stage is by the direct application of the y-momentum equation derived in section 4.5:

$$\frac{v^{n+\frac{1}{2}}_{j,k}-(VC)}{\frac{1}{2}\Delta t} + (CCT) + v^{n+\frac{1}{2}}_{j,k}\,(DCT) + (PRT) + v^{n+\frac{1}{2}}_{j,k}\,(FRT) = 0 \tag{4.108}$$

Solving for the single unknown, $v^{n+\frac{1}{2}}_{j,k}$, the following expression is obtained:

$$v^{n+\frac{1}{2}}_{j,k} = \frac{VC-\frac{1}{2}\Delta t\ [PRT+CCT]}{1+\frac{1}{2}\Delta t\ [DCT+FRT]} \tag{4.109}$$

Eq. 4.109 enables the point-by-point explicit calculation of the values $v^{n+\frac{1}{2}}_{j,k}$.

The formulation for the second stage is derived in a manner similar to that of the first stage. Implicit calculations are based on the y-momentum and continuity equations in their simplified indicial form at time level $(n+1)\Delta t$.

Y-Momentum

$$T\,\eta_{j,k}^{n+1} + A_k\,v_{j,k}^{n+1} - T\,\eta_{j,k+1}^{n+1} = B_k \tag{4.110}$$

in which

$$A_k = 1 + \tfrac{1}{2}\,\Delta t\;[(FR)(FRT) + DCT] \tag{4.111}$$

$$B_k = VC - \tfrac{1}{2}\,\Delta t\;(UAV)(CCT) \tag{4.112}$$

Continuity

$$C_k\,v_{j,k-1}^{n+1} + \eta_{j,k}^{n+1} + D_k\,v_{j,k}^{n+1} = E_k \tag{4.113}$$

in which

$$C_k = -\,\frac{\Delta t}{2\Delta y}(DS) \tag{4.114}$$

$$D_k = \frac{\Delta t}{2\Delta y}(DN) \tag{4.115}$$

$$E_k = WL - \tfrac{1}{2}\,\Delta t\;(DDU) \tag{4.116}$$

The subscript k implies that, unlike the first stage which computed values along a constant y-coordinate, the implicit solution of a variable string in the second stage is performed along a constant x-coordinate.

Explicit determination of the velocity, u, is accomplished by the following equation:

$$u_{j,k}^{n+\frac{1}{2}} = \frac{UC - \tfrac{1}{2}\Delta t\;[PRT + CCT]}{1 + \tfrac{1}{2}\Delta t\;[DCT + FRT]} \tag{4.117}$$

which is a simplified form of the x-momentum equation as determined in section 4.5.

The four operations described in this section constitute the basic procedural loop of the mathematical model. Ancillary routines are also necessary in order to provide the information necessary for the execution of the multi-stage solution method. These routines include the spatial smoothing process, the boundary relocation, and the time relocation. The spatial smoothing has already been described in Chapter 3. Boundary relocations are covered in the following section of this chapter.

4.7 BOUNDARY SPECIFICATION AND RELOCATION

Two boundary types can be specified in the model: closed and open boundaries. At closed boundaries, the most convenient specification is the condition of zero mass flux (i.e., zero velocity) in a direction perpendicular to the boundary. This makes it necessary for the model boundary to closely follow the x-y grid. At open boundaries, either mean velocity or water surface elevation may be specified, depending on which one better satisfies the modeling needs.

Centered finite differences such as those used in this model require information which lies outside the boundaries of the computational model. When faced with this problem, Leendertse (13) chose to exclude from the computation the terms requiring information outside the boundaries, i.e., the difference analogs of the convective inertia terms at points neighboring the closed boundaries. Although a zero velocity tangential to the wall is a realistic assumption (the no-slip velocity condition), a zero water level at the boundary can be grossly inaccurate and may lead to numerical stability problems. A satisfactory alternative is the relocation of interior values. A simple relocation technique was chosen in which exterior values were defined to be equal to those interior values adjacent to the boundaries. This is tantamount to a perfect slip condition, a reasonable assumption in turbulent flows in which the viscous effects have little influence on the horizontal velocity distribution. Flokstra's theoretical argument (6) that the no-slip condition is a requisite for the generation of secondary currents is in disagreement with the boundary relocation method used in this model.

4.8 NUMERICAL STABILITY

A pervasive problem in two-dimensional mathematical modeling is the lack of adequate theoretical numerical stability criteria. Physically speaking, instability occurs when small discontinuities in velocity generate short waves. The explicit-mode pressure term then becomes very significant, increasing the velocity discontinuity. After a few time steps, both velocities and water surface elevations increase unbounded, spoiling the entire calculation.

Linear stability theory classifies the multi-operational mode computation procedure as unconditionally stable. However, experience (25) has shown that it is only weakly stable. Two types of instability are associated with the procedure: nonlinear and Courant condition. Although this model is solved by a linearized scheme of finite differences, instabilities occur due to the nonlinear nature of the continuum system of equations. The nonlinear terms in the governing equations interact in such a manner as to transfer energy to progressively smaller scales. In the numerical model, characteristic lengths less than twice the spatial increment, $2\Delta x$, cannot be resolved by the grid, thus interrupting the energy cascade. The accumulation of energy at the grid level is thought to cause the numerical instabilities that occur during simulations of long duration. This type of error growth can be handled by the introduction of a sufficient amount of numerical diffusion in the formulation, in order to dissipate the energy piled up at the grid scale. Flokstra (7) has pointed out that three techniques are available to generate numerical diffusion. The first method implicitly creates diffusion by the selection of a difference scheme affected with numerical viscosity. A second method involves the explicit inclusion of an extra dissipation term in the difference equations. The technique used in this model introduces numerical diffusion by a velocity averaging routine which also happens to mimic the contribution of the effective stresses. Since this routine is not included in the equations defining the problem, the amount of numerical diffusion produced is dependent on the discretization parameters of the model, i.e., on Δx and Δt.

Courant stability criteria apparently does exist, although it is not clear how the physical and numerical variables interact to define the stability conditions. The variables that contribute to instability appear to be the mean velocity, flow depth, weighting factor for spatial smoothing, spatial increment, and time increment. A comprehensive theoretical stability criteria taking into account these parameters has yet to be formulated.

CHAPTER 5

NUMERICAL EXPERIMENTATION

5.1 INTRODUCTION

This chapter is a presentation of test results from numerical experiments performed with the depth-averaged model described in Chapter 4. A detailed discussion of the entire testing program is given in Chapter 6.

The objective of these experiments is the clarification of the circulation mechanism found in free surface water flow. Organization of this chapter basically reflects the manner in which the actual testing took place. Two hypothetical configurations are used and comprise the major headings (5.2 and 5.3) of this chapter. Subheadings are devoted to differences in handling the initial and boundary conditions, each subheading containing the results of a fairly standard battery of tests. These tests fall into three categories: (1) term, (2) parameter, and (3) combined. Term and parameter tests are sensitivity analyses of individual elements in the problem, terms being quantities found in the equation set, e.g. convective inertia; parameters being single variables, e.g., depth. Combined tests are simply experiments in which more than one element has been varied from the baseline to determine the interaction between components of the problem.

A computer plotting routine has been designed to facilitate visualization of all results from the testing program. The plots displayed are velocity vectors emanating from each grid point in the configuration. For the most part, plots are available at intervals of 50 time steps.

The purpose of this study is a fundamental investigation of the circulating flow mechanism, not the depiction of circulation in the context of a particular geometry. No attempt has been made to independently verify the magnitudes of the flow velocities observed. Confirmation of modeled phenomena is especially a shortcoming attendant to studies where secondary flow is involved. Indeed, the paucity of available field data has required physical model studies to evaluate the acceptability of numerical simulations.

Another limitation to the applicability of these test results is the steady nature of the problem considered. Although the unsteady capability of the mathematical model allows an arbitrary initial specification to achieve steady state, no tests have been performed which retain time dependent boundary conditions. Intuitively, the general derivation of the mathematical model would lead to the conclusion that a full range of application is possible. However, without detailed testing of unsteady flow situations, no such statement can be made.

5.2 POOL MODEL

The bulk of the testing program consists of experiments performed on the pool-channel system shown in Fig. 5.1. Channel dimensions are 4 meters in width by 30 meters in length while the pool is a 14 meter by 15 meter rectangle. Four series of tests are executed on this configuration, differing only in the initial and boundary conditions specified.

5.2.1 Channel Velocity Specified

In this testing series, a 0.5 meter per second velocity is specified in the channel as an initial condition and at the upstream end as a steady boundary condition. A water depth of 2.5 meters serves as both the initial condition and the steady downstream boundary condition. There is no velocity in the pool initially. Closed boundaries are represented by zero velocities perpendicular to walls. Without bed slope, the water in the configuration is driven solely by the upstream entrance velocity. Numerical parameters used in the baseline are weighting factor $\alpha = 0.1$; spatial increment $\Delta x = \Delta y = 1.0$ meter; and temporal increment $\Delta t = 1.0$ second.

The use of a completely specified velocity distribution in the channel as an initial condition is in response to difficulties encountered in introducing an entrance velocity into a motionless system. Waves which eventually lead to instability, set up immediately when such a boundary condition is attempted.

The development of circulation in the baseline case is seen in Figs. 5.2 to 5.6. Flow diverges from the mainstream as increasing velocities in the shear layer at the south end of the pool drive a weak circulation. Time step 80 reveals a well-developed circulation centered at coordinates (16.5,9). From time step 80 to time step 200, the center of circulation drifts to (18,10), a position two meters to the right of the pool centerline. A well developed circulation requires little or no divergence from the mainstream as the later plots illustrate.

A detailed analysis of the velocities and surface elevations indicates that a steady state has yet to be attained at the 200th and final time step. Velocities in the exit channel farthest from the pool increase to 0.58 meters per second while those nearest the pool decrease to 0.43 meters per second. Water levels in the pool increase in a general fashion from 2.50 to 2.52 meters with the highest depths found at the north and east sides of the pool. Entrance levels, however, fall continuously from 2.50 to 2.44 meters.

The first group of tests performed on the channel velocity-specified pool model is with terms found in the hydrodynamic equations. More specifically, the effective stresses, convective inertia, and friction are tested in this section.

Effective Stresses

In this numerical model, the representation of the effective stresses is not explicit in the discretized equation set found in Chapter 4. Rather, the action of the effective stresses is simulated by a velocity averaging technique which employs a weighting factor α to vary the magnitude of the effect. The necessity of modeling the effective stresses where physical circulation is present has been explained theoretically by Flokstra (6).

This test is designed to completely remove the effective stresses from the model by setting the weighting factor α to zero. Figure 5.7 is a plot taken at 150 time steps (seconds). There is negligible transfer of momentum from the mainstream to the pool. With no flow divergence into the pool, the initial conditions are virtually preserved. Data from the 190th (final) time step exhibit a tendency toward instability manifested by discontinuities in velocity and depth.

Convective Inertia

The convective inertia terms, $u\,\frac{\partial u}{\partial x}$, $v\,\frac{\partial u}{\partial y}$, $u\,\frac{\partial v}{\partial x}$, and $v\,\frac{\partial v}{\partial y}$, are often neglected in numerical modeling because the nonlinearity introduced by these terms is difficult to handle. Various authors have commented on the necessary presence of the convective inertia terms in the equation set when secondary flow is to be resolved.

To test this conclusion, all four convective inertia terms were set to zero. The plot at 100 time steps is presented in Fig. 5.8. Divergence of the flow from the channel into the pool is strong; however, no circulation sets up. As water in the channel reaches the upstream end of the pool, flow immediately is directed into the pool along the boundaries, preventing circulation from occurring. During the 100 second study period, velocities in the exit channel farthest from the pool have generally fluctuated between 0.50 and 0.52 meters per second while those velocities nearest the pool exited at 0.47 to 0.49 meters per second. Entrance water levels oscillated between 2.50 and 2.51 while the pool was steady at 2.50 meters.

In an attempt to further clarify the phenomenon of convective inertia, the effects of the cross-convective inertia terms, $v \frac{\partial u}{\partial y}$ and $u \frac{\partial v}{\partial x}$, were isolated from those of the direct-convective terms, $v \frac{\partial v}{\partial y}$ and $u \frac{\partial u}{\partial x}$. This was accomplished by setting only the cross-convective terms to zero in one test, and only the direct-convective terms to zero in another test. Figures 5.9 to 5.11 are plots at 50 time step intervals reflecting the omission of the cross-convective inertia terms. At 50 time steps, no circulation is apparent although momentum transfer in the shear layer is being accompanied by divergence from the main flow. More curvature and a crude circulation are visible in the plot at 100 time steps. A weak but well formed circulation has set up at (15,10) in the last plot, with mainstream divergence decreasing. Exit velocities are stable with the channel velocity farthest from the pool equal to 0.56 meters per second and the velocity nearest the pool equal to 0.43 meters per second. Over the duration of the study period, the entrance elevation drops slowly from 2.50 meters to 2.49 meters, while the pool elevation rises slowly from 2.50 to 2.51 meters.

The results of the converse test, with the direct convective inertia removed, are illustrated in Figs. 5.12 to 5.14. At 50 time steps a weak circulation is centered at coordinates (14,9). Divergence from the main flow is strong and the velocities in the shear layer are comparatively higher than the previous test. Time steps 100 and 150 display well formed circulation not unlike the baseline, with mainstream divergence decreasing.

Quantitative results show that exit velocities are fairly steady, 0.55 meters per second farthest from the pool and 0.45 meters per second nearest to the pool. Like the baseline, the entrance water level dropped steadily from 2.50 to 2.44 meters, while the pool increased slowly from a water level of 2.50 to 2.52 meters with the highest levels found at the north and east sides of the pool.

Friction

In the literature, the role of friction in circulation is a controversial subject. Leendertse removed the modeling of effective stresses from his 1967 model by claiming that the magnitude of the friction terms far exceeded those of the effective stress terms. Abbott believes the occurrence of circulation to be the result of the resistance forces overcoming the dynamic forces. However, Flokstra considers the bottom resistance to be of secondary importance when compared with the no-slip condition at the wall. As mentioned earlier, the relocation routine for dependent variables at closed boundaries in this model is tantamount to a perfect slip velocity condition.

The friction terms, $f_r u \frac{\sqrt{u^2+v^2}}{(\eta - z_b)}$ and $f_r v \frac{\sqrt{u^2+v^2}}{(\eta - z_b)}$ are eliminated from the computation by setting $f_r = 0$. Figure 5.15 is the plot at 100 time steps for this frictionless experiment. Both the plot and the detailed quantitative results are virtually indistinguishable from the baseline.

The next section is a collection of tests performed on the channel velocity-specified pool model by varying single parameters; essentially, a sensitivity analysis. Physical parameters, specifically velocity, depth, and friction factor, are tested first to identify and verify previously reported observations. Then, the numerical parameters, α, Δx, and Δt, are experimented with to reveal the effects of a discrete representation of reality.

Channel Velocity

This series of tests is designed to explore the effects of using a wide range of channel velocities in the model. Three velocities were tested: 1.0, 0.75, and 0.25 meters per second. All three tests developed circulating patterns in the pool area, however, the 1.0 meter per second and 0.75 meter per second velocities became unstable at 60 and 140 time steps, respectively. Plots of these runs before instability set in are shown in Figs. 5.16 and 5.17. These plots show that despite impending stability problems, strong and well developed circulations do occur. Characteristically, the instabilities found in the first two runs begin in the channel with discontinuities in water surface and velocity. The effect is pervasive as the entire computation is soon spoiled. Figures 5.18 to 5.20 are plots of circulation developing in the case of channel velocity equal to 0.25 meters per second. Compared with the baseline in real time, the smaller velocity sets up as quickly, with a more round and symmetrical circulation. The channel exit velocities are very steady, 0.28 meters per second farthest from the pool and 0.21 meters per second nearest the pool. Entrance and pool water levels are also very stable at the originally specified 2.50 meters.

Depth

The effect of an increase in depth has been documented by Bengtsson (3) following experiments performed on a lake model. His conclusion was that the influence of the horizontal turbulence terms was reduced with increasing depth. Horizontal dispersion of momentum is simulated by the effective stress terms in this model, i.e., the closure terms $\varepsilon\left(\frac{\partial^2 u}{\partial x^2} + \frac{\partial^2 u}{\partial y^2}\right)$ and $\varepsilon\left(\frac{\partial^2 v}{\partial x^2} + \frac{\partial^2 v}{\partial y^2}\right)$. It is therefore not obvious how depth should affect these terms.

Many tests were performed in this series due to the relative insensitivity of this parameter to stability criteria. Depths ranging from 0.04 to 50 meters were used in this experiment with instability occurring only in the 0.04 meter run. Single plots of salient results from the 0.16, 10.0, and 30.0 meter depths are shown in Figs. 5.21 to 5.23, while complete sets of plots for 0.04, 0.62, and 50.0 meter depths are shown in Figs. 5.24 to 5.31. Shallower depths have more divergence from the channel, larger velocities in the shear layer, and faster set up of circulation. In the extreme, however, the shallow depth is also subject to instability. Larger depths have less energy transfer to the pool and consequently little or no circulation. Although increased depth has a stabilizing influence on the computations, both large and small depth tests exhibit minor oscillations which are nonconvergent. At the entrance to the channel, depths vary between 49.95 to 50.04 meters and 0.623 to 0.644 meters in two extreme cases. Exit velocities for the 50 meter depth range from 0.573 to 0.580 meters per second at the south side of the channel to 0.391 to 0.398 meters per second at the north side, while the 0.62 meter depth velocities were 0.550 to

0.569 meters per second and 0.441 to 0.450 meters per second at the same locations. In the pool area, the location of deeper water alternates from west and south to east and north with an absolute variation of about 0.01 meters, irrespective of depth.

Friction

In earlier testing, the omission of friction was found to have a negligible effect as compared to the baseline data. This series of experiments is designed to determine what magnitude of friction factor, f_r, would be necessary to alter the baseline flow pattern. To this end, the nondimensional friction factor, f_r, is increased to roughly two and four times the baseline value, i.e. 0.01 and 0.02. The selection of 0.02 as the upper limit for this test is based on practical constraints of possible channel roughness. Plots for these two runs at time step 100 are shown in Figs. 5.32 and 5.33. A comparison of the baseline plot with these figures shows no detectable differences. Closer examination of the quantitative results show that higher friction increases water levels slightly and mildly damps velocity.

Weighting Factor

In this model, the velocity averaging routine serves a dual purpose: 1) a spatial smoothing device, and 2) a numerical analog of the mechanism for turbulent momentum transfer. The latter is usually attributed theoretically to the effective stresses and represents the closure assumption necessary in turbulence models. The parameter α, the weighting factor of the averaging routine, controls the intensity of the averaging effect. However, other than the theoretical limits of 0.0 and 1.0, no physical basis is available to choose the value of α. The purpose of this test is to assess the manner in which the averaging routine affects the computation.

Two sets of experiments are designed. The first set consists of six tests, each with a different α specified. The second set contains two tests in which α is changed during the simulation.

In the first set of tests, α was varied from 0.01 to 10.0. Both extremes became unstable, the 0.01 run at 170 time steps and the 10.0 run almost immediately. Figures 5.34 to 5.43 are plots at 50 and 100 time steps for α = 0.01, 0.2, 0.4, 0.8, and 1.0.

For $\alpha = 0.01$, a crude circulation sets up in the southeast corner of the pool and then disintegrates into a gradually developing instability. Generally speaking, the other plots with α = 0.2 to 1.0 are not very different from each other. Strong, well formed circulation is present in each case. As α is increased, divergence from the mainflow increases, shear layer velocities increase, and circulating velocities increase. Characteristically, large α runs possess flattened, less circular flow patterns in the pool where the center of circulation is higher and more west of center than the smaller α runs. Examination of the quantitative results shows that higher α reduces the range of extreme velocities at the exit. The $\alpha = 1.0$ run is extremely steady in all aspects. Whereas the baseline ($\alpha = 0.1$) entrance elevation falls continuously, runs with α greater than 0.1 and less than 1.0 have an oscillating entrance level with amplitude decreasing for increasing α. The maximum amplitude is 0.03 meters for the $\alpha = 0.2$ case. Similarly, pool elevations increase in an oscillating manner for this range of α, with the highest and most convergent water levels associated with the largest α.

Results from previous α testing led to questions concerning the nature of the circulation that formed in the pool. Once the circulation sets up, is there a continuous dependence on the effective stresses to maintain that circulation? If so, could the intensity of the effective stresses be reduced upon the advent of circulation? The first question is answered by running baseline conditions for 100 time steps and then setting α to zero for the remaining time steps. Results of this test appear in Figs. 5.44 to 5.48. At time step 80, a well formed circulation sets up as expected. After 20 time steps without the influence of the effective stresses, i.e. time step 120, the circulation has moved towards the east boundary and is still strong and well formed. However, at time step 160 the circulation has moved too near the wall and is rapidly losing the original flow structure. By time step 200, instability has set in and the computation is on the verge of being completely spoiled.

The second question is tested by using $\alpha = 1.0$ for the first 100 time steps and $\alpha = 0.01$ for the remainder of the study period. Plots of this experiment appear in Figs. 5.49 to 5.52. The circulation sets up before α is reduced. At time step 120, 20 time steps under the $\alpha = 0.01$ weighting factor, the circulating velocities have increased, accompanied by a rounder flow pattern in the pool. As time step 160 takes place, it is obvious that instability once again destroys the circulation and eventually the entire computation.

Time Increment

The time increment, Δt, like the space increments, Δx and Δy, is fundamental to the understanding of the numerical properties of a discrete model. Although found only in the local acceleration term, the time increment has important ramifications upon model stability. Particularly in explicit schemes, strict stability criteria involving the discretization parameters often renders an experiment economically infeasible. The fact that this numerical model does contain explicit computational schemes behooves an investigation into Δx, Δy and Δt.

In this experiment, two values of Δt are run, 0.5 and 2.0 seconds. Figures 5.53 and 5.54 are plots at 50 and 100 time steps with $\Delta t = 0.5$ seconds. Compared with the baseline, this run sets up a stronger, better formed circulation in less real time. Generalizing the detailed data from this test, runs with smaller time increments have less spatial velocity variation at the exit and are very steady with respect to velocity and water levels at all locations.

Figure 5.55 is the result at 50 time steps when Δt is set to 2.0 seconds. A well formed circulation, weaker than the real time baseline equivalent, sets up only to become completely unstable at the 100th time step. The shear layer for this large Δt is quite weak and without noticeable flow divergence from the channel.

Space Increment

Despite being a numerical parameter by nature, the space increment has a profound physical effect upon the spatial derivatives, inasmuch as the problem size has changed. To determine the magnitude of this effect, three tests varying the space increment from 0.1 to 10.0 meters were performed. The 0.1 meter space increment became unstable at 15 time steps, before circulation could set up. Instability also plagued the run with $\Delta x = \Delta y = 0.5$ meters at 100 time steps. However, as Fig. 5.56 illustrates, a well formed circulation did occur prior to the onset of instability. The final test, setting $\Delta x = \Delta y = 10$ meters appears in Fig. 5.57. The run was completely stable although only a weak, incoherent circulation occurred at 100 time steps. These results look very similar to the test in which the convective inertia terms were omitted from the simulation. Increasing the size of the problem tends to damp velocity and gradually increase water level throughout the configuration. The resulting water slope at 100 time steps in the channel is 0.00067.

The following section contains the final tests performed on the channel velocity-specified pool model. After the behavior of the model was identified for individual terms and parameters in previous sections, numerous questions arose as to the nature of these results. The search for unifying theories was a foremost consideration in the development of this phase of the testing program. All tests have at least two elements which deviate from the baseline.

Weighting Factor

Results of the experiments on the weighting factor, α, indicate that α is important to the circulation phenomenon and has a stabilizing effect upon the computations. It is these attributes that have provoked this series of tests.

Up until this point, circulation has not taken place where either the velocity averaging routine or the convective inertia has been absent. This test removes both elements simultaneously by setting α and the convective inertia terms to zero. The plot at time step 100 appears in Fig. 5.58. For all practical purposes there is no change from the initial conditions as momentum from the channel has not transferred to the pool.

The next test involves the diffusivity ε of the closure terms $\varepsilon(\frac{\partial^2 u}{\partial x^2} + \frac{\partial^2 u}{\partial y^2})$ and $\varepsilon\,(\frac{\partial^2 v}{\partial x^2} + \frac{\partial^2 v}{\partial y^2})$. The constant ε is defined to be equal to $\alpha\,\frac{(\Delta x)^2}{\Delta t}$. The objective of this experiment is to find common behavior when α and Δx are varied in such a manner as to preserve the baseline value of diffusivity. To produce this effect, α is reduced to 0.001 and Δx is increased to 10 meters. Results of this test at 150 time steps are plotted in Fig. 5.59. Only a negligible effect is visible in the pool as a slight divergence of flow from the channel and relatively small velocities in the shear layer are not sufficient to transfer momentum. The data indicate a very steady water level of 2.51 meters in the pool and at the channel entrance. Exit velocities show an increasing trend.

Large α has been shown to increase energy transfer to the pool area in earlier tests. However, the ability of α to overcome the velocity and circulation damping effects of large depth is unknown. This experiment seeks to provide information to determine the potential of the weighting factor in the context of strong damping.

Two sets of conditions are tested. The first test sets α to 1.0 while the depth is 50 meters. Figure 5.60 is the plot at 50 time steps. A well formed circulation sets up rapidly with high velocities in the pool. The run is very steady; plots at 100 and 150 time steps are not included since they were identical to the one plot presented. Exit velocities are 0.60 meters per second on the south side of the channel and 0.37 meters per second on the north side. The entrance elevation is 50.06 meters while the pool elevations range from 49.96 meters on the west side to 50.03 meters on the east side.

The second test was designed to balance the instability of an extremely large weighting factor with the damping effects of large depth. For this test 50 meters was again used as the depth while an α of 10.0 was specified. A value of 10.0 is outside the theoretical range of α, but it was desired to learn about such behavior. The simulation was highly unstable, lasting for less than 10 time steps.

The final weighting factor experiment in this section concerns the spatial smoothing properties of the velocity averaging routine. Observations from the sensitivity analysis with α, indicate that higher α tends to improve convergence to a steady state. Could a previously unstable set of conditions become stable merely by increasing the weighting factor? To answer this question, the unstable channel velocity 1.0 meters per second was treated with three weighting factors: 0.2, 0.4, and 1.0. In the original test with a 1.0 meter per second velocity, circulation set up before the computation became unstable at the 60th time step. The weighting factor used was the baseline value of 0.1.

Figure 5.61 is a plot at 50 time steps of the $\alpha = 0.2$ run. A strong well-formed circulation, which is strikingly similar to the baseline plot at 100 time steps, sets up before instability spoils the result at 80 time steps. This is 20 time steps longer than the $\alpha = 0.1$ test performed earlier.

The results for the $\alpha = 0.4$ test are in Figs. 5.62 to 5.64. At 50 time steps, a strong, perfectly centered circulation has set up. The current structure is still intact at time step 100 but increasing divergence from the channel and very large velocities in the shear layer soon disrupt the symmetry of the circulation. Quantitative results indicate that the last time step (190 seconds) is tending toward instability, judging from the discontinuities in velocity and water surface that are present.

A plot from the third test with $\alpha = 1.0$ appears in Fig. 5.65. Although the result displayed is from the 50th time step, it is identical to all subsequent plots. Circulation has set up strongly centered high in the pool at coordinates (15,11). The flow structure is well formed and extremely steady despite the presence of small flow inconsistencies in the southeast corner of the pool. Water level at the channel entrance is gradually rising to 2.57 meters while exit velocities are stable at 1.15 meters per second at the south wall and 0.92 meters per second at the north wall. Pool elevations are very steady, 2.55 meters at the west wall and 2.56 meters at the east wall.

Stability Criteria

Three parameters from the single parameter experiments, U, Δx, and Δt, displayed high sensitivity to instability. The fact that large stream velocities and time increments, as well as small space increments, caused stability problems, encouraged investigation into a Courant-type stability condition. According to this theory, if a given ratio of physical celerity to grid celerity results in a stable simulation, all other simulation with that particular ratio will also be stable. The converse argument with unstable simulations is also true. Normally, the physical celerity is taken to be the relative inertial wave celerity, $\sqrt{gd}$. However, previous testing indicates channel velocity, U, to be the celerity of interest. Grid celerity is always $\Delta x/\Delta t$. Thus, the Courant number for this model is $U \, \Delta t/\Delta x$, e.g., 0.5 for the baseline case.

In an earlier test, a time increment of 2.0 seconds caused instability. If a Courant condition does exist, then any Δt could be used as long as Δx and/or U was changed so as to create a Courant number within known stable constraints. This idea was tested by increasing Δt to 10 seconds and increasing Δx to 10 meters, preserving the stable baseline Courant number of 0.5. Plots at 50 and

100 time steps are in Figs. 5.66 and 5.67. Circulation sets up much as the baseline at similar time steps. Flow divergence from the channel into the pool is strong with high velocities in the shear layer. Detailed data show steady exit velocities of 0.55 meters per second along the south wall and 0.44 meters per second along the north wall. Entrance water levels oscillate between 2.50 and 2.53 meters while pool levels have increased in an oscillating manner to 2.52 meters.

To fully test the numerical stability theory described in this section, two other tests are proposed, both utilizing a channel velocity of 1.0 meter per second. This velocity in the context of the baseline conditions results in unstable representations. The first test reduces the baseline Δt to 0.5 seconds to restore the Courant number back to the "stable" value, 0.5. Results of this test appear in Figs. 5.68 to 5.70. At time step 50, a well formed circulation accompanied by high velocity shear flow and divergence from the channel takes place. In the next plot, circulating velocities have increased as the vorticity center has moved towards the east wall of the pool. The final plot at 150 time steps shows increased velocity in the north and east pool area with divergence from the channel increasing once more. Quantitative results reveal a diverging oscillation of exit velocities at the last time step: 1.07 to 1.16 meters per second along the south wall and 0.83 to 0.91 meters per second along the north wall. A similar phenomenon occurs at the entrance, where the final oscillation in water level is from 2.34 to 2.68 meters, and in the pool, where the range is 2.47 to 2.56 meters. High points on the pool surface oscillate from southwest to northeast.

The final test of the stability criteria matches a spatial increment of 2.0 meters with the previously used 1.0 meter per second channel velocity. $U \frac{\Delta t}{\Delta x}$ is again equal to 0.5. Plots for this test are in Figs. 5.71 to 5.73. Circulation at time step 50 is not strong but well formed at coordinates (15,9). As circulating velocities increase, the center moves to (18.5,9.5) at 100 time steps. The final plot displays increasing velocities near the east wall of the pool as channel flow divergence is reasserted. Explicit results are very similar to those found in the previous test. Oscillation characterizes all dependent variables: velocities of 1.07 to 1.16 meters per second and 0.83 to 0.92 meters per second at the extremes of the exit, 2.33 to 2.70 meter depths at the entrance, and water levels 2.47 to 2.57 meters in the pool. All values are taken from the last 20 time steps of the simulation.

Large Scale Friction

This is the final experiment performed on the channel velocity-specified pool model. Previous experiments with friction appear to dismiss the importance attached to it by some authors. However, no friction-related tests have been attempted on problems where the spatial increment was larger than 1.0 meter. To this end, three tests are run.

The first test increases $\Delta x = \Delta y$ to 10.0 meters and the nondimensional friction factor f_r to 0.04. Figures 5.74 to 5.76 are plots at 50,100, and 150 time steps. Apparently, this combination of friction and scale precludes the generation of circulation. Flow from the channel diverges immediately into the west side of the pool only to exit at the southeast corner. As the simulation continues, channel divergence sends currents deeper into the pool with increasing velocity but still without circulation. Data from this run suggests that a steady state has not been achieved. Exit velocities are increasing continuously from 0.34 meters per second at the 60th time step to 0.52 meters per second at the final time step (190). Water levels at the entrance increase steadily, though a convergence to 2.60 meters is seen in the last 50 time steps. In the pool, water levels rise throughout the simulation to 2.57 meters, however, the location of the deeper water fluctuates from west to east.

The next test consists of removing frictional effects in a large scale model. Experience from the stability analysis testing led to the use of a time increment of 100 seconds to accompany the scale increase to 100 meters per space interval. The friction factor was set to zero. Figures 5.77 to 5.79 are plots taken at 50, 100, and 150 time steps of this run. The development and structure of the circulation is for all practical purposes identical to the baseline, even in the detailed numerical results.

The results of the previous test encouraged the final test of this series. Baseline friction, $f_r = 0.0045$, is used with the same numerical parameters as before, $\Delta x = \Delta y = 100$ meters and $\Delta t = 100$ seconds. Results at the 50th time step are plotted in Fig. 5.80. The steadiness of this run permitted the omission of plots at 100 and 150 time steps. Flow diverges immediately into the pool near the upstream wall, penetrating to the center, before leaving the pool along the downstream wall. The flow pattern is very similar to that seen in an earlier test in which convective inertia was removed. Exit velocities across the channel range from 0.54 to 0.49 meters per second. Stream elevations display a slope of 0.00033 starting with 2.60 meters upstream and ending with 2.50 meters downstream. The pool surface is perfectly horizontal at 2.56 meters.

5.2.2 Slope Specified

In a mathematical model, the interaction of the initial and boundary conditions with the partial differential equation set is what determines the unique solution. Therefore, to be consistent with the fundamental objectives of this study, the numerical experiments performed must include various combinations of initial and boundary conditions.

Baseline

A bed slope and new specifications for the channel are introduced into the configuration used in section 5.2.1. The 0.0005 bottom slope in this testing series applies to the entire channel-pool system. A water slope parallel to the bed at a depth of 2.5 meters replaces the velocity specification previously used as the initial condition. Open boundary conditions at the channel end points are water levels which correspond to the initial slope condition. Closed boundaries remain to be defined by zero perpendicular velocities. All other parameters are the same as in the channel velocity-specified testing baseline, i.e. α = 0.1, $\Delta x = \Delta y$ = 1.0 meter, Δt = 1.0 second, and f_r = 0.0045.

Plots of the baseline at various stages of development are in Figs. 5.81 to 5.83. In the first plot at 50 time steps, flow from the channel diverges strongly into the pool and exits without circulating. As velocities increase at time step 100, divergence of flow into the pool occurs only on the downstream half of the shear layer causing a crude circulation to set up in the southwest corner of the pool. In the final plot, a perfectly centered circulation develops at coordinates (16,9.5).

The detailed output displays a very stable and continuous water surface despite continually increasing velocities. Although the initial water slope is preserved in the channel for the most part, higher slopes are noticed at the downstream junction of the pool and channel. The pool surface is horizontal with an average depth of 2.50 meters. Channel velocities increase throughout the simulation without achieving a steady state. There is an upstream effect on the distribution of velocity across the channel entrance. Higher velocity occurs along the north wall while the opposite behavior is found at the channel exit. It should be noted that the steady channel velocity associated with this configuration and friction factor is 1.1 meters per second. The final velocity observed during the 190 time steps simulation is 0.70 meters per second, which implies that a steady state has not developed. However, the time required to obtain steady conditions is prohibitive from a computer resources viewpoint and thus, the decision was made to base the analysis on the formative stages of flow structure development.

The testing program designed for this section is essentially an abbreviated replication of the channel velocity-specified experiments. First, terms from the hydrodynamic equations will be tested for physical significance in the circulation phenomenon. Then, single parameters will be varied in a sensitivity analysis. Finally, combinations of various factors will be tested. In section 5.2.1, the conclusions drawn were based on comparisons with the baseline. Although a baseline does exist for the slope-specified pool model, the primary objective of testing in this section is a verification of behavior observed in similar tests performed earlier.

Effective Stresses

In the previous section, removal of the effective stress closure terms resulted in the loss of momentum transfer from the main stream flow to the pool area. Without this transfer, circulation did not occur. Figures 5.84 to 5.86 are plots of the same test with the slope-specified conditions. At 50 time steps, a strong divergence of flow into the pool occurs with velocities larger than those found in the baseline. Unlike earlier tests however, a strong spiraling circulation appears in the southwest corner of the pool after 100 time steps. Evidence of impending instability in the guise of velocity and water surface discontinuities is also present in the channel area. By the 150th time step, the circulation has completely dissolved into a collection of disarray. The instabilities present in the previous plot are aggravated by the increasing velocities. At time step 190, the channel velocities range from -0.4 to 2.6 meters per second.

Convective Inertia

Earlier testing with the convective inertia revealed that its omission prevented the occurrence of vorticity. Flow would enter and exit the pool strongly without the development of a shear layer. The plot at 100 time steps for slope-specified conditions is presented in Fig. 5.87. Other plots taken at different times in this experiment were similar in character, differing only in the velocity magnitudes displayed. Perfectly symmetrical flow structure takes place without circulation as water enters the pool along the west wall and leaves along the east wall. Quantitative results show very stable and continuous water levels with the pool possessing a horizontal surface averaging 2.50 meters in depth. Velocities in the channel increase throughout the study period with the highest velocities occurring along the south wall. At the 200th time step, the highest entrance velocity is 0.81 meters per second.

Friction

Results of tests performed on the velocity-specified pool model suggest that frictional effects in small scale problems are negligible. Plots from the friction omission test under slope-specified conditions appear in Figs. 5.88 to 5.90. All three plots correspond almost perfectly to the baseline plots. The only difference between the baseline and this run is found in the detailed output of velocities which show slightly higher velocities for the frictionless run.

The next series of tests represent the sensitivity analyses of single parameters.

Depth

Previous experiments indicate that depth is linked directly to the transfer of momentum. Additionally, the damping effects of large depth were identified for their stabilizing influence on the computation. To verify these conclusions with the present model representation, the extreme case of a 50 meter depth was chosen. Figures 5.91 to 5.93 are the plots for this test. The plot at 50 time steps reveals negligible current magnitudes in the pool while flow divergence from the channel is barely noticeable. At 100 time steps, a weak but noncirculating flow pattern develops in the pool. By time step 150, it is apparent that a circulation will eventually set up in the pool albeit a feeble circulation. The channel velocities are comparable to the baseline values; however, the velocities in the pool are substantially less than baseline values. Highest entrance velocities are not found along the north channel wall but near midstream. The pool is horizontal with an average depth of 49.99 meters.

Friction

Increases in bed resistance at the baseline length scale have not demonstrated a visible influence on the velocity-specified testing of the pool model. This experiment seeks to determine whether the slope-specified boundary conditions will alter this result. Figures 5.94 to 5.96 are plots from a test where the magnitude of the friction factor, f_r, is increased by an order of magnitude to 0.04. Flow patterns are quite similar to the baseline with a circulation appearing at 150 time steps, centered about coordinates (15,10). Velocities are significantly lower than those in the baseline. At the final time step (190), channel velocities are damped by about 30% while pool velocities experience even greater differences. There appears to be a time lag in the development of the flow structure although the water surface is steady and continuous matching the baseline throughout the simulation.

Weighting Factor

Earlier in this section, the absence of the effective stresses, as modeled by the velocity averaging routine, did not prevent the generation of secondary flow. At the time, this was a unique result. To develop a clearer understanding of the effects produced by the averaging routine, two more weighting factors are tested, 0.4 and 1.0. Results from the 0.4 run are shown in Figs. 5.97 to 5.99. The nature of this sequence of plots appears to be very similar to the baseline; however, the development of current patterns is much slower. Velocities at all locations in the configuration are roughly 40% less than the baseline values of comparable time periods. The shear layer that is setting up is wider than that of the baseline which suggests that once circulation does set up, it will occur deep in the pool. Although a strong circulation is not visible in the last plot, data from time step 190 indicate a well formed pattern is eventually produced. Quantitative results show stable and continuous water surfaces and slowly increasing velocities. The horizontal pool is steady at 2.50 meters depth while the largest velocity entering the channel is 0.43 meters per second.

Plots from the $\alpha = 1.0$ test are given in Figs. 5.100 to 5.102. The increased weighting factor has damped velocities to about one-third of the baseline velocities. Consequently, no circulation is observed due to the time constraints of the experiment. Some flow is present in the pool adjacent to the channel, but for the most part, all velocities are directed from west to east. Detailed data show that the velocity in the channel increases at an almost imperceptible rate to 0.21 meters per second in the final time step (190). The pool is level at an average depth of 2.50 meters and the channel water slope and is fairly continuous except for a 0.02 meter elevation increase at the upstream pool entrance.

Time Increment

Experiments on the velocity-specified pool model demonstrated the sensitivity of the Δt parameter to instability. The two time increment tests performed in that section were repeated on the slope-specified pool model. In the first run, Δt is equal to 0.5 seconds, one-half the baseline value. Plots at 50, 100, and 150 time steps are reproduced in Figs. 5.103 to 5.105. The development of currents in the pool area closely follows the baseline sequence if compared in terms of real time. As flow diverges into the pool, high velocities occur in the southeast corner without circulating. Although actual circulation is not observed in the plots, the shift of large velocities to the downstream end of the pool is the typical prelude to the generation of circulation. The simulation simply was not carried out long enough to permit the set up of circulation to be seen. Detailed results show that while channel velocities are slightly smaller than those in the baseline, pool velocities are larger. Water levels are identical for the two cases.

The second test in this series doubles the baseline Δt to 2.0 seconds, a previously unstable result. Figures 5.106 to 5.107 are plots at 50 and 100 time steps. At 50 time steps a concentration of diverging flow from the channel is seen in the southeast corner of the pool. As velocities increase in the channel, a strong, well-formed circulation sets up about coordinates (17,9.5) at time step 100. Strong v-component contributions to the entrance velocities signal possible stability problems. The simulation remained stable for 20 more time steps.

<u>Space Increment</u>

Tests performed earlier indicate that the space increment influences both the physical and numerical behavior of the mathematical model. While smaller space increments were subject to stability problems, the larger values induced an effect similar to that observed on the removal of convective inertia. The first test in this series sets $\Delta x = \Delta y = 0.5$ meters; results appear in Figs. 5.108 to 5.110. A well-formed circulation develops in the 150th time step in a manner similar to the baseline sequence. At comparable times however, the velocities found in the pool and shear layer are noticeably smaller. At time step 150, relatively large v-component contributions to the entrance velocities are present which normally precede the onset of instability. This test becomes unstable at the 180th time step.

The last test of the space increment involves an increase from 1.0 to 10.0 meters. Flow patterns for the various plots are all similar in character, varying only in velocity magnitude. For this reason, only the plot at 100 time steps is presented in Fig. 5.111. Flow from the channel diverges immediately up the west wall of the pool and exits in much the same fashion without circulating. Channel velocities are obviously larger than those from the baseline at comparable times, the largest entrance velocity being 0.91 meters per second. The water slope in the channel is well behaved while the pool displays fluctuations which reverse the high water levels from west to east. The magnitude of these fluctuations is about 0.01 meter.

Large Scale Friction

An important result from the velocity-specified testing program was the effect of neglecting friction at large scales. Circulation in large scales occurred only when friction was not present in the equations. A confirmation of this observation was sought with the present testing series. Two tests were proposed. The first test set the space and time increments to 100 meters and 100 seconds, respectively. The second test used the same increments but omitted the friction term from the computation. Both tests were highly unstable with the frictionless run lasting 10 time steps, 10 time steps less than the run including friction.

5.2.3 No Slip Condition at the Wall

In previous tests, a perfect slip velocity condition has been implemented at all closed boundaries with physically realistic results. This is in direct contradiction to Flokstra's theoretical determination that the no-slip velocity condition is essential for the occurrence of circulating flow. Despite this discrepancy, there is instructive value in performing experiments under the influence of a no-slip boundary condition.

The computational specification of this problem is exactly the same as the slope-specified pool model except for the velocity relocation scheme used at the walls of the configuration. Actually, a true no-slip condition cannot be specified because velocity tangential to the wall surface does not exist under the subgrid scheme used in this model. However, the condition can be approximated by setting all velocities located outside of the physical boundaries to zero.

The results of this experiment appear in Figures 5.112 to 5.114. Compared with the baseline under slope-specified boundary conditions, the no-slip model experiences strong damping of velocity although the development of circulation is apparent. At the entrance, highest velocities occur along the north wall while at the exit, highest velocities are found in midstream. The detailed output indicates that circulation does set up by the 190th time step. A fairly steady velocity of 0.28 meters per second occurs at the entrance which yields an effective friction factor 15 times larger than the specified 0.0045. Water surfaces are steady and continuous.

5.2.4 Cold Start

The final testing on the channel-pool geometry is with initial and boundary conditions which offer the most realistic specification of the problem than previous attempts. The bottom slope of 0.0005 used in the previous section is retained; however, the initial condition is now a horizontal water surface with no velocity. Flow is driven by the gradual lowering of the downstream water level over 20 time steps, after which the upstream and downstream depths are both specified to be 2.5 meters. All other boundary conditions and parameters remain as before.

Three tests are performed in this section to clarify the effect of the velocity averaging routine on the simulation results. The first test can be regarded as the baseline for this series, with the weighting factor, α, equal to 0.1. Plots for this test appear in Figs. 5.115 to 5.118. In the first plot at 50 time steps, flow from the channel enters the pool along the upstream half and exits through the downstream half; no circulation takes place. The next plot shows a concentration of flow entering and leaving the southeast corner of the pool. At 150 time steps, a perfectly formed circulation sets up as flow divergence from the channel declines. Finally, at 200 time steps, the center of circulation has shifted slightly from (16,9.5) to (17,10) while all velocities have increased. Data from the detailed output reveals a well behaved and stable water surface in the channel. The pool elevations are horizontal with an average depth of 2.50 meters. Largest channel velocities are found along the north wall at the entrance and the south wall at the exit. Velocities in the channel increase continuously throughout the simulation. In the last time step, 0.72 meters per second is the largest velocity observed.

The next test uses a weighting factor of zero, i.e. omitting the representation of the effective stresses. In the previous section, a spiraling circulation was generated but not maintained in a similar test. Results for the present testing series are in Figs. 5.119 to 5.122. The first plot at 50 time steps displays a strong current entering and leaving the pool much as the baseline did. After 100 time steps, a crude circulation appears in the southwest corner accompanied by general disarray. The next two plots at 150 and 200 time steps illustrate a gradually developing instability which destroys any semblance of the circulation seen previously.

The final test of the weighting factor is performed with $\alpha = 1.0$. An earlier experiment disclosed a strong velocity damping effect with such a high weighting factor. For the test in this series, only the plot at 200 time steps is presented in Fig. 5.123. All velocities are damped substantially to one third the baseline magnitudes. The shear layer, as defined by the horizontal velocities in the bottom of the pool area, is relatively wide. Other areas of the pool are virtually unaffected. Channel velocities are increasing at the rate of about 0.0001 meters per second at the 200th time step. The pool and channel water surfaces are stable and continuous at 2.50 meters in depth except for an anomaly near the upstream entrance to the pool where an increase of 0.02 meters in depth is found.

5.3 EXPANSION MODEL

Testing of the pool model under the various sets of initial and boundary conditions provided the basis for many conclusions. However, the generality of these conclusions is quite suspect if they are gleaned from the testing of a single configuration. For this reason, a second configuration, an abrupt channel expansion which is known to generate secondary flow, is designed and tested.

Secondary flow in sudden expansions is of a slightly different nature than the channel-pool system tested earlier. This is due in part to the bending of currents into the expansion and the increased exposure of the vorticity to mainstream effects. Abbott and

Rasmussen (2) developed an expansion model from which results and conclusions were presented. An attempt is made here to verify these conclusions using a similar geometry.

Figure 5.124 is a sketch of the channel expansion used in this testing section. The entrance channel is 9 meters wide and 7.5 meters long while the expanded channel is 17 meters wide and 22.5 meters long. A fixed bed slope of 0.0005 is specified for the entire configuration.

5.3.1 Slope Specified

In this testing series, the initial condition is a water slope parallel to the bed at a depth of 2.5 meters. All velocities are set to zero in the beginning of the simulation. Open boundary conditions at both upstream and downstream ends are water levels which match the initial conditions. Closed boundaries are zero velocities perpendicular to walls enclosing the expansion. Friction in this model is governed by a dimensionless friction factor, f_r, which is equal to 0.0045. The weighting factor is set to 0.1 while the space increment is 1.0 meter and the time increment is 1.0 second.

Essentially, the testing of the slope-specified expansion model will consist of the same experiments performed on the slope-specified pool model. The baseline run for this series is represented by two plots in Figs. 5.125 and 5.126. At time step 50, flow from entrance channel veers into the expansion, without circulation, and becomes uniform upon reaching the channel exit. Entrance velocities vary from 0.32 meters per second at the bottom wall to 0.33 meters per second at the top wall. At the exit, the distribution is 0.19 to 0.16 meters per second from bottom to top. The second plot features a well-formed circulation in the corner of the expansion. Entrance velocities now range from 0.72 meters per second at the bottom wall to 0.77 meters per second at the top wall while exit velocities vary from 0.44 to 0.30 meters per second, bottom to top. Water levels throughout the simulation are continuous and stable. The largest water slope occurs at the junction of the expansion and entrance channel where the surface falls 0.01 meters over the space increment; however, this is a very isolated point. Slightly lower elevations are found within the circulation. Velocities increase steadily throughout the computation with an attendant increase in the downstream length of the circulation.

Effective Stresses

The effective stresses, as modeled by the velocity averaging routine, have yielded different results for different boundary conditions. In the velocity-specified pool model, the absence of the effective stresses resulted in no circulation being produced. However, the same configuration with a bottom slope was able to generate a spiraling secondary flow. Testing in this series proceeds exactly as previous tests by setting the weighting factor, α, to zero.

Figures 5.127 and 5.128 are plots at 50 and 100 time steps. The first plot is the typical beginning flow pattern at low velocities, not very different from the baseline. In the second plot, a strong spiraling secondary current, displaying velocities two and three times those found in the baseline, has developed. An instability develops in the next 30 time steps, spoiling the computation. Channel velocities were slightly higher than the baseline until the instability began to develop.

Convective Inertia

Results from tests where convective inertia is removed have been very consistent. Flow tends to follow the geometry without shear layers developing; consequently, no circulation has been observed in conjunction with this particular test.

All plots exhibit the same pattern of current, thus only the plot at 100 time steps is reproduced in Fig. 5.129. As the water moves into the expansion, flow nearest the top wall of the entrance channel immediately diverts along the expansion boundaries. No circulation ever sets up. Water levels are very consistent throughout the run with channel velocities damped by about 30% when compared with the baseline at comparable time steps.

Friction

Small scale testing of friction in this study has been very consistent up to this point. Deletion of friction has simply not affected baseline results where the space increment is of the order 1.0 meter. Results from this testing series are shown in Figs. 5.130 and 5.131. The two plots are indistinguishable from the baseline plots at the same time steps. Detailed output reveals a slightly higher set of channel velocities as the only difference detectable between this run and the baseline.

Depth

In extreme cases, the depth parameter has been shown to cause significant changes in the model behavior. Large depths appear to damp the lateral transfer of turbulent momentum, slowing the development of secondary flow. This experiment is designed to test the effect of large depth, 50 meters, specifically, on the expansion model.

Figures 5.132 and 5.133 are plotted results from time steps 50 and 100. The first plot reveals a marked difference between the flow structure in the expanded area along the north wall of the channel, and the current proceeding from the entrance channel along the south wall. Velocities in the expanded portion are just a fraction of those in the mainstream while flow divergence in this area is much larger than in the mainstream. At the exit, two separate uniform flows exist adjacently. The second plot is merely a reprise of the first plot with larger velocity magnitudes. No circulation is visible in either plot; however, quantitative results at time step 150 indicate that circulation does occur. Entrance velocities range from 0.91 meters per second at the south wall to 1.44 meters per second along the north wall, roughly 0.5 meters per second slower than the baseline. The water surface is reasonably steady and continuous except for high levels along coordinate $j = 8$.

<u>Friction</u>

Based on the outcome of earlier testing, the omission of friction at the baseline scale apparently is not significant. However, the effects of very high friction have not been completely defined. In this test, the influence of friction is increased by setting the nondimensional friction factor, f_r, to 0.04. Figures 5.134 and 5.135 are the results of this test. The plot at time step 50 is practically identical to the baseline. A circulation does set up in the corner of the expansion at the 100th time step; however, the circulating velocities are a fraction of the baseline values. Although channel velocities increase continually, the baseline velocities are considerably larger at every time step. The behavior of the water surface is very stable and consistent with that found in the baseline.

Weighting Factor

Weighting factor tests performed on the pool model demonstrate that high α is responsible for at least two different effects upon the current structure. One is a capacity for energy transfer and the other is a damping of velocities. To test the expansion model for the presence of similar behavior, an experiment using a 1.0 weighting factor is proposed.

Plots of this test at 50 and 100 time steps appear in Figs. 5.136 and 5.137. The first plot shows noticeably smaller velocities than the baseline and the presence of negative v-component contributions in the entrance channel. In the second plot, a very weak circulation is visible in the expansion corner. Water elevations in the circulation area are slightly higher than the baseline but the total surface is more continuous and stable.

Time Increment

A sensitivity to stability problems was identified for the time increment in tests done on the pool configuration. To confirm this behavior in the expansion model, the experiment will be performed with the same values of Δt used in earlier sections.

The first test specifies Δt to be equal to 0.5 seconds; a plot of the result at 100 time steps is in Fig. 5.138. In real time, the flow pattern in virtually identical to the baseline. Quantitative results indicate that a circulation is beginning to develop at time step 150, the last time step in the simulation. Less variation in velocity is seen at the entrance than with the baseline. The water surface in this test is continuous at all points and very stable.

The second test of the time increment, $\Delta t = 2.0$ seconds, has proved to be unstable in all previous attempts. Figure 5.139 shows that at time step 50 a circulation which is rounder but weaker than the baseline circulation has set up. Entrance and exit velocities are also less uniform than the baseline counterparts. Eventually, the entire computation becomes unstable at the 70th time step.

<u>Space Increment</u>

The space increment, like the time increment, appears to be contrained by a stability condition which in this case, limits the minimum interval between spatial nodes. Additionally, when large space increments increase the problem size, the physics of the problem also changes.

The first test in this experiment is with a space increment of 0.5 meters. Plots at 50 and 100 time steps are presented in Figs. 5.140 and 5.141.

The first plot is similar to the baseline; currents bend into the expansion without circulating and leave the configuration in an almost uniform flow. Closer examination reveals that the divergence of flow into the expansion is slightly more gradual than the baseline. At 100 time steps, a large elongated circulation has set up at coordinates (17.5, 14.5). Velocities in the circulation are almost three times the magnitude of the baseline values. A very large velocity has developed along the north boundary of the entrance channel which is over 40% larger than the adjacent values. Both ends of the configuration display extreme ranges of velocity, 0.828 to 1.317 meters per second from south to north at the entrance and 0.595 to 0.104 meters per second south to north at the exit. An instability at time step 120 has been foreshadowed by the presence of significant y-direction component velocities at the entrance.

A space increment of 10.0 meters is used in the second and last test of this series. Previous testing with large space increments resulted in flow patterns which resembled those found when the convective inertia terms were omitted. Figures 5.142 and 5.143 are plots of the expansion test. At 50 time steps, the plot is similar to the baseline except that there is more velocity in the corner of the expansion. The only difference in the next plot at 100 time steps is an increased velocity. However, all velocities are considerably less than corresponding baseline velocities especially as the simulation continues. Water levels are consistent and well behaved at all locations in the configuration.

5.3.2 Cold Start with Increased Resolution

The final experiment with the channel expansion is designed to determine whether the spiraling circulation, which occurred without the benefit of effective stress modeling, has a numerical or physical nature. Theoretically, numerical effects should be minimized as the discretization of the problem domain is made exceedingly small. To this end, both space and time increments are reduced although the problem size remains constant. The values of these parameters for this test are $\Delta x = \Delta y = 0.5$ meters and $\Delta t = 0.5$ seconds.

A horizontal water surface without velocity is specified as the initial condition. As the simulation begins, the downstream water level will be lowered in 40 time steps to a depth of 2.5 meters, the same depth as the upstream boundary condition. Thus, a line drawn through the end point water levels will be parallel to the bed slope.

The weighting factor for this experiment is zero while the non-dimensional friction factor is 0.0045. Four plots are generated at 50 time step intervals, and are shown in Figs. 5.144 to 5.147.

Velocities in the first plot are very uniform as flow gradually enters the expansion along the boundaries. The second plot displays the inception of secondary flow at the corner where the entrance channel joins the expansion. At time step 150 a strong "circulation" has set up. The character of this "circulation" is somewhat similar to those seen in previous slope-specified experiments, where no actual separation from the main flow occurs. Velocities in the vorticity seem to be spiraling, not circulating, about a central point. In the last plot, increased channel velocities have shifted the vorticity downstream. Deviations in the v-component of entrance channel velocities are precursors of instability. Water surface data indicate that depths are shallower within the circulation by 0.02 meters, while depths are consistent and continuous elsewhere.

CHAPTER 6

ANALYSIS AND EVALUATION

6.1 INTRODUCTION

This chapter contains an analysis and interpretation of the experimental results reported in Chapter 5. The large numbers of tests performed on the numerical model, varying both boundary conditions and configuration, have created a large bank of information from which to draw general conclusions. Such an extensive testing program was justified in order to assess the behavior of the model under a wide range of conditions. Consistent with the objectives of this study, conclusions delineating the secondary flow phenomena comprise the major portion of this chapter. Additionally, a discussion of the numerical properties attributable to the mathematical model formulation is also included.

A detailed evaluation of all terms found in the partial differential equation set has been performed, and the results are tabulated in Table 6.1. Magnitudes of each term are determined at different locations and times in selected tests. These results have proven to be an invaluable tool in the understanding of the individual mechanisms which interact to produce the flow phenomena.

The analysis begins in section 6.2 where the effect of boundary conditions and channel configuration are considered. Section 6.3 is an interpretation of the physical processes involving quantities found in the governing equations. In section 6.4, model stability is separated into the contributing elements and then recombined into a coherent theory of general applicability.

6.2 CONFIGURATION AND BOUNDARY CONDITIONS

Unique solutions for the mathematical model used in this study can be obtained only after the boundary conditions for a given configuration are fully specified. The degree to which the model behavior is altered by changes in the boundary treatment then becomes a topic of the highest importance. To this end, the testing program was designed to reveal the effects of an assortment of boundary conditions on the two selected configurations.

For the most part, the response of the channel expansion was not different from that of the channel-pool system. Of the discrepancies that did exist, at least one was anticipated: the presence of higher velocity in the expansion model. This was a result of the wider channel used, effectively reducing the resistance effects encountered in the pool model. Unexpected behavior did occur, however, in response to the removal of convective inertia. Although the primary phenomenon of noncirculating flow was found in both configurations, damped velocities occurred in the channel expansion while accelerated velocities were found in the channel-pool system. This probably is the result of the sudden bending of flow into the expansion, requiring more energy than the baseline flow which enters a gradual expansion around a separation zone. When convective inertia is not present, congestion occurs at the point of expansion with a backwater effect, evidenced by higher water levels in the entrance channel. This reduces the velocity of water entering the configuration. Of course, similar behavior will occur in the channel-pool system, but in this case the baseline experiences an even larger backwater effect due to the diversion of energy to the circulation in the pool area.

Boundary conditions and the computational treatment of boundaries in this model are responsible for modifications in behavior occurring under similar testing procedures. The use of specified water levels at the open boundaries proved to be a better boundary condition than the velocity specified in the first testing series. When a difference in water levels is the driving force for flow through the configuration, both velocity and water surface are steady and continuous, with few, if any, anomalies. This is in contrast to the channel velocity-specified model which requires a special initial condition before simulation can begin. In addition, oscillating water levels and velocities plague many of the velocity-specified simulations.

Specific differences in model behavior due to a change in boundary conditions are found only in the testing of α, the weighting factor used in the velocity-averaging routine. In the velocity-specified model, circulation did not occur without the presence of the closure terms, $\varepsilon(\frac{\partial^2 u}{\partial x^2} + \frac{\partial^2 u}{\partial y^2})$ and $\varepsilon(\frac{\partial^2 v}{\partial x^2} + \frac{\partial^2 v}{\partial y^2})$, in the computations. However, a spiraling secondary flow did appear in all water slope models when tested without the effective stresses represented. This does not invalidate Flokstra's theory that circulation cannot occur without the modeling of the effective stresses because his analysis was based on the existence of a closed streamline separating the circulation from the main flow. This is not the case with the spiraling flow structure found in these tests. In each instance, the phenomenon could not be sustained.

The "no-slip" velocity condition at physical boundaries has been professed by Flokstra to be a requisite for the modeling of circulating flow. While acknowledging the "no-slip" condition in nature, testing of this model has been performed primarily with a "perfect slip" boundary specification for computational reasons. The discrete scheme describing the physics of this problem is incapable of resolving tangential velocities at the location of closed boundaries. For this reason, numerical derivatives at nodes adjacent to these boundaries require the value of dependent variables located outside the physical problem domain to enable the spatially-centered derivative scheme to be used. Generation of these "outside" values has been achieved by a boundary relocation routine. This routine assigns the value of dependent variables situated adjacent to walls, to a fictitious location directly across the wall, outside the configuration. Velocities and water levels on either side of physical boundaries are thus identical; a perfect slip condition.

In the experiment involving the specification of zero velocities outside the boundary geometry, strong resistance effects resulted. Obviously, any consideration of a no-slip boundary condition must be coordinated with an accompanying reduction in the bed resistance effects. This amounts to a calibration problem since the effect of the boundaries is dependent upon the distance between boundaries.

6.3 PHYSICAL PROCESSES

Mathematical models intended for wide application are normally designed with meticulous attention directed at the important physical processes of the modeled phenomena. It is not sufficient to merely calibrate a result which matches the natural behavior; the generation of the result must proceed with a modeling of the physical interactions which are responsible for the phenomenon.

In the depth-averaged mathematical model used in this study, a strong emphasis was placed on the accurate fundamental derivation of the equations governing open channel flow in two dimensions. The rigorous theoretical basis inherent to this model permits an analysis of the individual mechanisms contributing to the displayed flow structure. Of particular interest is the examination of the role played by the effective stresses, convective inertia, and bed resistance. The combined action of these processes is largely responsible for the presence or absence of secondary flow in nature. With the aid of Table 6.1, this section presents an interpretation of the manner in which each of the aforementioned processes influences secondary flow behavior.

6.3.1 Effective Stresses

The effective stress terms

$$T_{xx} = \frac{1}{h}\int_{z_b}^{\eta} [2\rho\ \nu\frac{\partial u}{\partial x} - \rho\overline{u'^2} - \rho\ (u-\bar{u})^2]dz$$

$$T_{xy} = \frac{1}{h}\int_{z_b}^{\eta} [\rho\ \ \nu(\frac{\partial u}{\partial y} + \frac{\partial v}{\partial x}) - \rho\overline{u'v'} - \rho(u-\bar{u})(v-\bar{v})]dz$$

$$T_{yy} = \frac{1}{h}\int_{z_b}^{\eta} [2\rho\ \ \nu\frac{\partial v}{\partial y} - \rho\overline{v'^2} - \rho(v-\bar{v})^2]dz$$

are actually the agglomeration of three rather distinct processes: 1) viscous shear stress; 2) turbulent momentum transfer; and 3) the effect of vertical nonuniformity. Ideally, a separate closure assumption relating flow parameters to each process involved should be established. However, the importance of the three mechanisms is not the same. Viscous shear forces become significant only at locations close to the laminar sublayer adjacent to boundaries. At best, only a minor influence on the large scale flow considered in this study, the viscous effects have traditionally been dispensed with. Probably the most important process found in the effective stresses is the exchange of turbulent momentum, i.e. the Reynolds stress. This is because the existence of secondary flow is largely dependent on the energy transfer mechanism provided by turbulence. Finding a closure assumption for the effects of velocity nonuniformity in the vertical is a problem unique to two-dimensional modeling. Flokstra (6) has theoretically determined that the nonuniformity effects are responsible for the dissipation of vortex energy. Information as to the importance of this process is virtually nonexistent, although the type of problems considered by this study does not include those with strongly nonuniform distributions of velocity in the vertical. Such problems are best coped with in a three-dimensional formulation. The theoretical expressions of the effective stresses in Eqs. 6.1 to 6.3 contain an averaging process which includes a division by the depth of flow. This would seem to confirm Bengtsson's (3) observation that the effective stresses are inversely dependent on the fluid depth.

For a closure assumption representing the effective stresses to be deemed acceptable, the important processes must be reproduced in a reasonable fashion. A velocity averaging technique has been selected to fill this assignment. The closure terms which result from this method are $\varepsilon(\frac{\partial^2 u}{\partial x^2} + \frac{\partial^2 u}{\partial y^2})$ and $\varepsilon(\frac{\partial^2 v}{\partial x^2} + \frac{\partial^2 v}{\partial y^2})$ where diffusivity, $\varepsilon = \alpha \frac{(\Delta x)^2}{\Delta t}$. This numerical analog of the effective stresses satisfactorily exhibited the traits judged essential in earlier discussion.

Results from the testing program are reasonable and encouraging, despite the presence of two flaws traceable to the representation of the effective stresses. First, there is yet to be found a physical basis to choose the appropriate weighting factor, α, in the velocity averaging routine. There are instances in the literature where physical processes have been replaced successfully by numerical techniques in a general manner. Although the selection of the weighting factor is presently a manageable calibration task, a physical link to the turbulence process remains to be identified.

The second drawback in the effective stress representation is somewhat more serious than the first. Much of the success in fulfilling the required profile of traits by the closure terms is due to the effect of numerical viscosity. As the weighting factor is increased, the model reacts as if the fluid is becoming more viscous, thus increasing the exchange of lateral momentum and increasing viscous damping. Essentially, viscosity is used to model a turbulence effect. Therefore, care must be exercised when using the velocity averaging routine; a balance must be struck between the simulation of the effective stresses and the associated change in fluid properties. Not surprisingly, different fluids in identical circumstances display dissimilar flow patterns.

This study has experimentally verified Flokstra's conclusion that true circulation, i.e. a flow pattern possessing a separation zone with circular streamlines, requires the modeling of effective stresses. Table 6.1 shows that in all instances where circulation occurs, the magnitude of the effective stresses is significant and greater than the bed resistance term. As mentioned earlier, a spiraling secondary current did appear when the closure terms were absent, but this is judged to be a temporary phenomenon confined to the early stages of developing flow in sloping models.

Table 6.1 also illustrates that the effective stress behavior changes with location in the configuration. In the channel, the effective stress magnitudes are increasing negative as circulation develops, while the shear layer exhibits decreasing positive values. The latter result is a manifestation of the secondary flow development. Prior to the set up of steady circulation, the divergence of the velocity vectors into the pool or expansion is very large. As the flow pattern stabilizes, divergence is reduced almost completely. Within the vorticity, the effective stresses are significant though considerably smaller than the values found in the shear layer and channel.

Circulation requires a continuous exchange of turbulent energy across the shear layer to be maintained. Withdrawal of the effective stresses after a steady flow pattern has set up dissolves the circulation and ultimately leads to instability.

The physical response of an increase in the action of the effective stresses is a higher rate of lateral momentum transfer and the damping of velocity throughout the configuration. Accompanying the increase in momentum transfer is a widening of the shear layer which moves the circulation deeper into the pool or expansion. Damping effects of depth and scale can, in many cases, be overcome by comparable increases in the effective stress magnitude.

6.3.2 Convective Inertia

Convective inertia in this model study is described by the following four terms: $u \frac{\partial u}{\partial x}$, $v \frac{\partial u}{\partial y}$, $u \frac{\partial v}{\partial x}$, and $v \frac{\partial v}{\partial y}$. A consensus exists in the literature to the effect that the convective inertia terms are absolutely necessary if circulating flow is to be resolved. This conclusion has also been verified by this study.

The nonlinear nature of the convective inertia terms makes it difficult to use in conjunction with efficient linear numerical solution schemes. For this reason, these terms are often neglected. Although there are circumstances where convective inertia is not significant and can be omitted, this would not normally be known unless a full equation set was modeled.

Table 6.1 reveals that convective inertia is significant in the channel and shear layer for all instances where circulation occurs. Conversely, no circulation occurs in the absence of convective inertia. In this case, flow closely follows the contour of the boundary geometry, even where sudden changes exist. The presence of inertia allows flow to retain uniform structure for a distance beyond the location of a configuration change, enabling the development of a separation zone adjacent to the free extension of the uniform flow. Ultimately, this separation of flow develops into a circulating flow pattern.

Merely including the convective inertia in a mathematical model will not ensure the generation of secondary flow. Even with the additional stipulation that the effective stresses and all other quantities be precisely described, circulation may yet be inhibited by frictional effects. Table 6.1 effectively demonstrates the capacity of bed resistance to overwhelm convective inertia. In every case where secondary currents do not occur, the resistance term is significant and larger than the convective inertia terms.

The fact that the convective inertia terms contain spatial gradients of velocity makes them particularly sensitive to scale effects. In small scale problems, lateral differences in velocity occur over relatively small distances, creating large velocity gradients. The large magnitudes of the convective inertia terms render the bed resistance effects negligible. Conversely, large scale problems reduce the magnitude of both the convective inertia and the effective stresses to such a degree that the friction terms becomes significant. The result is a flow pattern similar to that displayed in the absence of convective inertia, i.e. no circulation.

A finer distinction of the convective inertia terms can be made by examining the cross terms, $u \frac{\partial v}{\partial x}$ and $v \frac{\partial u}{\partial y}$, as opposed to the direct terms, $u \frac{\partial u}{\partial x}$ and $v \frac{\partial v}{\partial y}$. Controlling influence of the convective inertia is found to lie in the cross terms, as very little change can be detected when the direct terms are left out of the simulation. Since part of the effective stress cross term is derived from the cross convective inertia term in three dimensions, a plausible extension would confer similar significance to the effective stress cross term, T_{xy}. This is in agreement with Flokstra's analysis regarding the relative magnitude of the effective stresses.

Data from Table 6.1 allow a detailed interpretation of the convective inertia mechanism. In channels, the direct terms are always significant and increase negatively as circulation develops. However, it is the cross terms which are consistently among the dominant quantities in the shear layer. The cross terms are also negative, but the tendency here is for a decrease in magnitude over the duration of the study period. Unexpectedly, convective inertia is not significant within the vortex flow structure.

6.3.3 Bed Resistance

Turbulence effects due to bottom roughness are modeled with the Chézy resistance equation. This is actually a closure assumption, although the validity of this empirical expression has been thoroughly verified in practice. The Chézy equation was designed for steady uniform flow, but it is used in this model in the absence of a formulation to account for unsteady flow resistance effects.

Resistance effects are quite controversial in mathematical modeling of circulation. Leendertse cited the relatively large magnitude of friction, which allowed him to omit the effective stresses from his estuary model. Abbott described the onset of circulation as the resistance forces overcoming the dynamic forces. Flokstra believes that in comparison to the no slip velocity specification at vertical boundaries, bed resistance is unimportant.

This study has found that bottom friction is the largest deterrent to the existence of circulating flow. A competition seems to exist between the convective inertia and the bed resistance forces. Table 6.1 illustrates this principle concisely; no circulation is found where the magnitude of the resistance term exceeds both types of convective inertia. In small scale problems, i.e. where changes in velocity or water level take place over small distances, resistance is entirely superfluous to the appearance of circulation. No reasonable friction factor can affect this mechanism. Large scale problems display contrasting behavior; convective inertia is effectively reduced to the point where the resistance effects totally inhibit the generation of secondary flow. The requirements for plane flow circulation in large scale configurations are quite severe, and a question may be posed as to the actual existence of very large scale circulation.

The presence of the flow depth variable in the denominator of the resistance terms leads to an expectation that the friction effects should become negligible where large flow depths occur, thus permitting the occurrence of circulating flow in large scale problems. Magnitudes of the convective inertia and resistance terms reflect this effect. However, increases in flow depth result in much lower turbulent momentum exchange rates which preclude secondary flow development.

6.4 CONSIDERATIONS OF NUMERICAL STABILITY

The problems of numerical stability derive from the representation of a continuous phenomena in a discrete grid domain. Due to an unfortunate combination of model parameters, the numerical model is incapable of resolving the physics of the problem.

In practice, numerical instability is a term encompassing various types of numerical effects which lead to a complete disruption of the computational process. This model displays at least two different instability mechanisms: nonlinear and Courant. Techniques to correct stability problems are tailored to the specific type of instability. Nonlinear instability is treated with smoothing techniques while Courant instability is alleviated by a judicious selection of numerical parameters.

6.4.1 Nonlinear Instability

Nonlinear instability is theoretically described as the inability to resolve energy at scales smaller than twice the spatial grid increment. Physically, energy is "cascaded" to smaller and smaller scales by the action of the nonlinear terms in the governing equations. At the very smallest scales, energy is dissipated by viscous effects. The discrete formulation of the numerical model interrupts the energy cascade at the resolution of the grid. Thus, energy accumulates at this scale and eventually spoils the computations.

Nonlinear instability is characterized by gradually developing water surface discontinuities accompanied by a similar behavior in the calculated velocities. The process is usually slow, and can take as many as 100 time steps to develop.

Smoothing techniques can be used to improve all types of instability, although these techniques are especially well suited to treat nonlinear instability. Bed resistance provides a smoothing effect on the computation; however, this is not a practical technique due to the physical limitations of a friction factor selection. The smoothing procedure used in this model is the velocity-averaging routine used here primarily as an analog of the effective stress terms.

Velocity averaging after each computational half-time step has the effect of smoothing extreme values which could otherwise create discontinuities eventually leading to instability. Physically speaking, the use of the velocity averaging routine introduces a stronger viscous dissipation mechanism into the fluid. Energy no longer must be transferred to scales smaller than the grid resolution for viscous effects to act.

In this numerical model, nonlinear instability requires the velocity averaging technique to be present in all simulations although the weighting factor need not be very large. Most runs were stable with $\alpha = 0.1$. This is rather fortunate because the use of larger weighting factors significantly alters the behavior of the fluid. As it might be expected, the large weighting factors provide the most stable results. If a small weighting factor proves to be insufficient in alleviating nonlinear instability, this cannot be changed by allowing a stable flow pattern to set up under a higher weighting factor and then introducing the small α.

6.4.2 Courant Instability

Courant instability occurs when the ratio of physical celerity to numerical celerity defined as the Courant number, exceeds a characteristic value. The physical celerity for this model is the maximum channel velocity, U_{max}, while the numerical celerity is always defined $\frac{\Delta x}{\Delta t} = \frac{\Delta y}{\Delta t}$. Thus, the criteria involved is of the form $U_{max} \frac{\Delta t}{\Delta x} \leq \xi$, where ξ is the characteristic limit.

Courant instability is normally associated with explicit computational schemes which tend to have a somewhat restrictive stability criteria. The two explicit operations contained in the calculation procedure are presumably the origin of the Courant stability condition found in this model.

Courant instability is characteristically a very rapid process. The simulation proceeds without noticeable difficulty until a sudden discontinuity appears in one of the dependent variables. Within a few time steps the entire computation is spoiled. These problems arise in response to large velocity, large time increment, and small space increment, as can be seen from the structure of the Courant criterion.

The limiting value of the Courant number is dependent on the weighting factor used in the velocity-averaging routine. This is to be expected since large weighting factors can smooth instabilities that would otherwise occur if smaller weighting factors were used. For $\alpha = 0.1$ the Courant number in this model must be less than or equal to 0.5.

CHAPTER 7

CONCLUSIONS AND RECOMMENDATIONS

A mathematical model for the depth-averaged two-dimensional flow considered here is derived from basic principles under the assumption of negligible vertical velocity and acceleration. In essence, the mathematical model is based on the integration over the flow depth of the three-dimensional equations of turbulent flow, to yield the continuity and momentum equations in a two-dimensional spatial framework. Of particular interest in the description of circulation is the appearance of the effective stresses in the momentum equations. These stresses consist of three contributions: (1) viscous stresses; (2) turbulent stresses; and (3) stresses arising from the vertical integration of the corrective inertia terms. No rigorous physically-based relation exists to model the effective stresses; therefore, a closure assumption must be made. In this study, an eddy viscosity term is used to close the equation set.

The computational procedure is based on the method of finite differences. A discrete grid replaces the continuous independent variable domain, and the function and partial derivatives are defined on this grid. The numerical solution of the discretized equation set consists of a multi-operational method, utilizing both implicit and explicit components. The alternating-direction implicit (ADI) method is used to enable the separation of the two-dimensional problem into a sequence of two one-dimensional problems. In addition, an explicit mode is used after each implicit computation.

Two problem configurations were tested in this study: (1) a channel-pool system; and (2) a channel expansion. For each set of boundary conditions applied to a particular geometry, a standard series of experiments were performed. These tests were designed to identify the flow behavior resulting from the parameters and terms found in the equation set. Additionally, the interaction of two or more problem elements were also studied to a limited extent.

7.1 CONCLUSIONS

Major conclusions from this study are as follows:

1. In the mathematical modeling of depth-averaged flow, a simplified representation of the effective stresses produces results which appear to be reasonable. Modeling of the energy transfer properties attributable to the effective stresses is a requirement for the resolution of steady, closed-streamline circulation. Secondary flow phenomena, without separation streamlines, are possible when effective stresses are not modeled; however, the structure of these secondary currents cannot be maintained. Although the behavior produced by the velocity averaging routine is consistent with theoretical characteristics of the effective stresses, it is possible that these effects are the result of a numerically increased fluid viscosity.
2. The inertia provided by the convective acceleration terms in the momentum equation permits secondary currents to develop in the area near sudden changes in boundary configuration. In the absence of inertia, flow will simply follow along the perimeter of the enclosure without circulating. The spatial gradient found in each convective inertia term results in a strong sensitivity to the scale of the problem being

considered. Large scale problems simply do not possess the large velocity variations necessary for the convective inertia to make a significant contribution; thus, the occurrence of cirulation is precluded in these instances. When secondary flow does occur, it is the action of the cross term which dominates the physical process of convective inertia.

3. A competition exists between convective inertia and the resistance effects at the bed. Circulating flow is possible only where bed resistance is absent or of minor influence, e.g., at small length scales. Conversely, at large length scales, circulation is inhibited by the overwhelming action of the bed resistance. At the walls of the configuration, a no slip velocity condition is a physical reality though not a modeling necessity as circulation can be resolved with or without such a boundary specification. If the no slip condition at the wall is specified, the increased resistance effects must be corrected by reducing the friction factor used in the modeling of bed resistance.

4. The choice of boundary condition specification for a given problem can have a significant effect on the resulting flow patterns. In this study, the most consistent and physically reasonable results were obtained in tests in which the driving force for the flow was due to a difference between upstream and downstream water elevations.

5. Stability problems in this model fall basically into two categories: (1) nonlinear; and (2) Courant. Nonlinear instability is characterized by gradually diverging velocities

and water levels which result from the inability of the discrete model to dissipate energy at the subgrid scale. These effects can be eliminated by spatial smoothing techniques which introduce numerical viscosity into the calculation. The Courant instability found in this study is thought to originate in the explicit computational modes used in the solution procedure. Unlike nonlinear instability, Courant instability is very sudden and results from the inability of a discretized representation to resolve characteristic celerities occurring in the model.

7.2 RECOMMENDATIONS

The following recommendations are offered for future research:

1. Within the realm of depth-averaged flow, the derivation of the mathematical model considered here is intended to be of general applicability. The greatest source of uncertainty is the modeling of the effective stresses. Although simplified methods of representing the effective stresses have yielded reasonable results, it is surmised that a higher level of sophistication will be needed in order to handle complex flow phenomena. In such cases, it may prove of necessity to separately account for the three components of the effective stresses. At present, individual closure assumptions are not available.
2. Additional studies are needed in order to identify the numerical effects of various discretization schemes and techniques used to represent the physical boundaries.

3. Although not directly benefiting the formulation of mathematical models, the compilation of physical data on various circulating flows would certainly be instrumental in the development of management models capable of high accuracy simulation.

4. Most importantly, the ultimate aim of the modeling effort is the simulation of pollutant dispersion, sediment transport and heat dissipation in rivers and estuaries. Once a reasonably accurate solution of the water phase is obtained, including secondary flow phenomena such as circulation, the solution of these pressing problems can be attempted with a increased level of confidence.

APPENDICES

BIBLIOGRAPHY

APPENDIX I. - BIBLIOGRAPHY

1. Abbott, M. B., "Computational Hydraulics: A Short Pathology," Journal of Hydraulic Research, Vol. 14, No. 4, 1976, pp. 271-285.

2. Abbott, M. B., and Rasmussen, C. H., "On the Numerical Modeling of Rapid Expansions and Contractions in Models that are Two-Dimensional in Plan," Paper A104, 17th Congress of the International Association for Hydraulic Research, Baden-Baden, Germany, Vol. 2, 1977, pp. 229-237.

3. Bengtsson, L., "Wind Induced Circulation in Lakes," Nordic Hydrology, Vol. 9, No. 2, 1978, pp. 75-94.

4. Cunge, J. A., "On the Subject of a Flood Propagation Computation Method (Muskingum Method)," Journal of Hydraulic Research, Vol. 7, No. 2, 1969, pp. 205-230.

5. Falconer, R. A., "Numerical Modeling of Tidal Circulation in Harbors," Journal of the Waterway, Port, Coastal and Ocean Division, ASCE, Vol. 106, No. WW1, Proc. Paper 15187, Feb., 1980, pp. 31-48.

6. Flokstra, C., "Generation of Two-Dimensional Horizontal Secondary Currents," Report S 163-II, Delft Hydraulics Laboratory, Delft, The Netherlands, Jul., 1976.

7. Flokstra, C., "The Closure Problem for Depth-Averaged Two-Dimensional Flow," Paper A106, 17th Congress of the International Association for Hydraulic Research, Baden-Baden, Germany, Vol. 2, 1977, pp. 247-256.

8. Forester, C. K., "Higher Order Monotonic Convective Difference Schemes," Journal of Computational Physics, Vol. 23, 1977, pp. 1-22.

9. Hansen, W., "Hydrodynamic Methods Applied to Oceanographic Problems," Proceedings of the Symposium on Mathematical-Hyrodynamical Methods of Physical Oceanography, Institute für Meereskunde der Universität Hamburg, Hamburg, West Germany, 1962, pp. 25-34.

10. Kuipers, J., and Vrengdenhil, C. B., "Calculations of Two-Dimensional Horizontal Flows," Report S 163-I, Delft Hydraulics Laboratory, Delft, The Netherlands, Oct., 1973.

11. Launder, B. E., and Spalding, D. B., "The Numerical Computation of Turbulent Flows," Computational Methods in Applied Mechanical Engineering, Vol. 3, 1974, pp. 269-289.

12. Lean, G. H., and Weare, T. J., "Modeling Two-Dimensional Circulating Flow," Journal of the Hydraulics Division, ASCE, Vol. 105, No. HY1, Proc. Paper 14312, Jan., 1979, pp. 17-26.

13. Leendertse, J. J., "Aspects of a Computational Model for Long-Period Water Wave Propagation," RM-5294-PR, The Rand Corporation, Santa Monica, California, May, 1967.

14. Leendertse, J. J., "A Water-Quality Simulation Model for Well-Mixed Estuaries and Coastal Seas: Volume I, Principles of Computation," RM-6230-RC, The Rand Corporation, Santa Monica, California, Feb., 1970.

15. Leendertse, J. J., and Liu, S.-K., "A Three-Dimensional Model for Estuaries and Coastal Seas: Volume I, Principles of Computation," R-1417-OWRR, The Rand Corporation, Santa Monica, California, Dec., 1973.

16. McGuirk, J. J., and Rodi, W., "A Depth-Averaged Mathematical Model for the Near Field of Side Discharges into Open Channel Flow," Journal of Fluid Mechanics, Vol. 86, Part 4, 1978, pp. 761-781.

17. O'Brien, G. G., Hyman, M. A., and Kaplan, S., "A Study of the Numerical Solution of Partial Differential Equations," Journal of Mathematical and Physics, Vol. 29, No. 4, 1950, pp. 223-251.

18. Patankar, S. V., and Spalding, D. B., "A Calculation Procedure for Heat, Mass, and Momentum Transfer in Three-Dimensional Parabolic Flows," International Journal of Heat and Mass Transfer, Vol. 15, 1972, pp. 1787-1806.

19. Platzman, G. W., "A Numerical Computation of the Surge of 26 June 1954 on Lake Michigan," Geophysics, Vol. 6, No. 3-4, 1959, pp. 407-438.

20. Ponce, V. M., and Chen, Y. H., Discussion of "Modeling Two-Dimensional Circulating Flow," Lean, G. H., and Weare, T. J., Journal of the Hydraulics Division, ASCE, Vol. 105, No. HY11, Proc. Paper 14935, Nov., 1979, pp. 1469-1470.

21. Pritchard, D. W., "Two-Dimensional Models," Estuarine Modelling: An Assessment, G. H. Ward, et al., eds., Water Pollution Control Research Ser 16070DZV, Environmental Protection Agency, Springfield, Va., Feb., 1971, pp. 5-34, (National Technical Information Service Report No. PB206-807).

22. Rastogi, A. K., and Rodi, W., "Predictions of Heat and Mass Transfer in Open Channels," Journal of the Hydraulics Division, ASCE, Vol. 104, No. HY3, Proc. Paper 13639, Mar., 1978, pp. 397-420.

23. Tee, K. T., "Tide-Induced Residual Current, A Two-Dimensional Nonlinear Numerical Tidal Model," Journal of Marine Research, Vol. 34, No. 4, Nov., 1976, pp. 603-628.

24. Wang, J. D., and Connor, J. J., "Mathematical Modeling of Near Coastal Circulation," Report No. 200, Ralph M. Parsons Laboratory, Massachusetts Institute of Technology, Cambridge, Massachusetts, April, 1975.

25. Weare, T. J., "Instability in Tidal Flow Computational Schemes," Journal of the Hydraulics Division, ASCE, Vol. 102, No. HY5, Proc. Paper 12100, May, 1976, pp. 569-580.

TABLES

APPENDIX II. - TABLES

Table 6.1 Significance of terms found in the momentum equation†

Fig.	B.C.	Time Step	Loc	Circ	ACCEL	DCT	CCT	PRESS	FRIC	EFF
5.83	S	150	C	+	25000*	-38400[1]	-2000	0	5400*	-12500*
5.79	V	150	C	+	-10	-154*	-5	981[1]	0	-150*
5.6	V	10	C	+	-1500*	-4980*	70	0	4460*	-8500[1]
5.6	V	20	C	+	-3000*	-7460*	-200	0	-4440*	-14000[1]
5.6	V	150	C	+	-1000	-17800*	-680	98100[1]	4700	-14500*
5.31	V	150	C	+	500	-32200*	-4300	98100[1]	260	-21000*
5.80	V	150	C	-	0	-290*	-14	-980*	1370[1]	15
5.128	S	150	C	0	97500*	-62800*	7100	196200[1]	8000	0
5.83	S	150	S	+	10000*	8400*	-38600[1]	0	1000	35000*
5.79	V	150	S	+	-5	135*	-99*	981[1]	0	365*
5.6	V	10	S	+	78000*	-2400	-9200*	0	250	78500[1]
5.6	V	20	S	+	29000*	-3100	-20400*	0	400	45000[1]
5.6	V	150	S	+	-1000	14600*	-11000*	98100[1]	4700	36500*
5.31	V	150	S	+	500	-1320	-40000*	0	2	131000[1]
5.80	V	150	S	-	-5	-88	-234*	-981[1]	699*	135*
5.128	S	150	S	0	76000	198700*	-780200[1]	392400*	5500	0
5.83	S	150	V	+	-3000*	-370*	-130	0	-20	3500[1]
5.79	V	150	V	+	0	7.8*	14.0*	0	0	40[1]
5.6	V	10	V	+	-2500[1]	-45	20	0	0	-1000*
5.6	V	150	V	+	-500*	570*	1300*	0	-30	3000[1]
5.31	V	150	V	+	-500*	-60	-370	0	0	2000[1]
5.80	V	150	V	-	0	22.5*	-19*	0	46[1]	0
5.128	S	150	V	0	-131500*	-51800*	1500	294300[1]	-400	0

B.C. (Boundary Conditions)
1. S = Slope-specified
2. V = Velocity-specified

Loc (Location in Configuration)
1. C = Channel
2. S = Shear layer
3. V = Vorticity

Circ (Circulation)
1. + = Closed streamline circulation
2. 0 = Open streamline circulation
3. - = No circulation

ACCEL (Local Acceleration Term)
DCT (Direct Convective Term)
CCT (Cross Convective Term)
PRESS (Pressure Term)
FRIC (Friction Term)
EFF (Effective Stress Term)
[1]largest magnitude

*significant magnitude

†magnitudes are based on an arbitrary scale

FIGURES

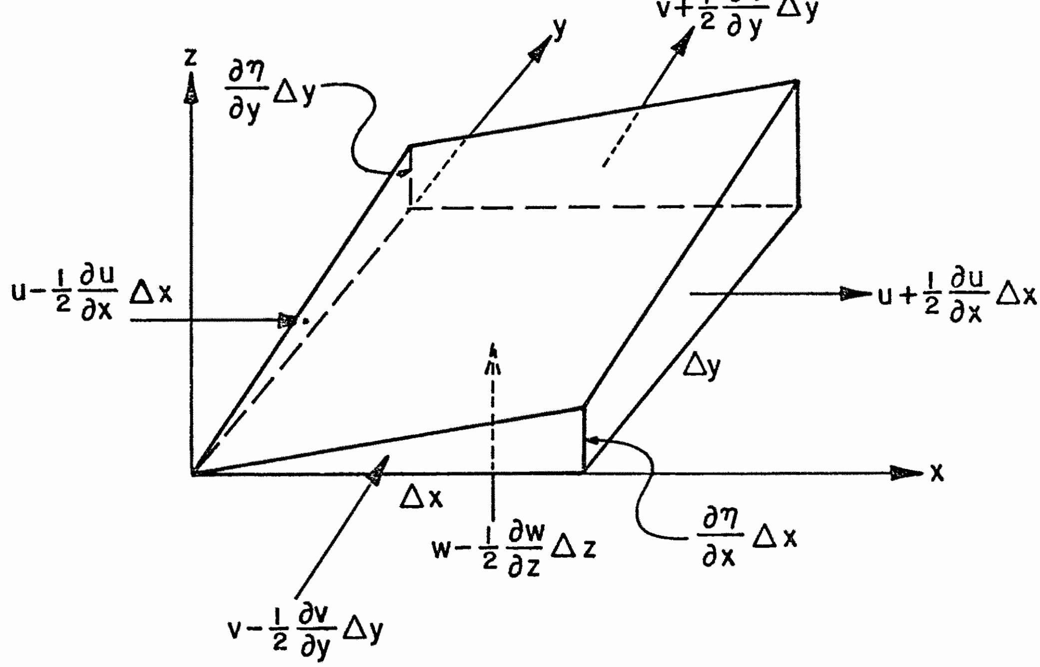

Figure 3.1. Surface volume element.

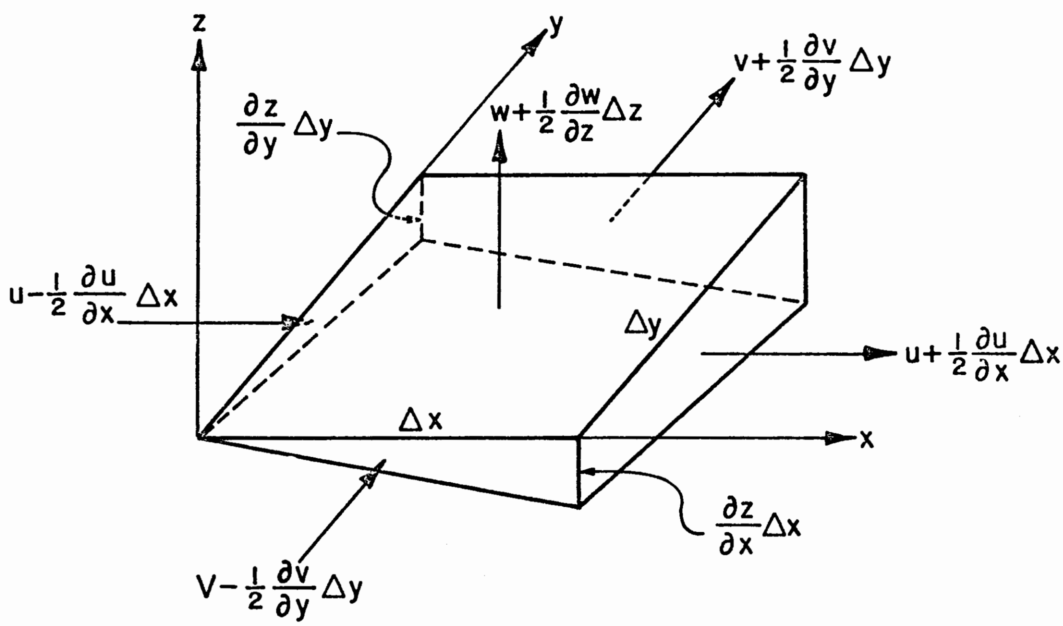

Figure 3.2. Bottom volume element.

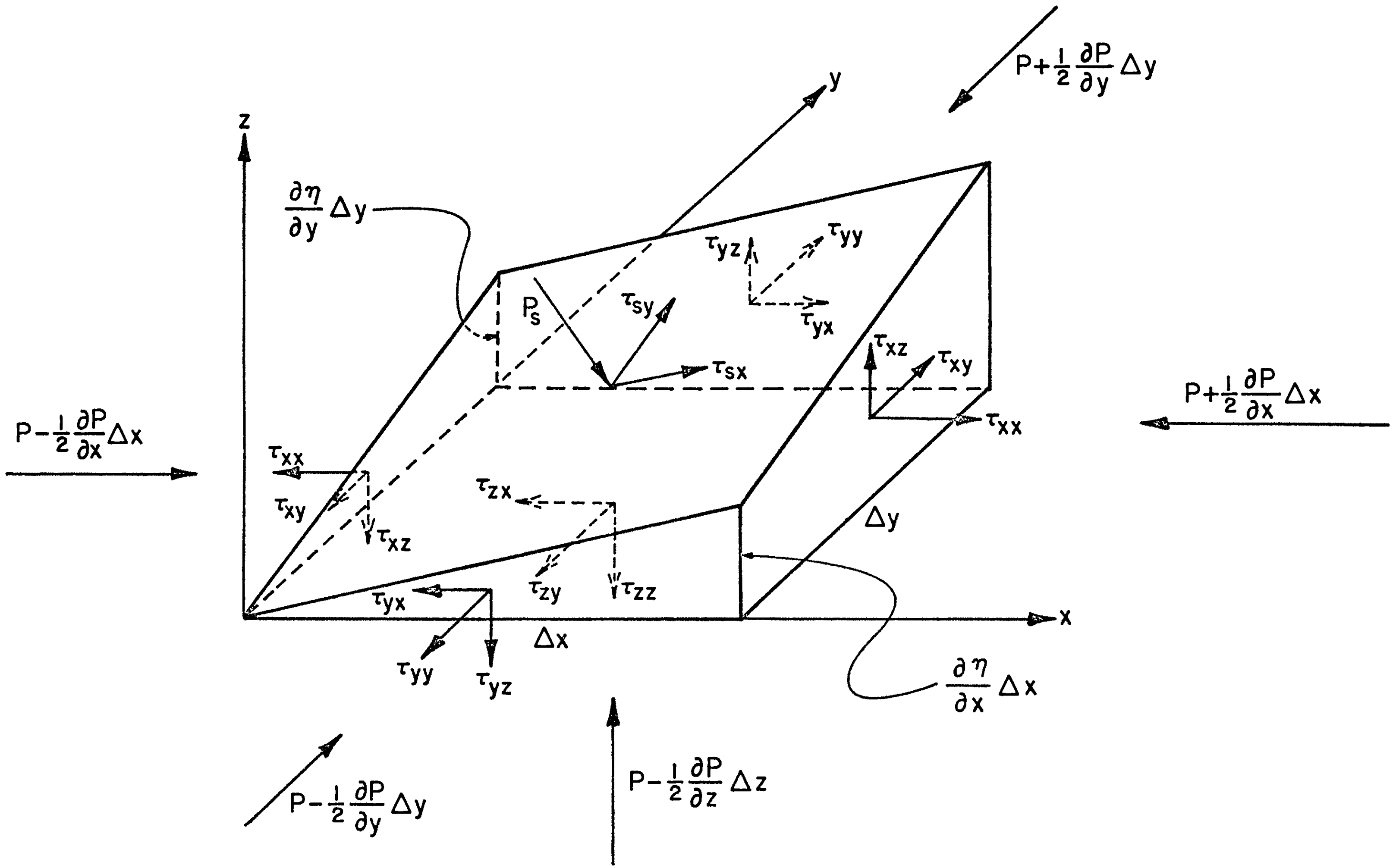

Figure 3.3. Surface stress element.

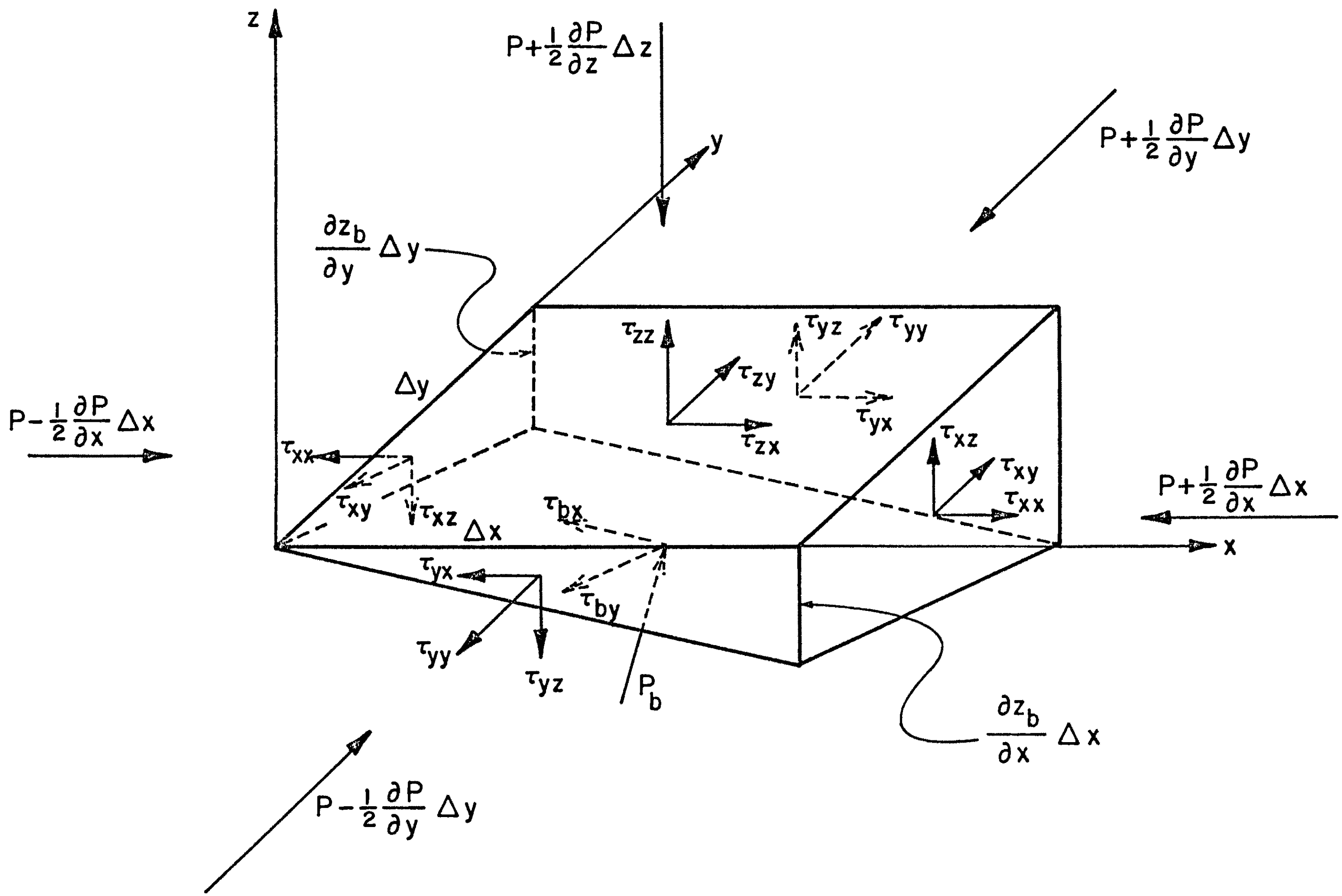

Figure 3.4. Bottom stress element.

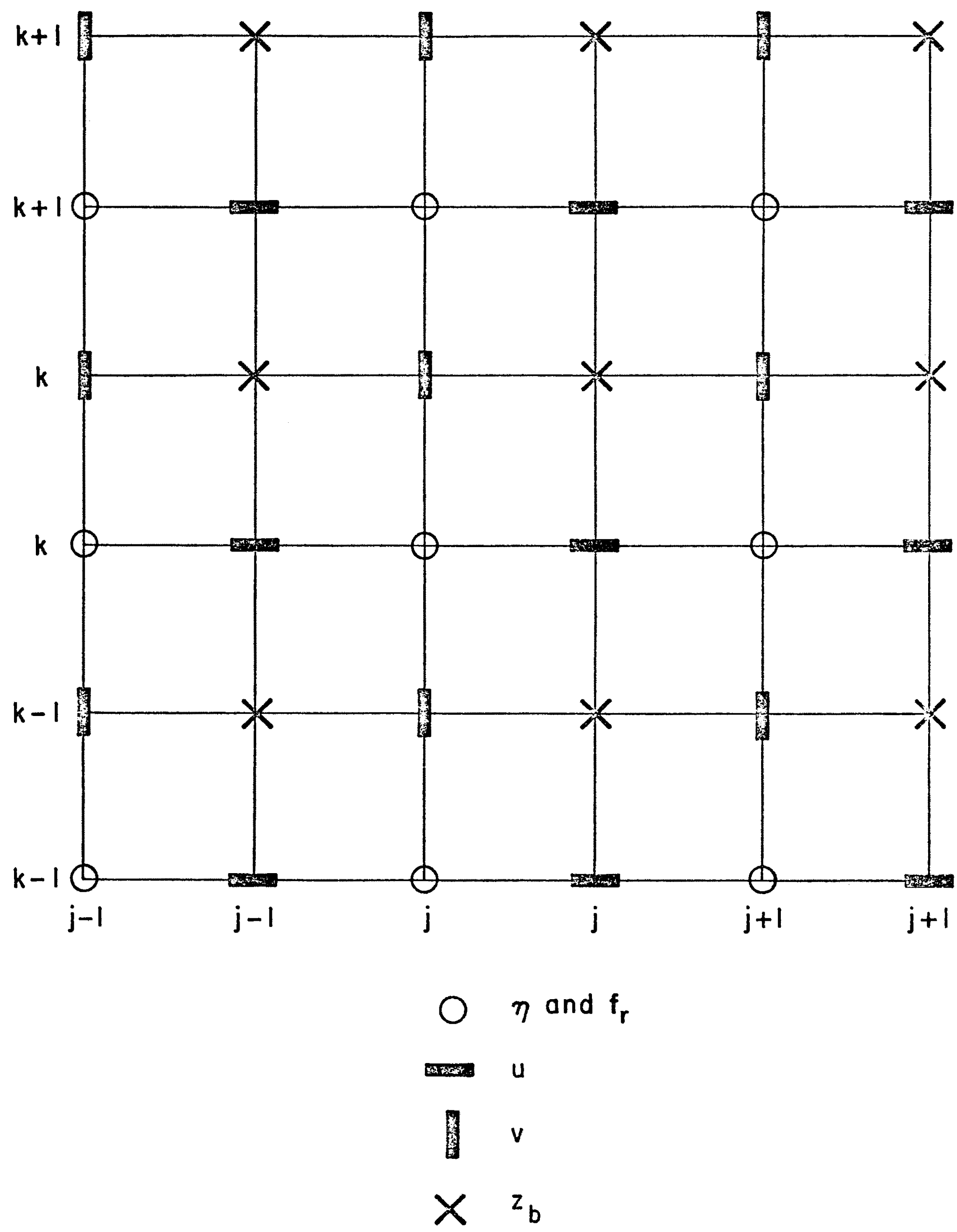

Figure 4.1. Typical spatial grid at time level η.

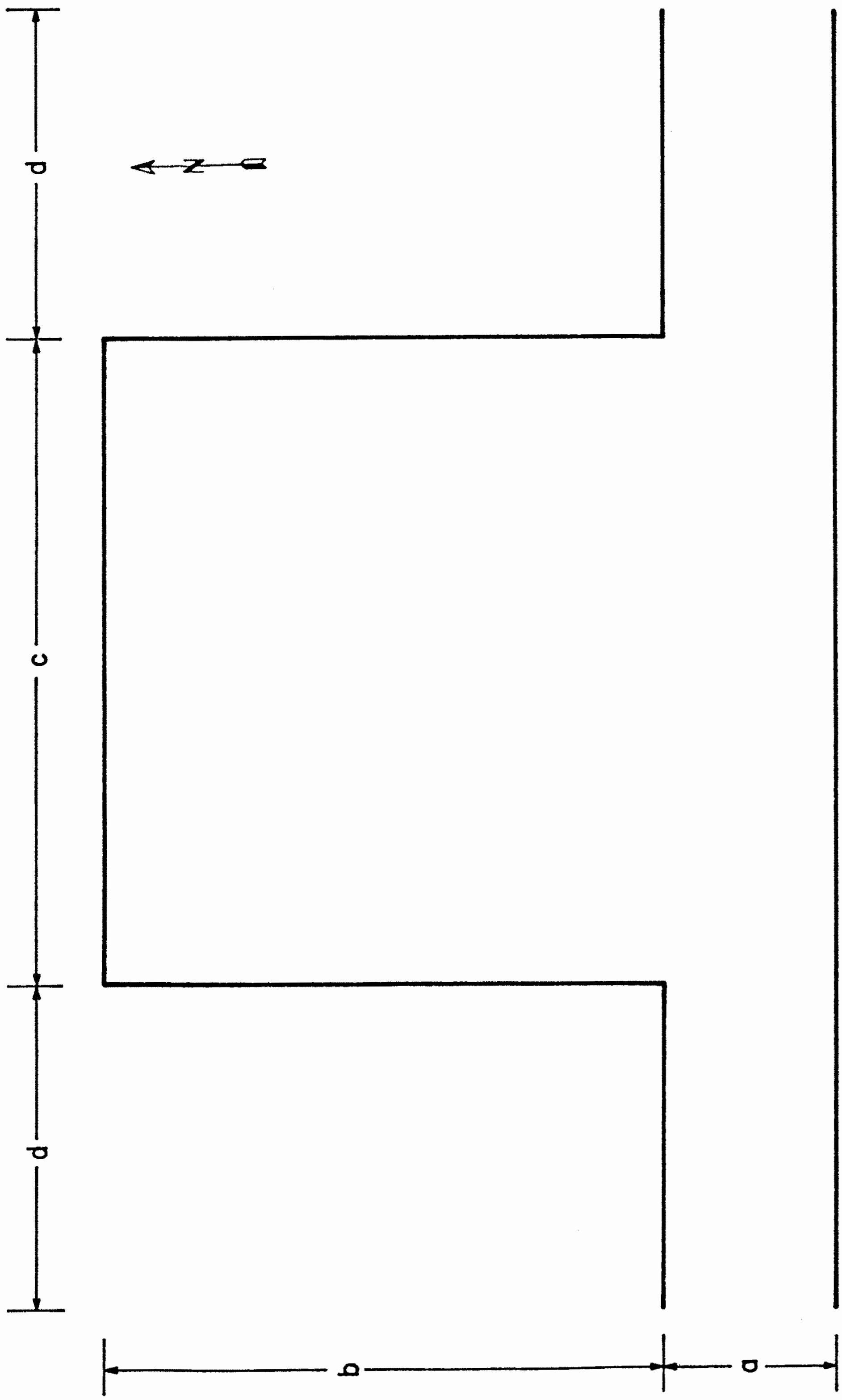

Figure 5.1. Pool-channel configuration.

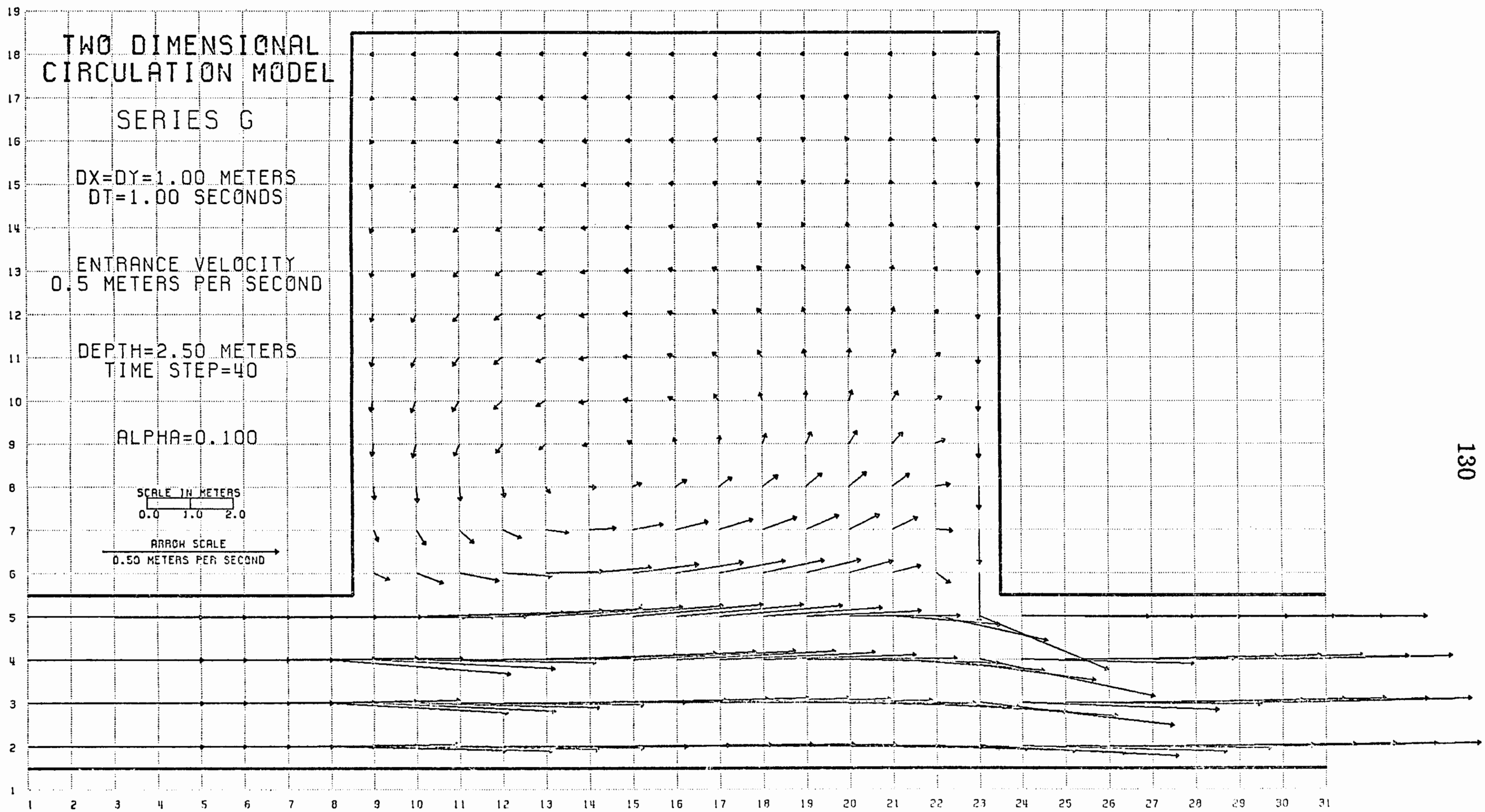

Figure 5.2. Channel velocity-specified baseline: time step 40.

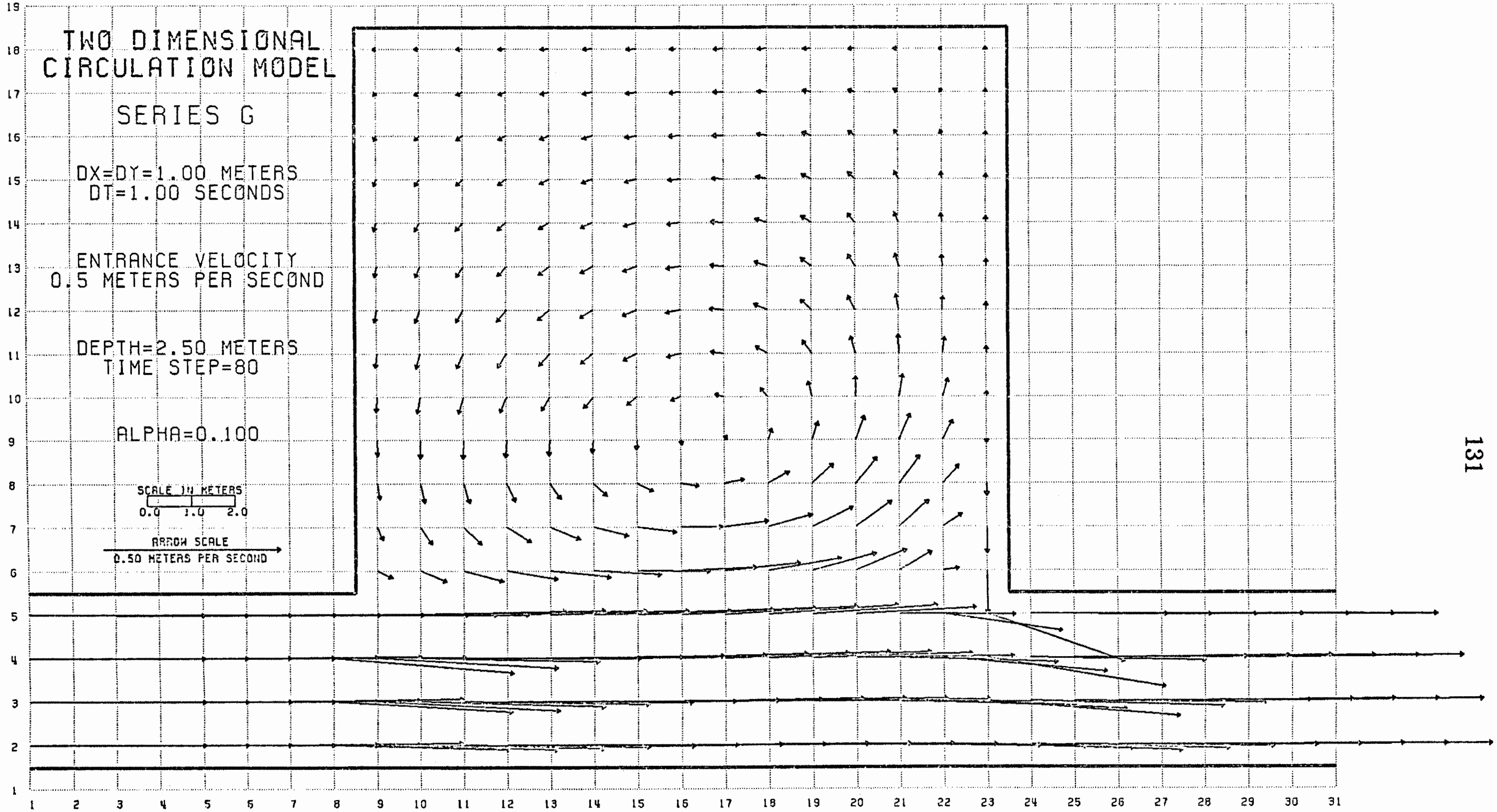

Figure 5.3. Channel velocity-specified baseline: time step 80.

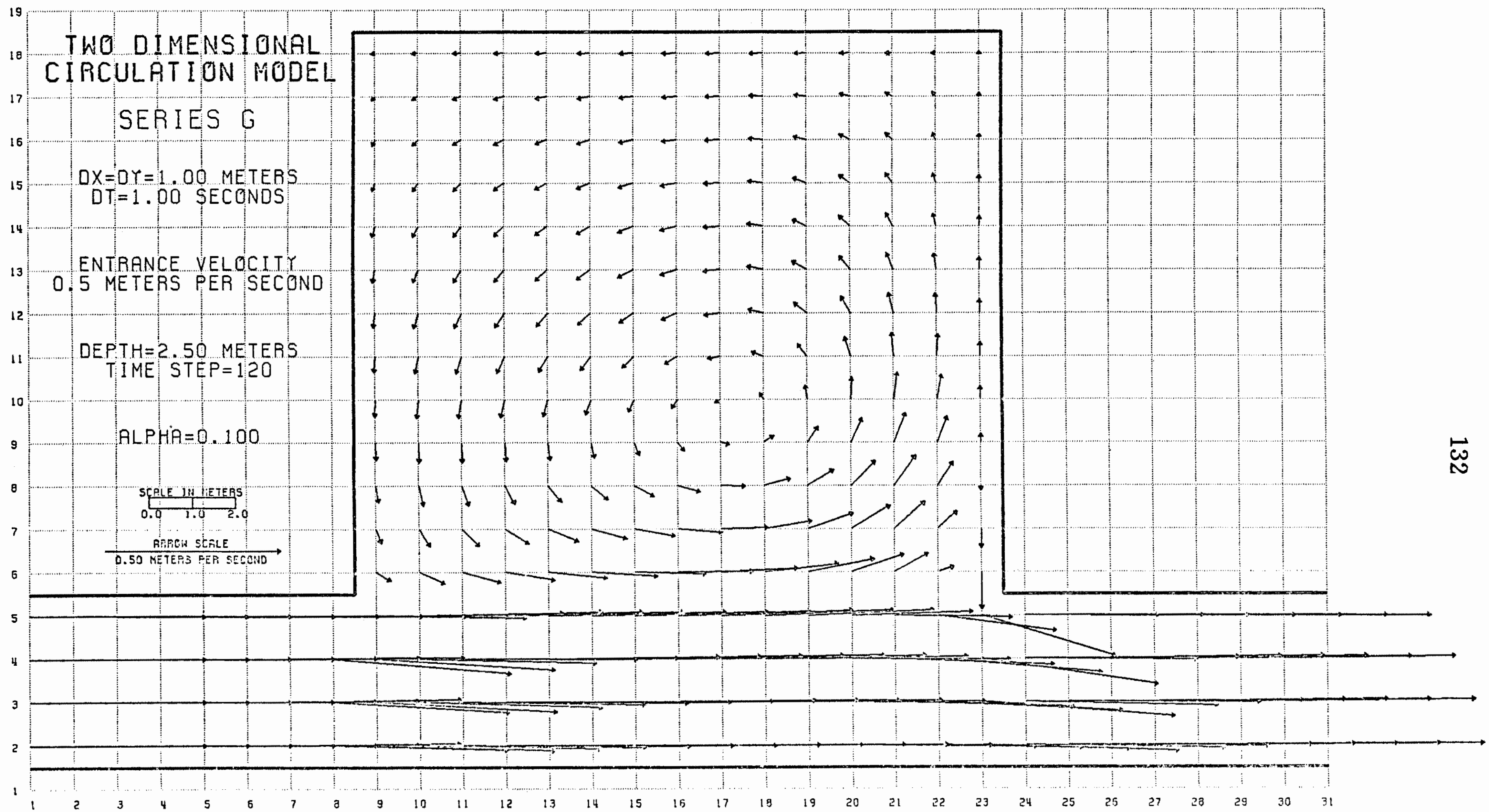

Figure 5.4. Channel velocity-specified baseline: time step 120.

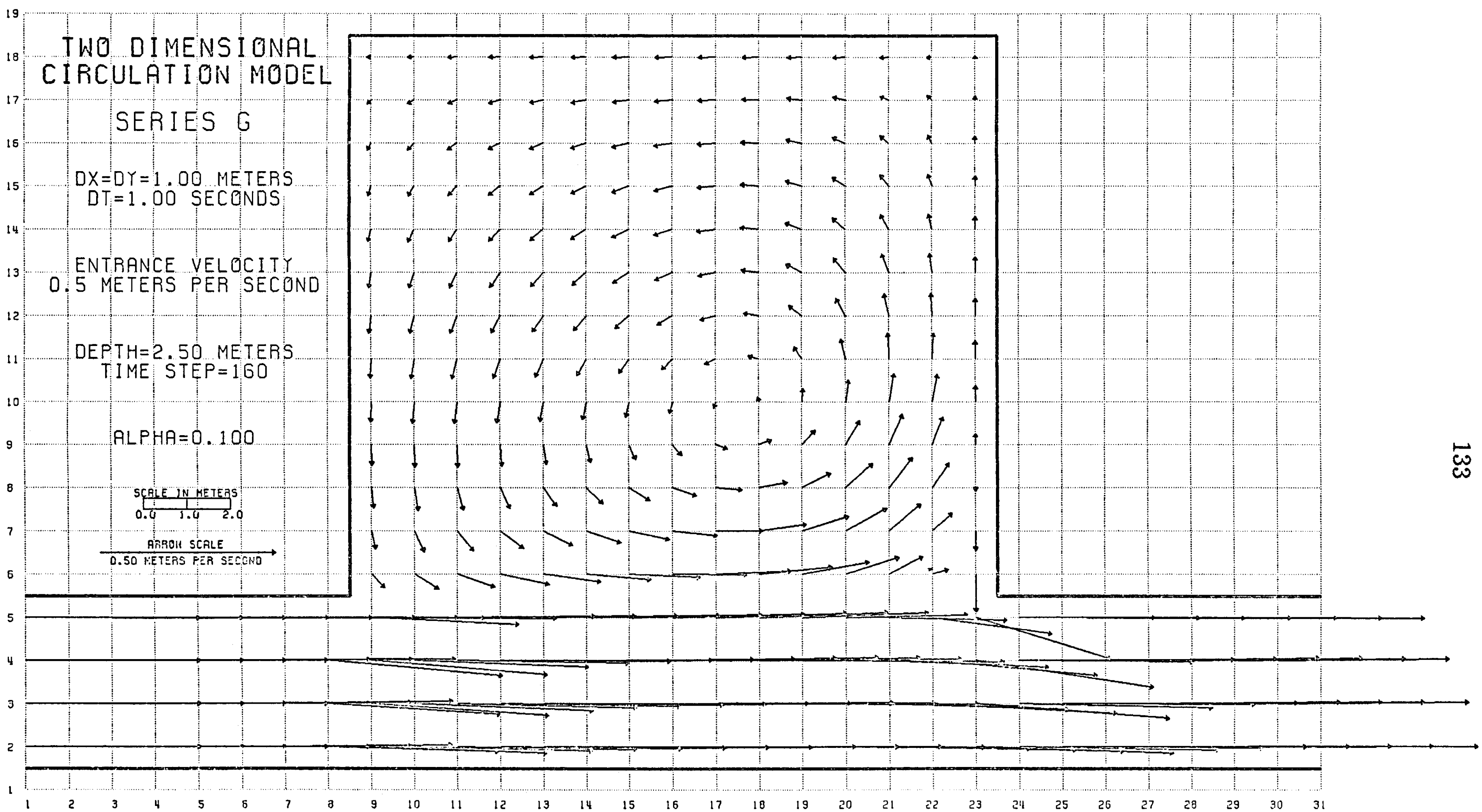

Figure 5.5. Channel velocity-specified baseline: time step 160.

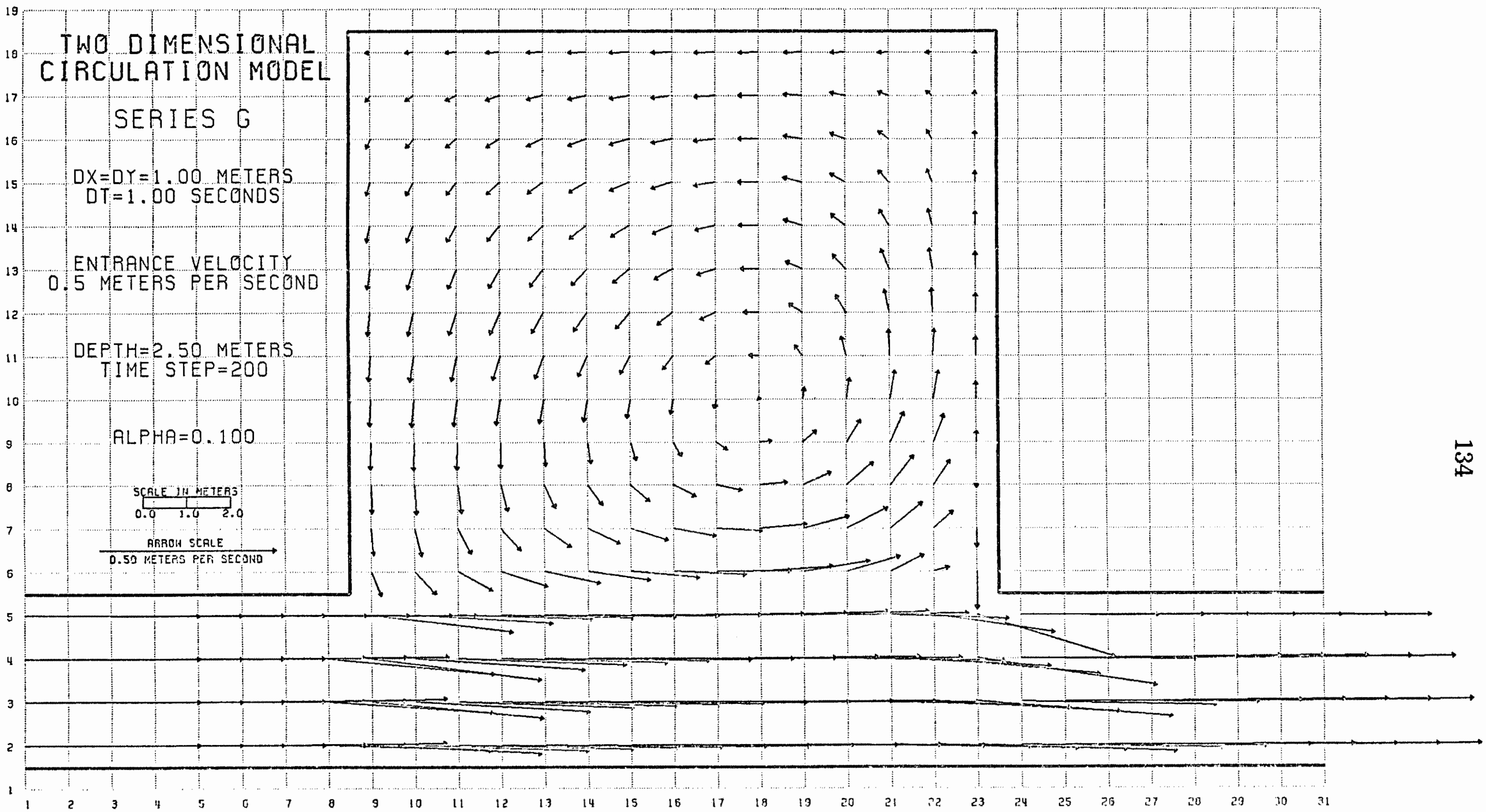

Figure 5.6. Channel velocity-specified baseline: time step 200.

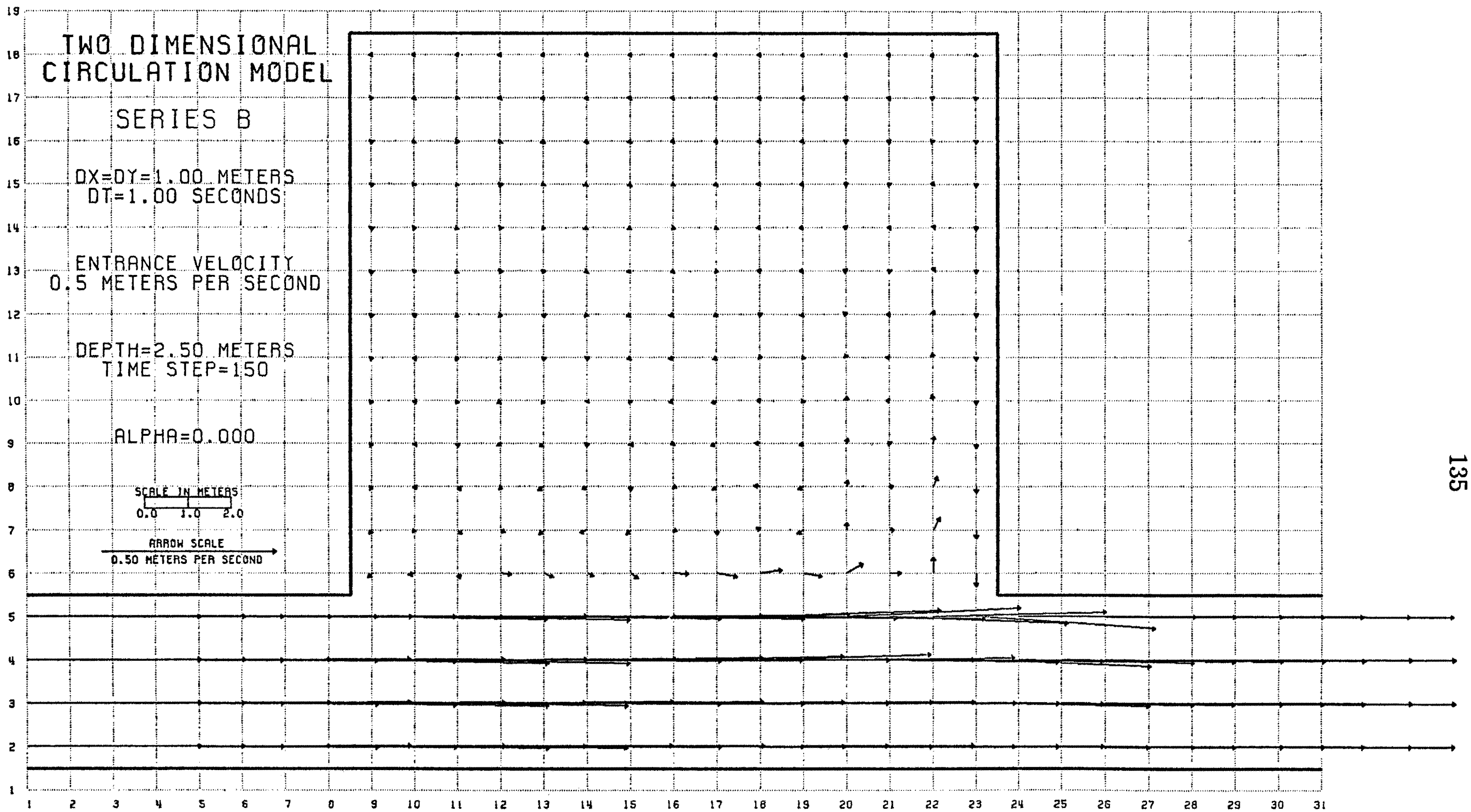

Figure 5.7. Omission of effective stresses: time step 150.

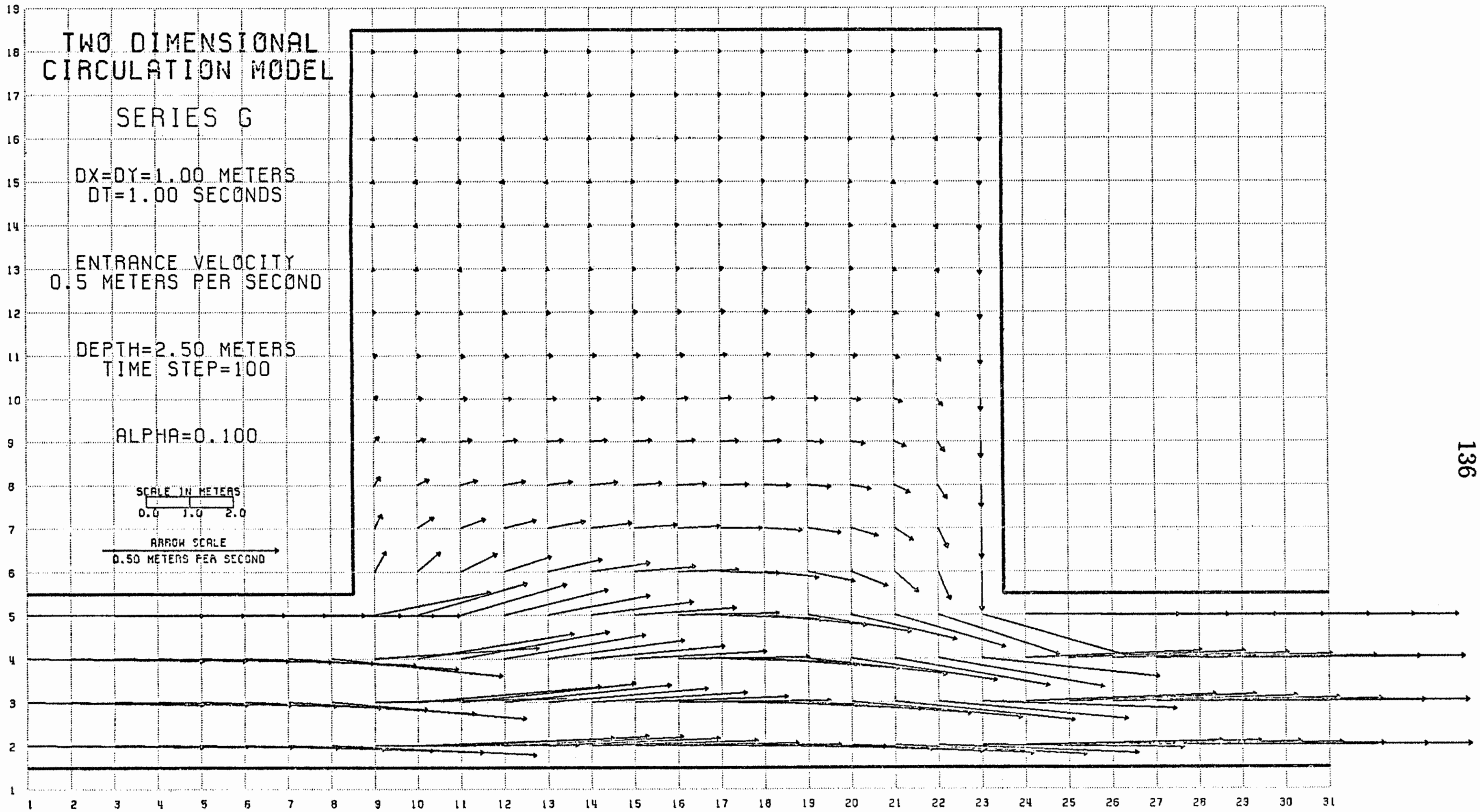

Figure 5.8. Omission of convective inertia: time step 100.

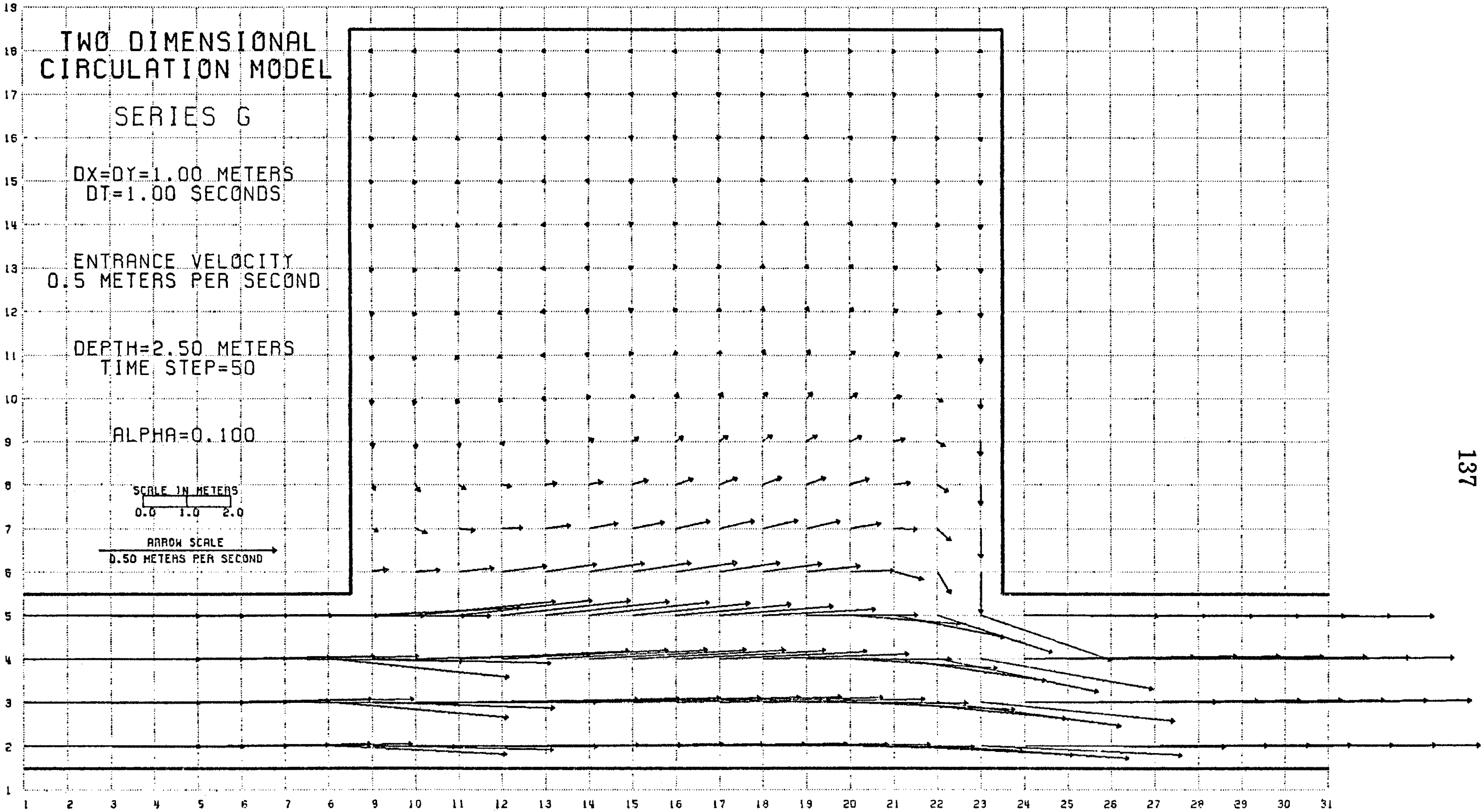

Figure 5.9. Omission of cross-convective terms: time step 50.

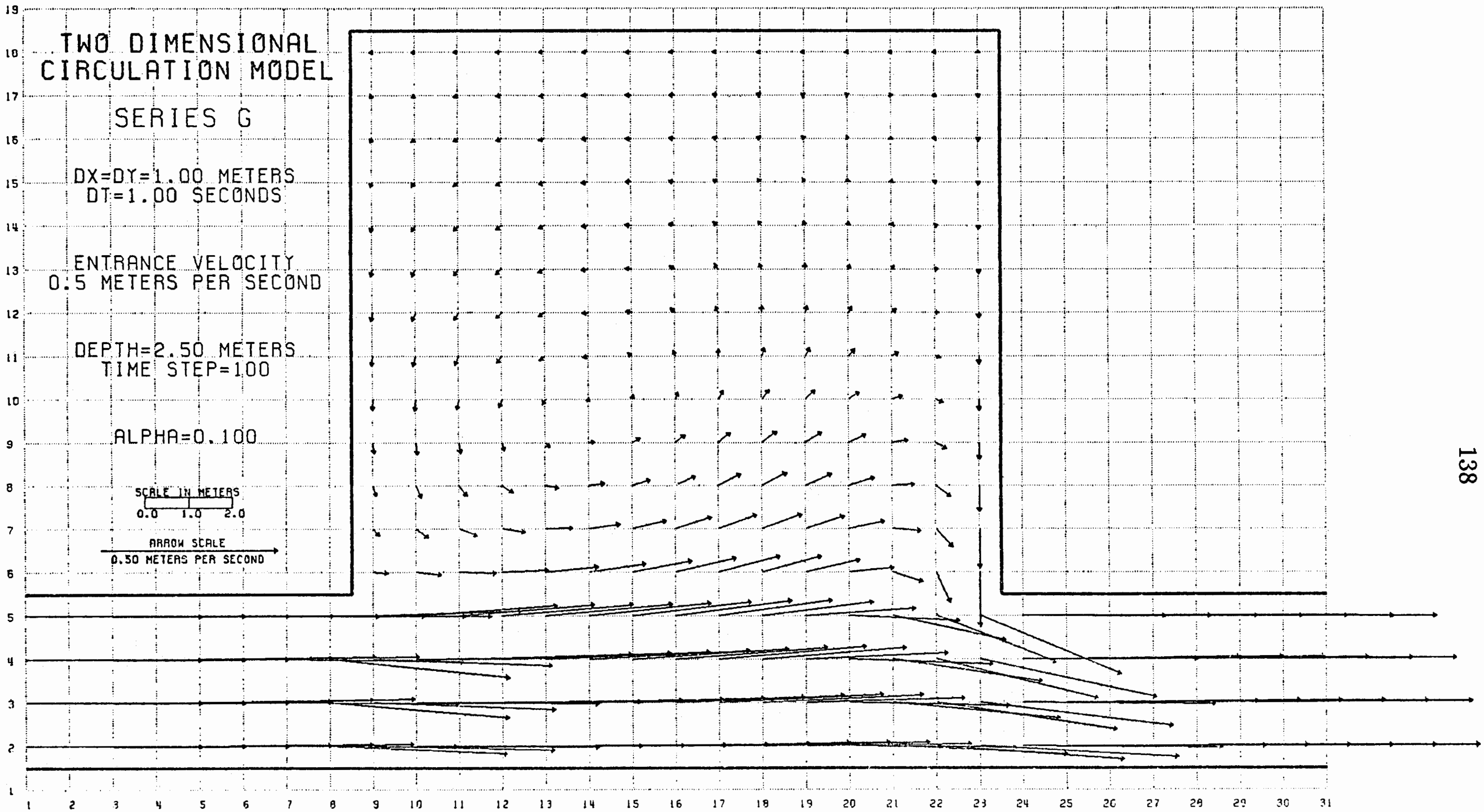

Figure 5.10. Omission of cross-convective terms: time step 100.

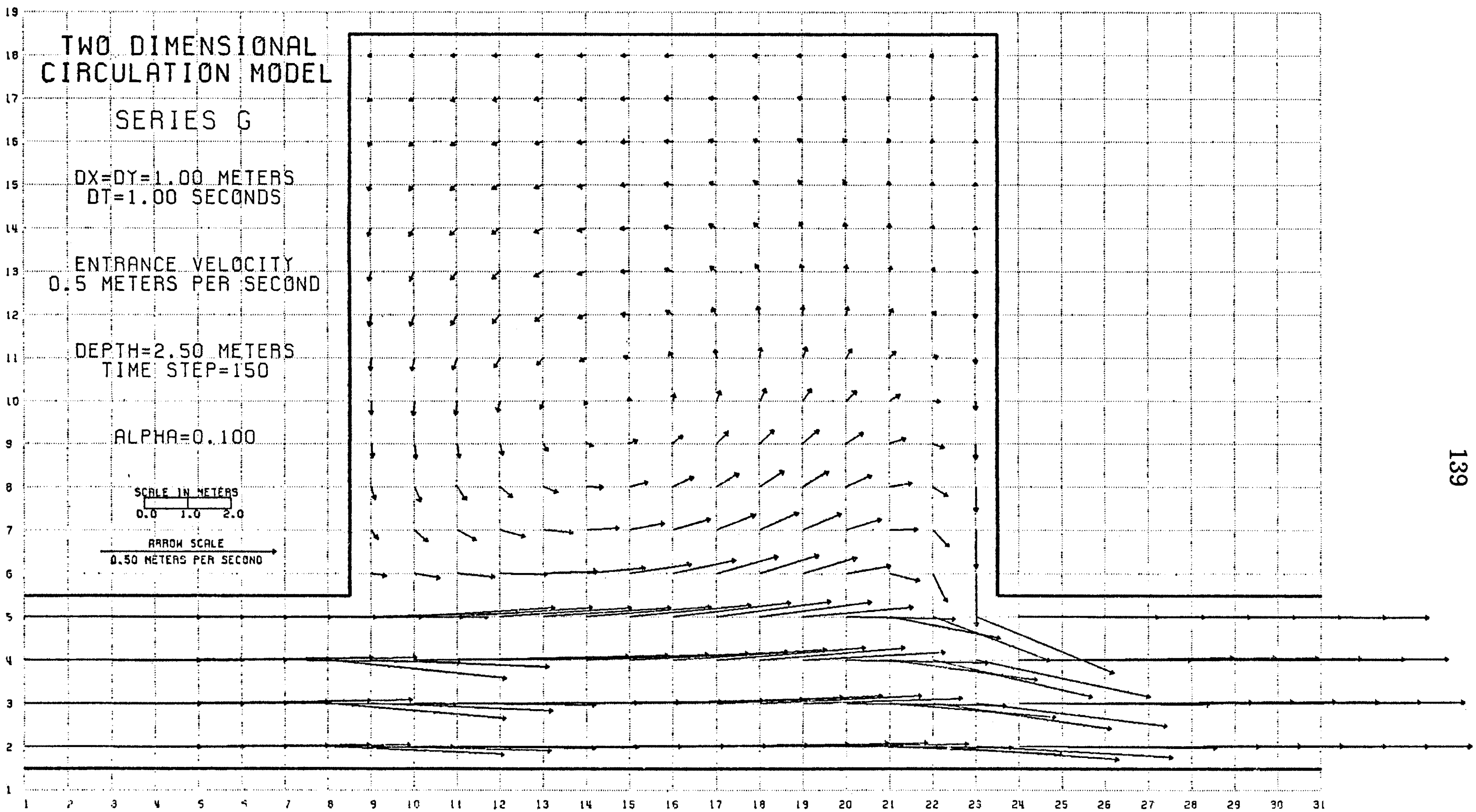

Figure 5.11. Omission of cross-convective terms: time step 150.

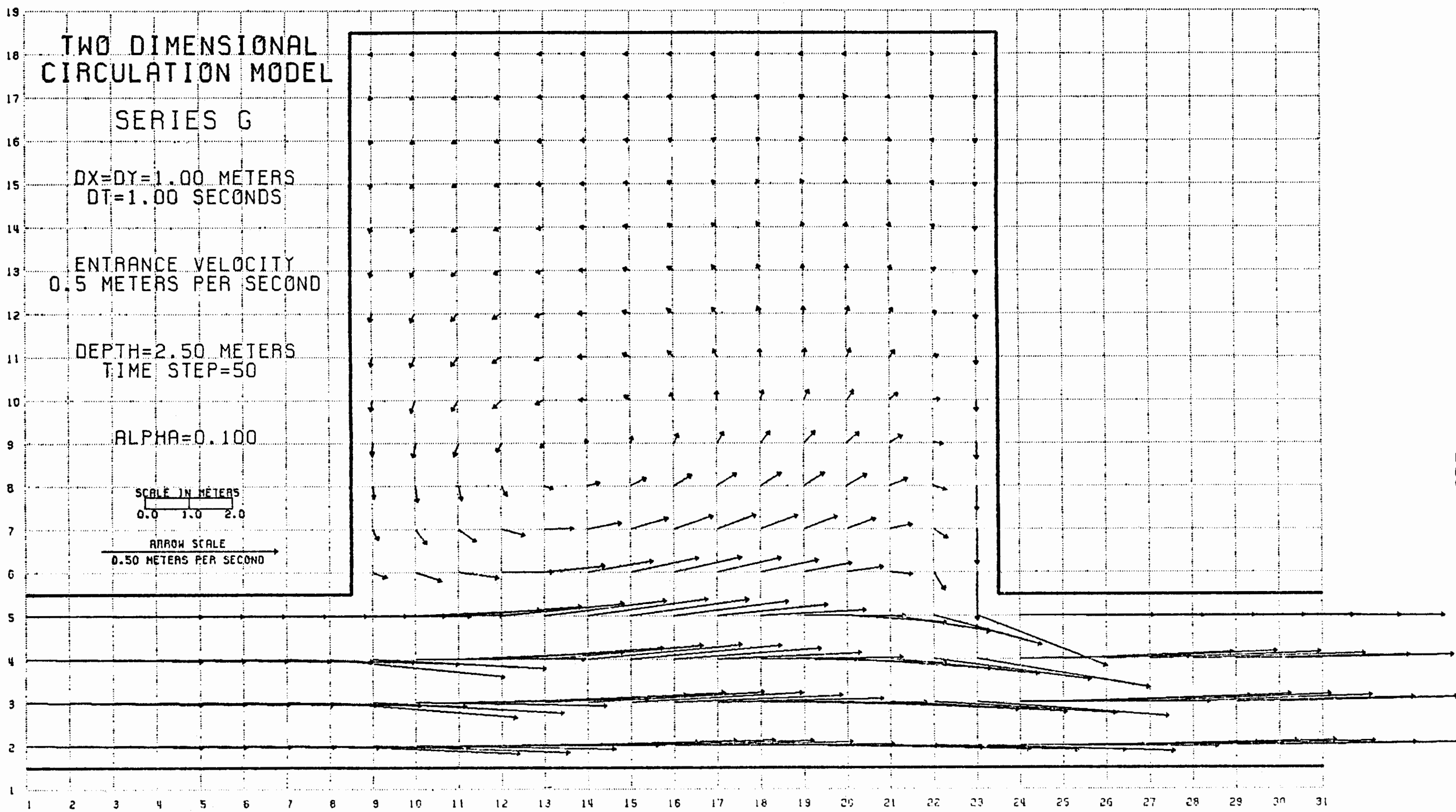

Figure 5.12. Omission of direct-convective terms: time step 50.

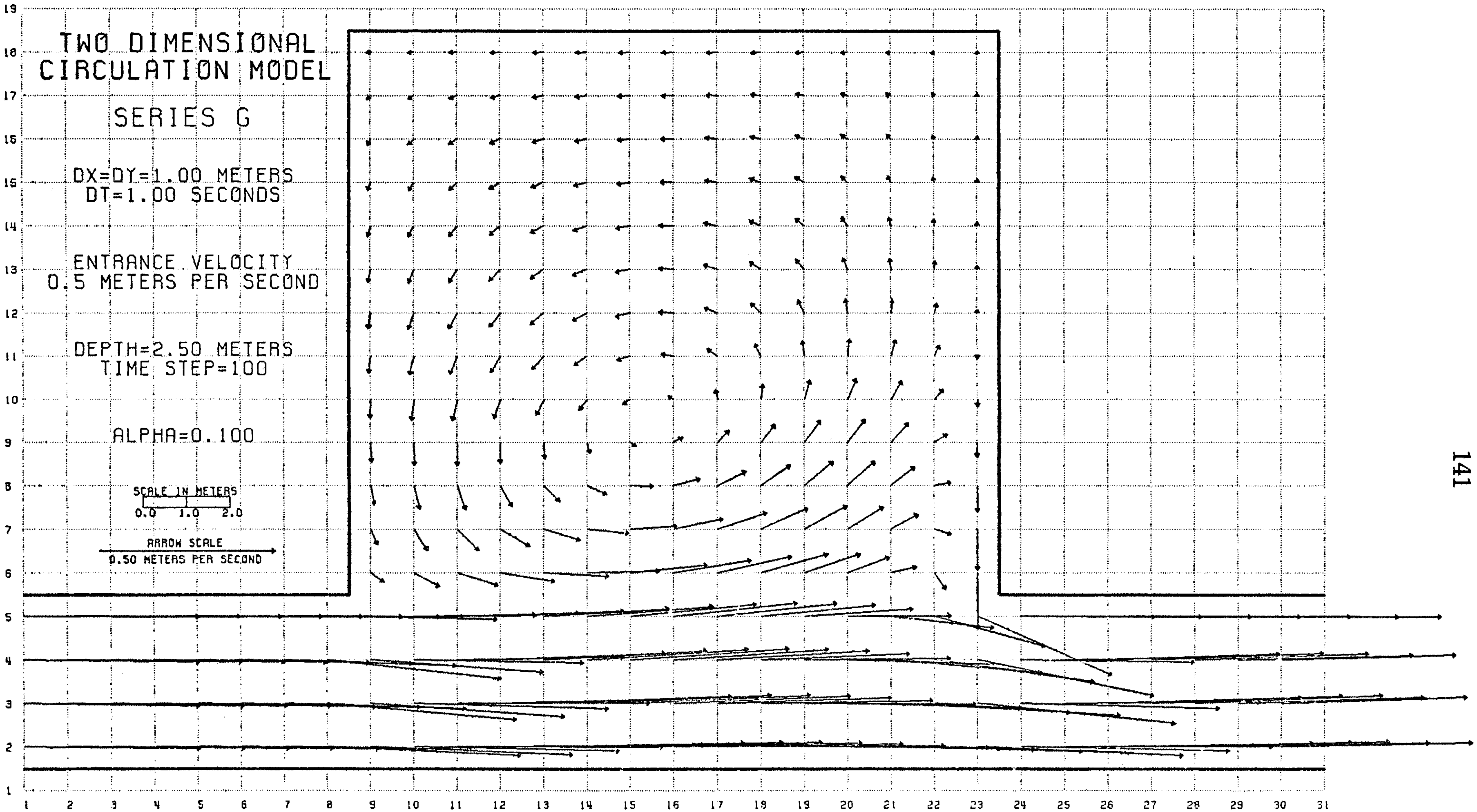

Figure 5.13. Omission of direct-convective terms: time step 100.

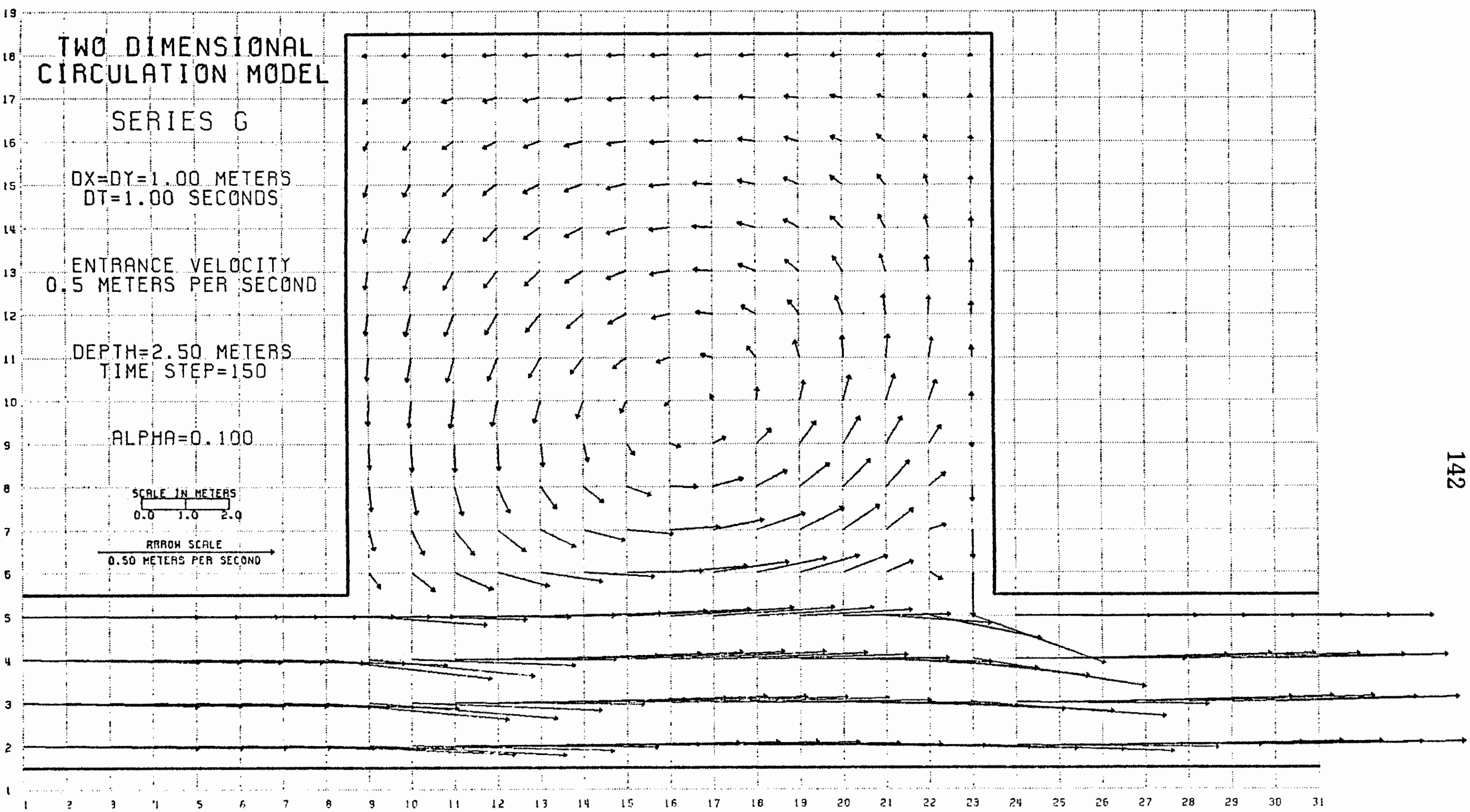

Figure 5.14. Omission of direct-convective terms: time step 150.

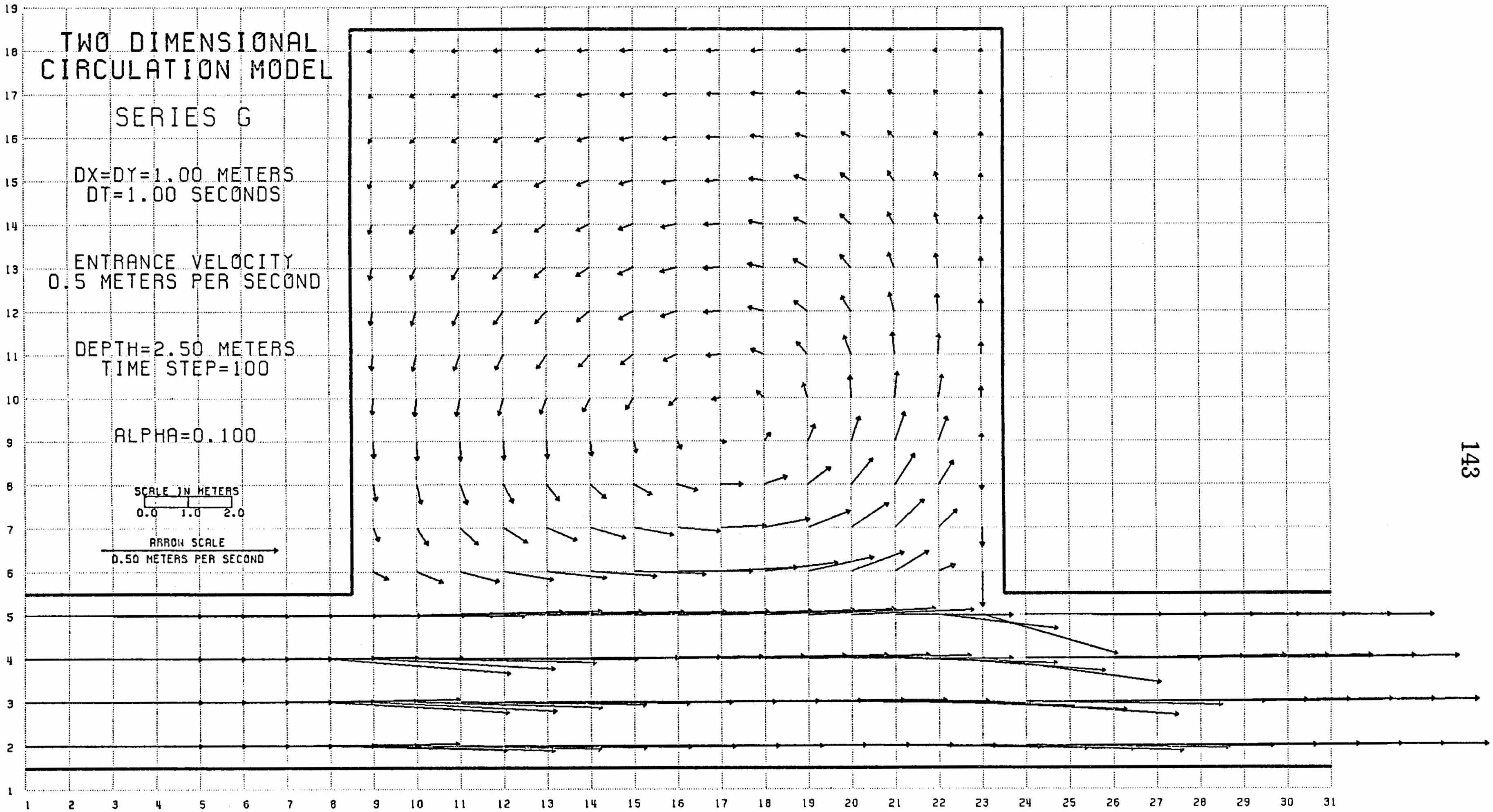

Figure 5.15. Omission of bed resistance: time step 100.

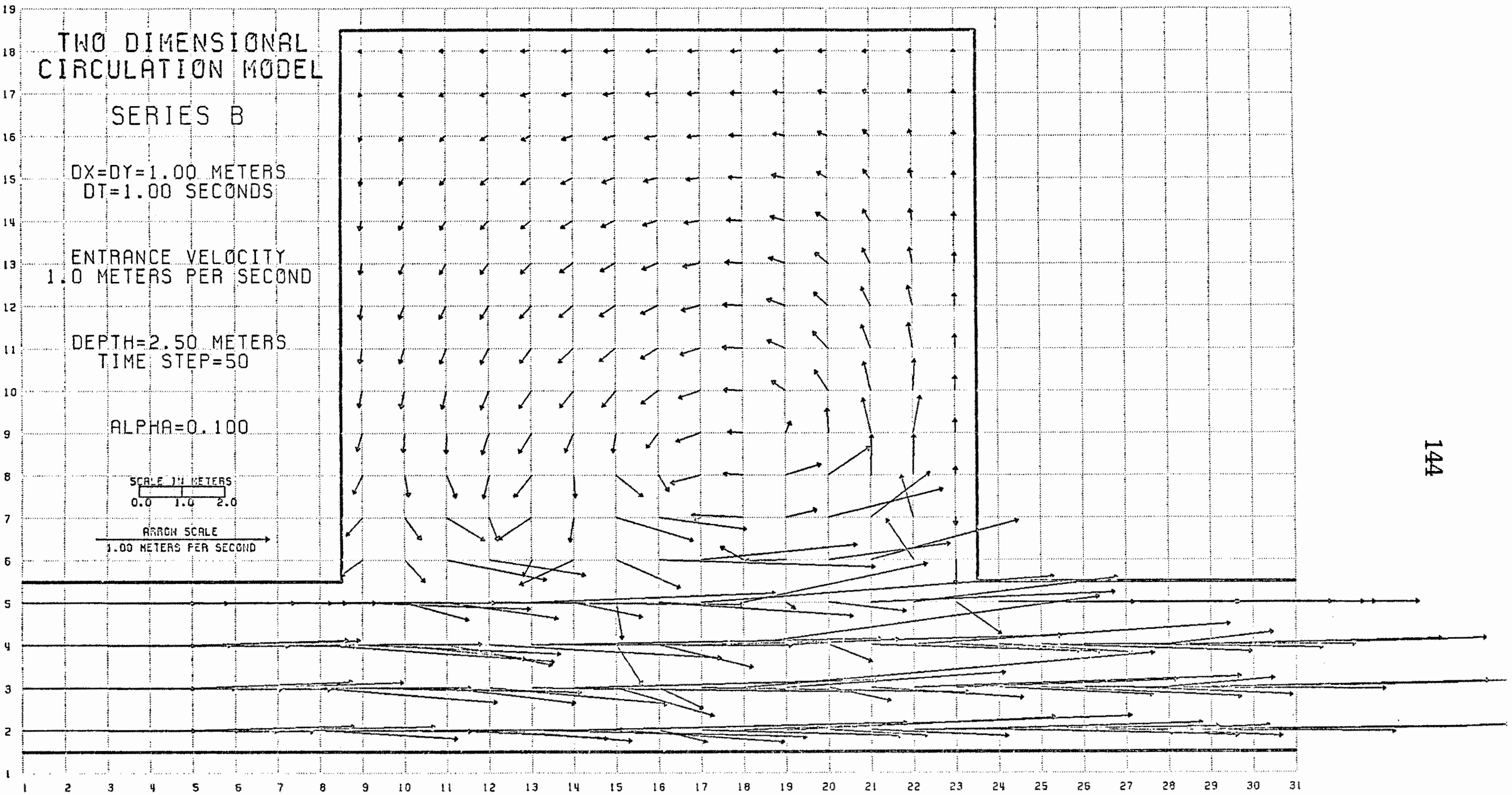

Figure 5.16. Channel velocity, U = 1.0 m/s: time step 50.

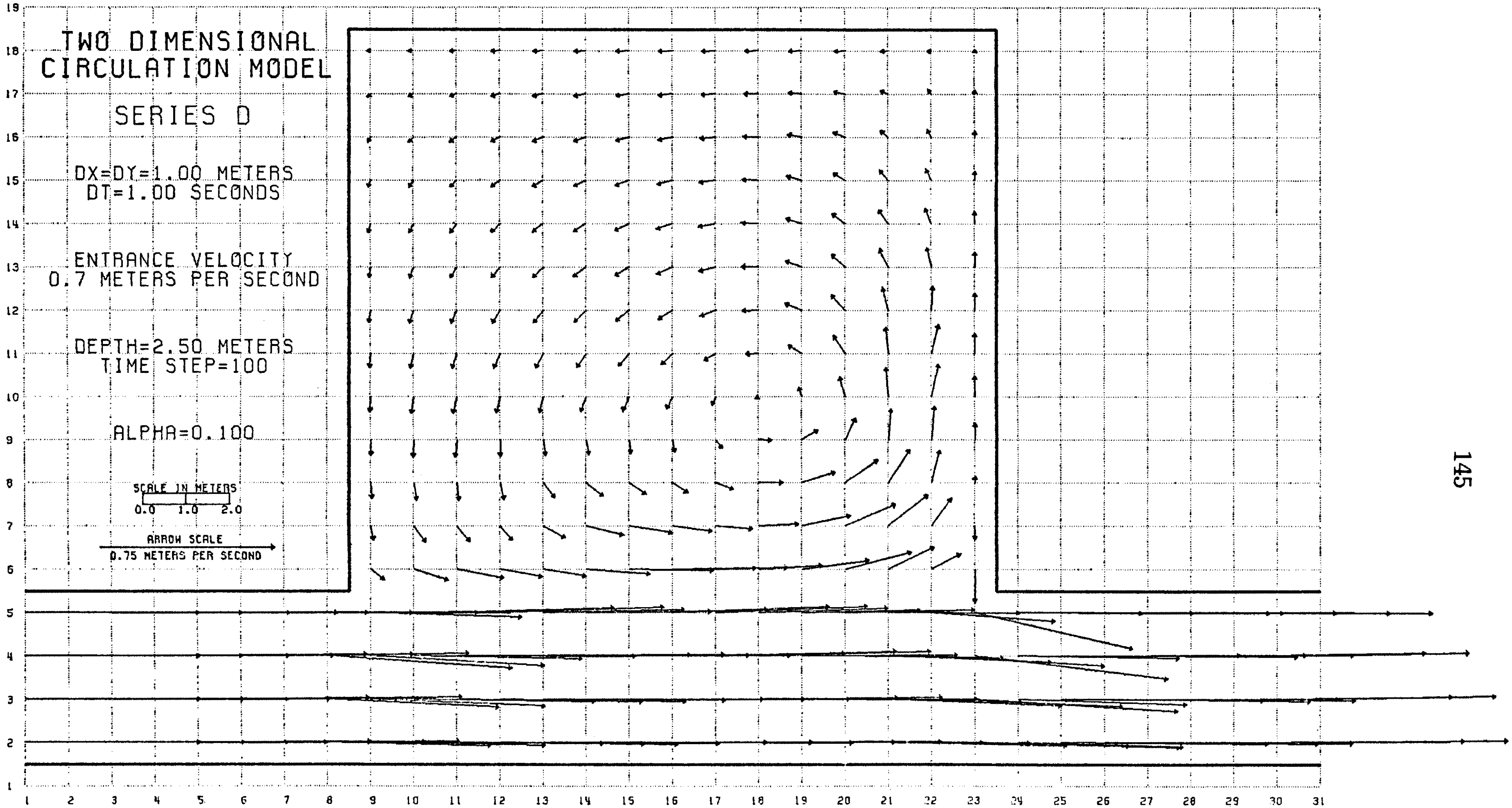

Figure 5.17. Channel velocity, U = 0.75 m/s: time step 100.

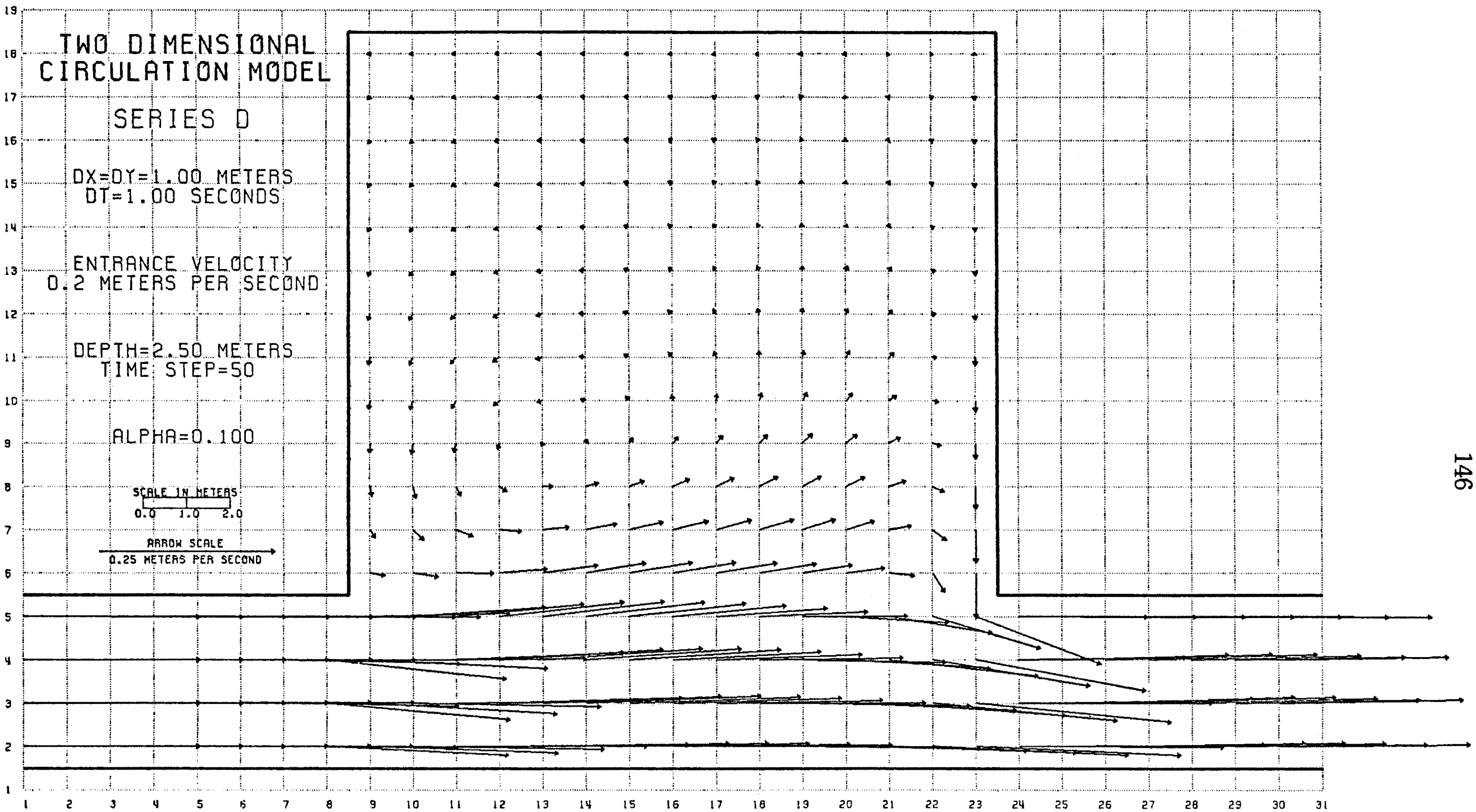

Figure 5.18. Channel velocity, U = 0.25 m/s: time step 50.

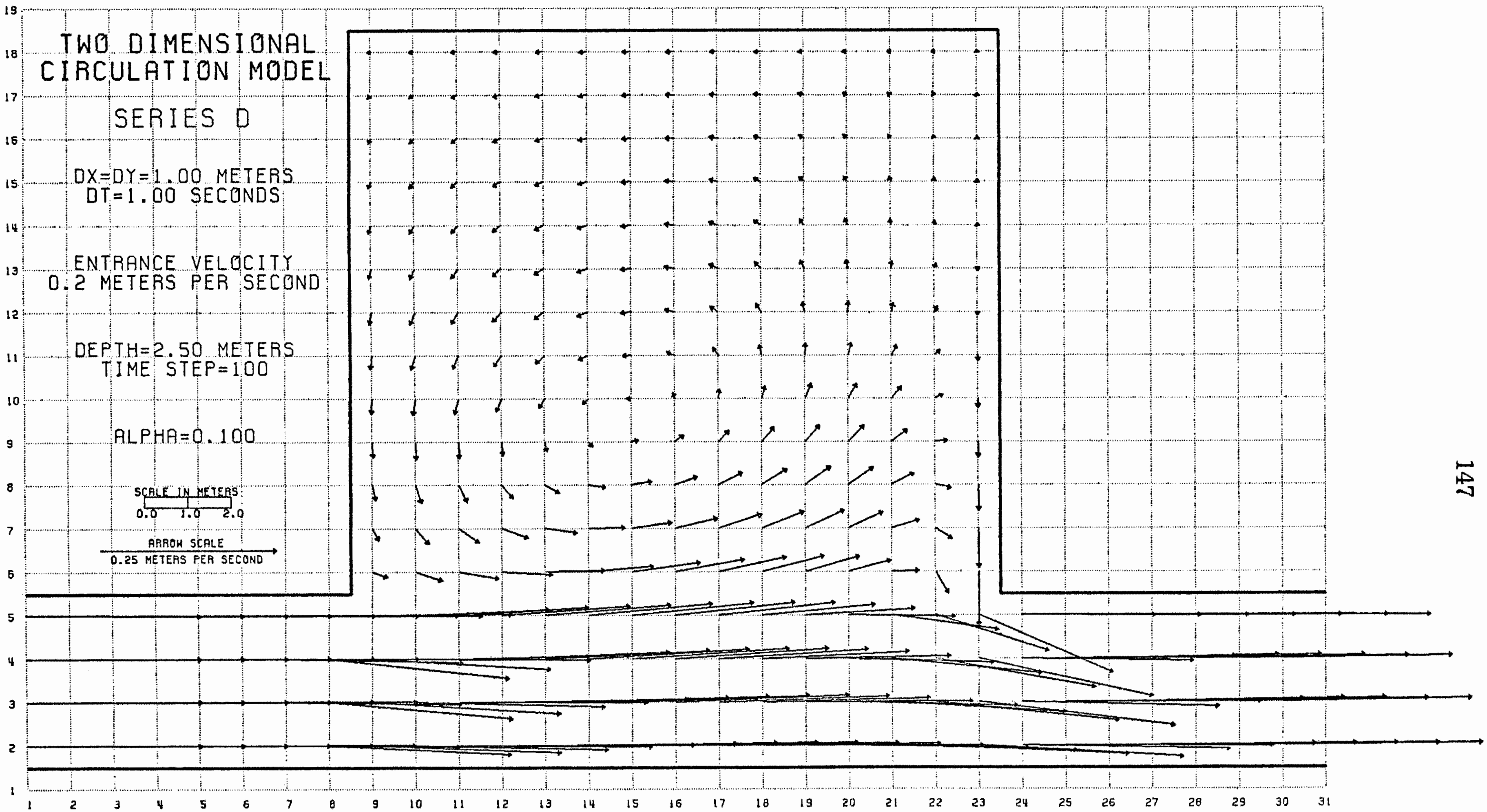

Figure 5.19. Channel velocity, U = 0.25 m/s: time step 50.

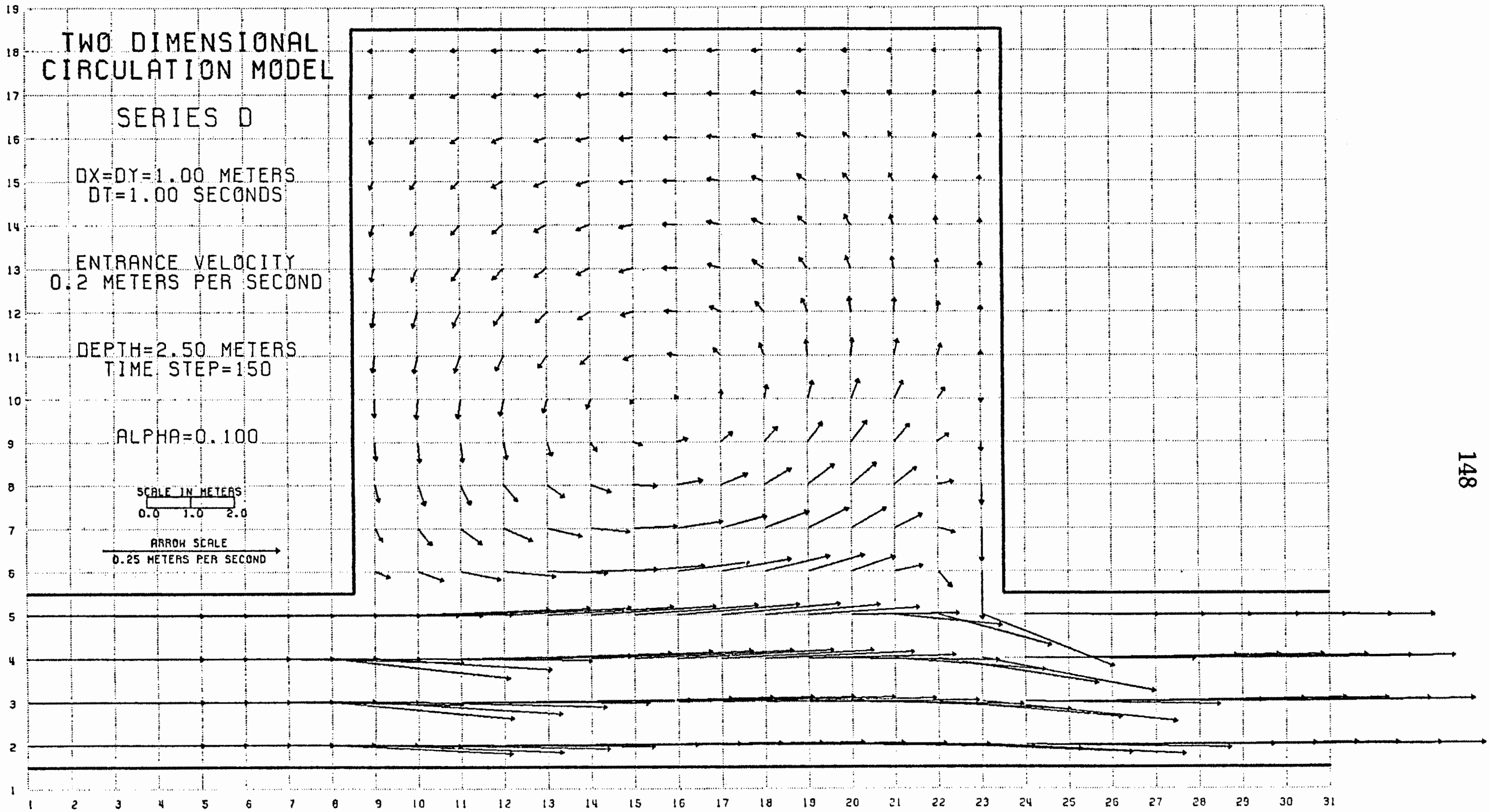

Figure 5.20. Channel velocity, U = 0.25 m/s: time step 150.

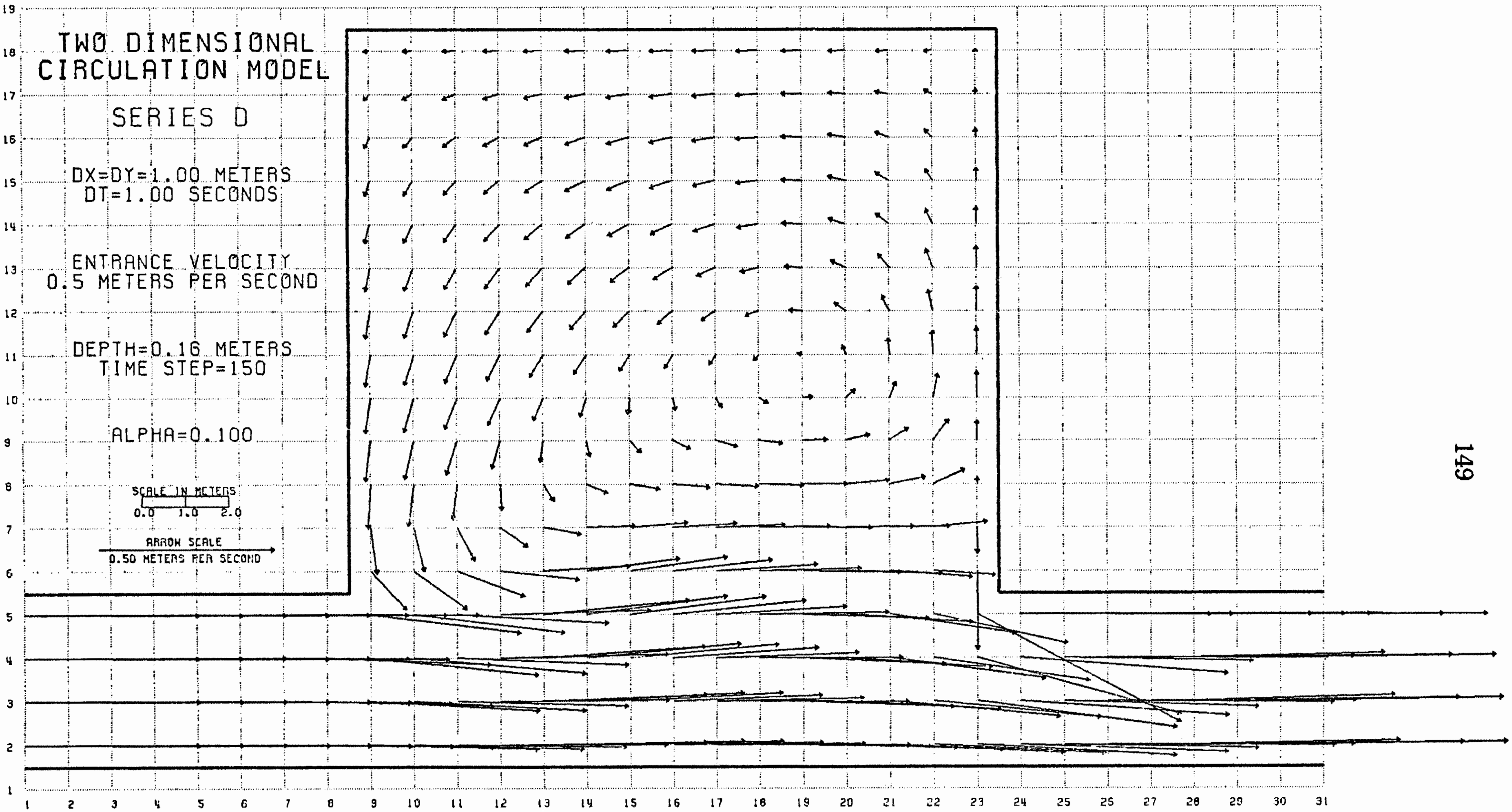

Figure 5.21. Depth, d = 0.16 meters: time step 150.

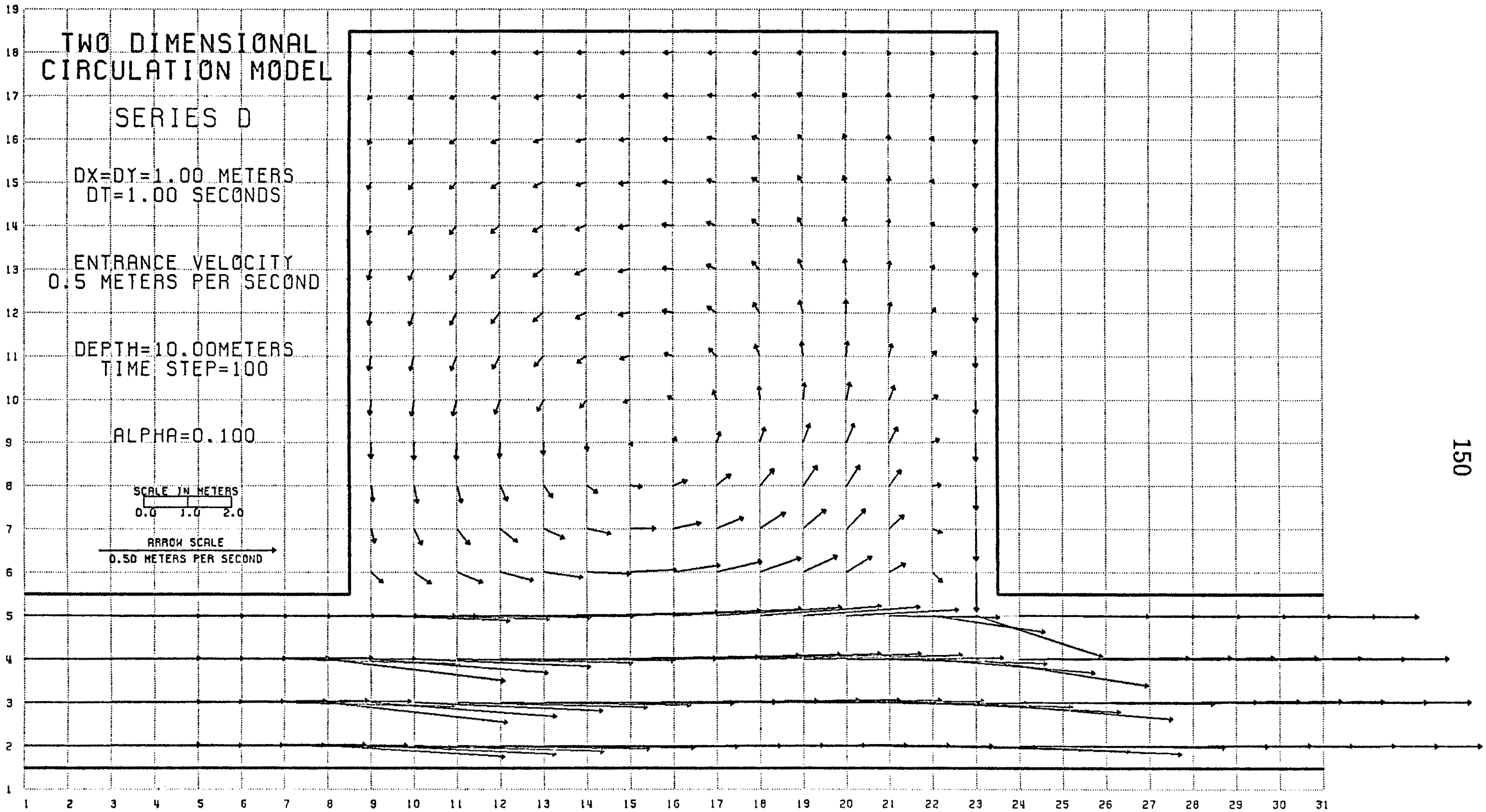

Figure 5.22. Depth, d = 10.0 meters: time step 100.

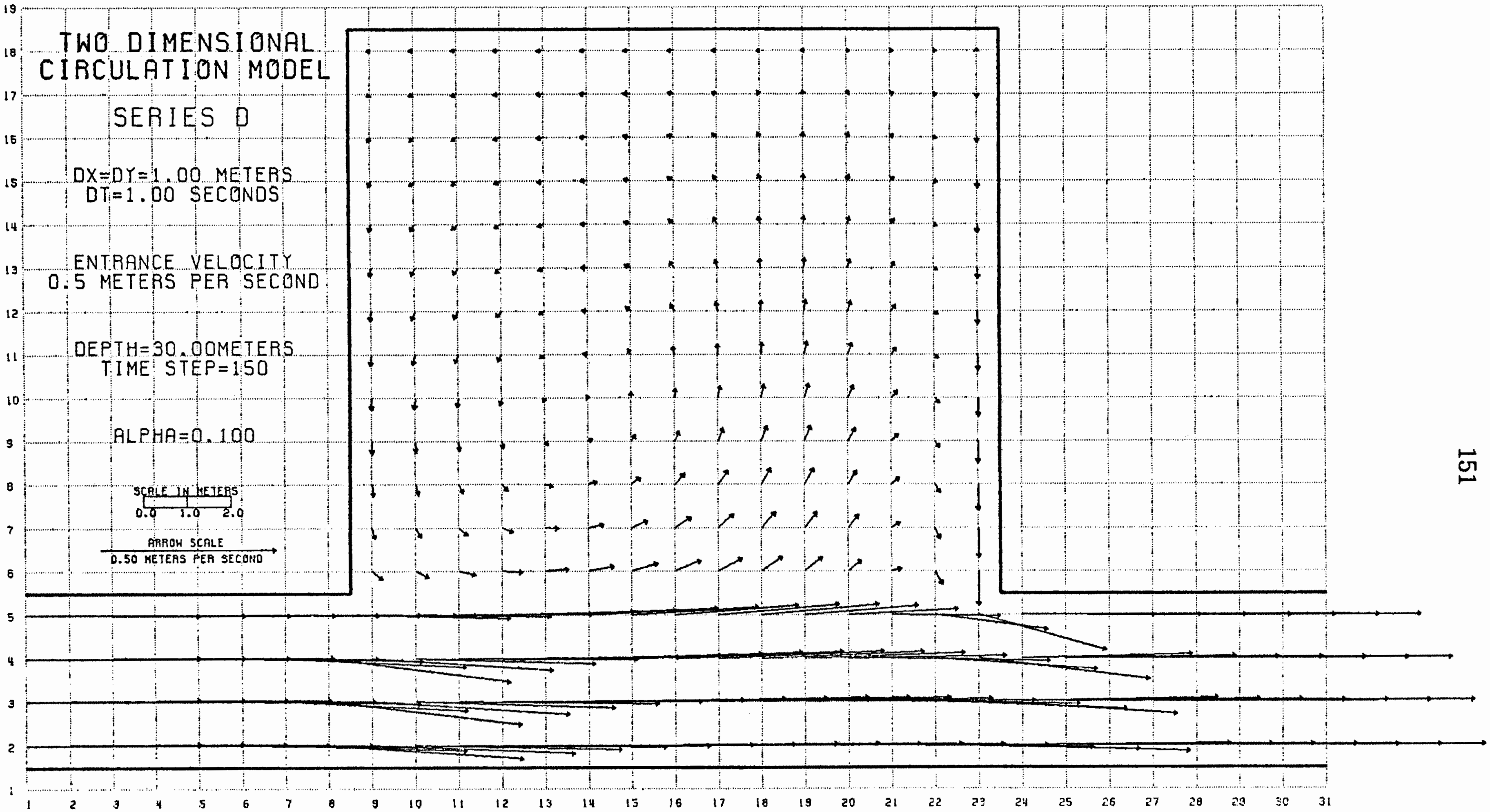

Figure 23. Depth, d = 30.0 meters: time step 150.

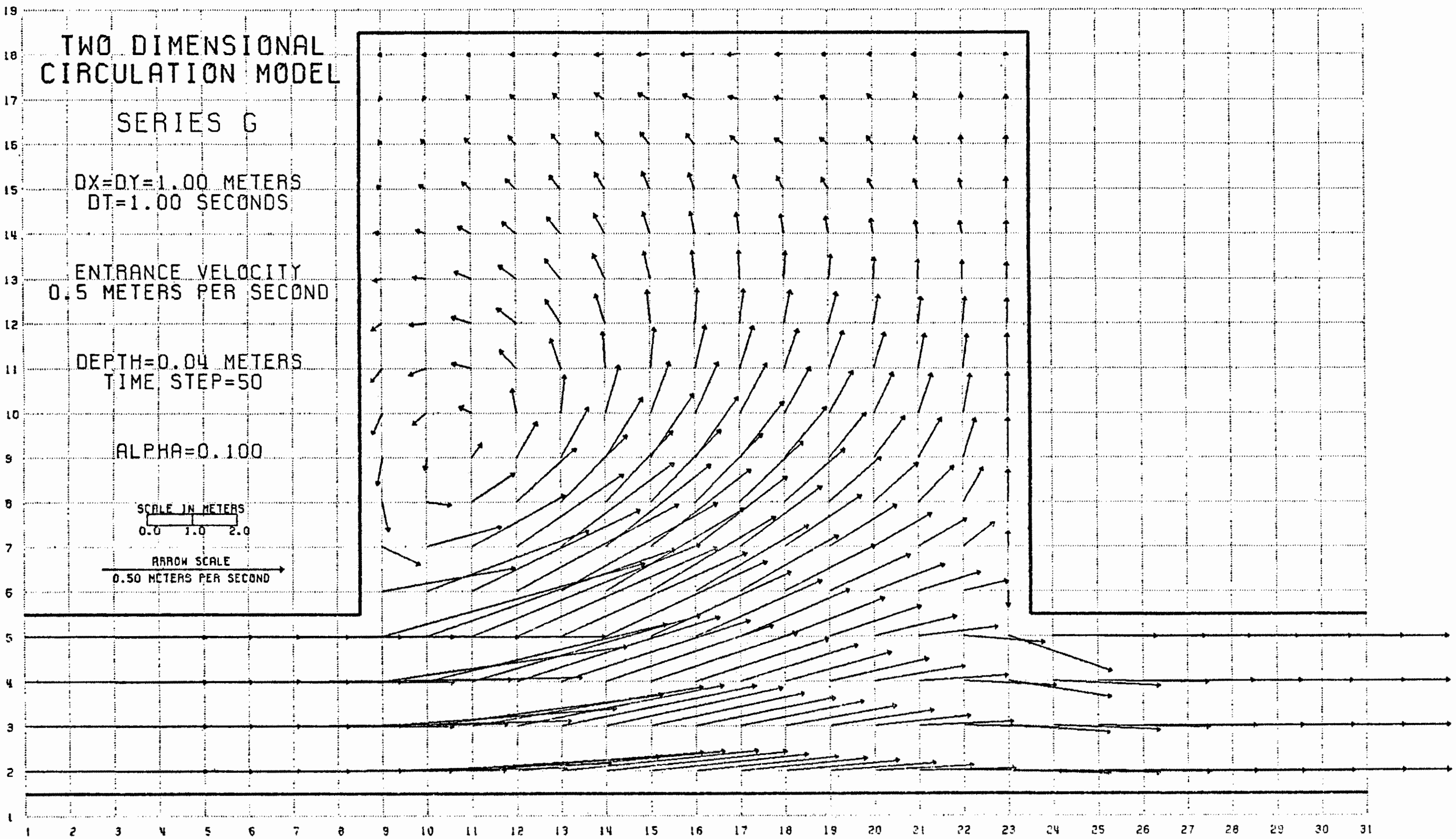

Figure 5.24. Depth, d = 0.4 meters: time step 50.

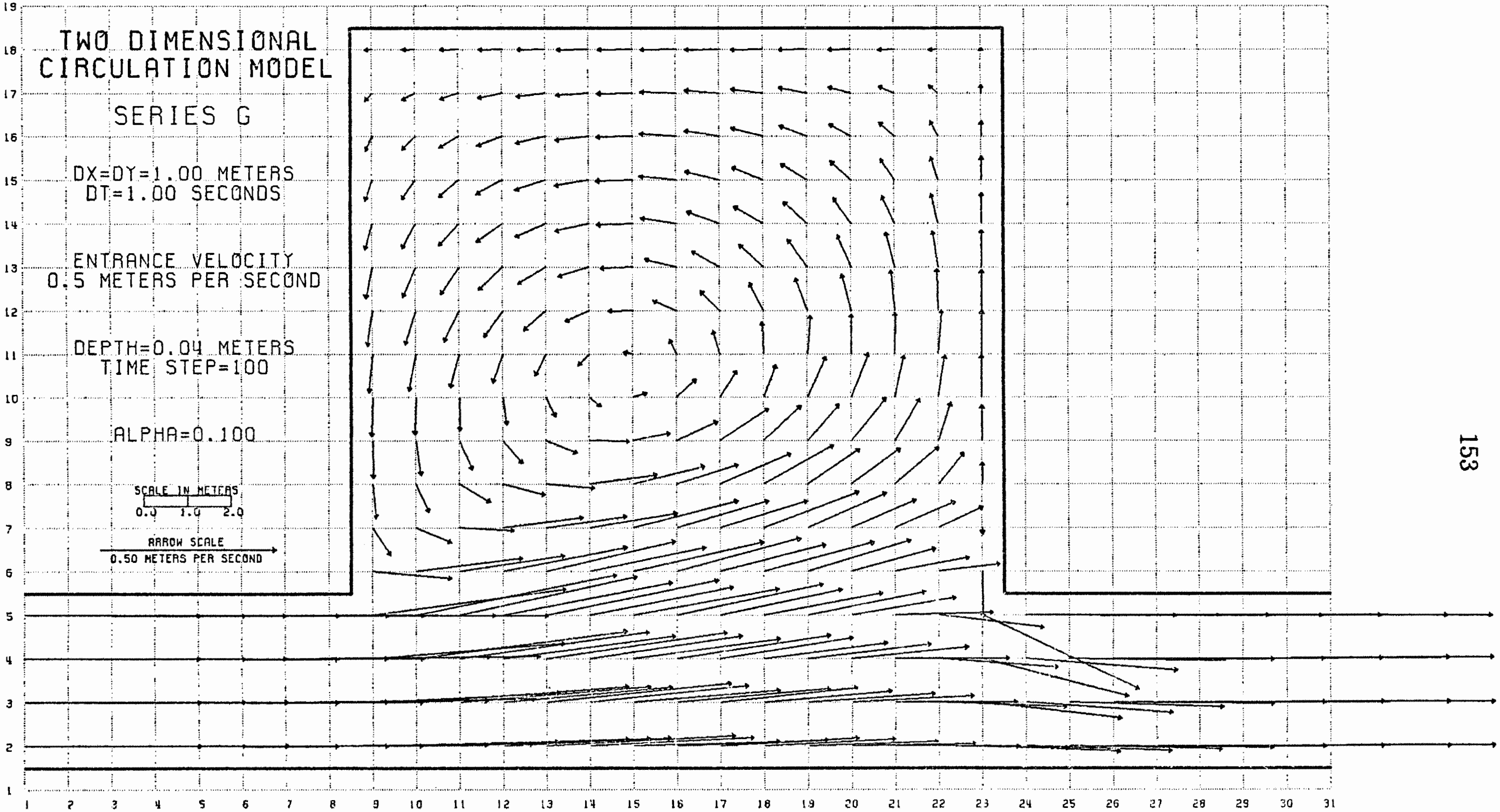

Figure 5.25. Depth, d = 0.04 meters: time step 100.

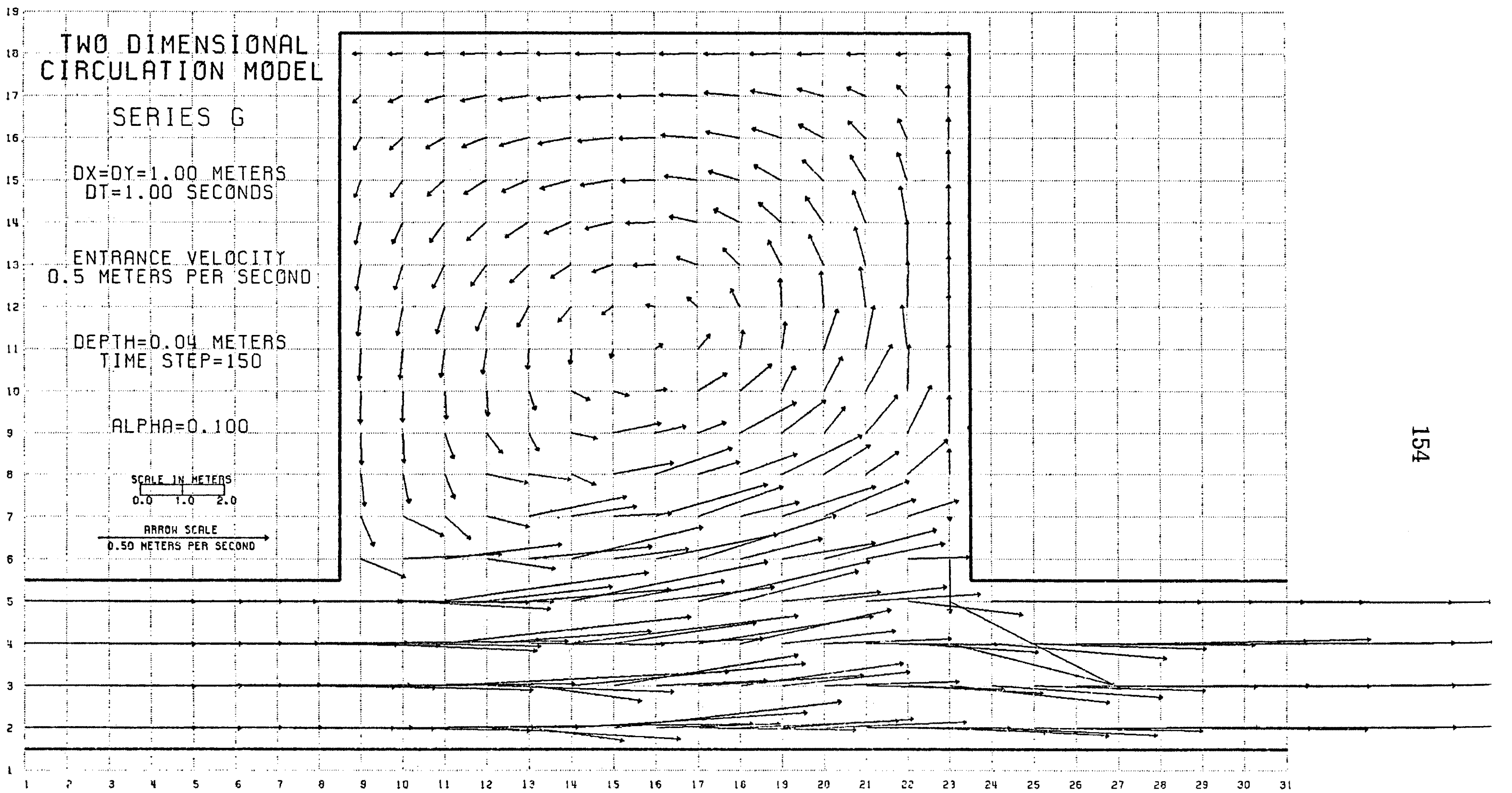

Figure 5.26. Depth, d = 0.04 meters: time step 150.

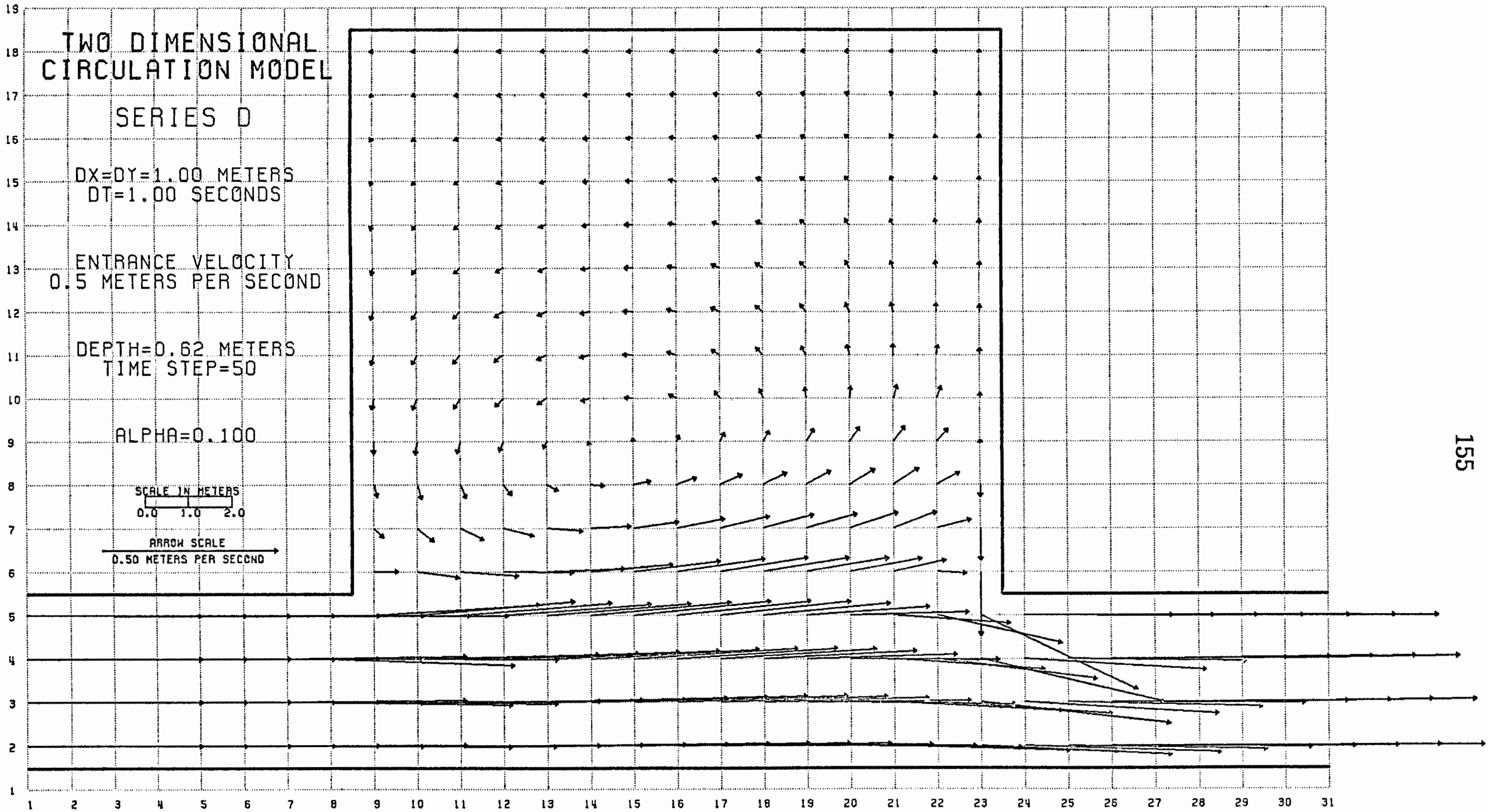

Figure 5.27. Depth, d = 0.62 meters: time step 50.

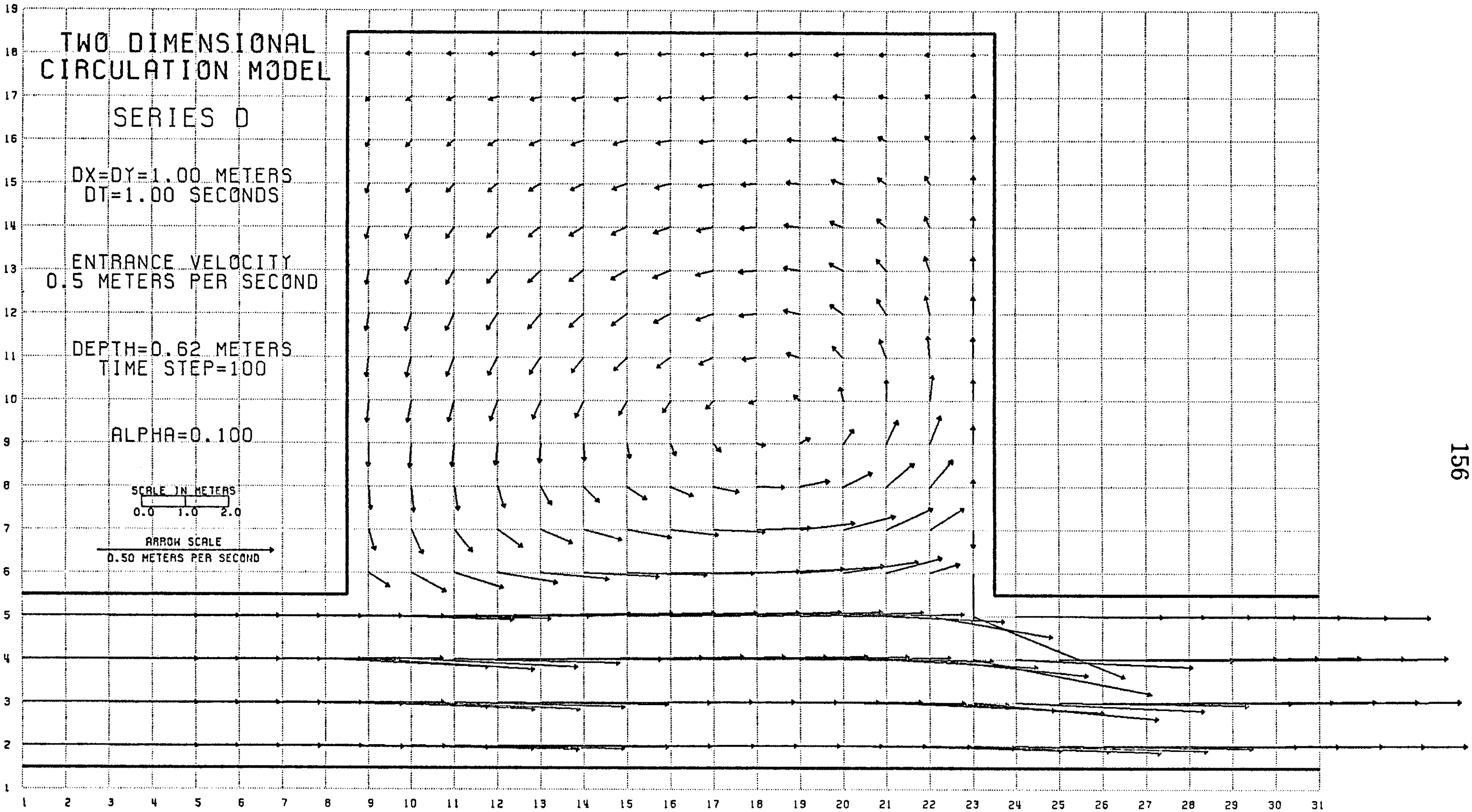

Figure 5.28. Depth, d = 0.62 meters: time step 100.

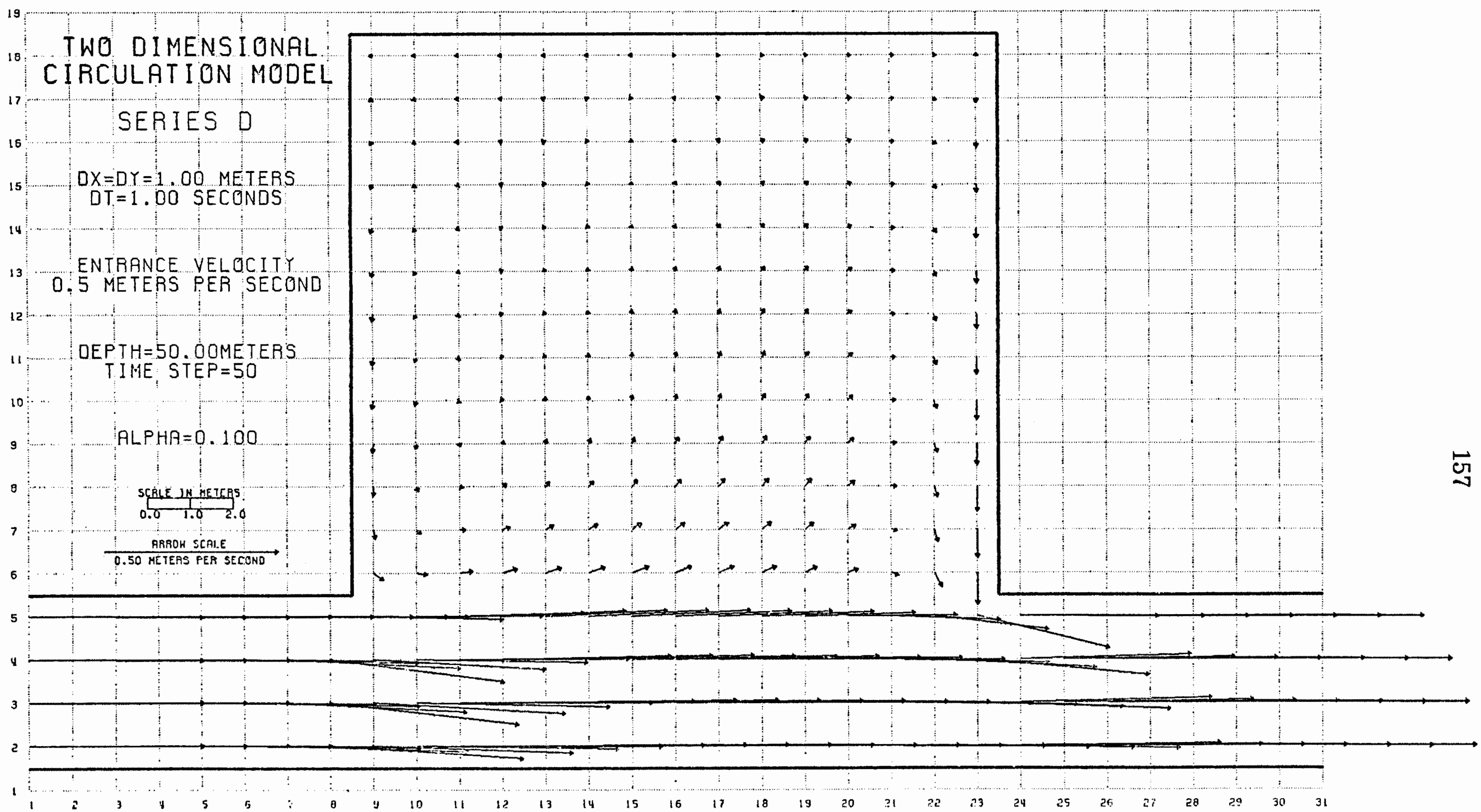

Figure 5.29. Depth, d = 50.0 meters: time step 50.

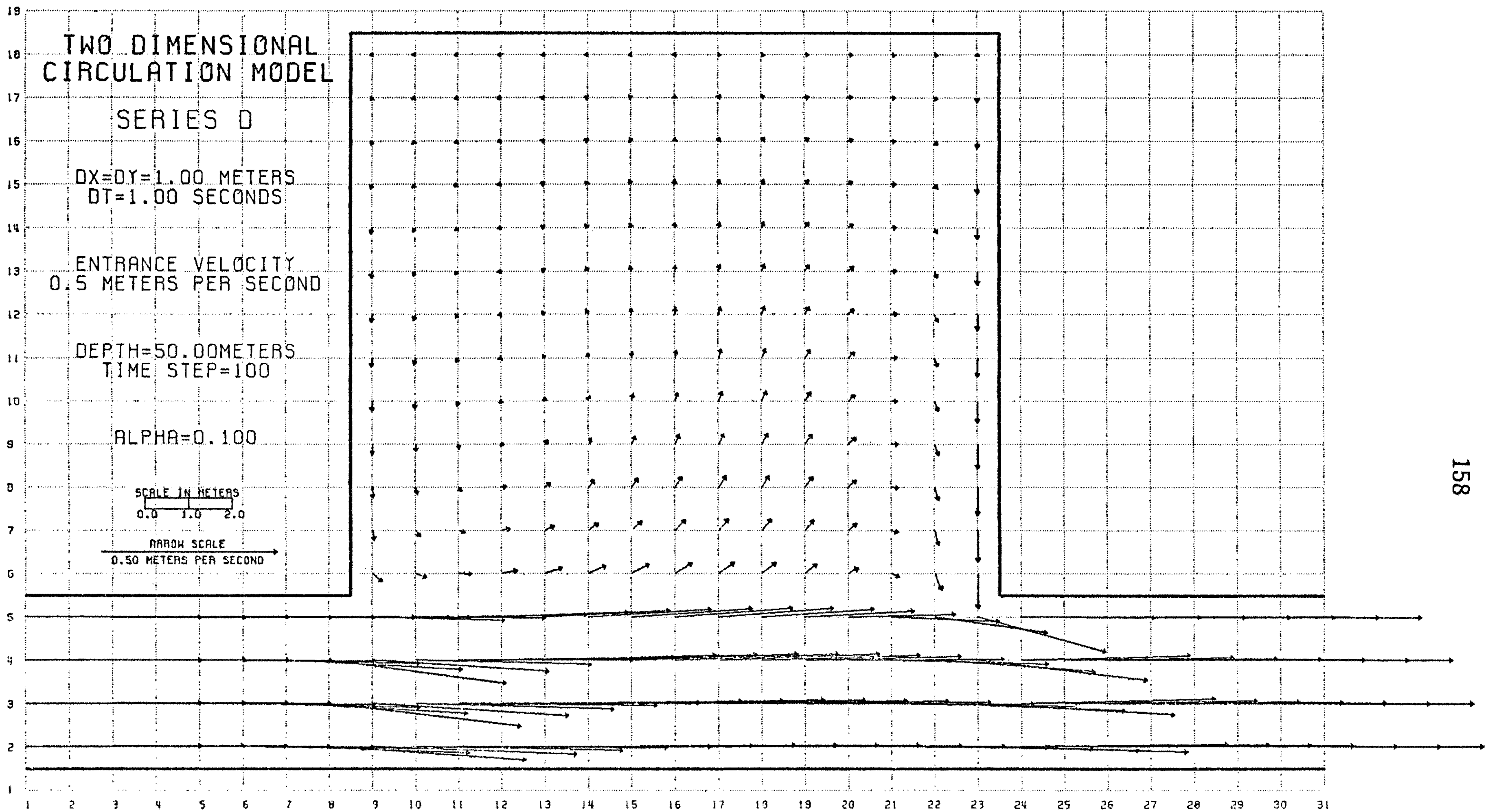

Figure 5.30. Depth, d = 50.0 meters: time step 100.

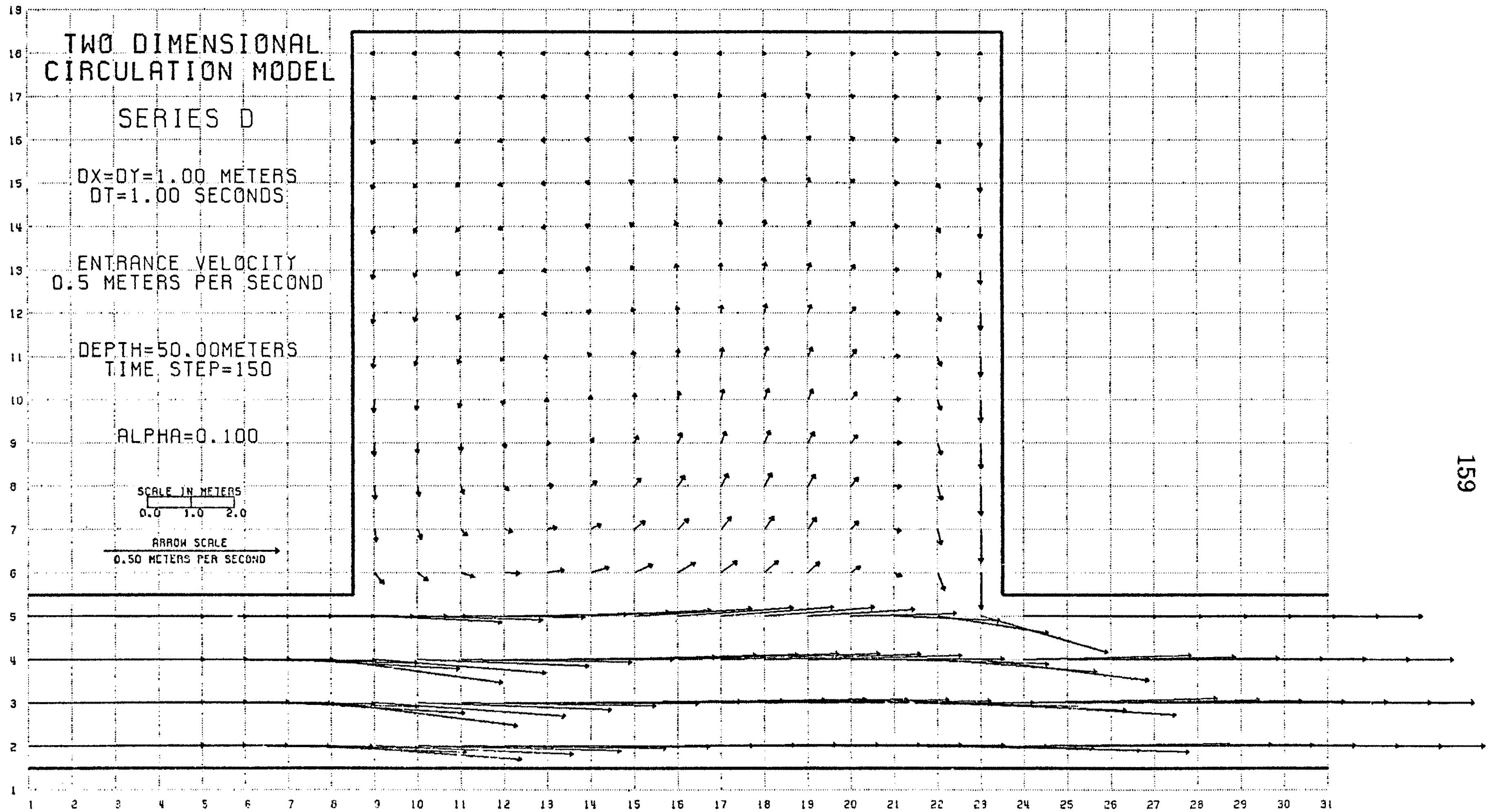

Figure 5.31. Depth, d = 50.0 meters: time step 150.

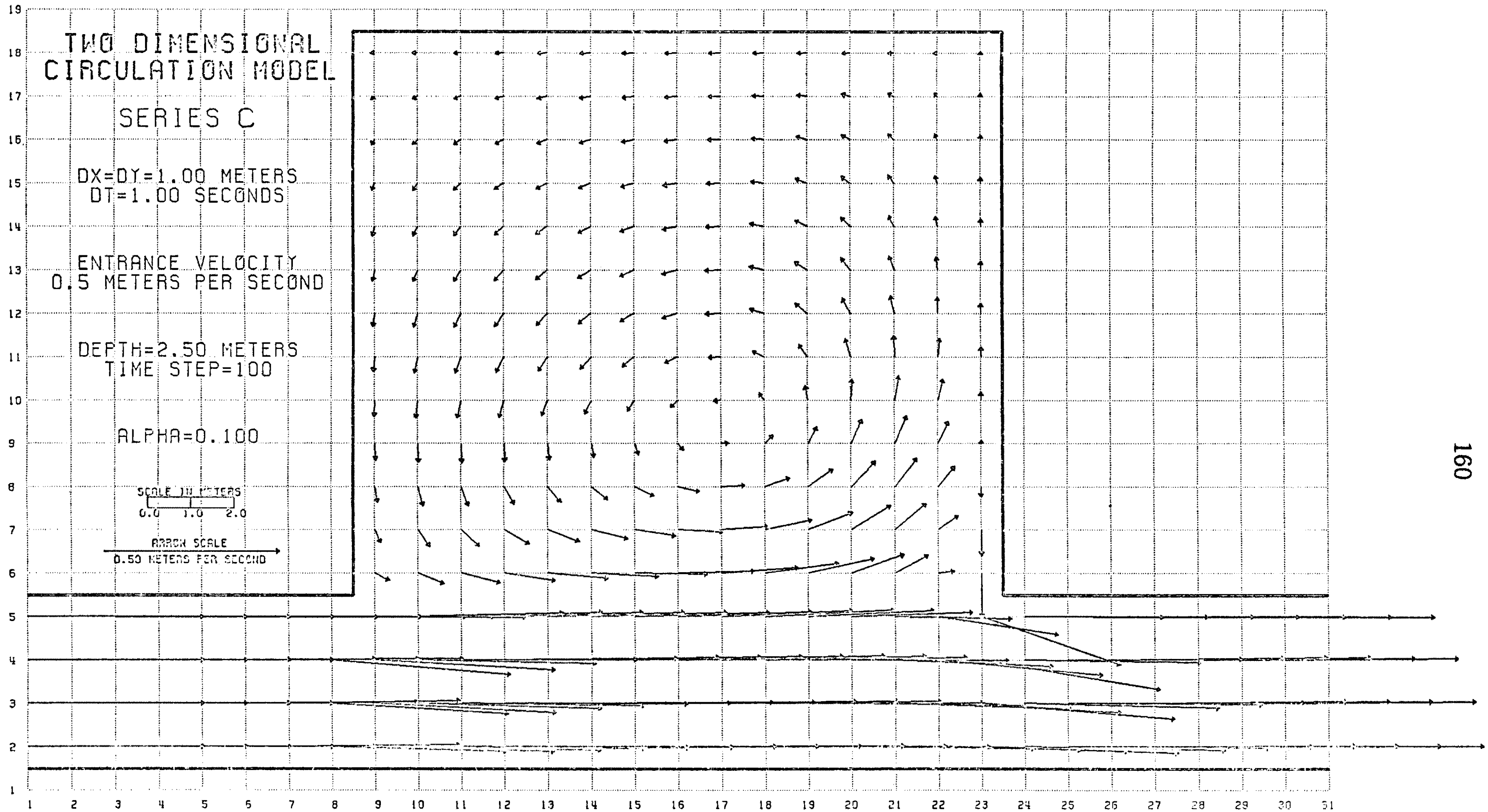

Figure 5.32. Friction factor, f_r = 0.01: time step 100.

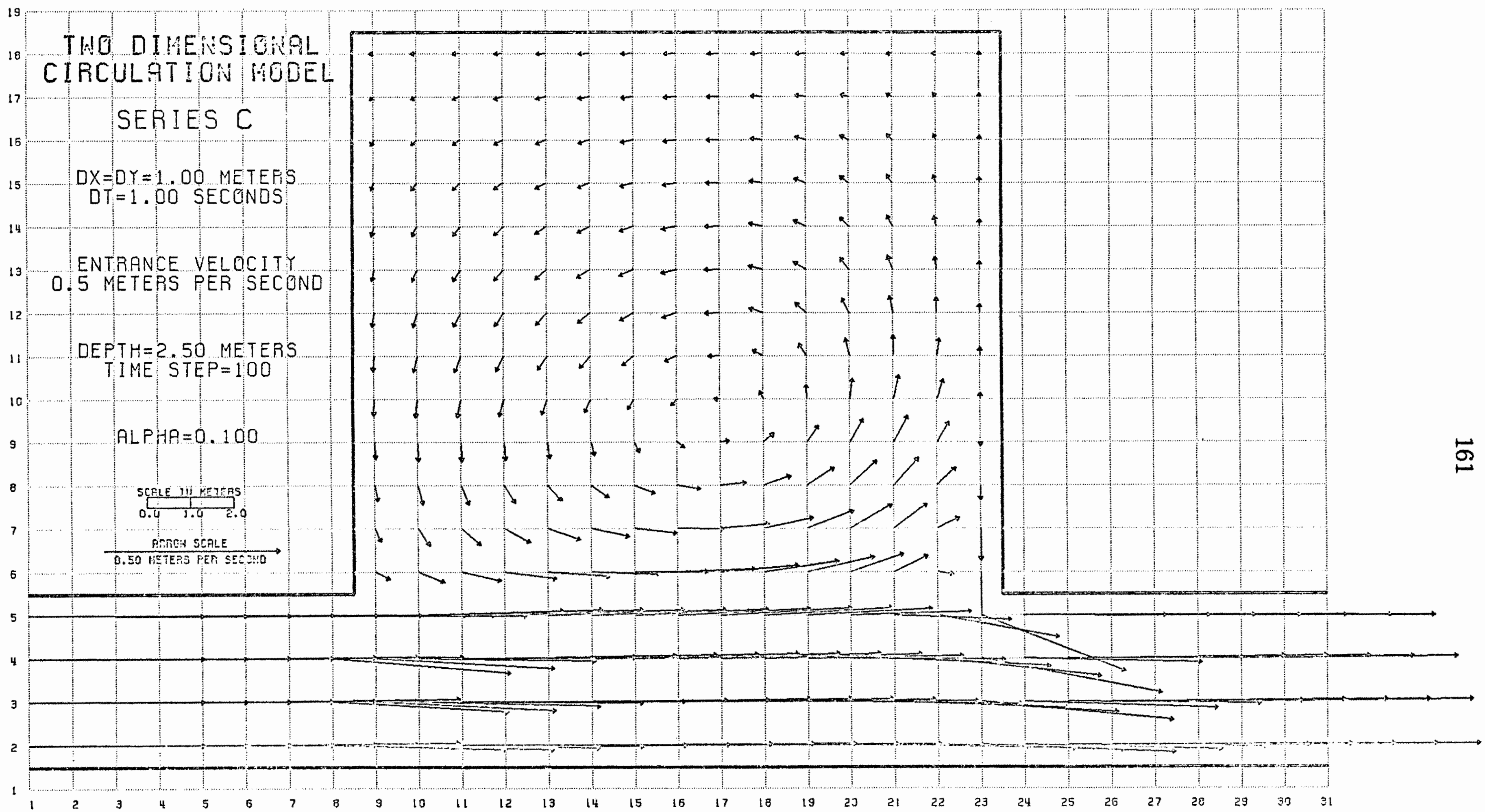

Figure 5.33. Friction factor, f_r = 0.02: time step 100.

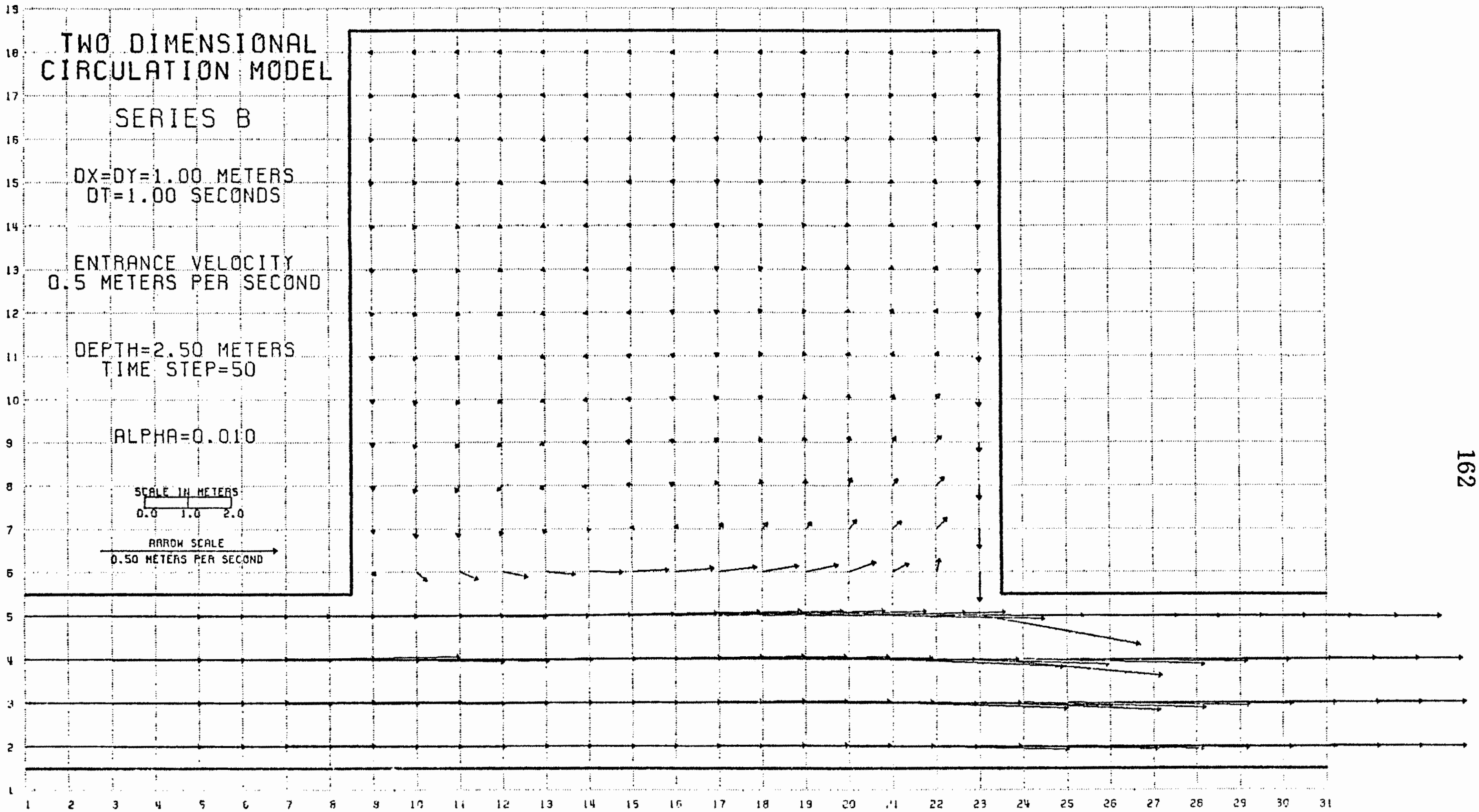

Figure 5.34. Weighting factor, α = 0.01: time step 50.

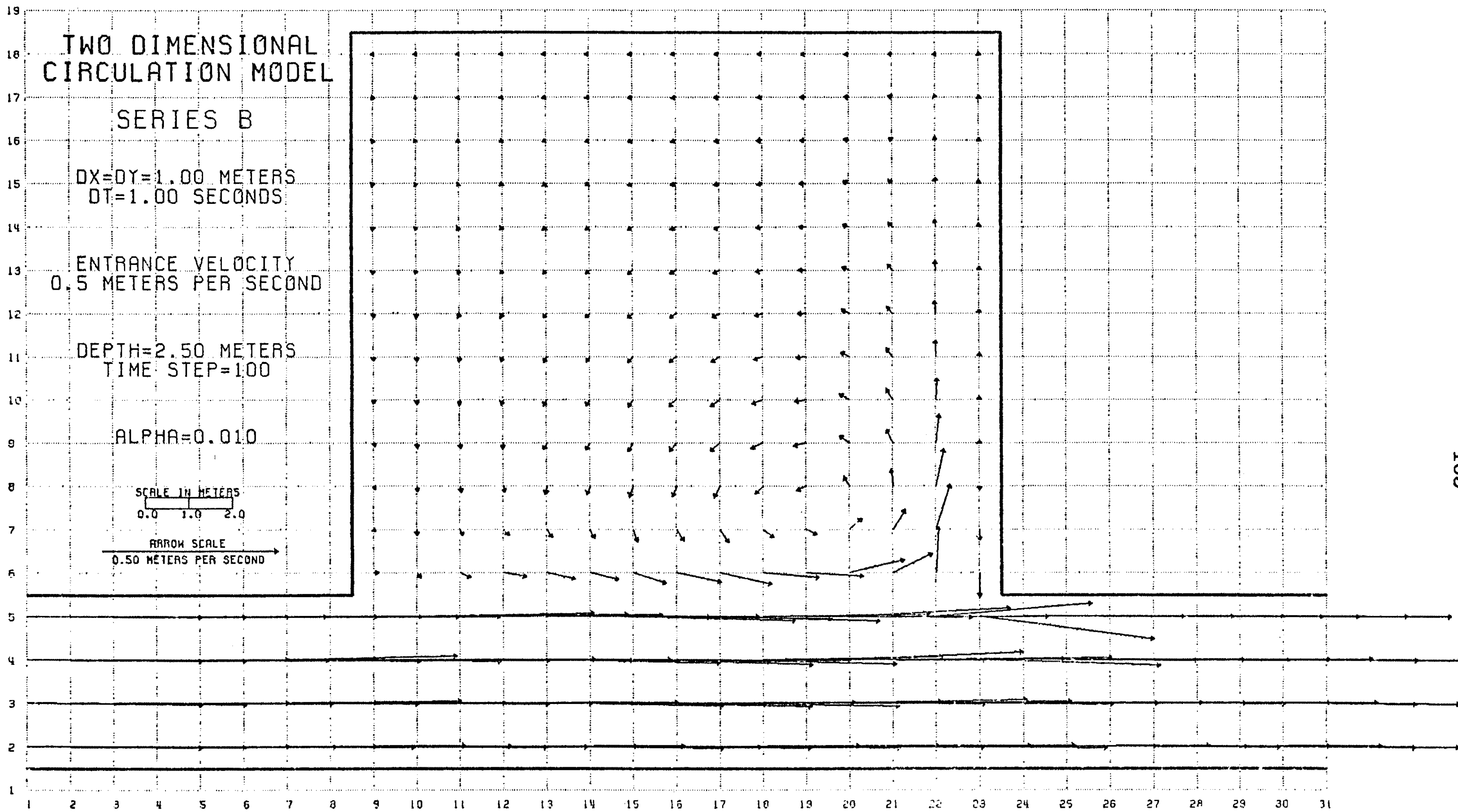

Figure 5.35. Weighting factor, α = 0.01: time step 100.

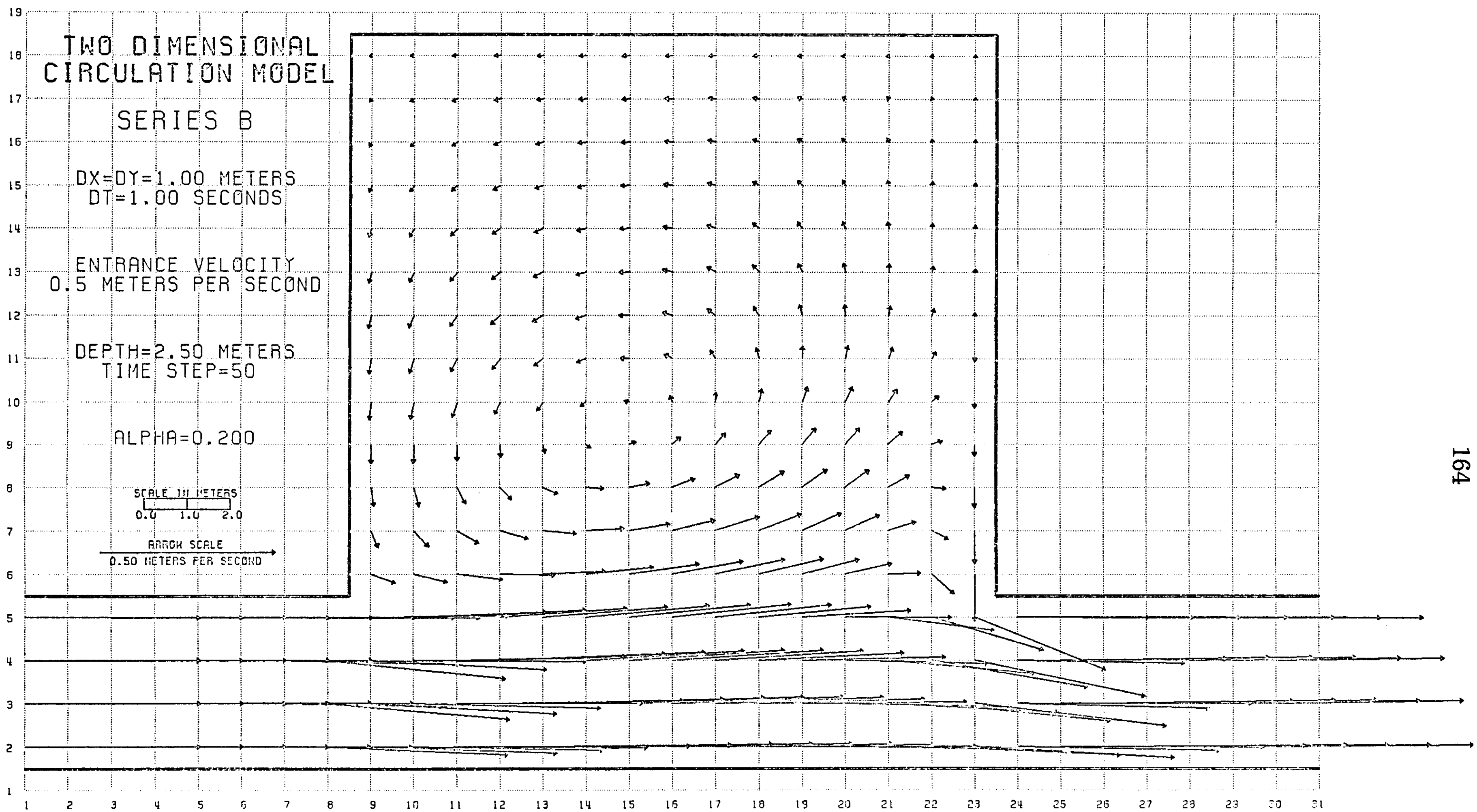

Figure 5.36. Weighting factor, α = 0.2: time step 50.

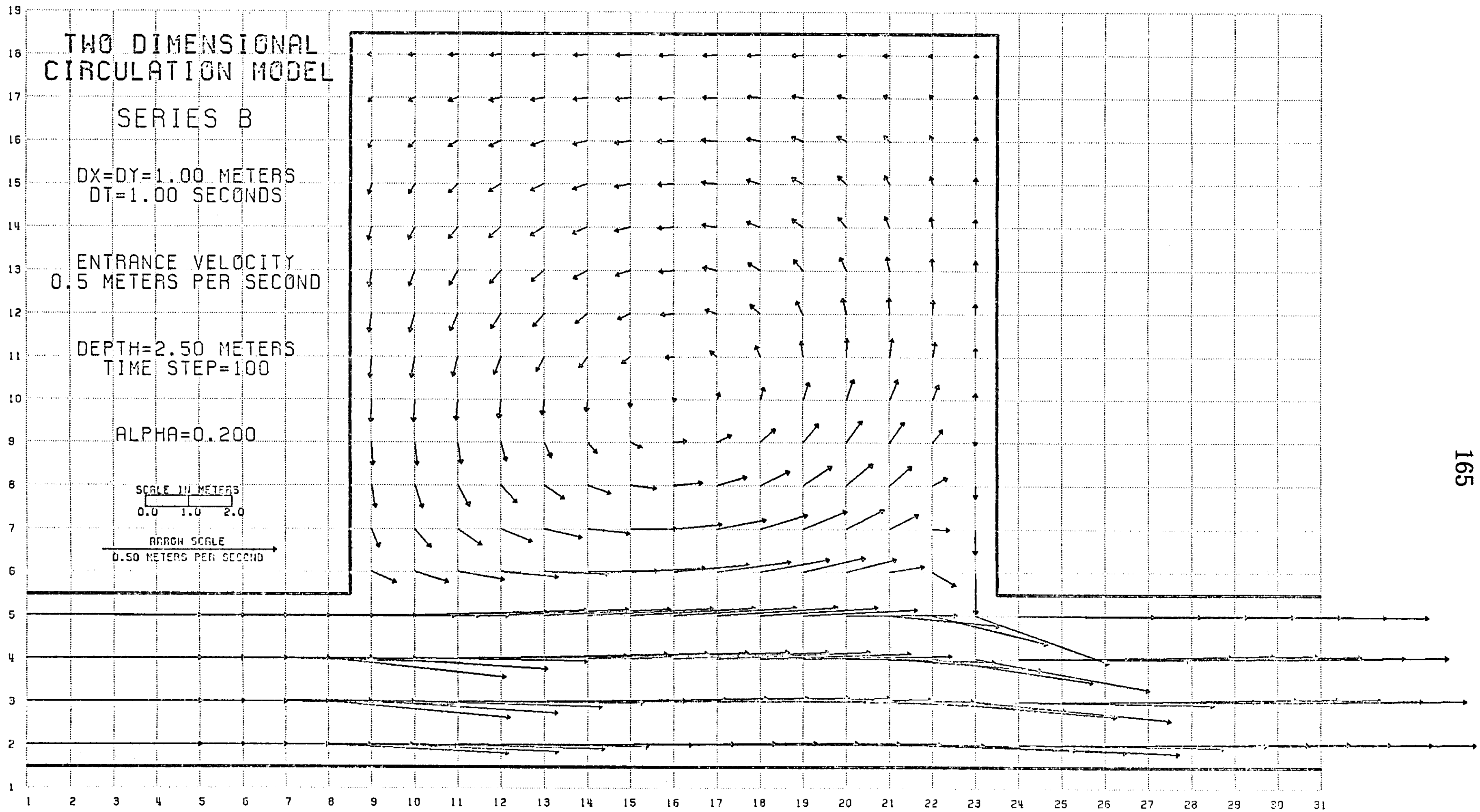

Figure 5.37. Weighting factor, α = 0.2: time step 100.

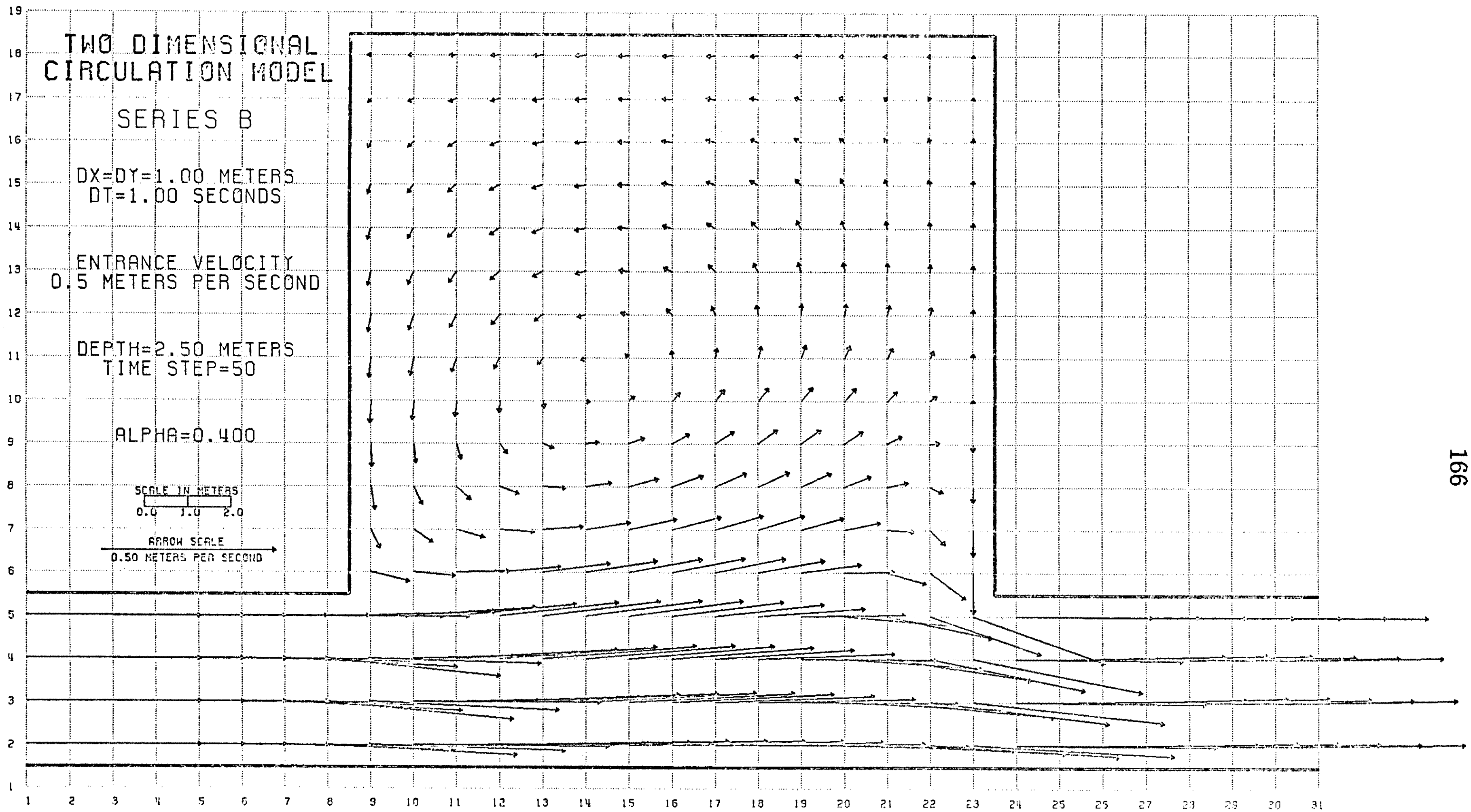

Figure 5.38. Weighting factor, α = 0.4: time step 50.

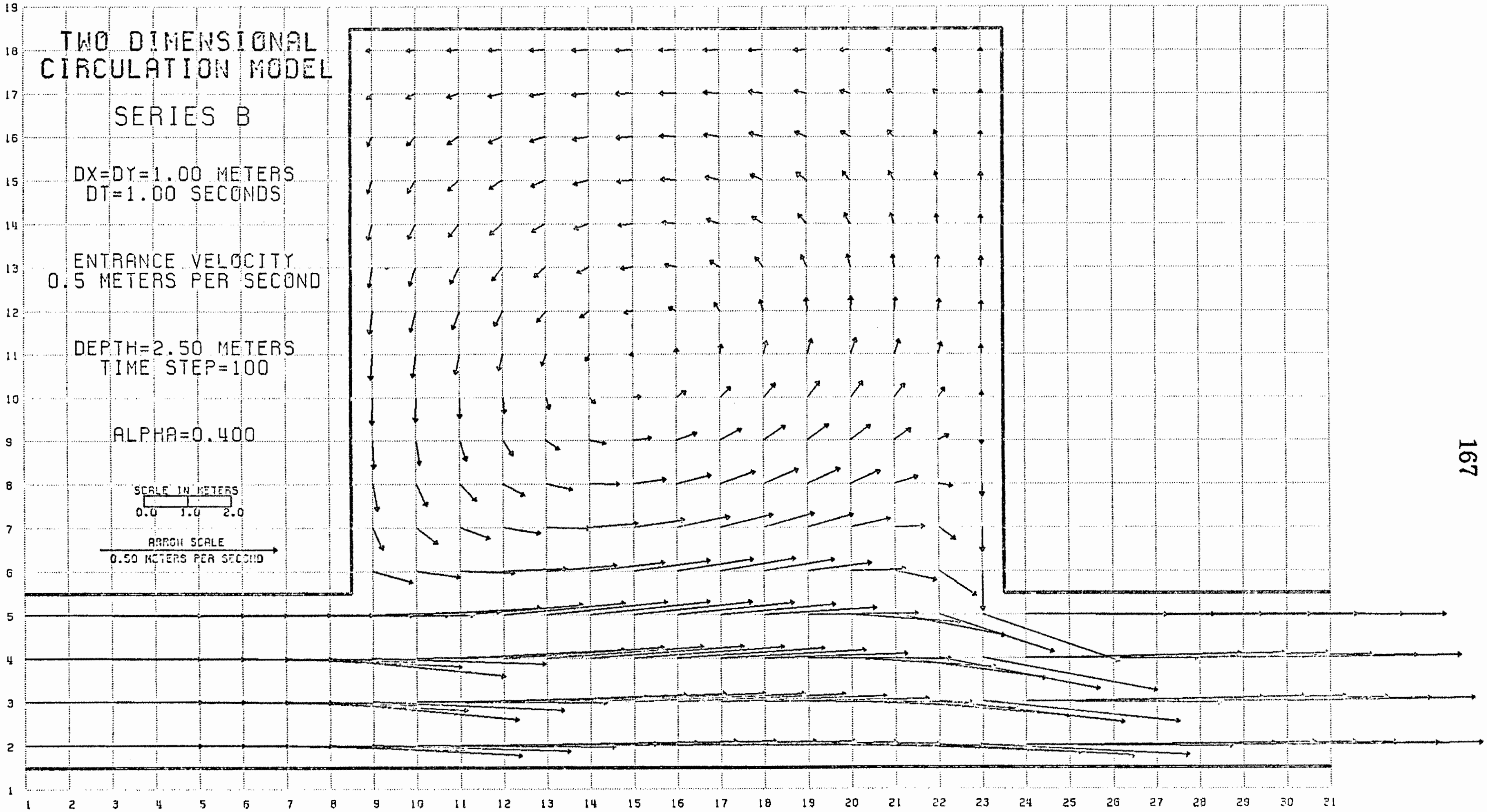

Figure 5.39. Weighting factor, α = 0.4: time step 100.

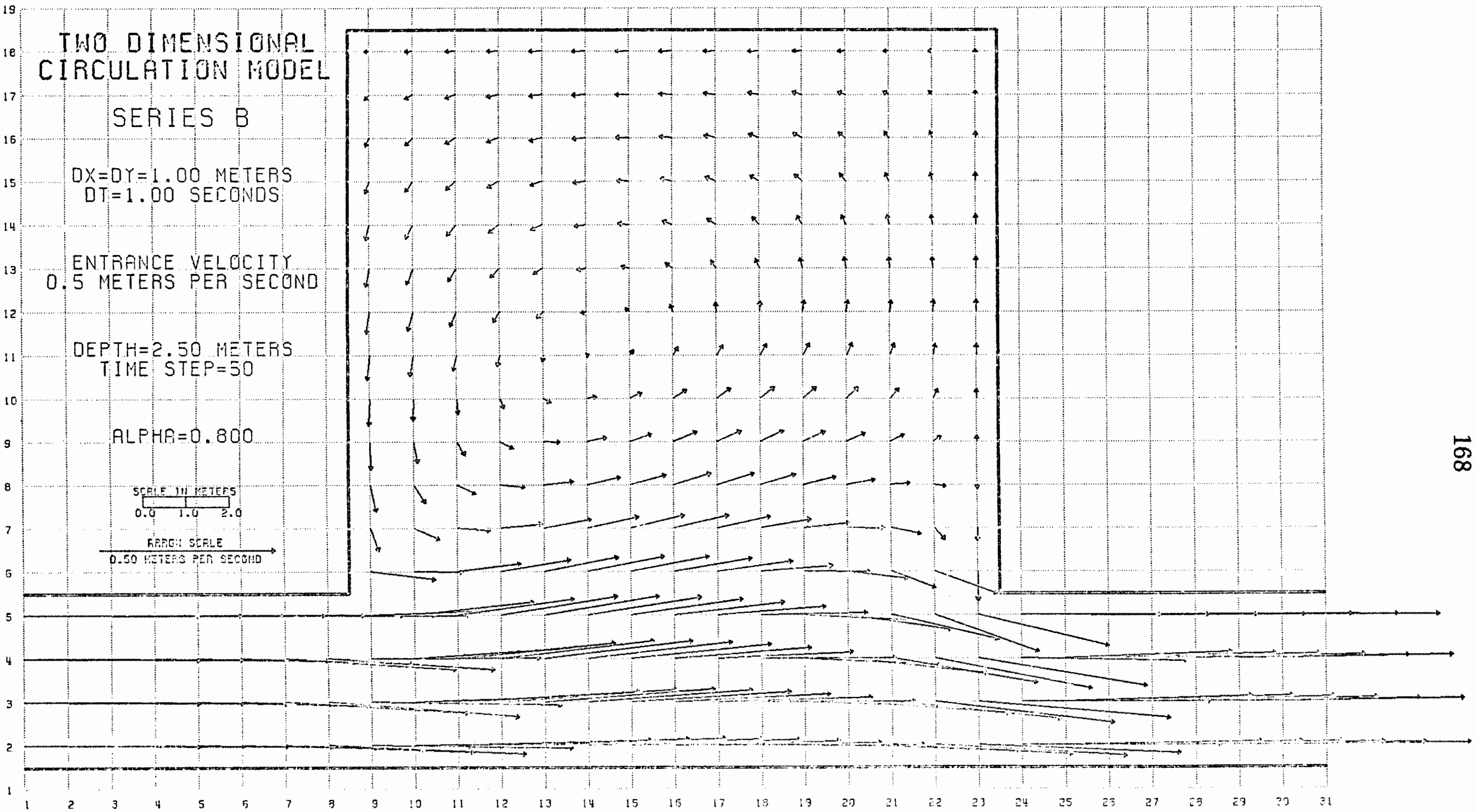

Figure 5.40. Weighting factor, α = 0.8: time step 50.

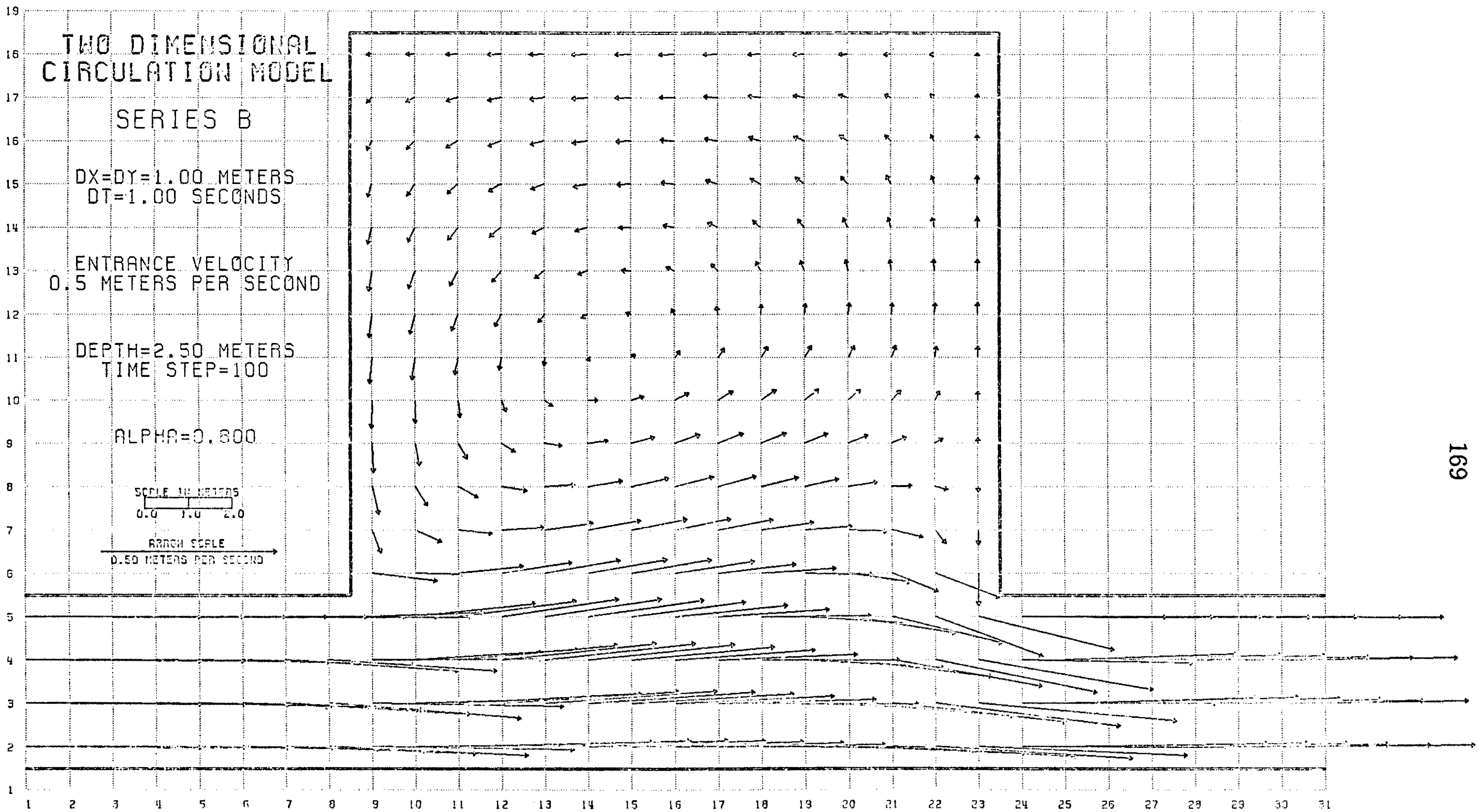

Figure 5.41. Weighting factor, α = 0.8: time step 100.

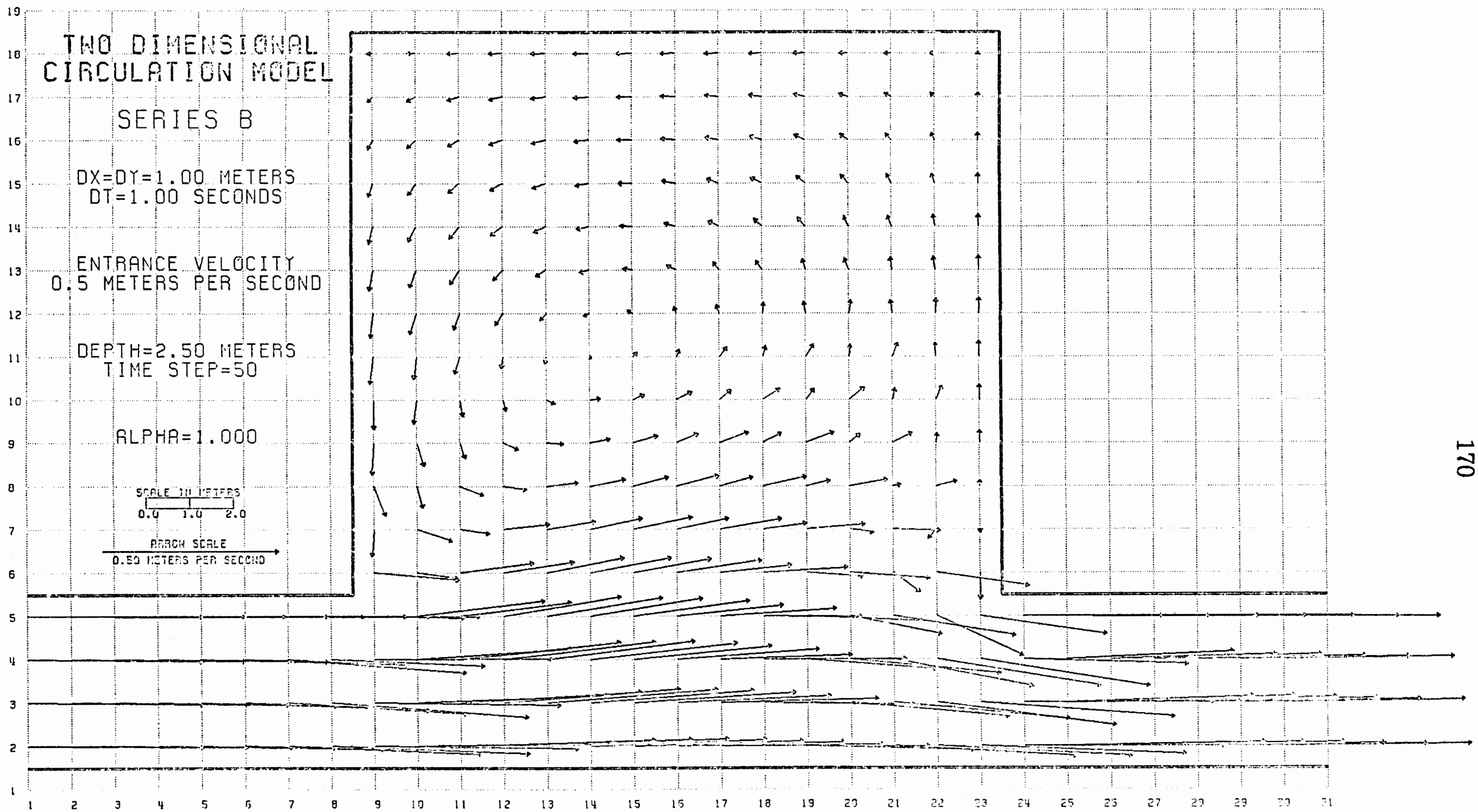

Figure 5.42. Weighting factor, α = 1.0: time step 50.

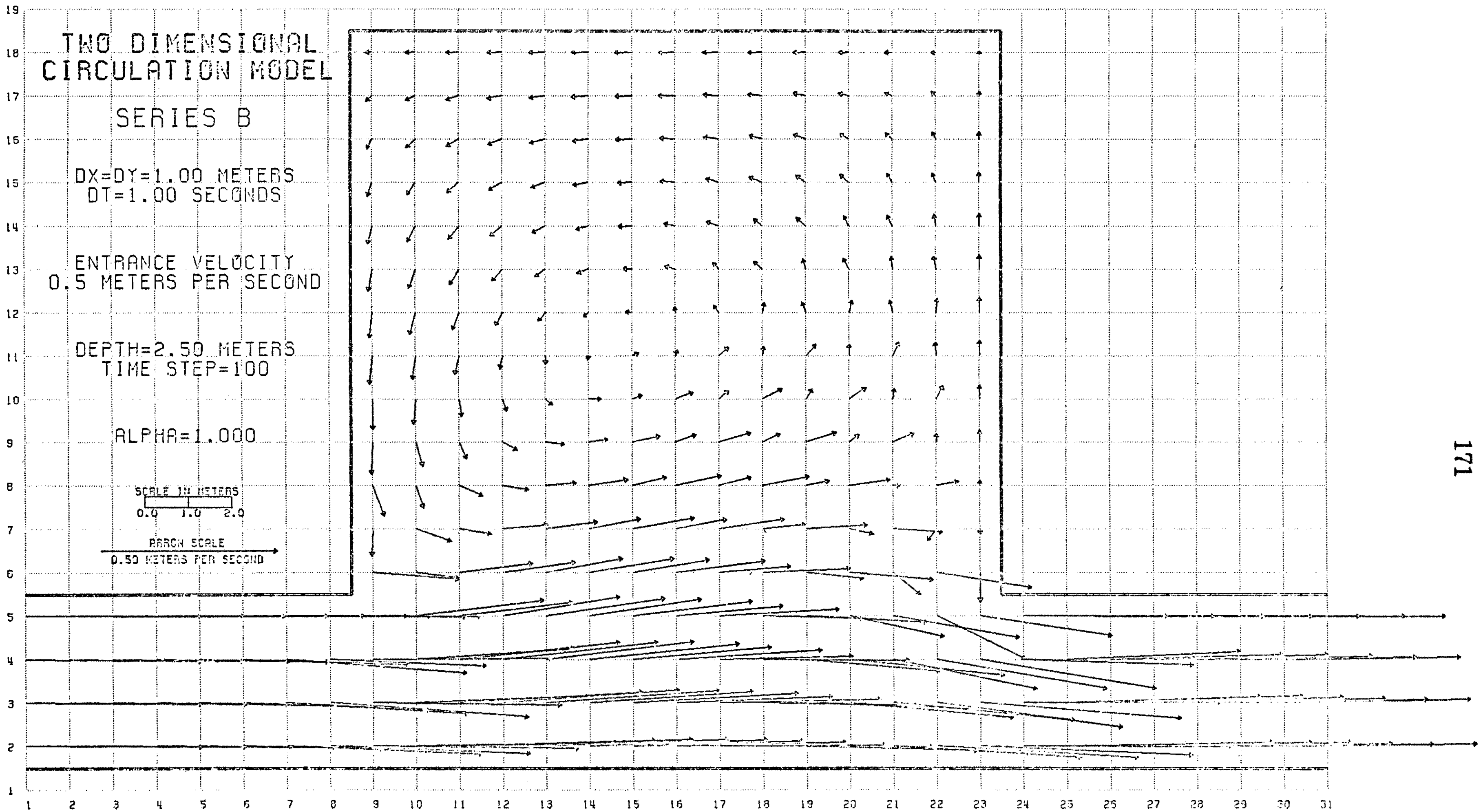

Figure 5.43. Weighting factor, α = 1.0: time step 100.

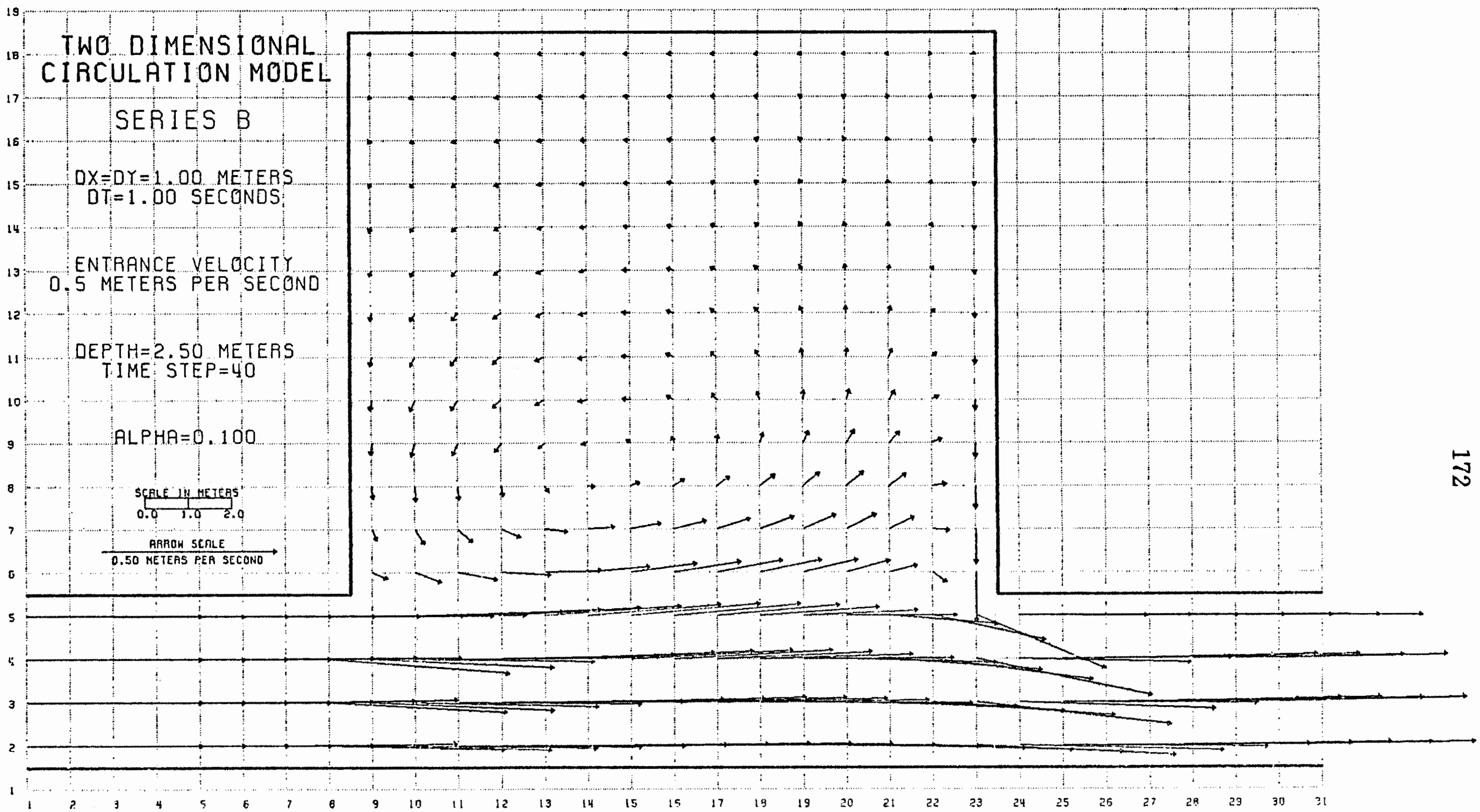

Figure 5.44. α = 0.1, n ≦ 100; α = 0.0, n > 100: time step 40.

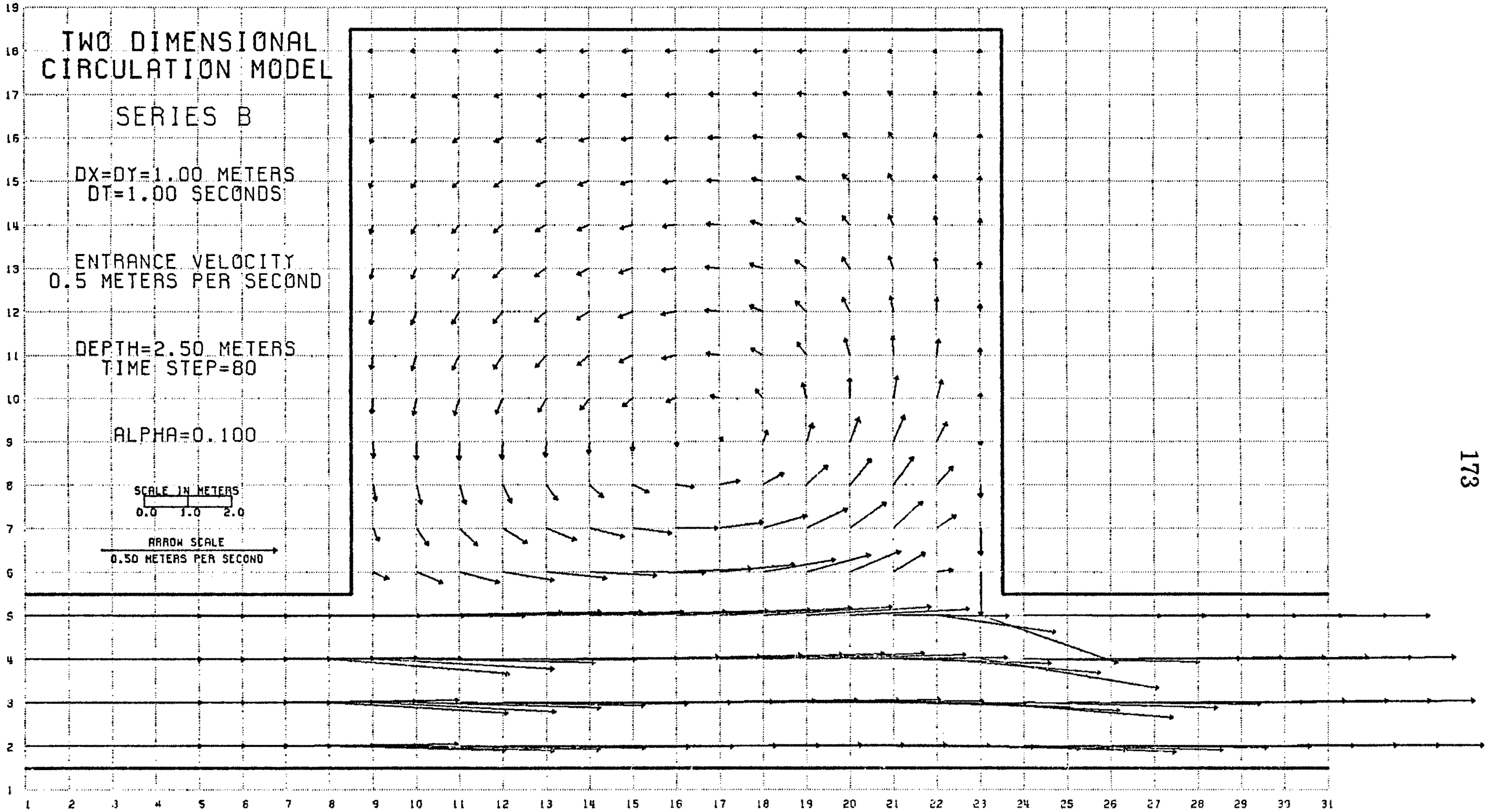

Figure 5.45. α = 0.1, N $\leqq$ 100; α = 0.0, N > 100: time step 80.

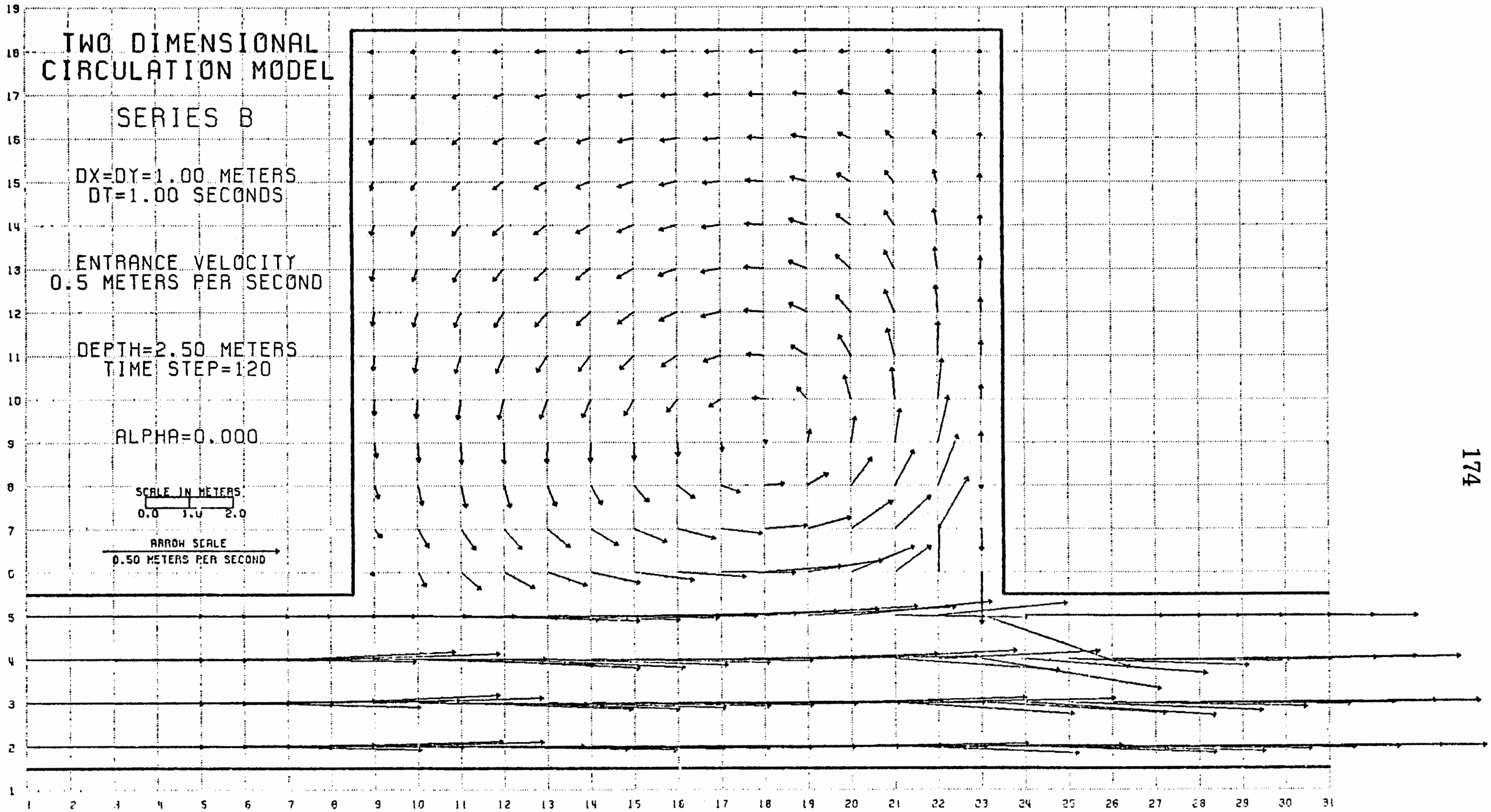

Figure 5.46. α = 0.1, N ≦ 100; α = 0.0, N > 100: time step 120.

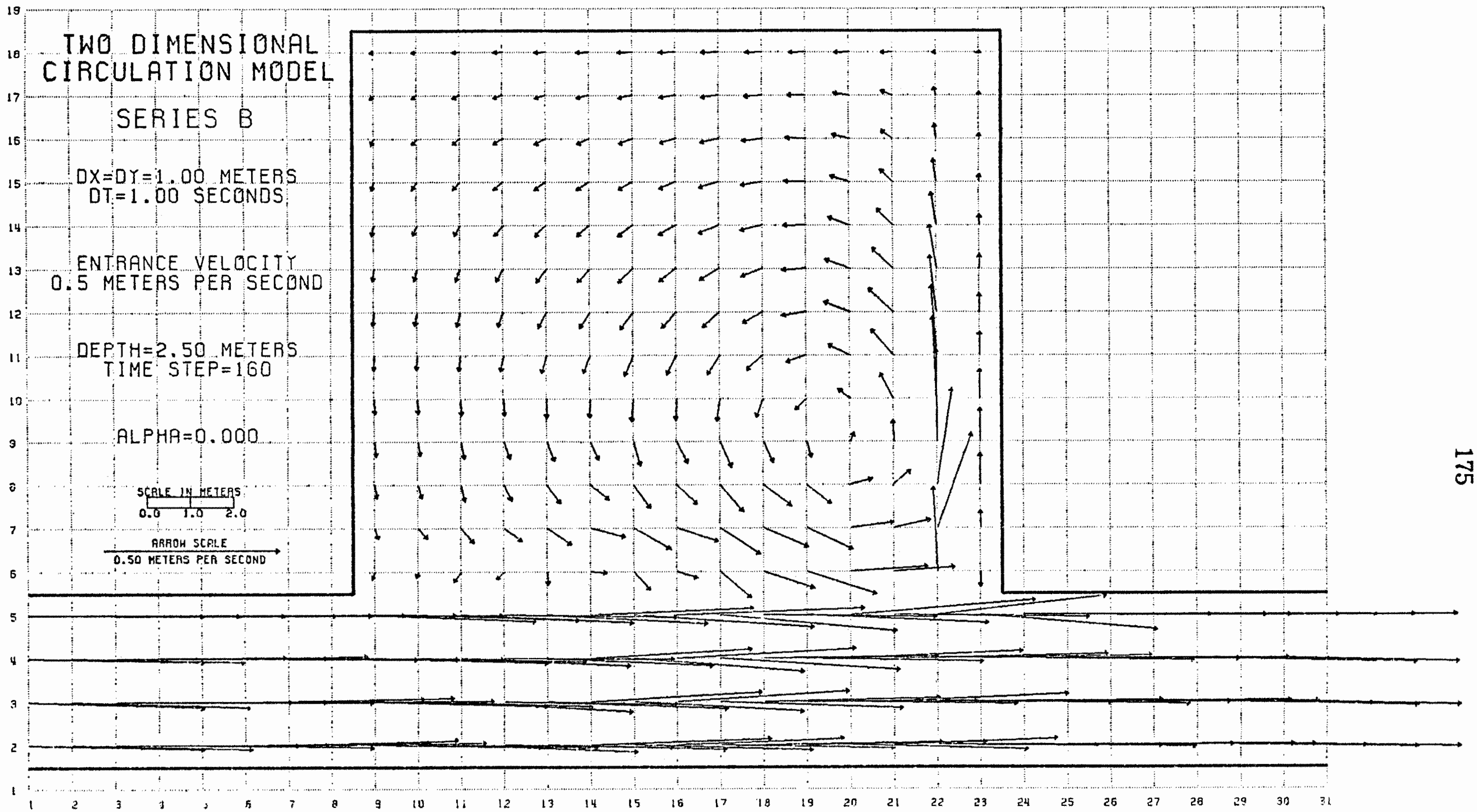

Figure 5.47. $\alpha = 0.1$, $N \leqq 100$; $\alpha = 0.0$, $N > 100$: time step 160.

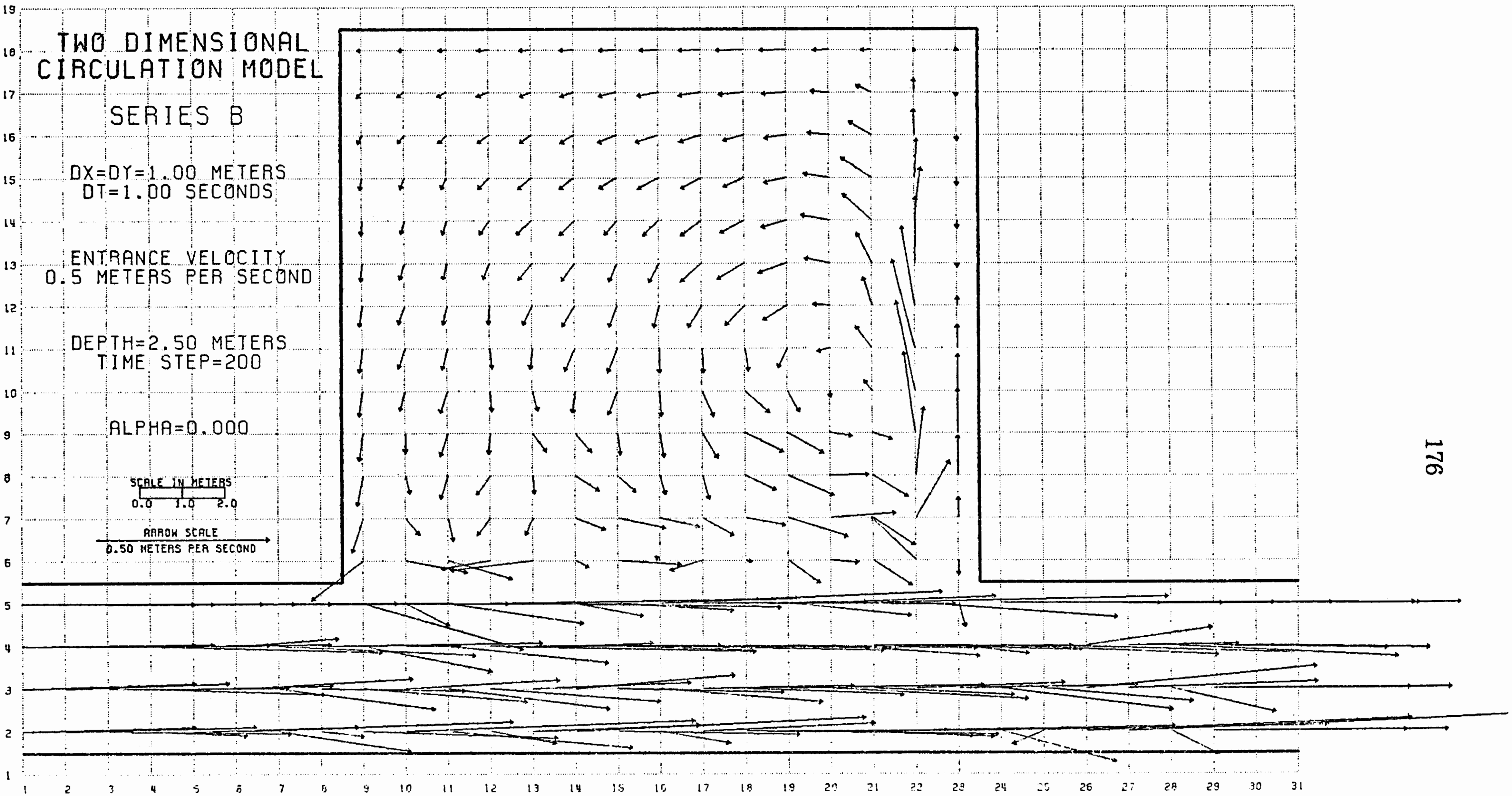

Figure 5.48. α = 0.1, N ≦ 100; α = 0.0, N > 100: time step 200.

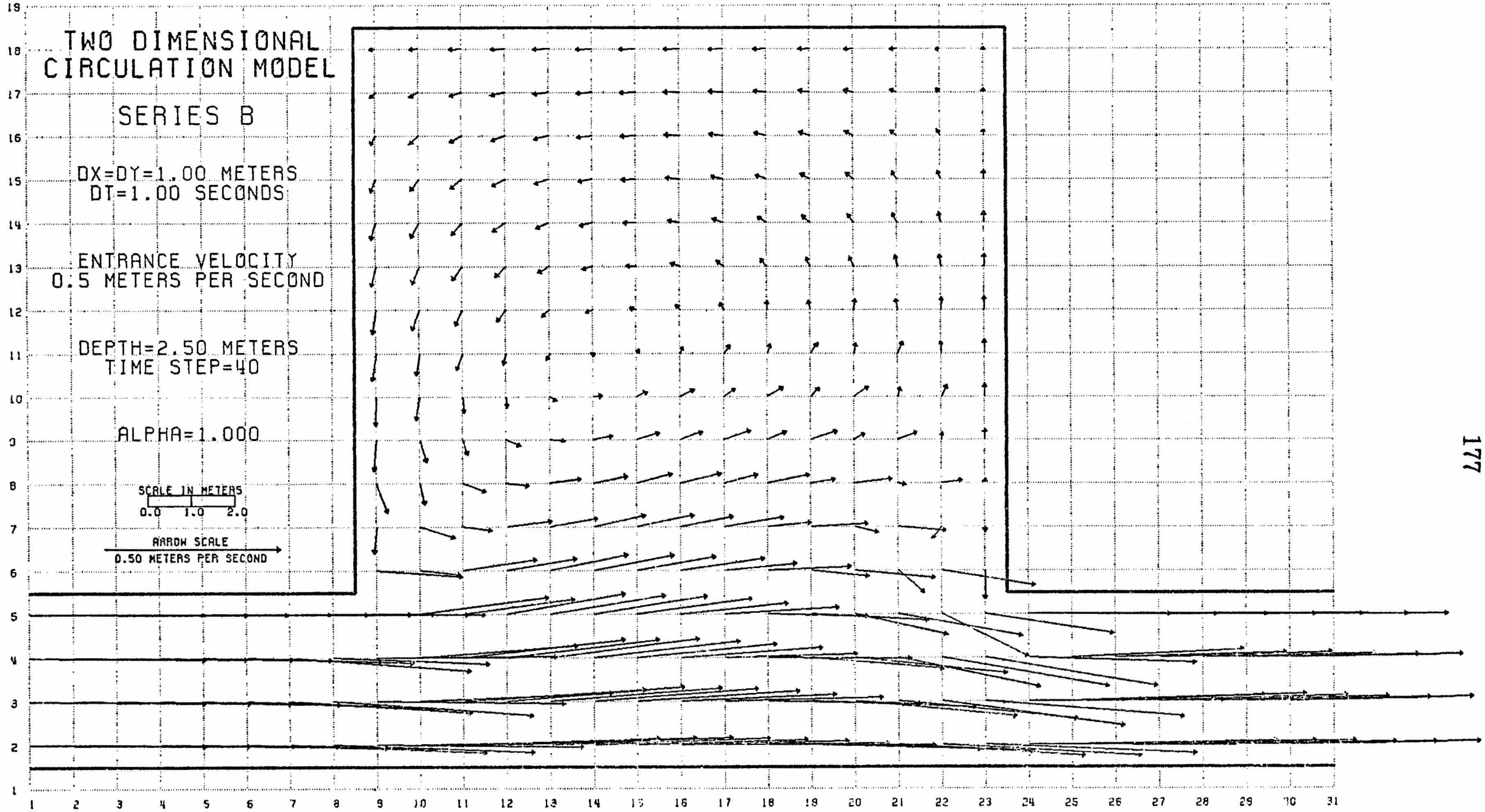

Figure 5.49. α = 1.0, n $\leqq$ 100; α = 0.01, n > 100: time step 40.

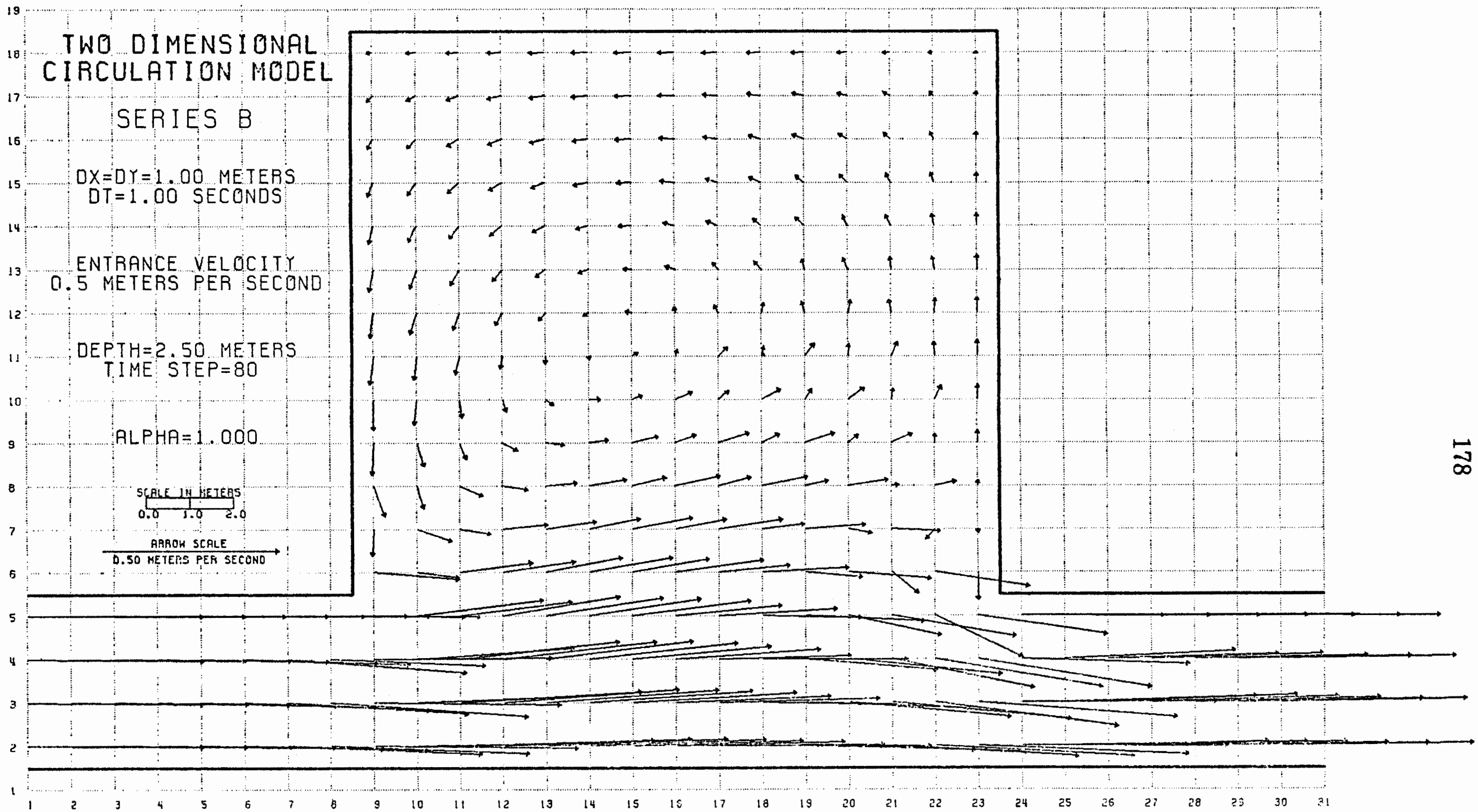

Figure 5.50. α = 1.0, N ≦ 100; α = 0.01, N > 100: time step 80.

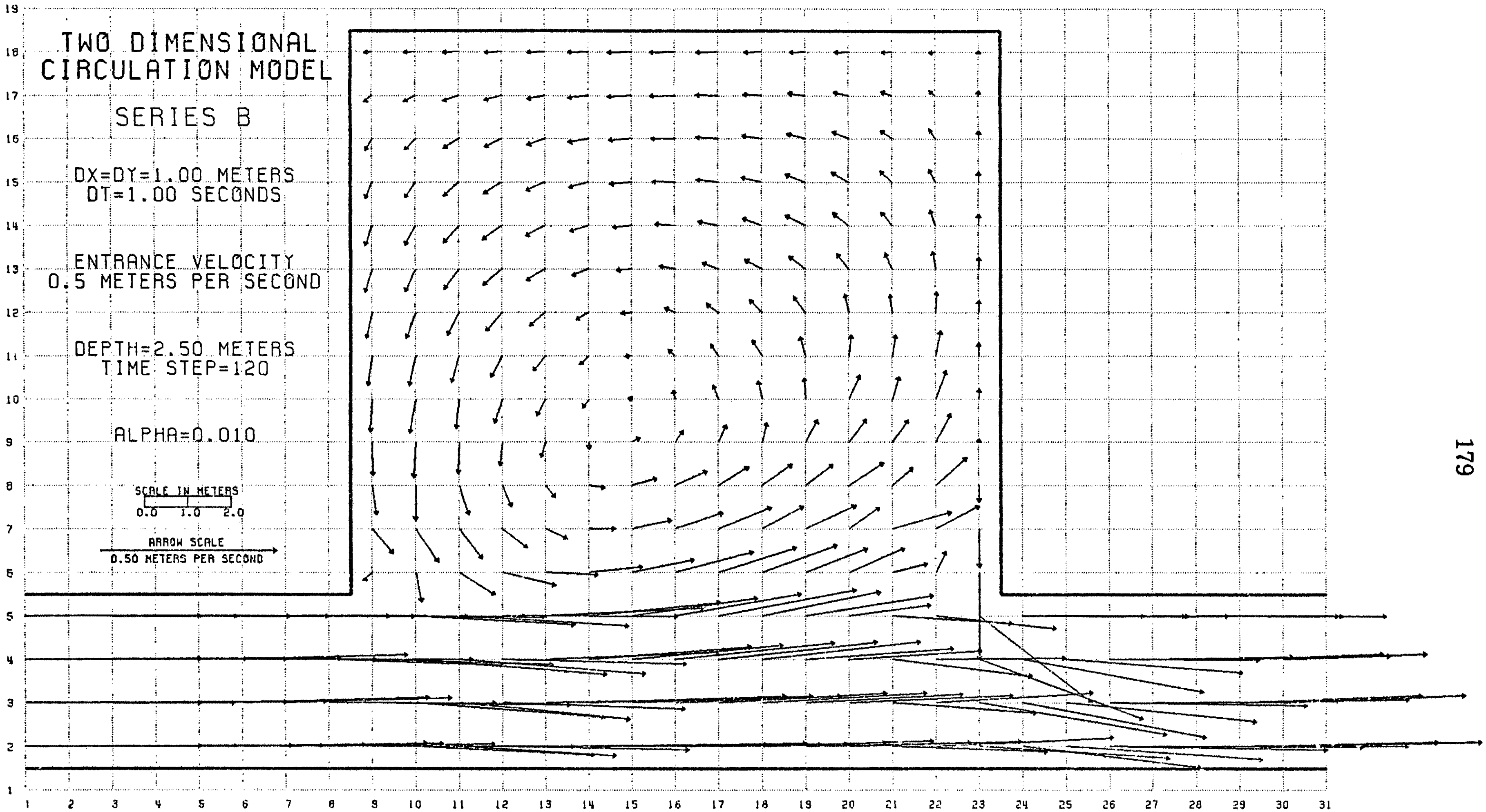

Figure 5.51. α = 1.0, n ≦ 100; α = 0.01, n > 100: time step 120.

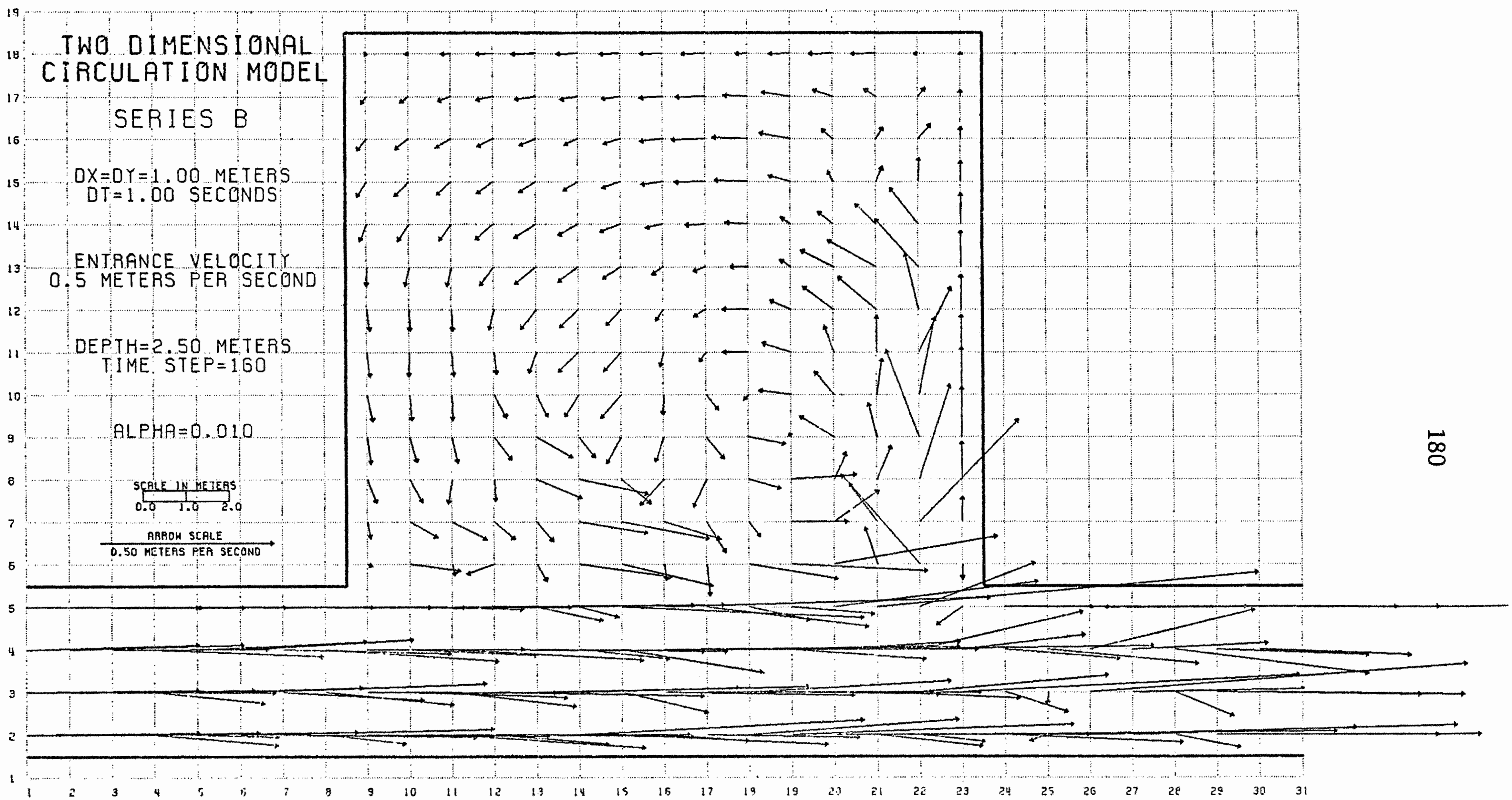

Figure 5.52. α = 1.0, N ≦ 100; α = 0.01, N > 100: time step 160.

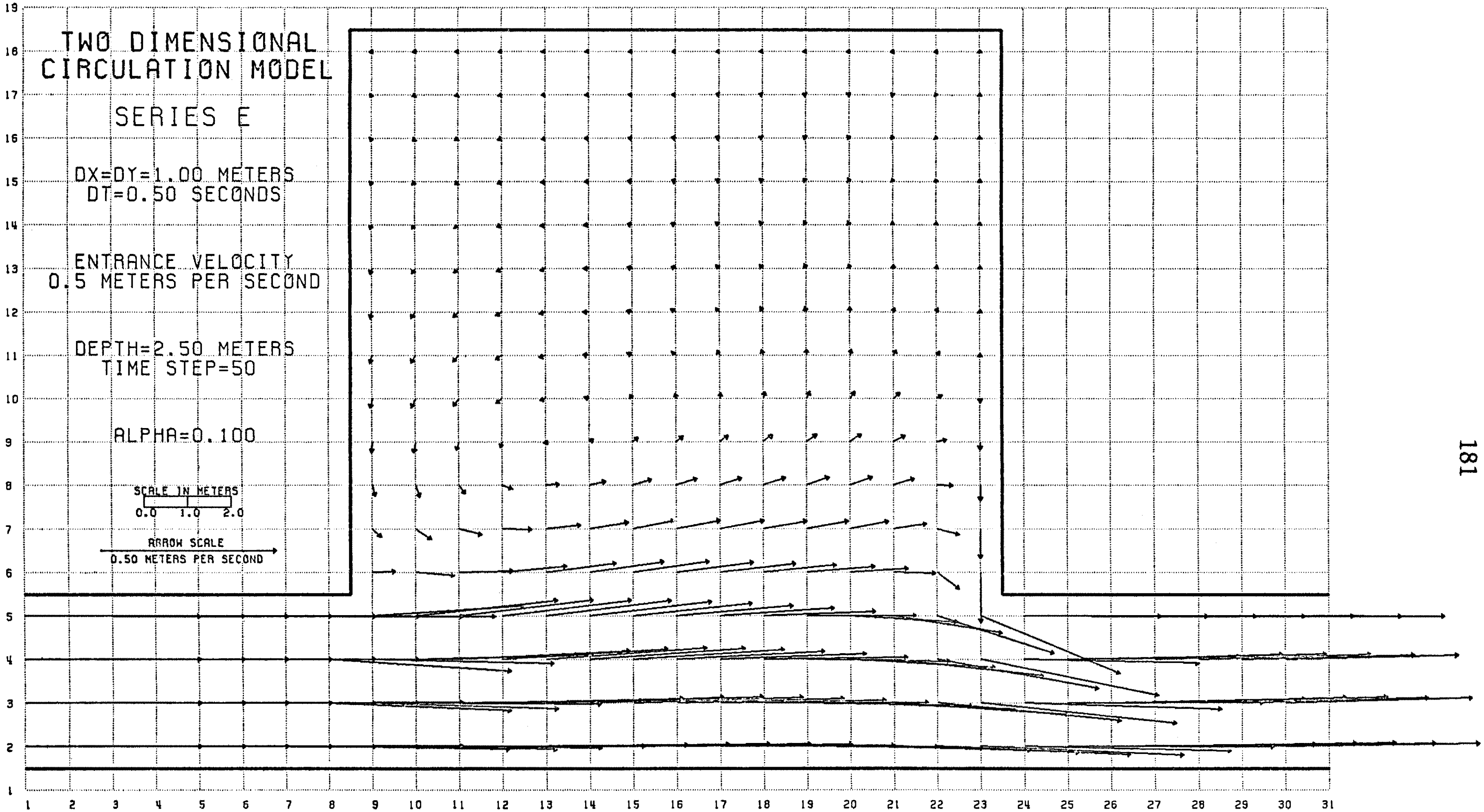

Figure 5.53. Time increment, Δt = 0.5 seconds: time step 50.

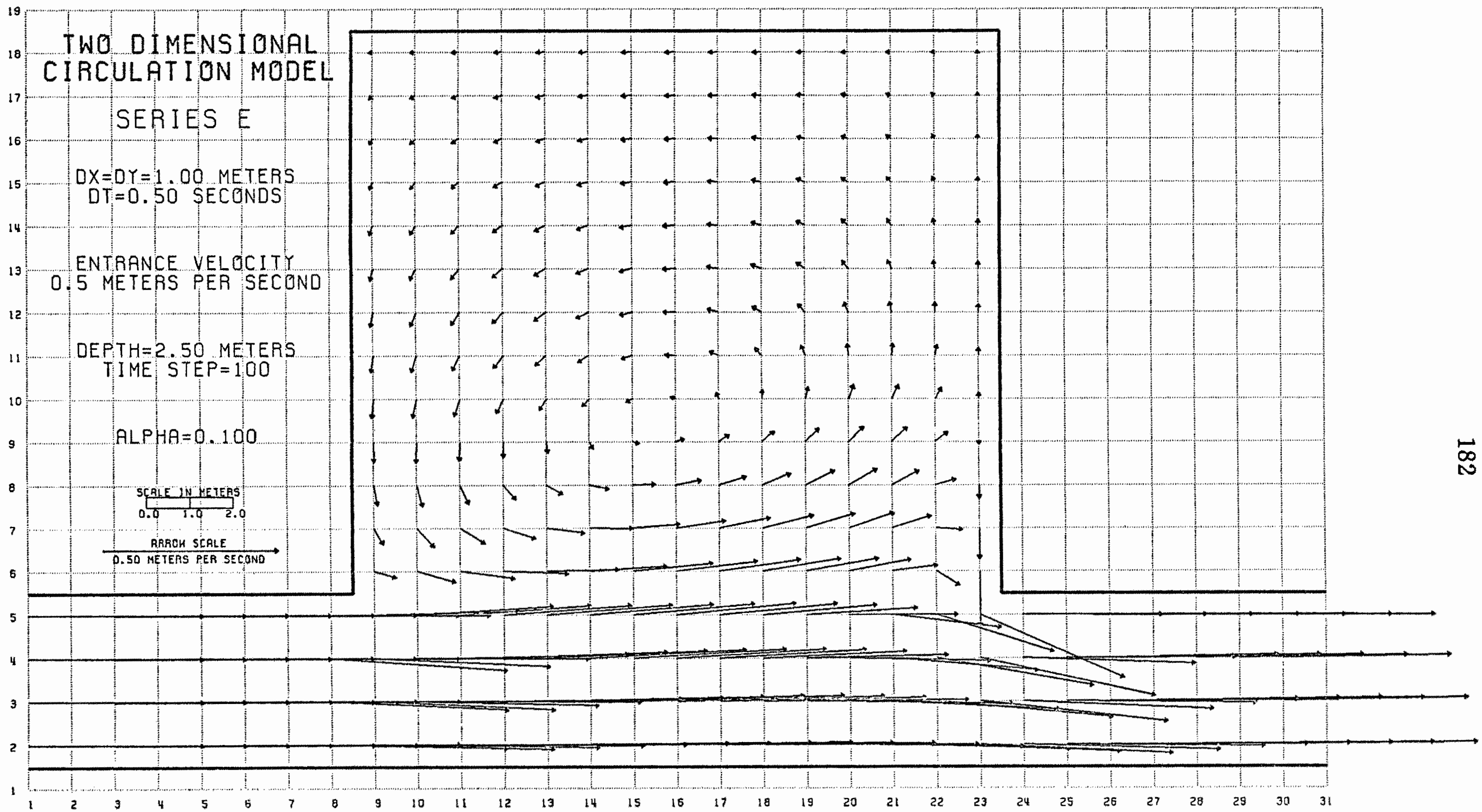

Figure 5.54. Time increment, Δt = 0.5 seconds: time step 100.

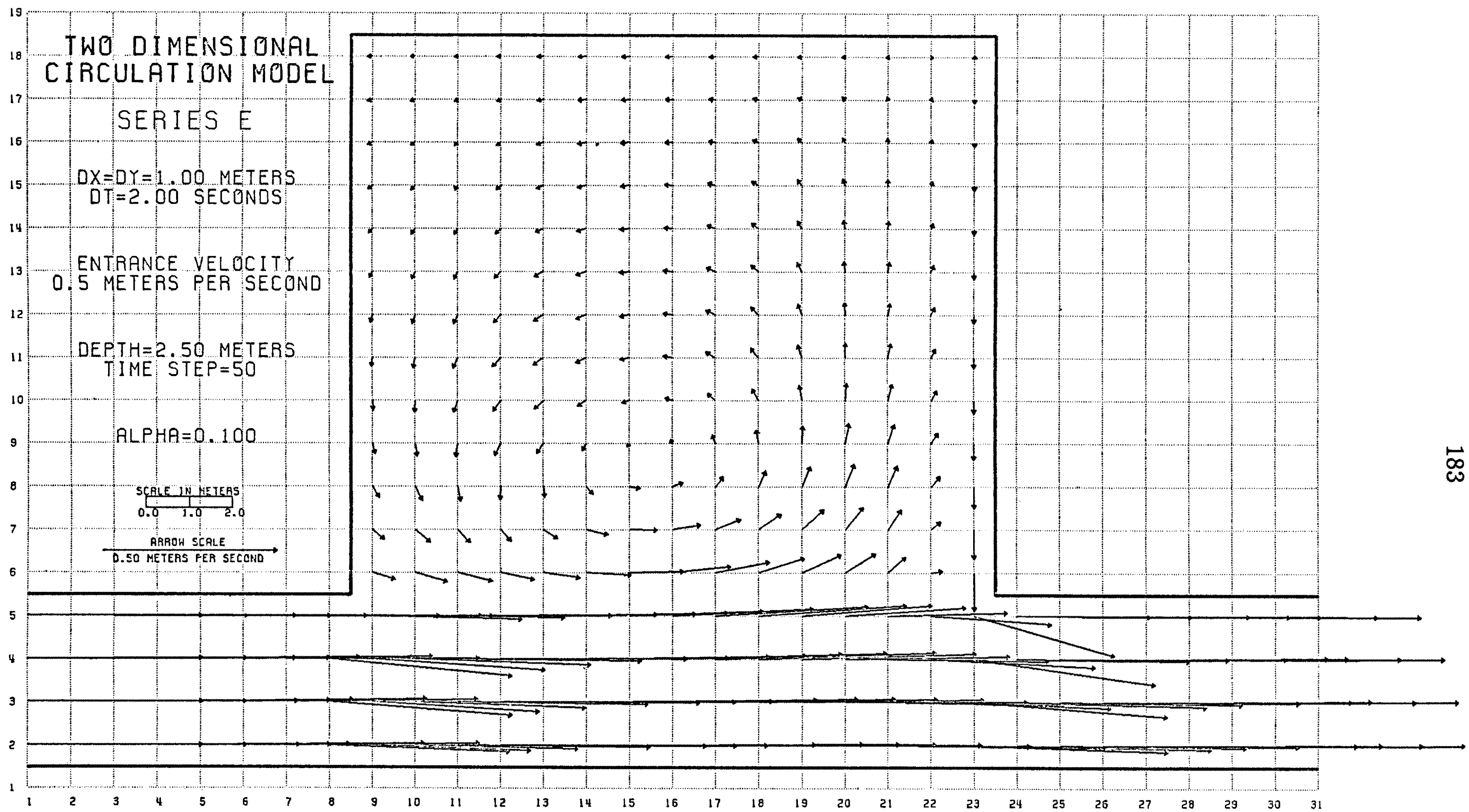

Figure 5.55. Time increment, $\Delta t = 2.0$ seconds: time step 50.

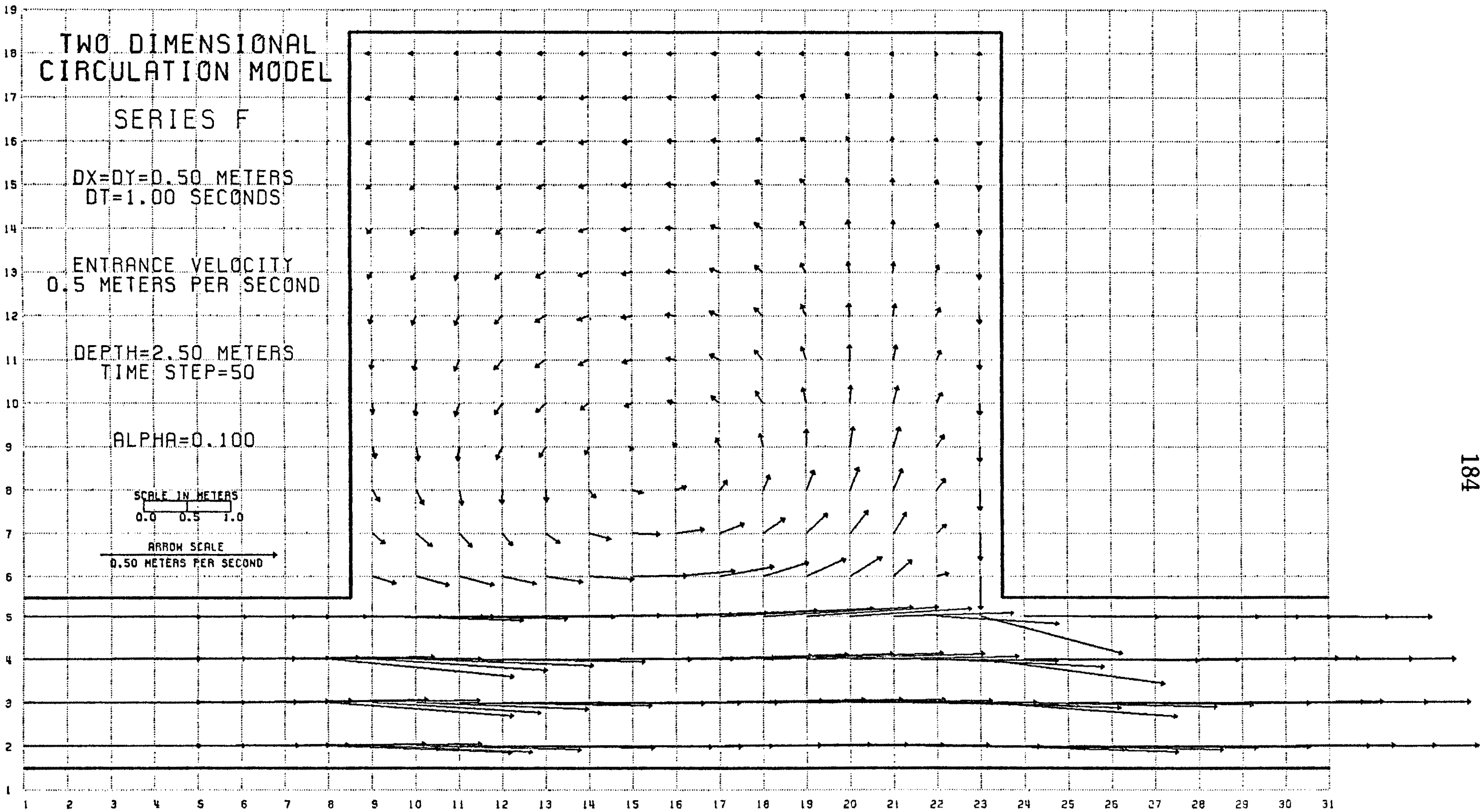

Figure 5.56. Space increment, Δx = Δy = 0.5 meters: time step 50.

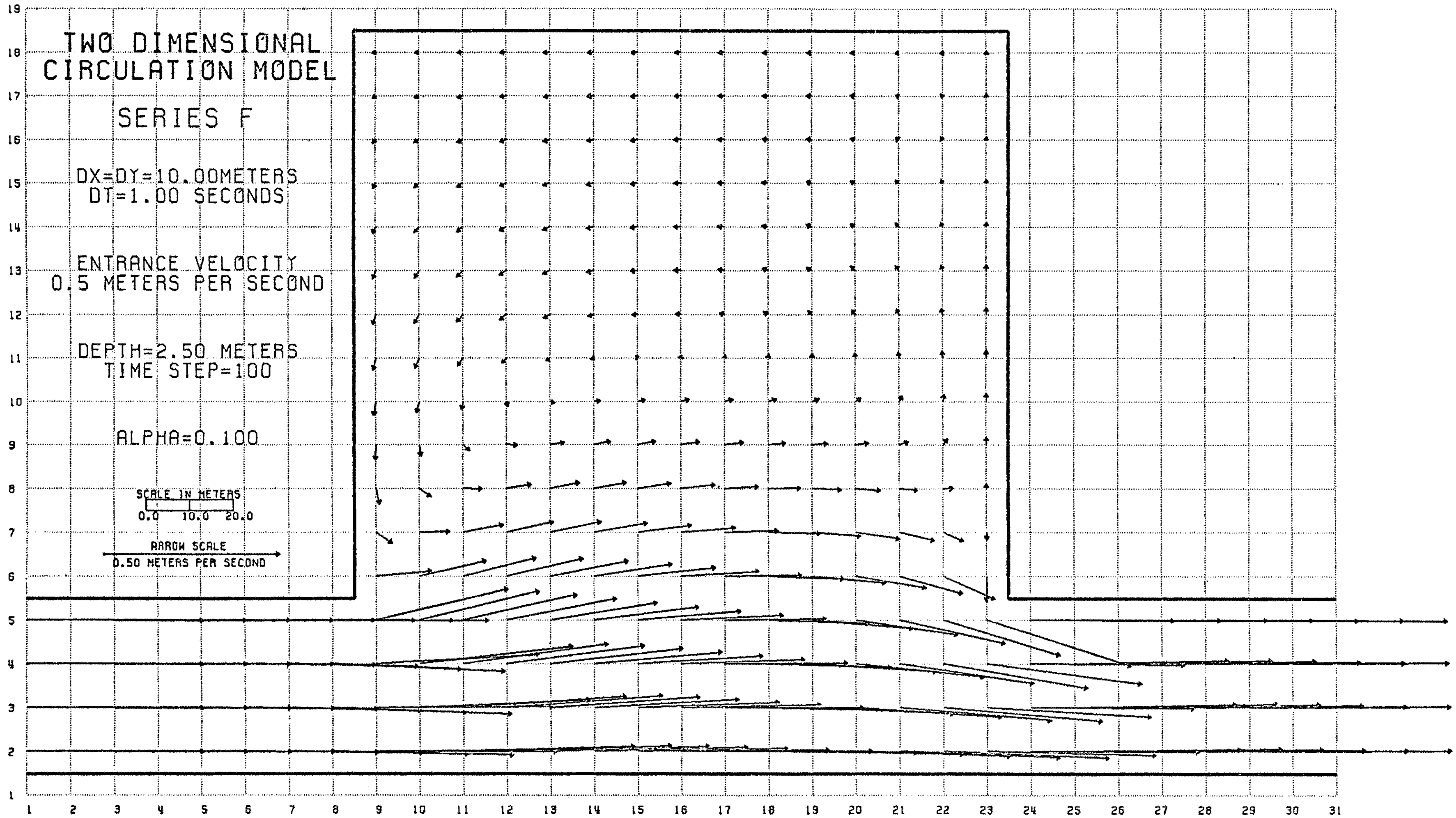

Figure 5.57. Space increment, $\Delta x = \Delta y = 10.0$ meters: time step 100.

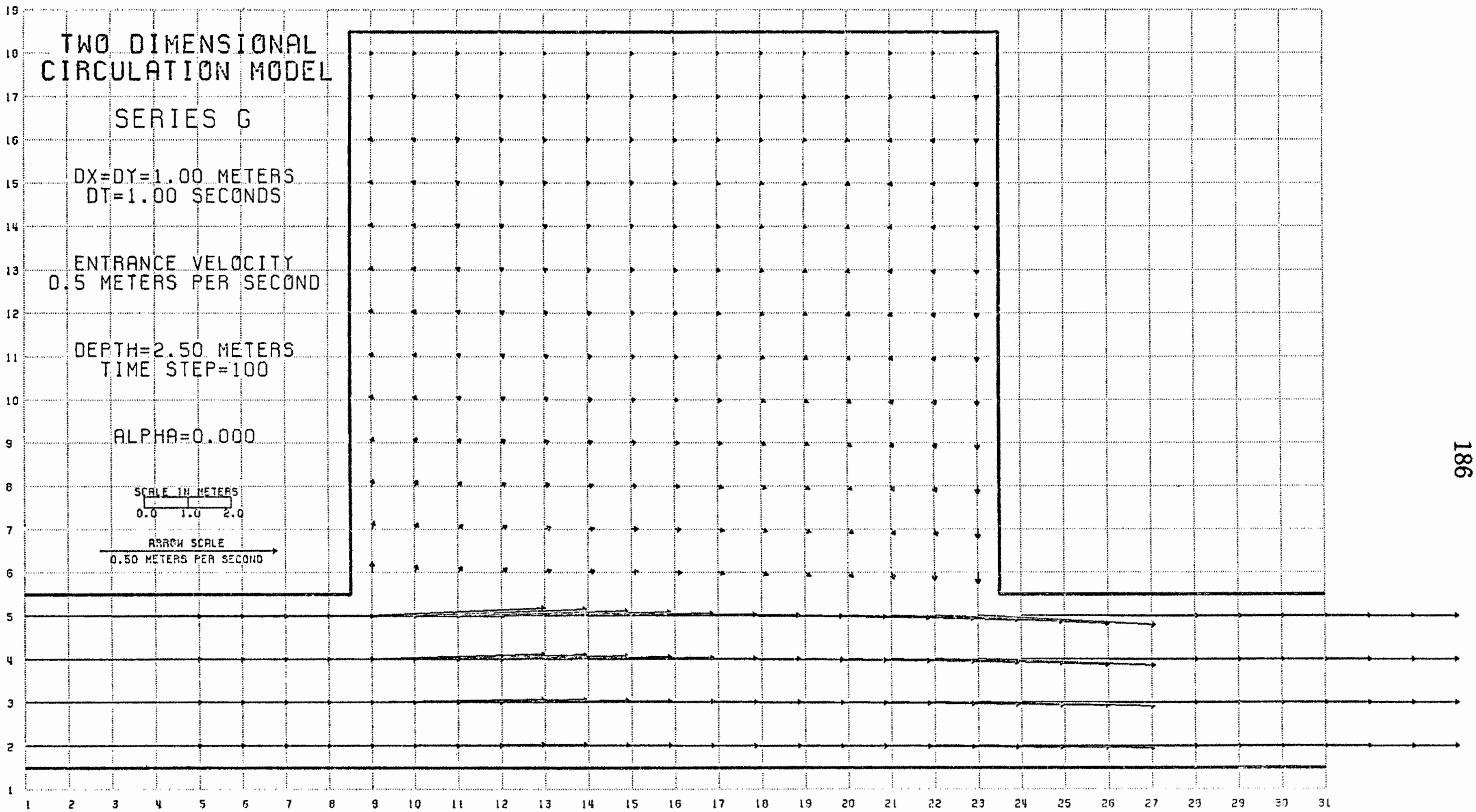

Figure 5.58. Omission of effective stresses and convective inertia: time step 100.

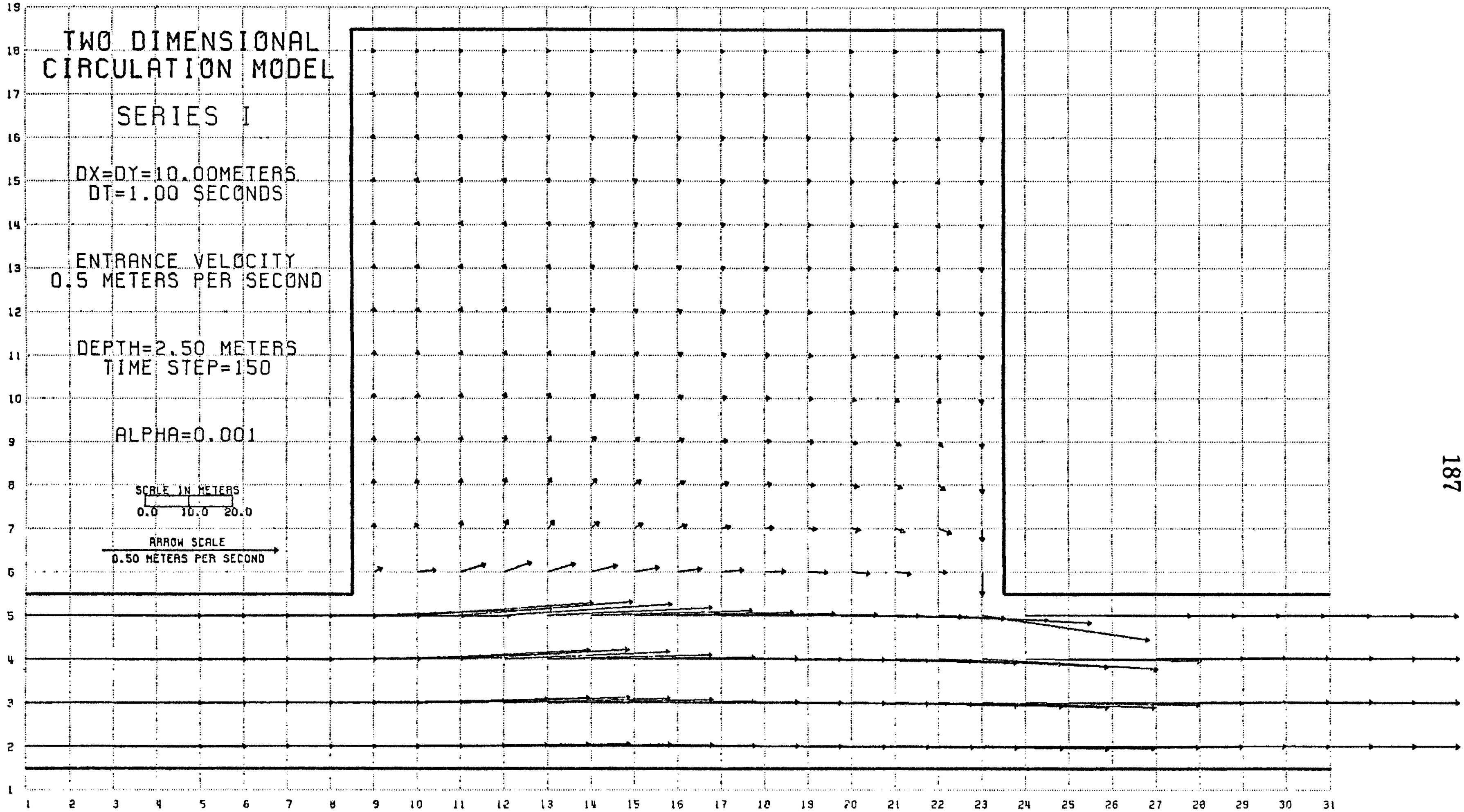

Figure 5.59. α = 0.001 and Δx = Δy = 10.0 meters: time step 150.

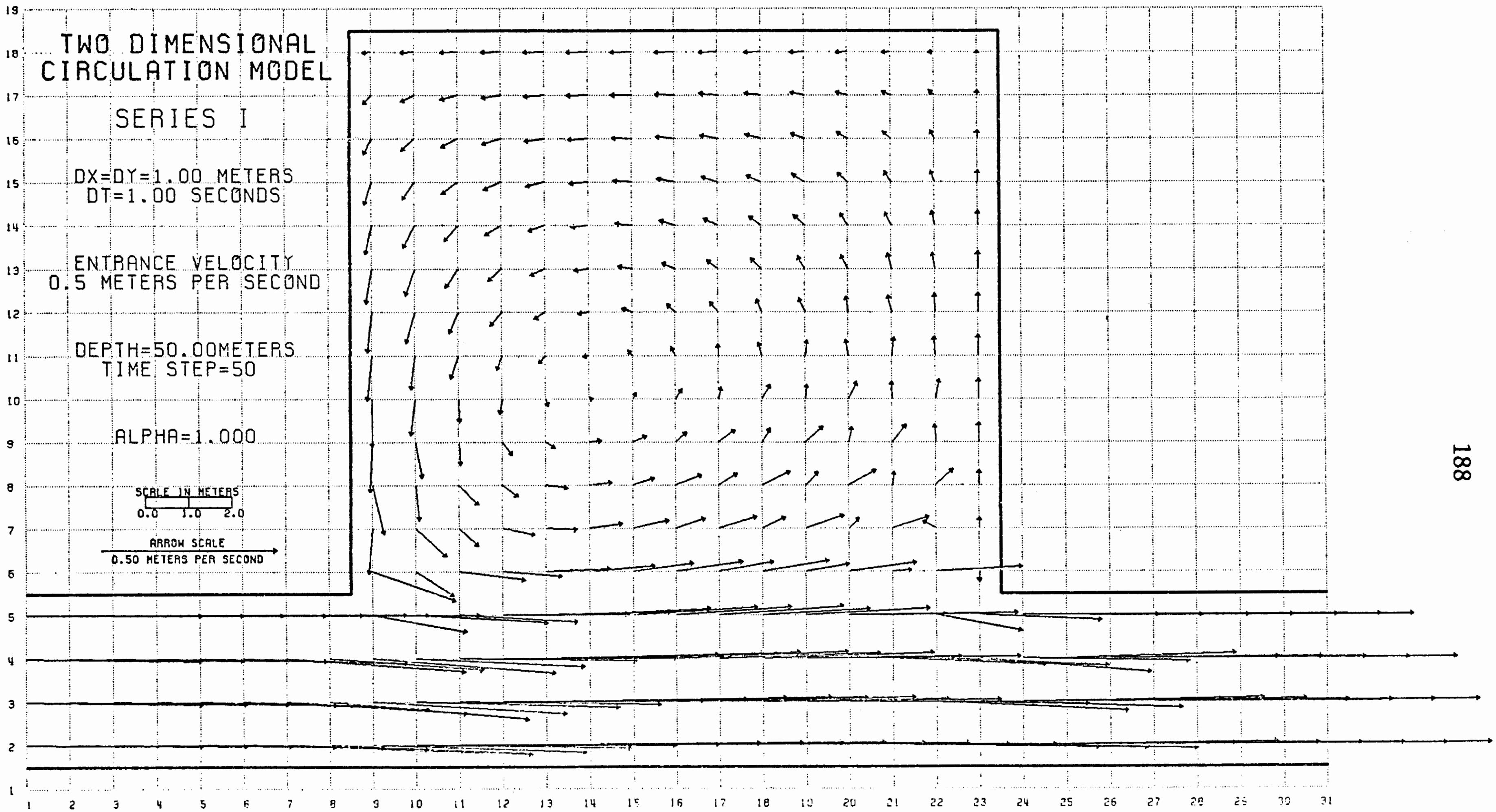

Figure 5.60. α = 1.0 and d = 50.0 meters: time step 50.

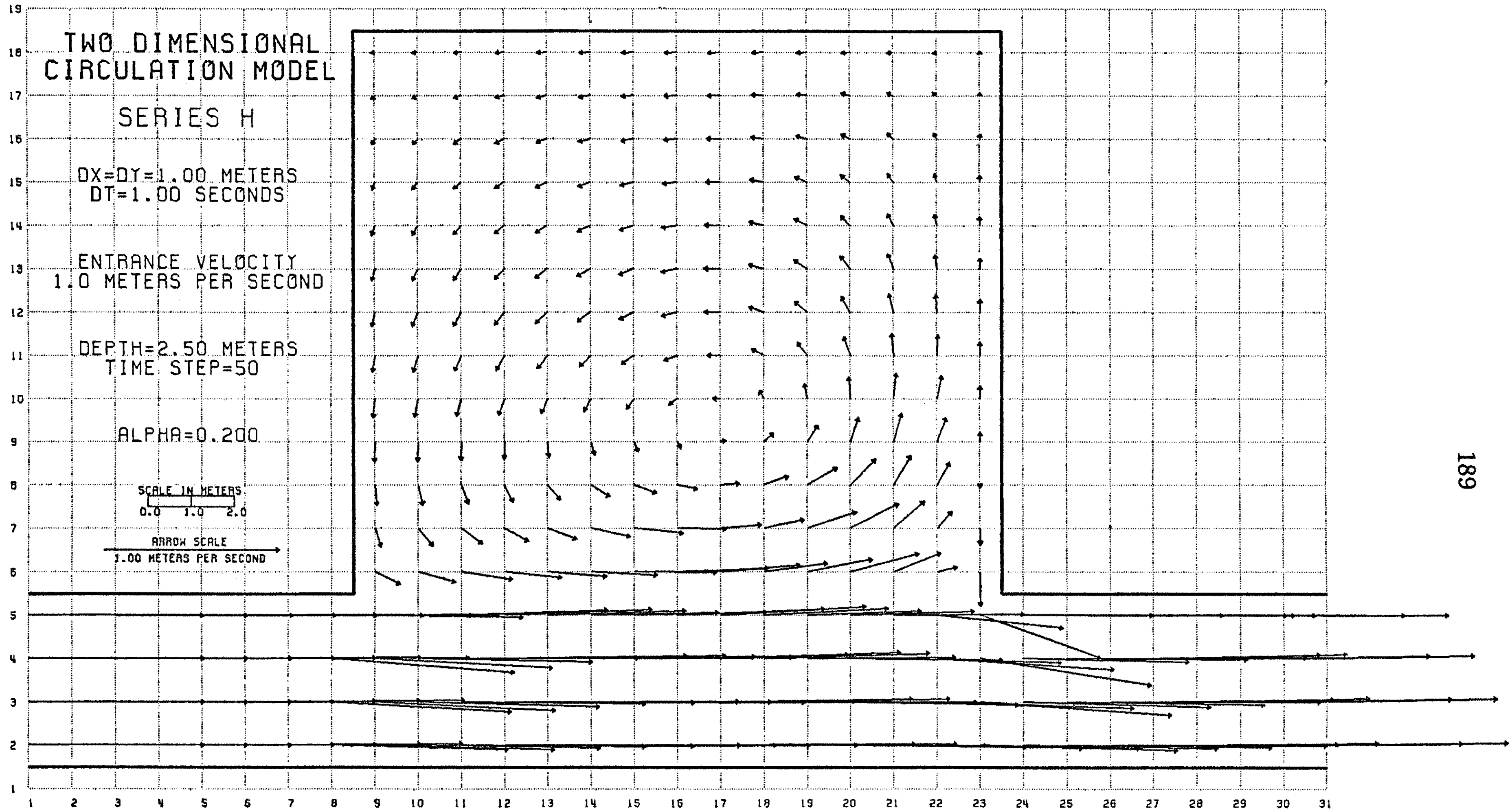

Figure 5.61. U = 1.0 m/s and α = 0.2: time step 50.

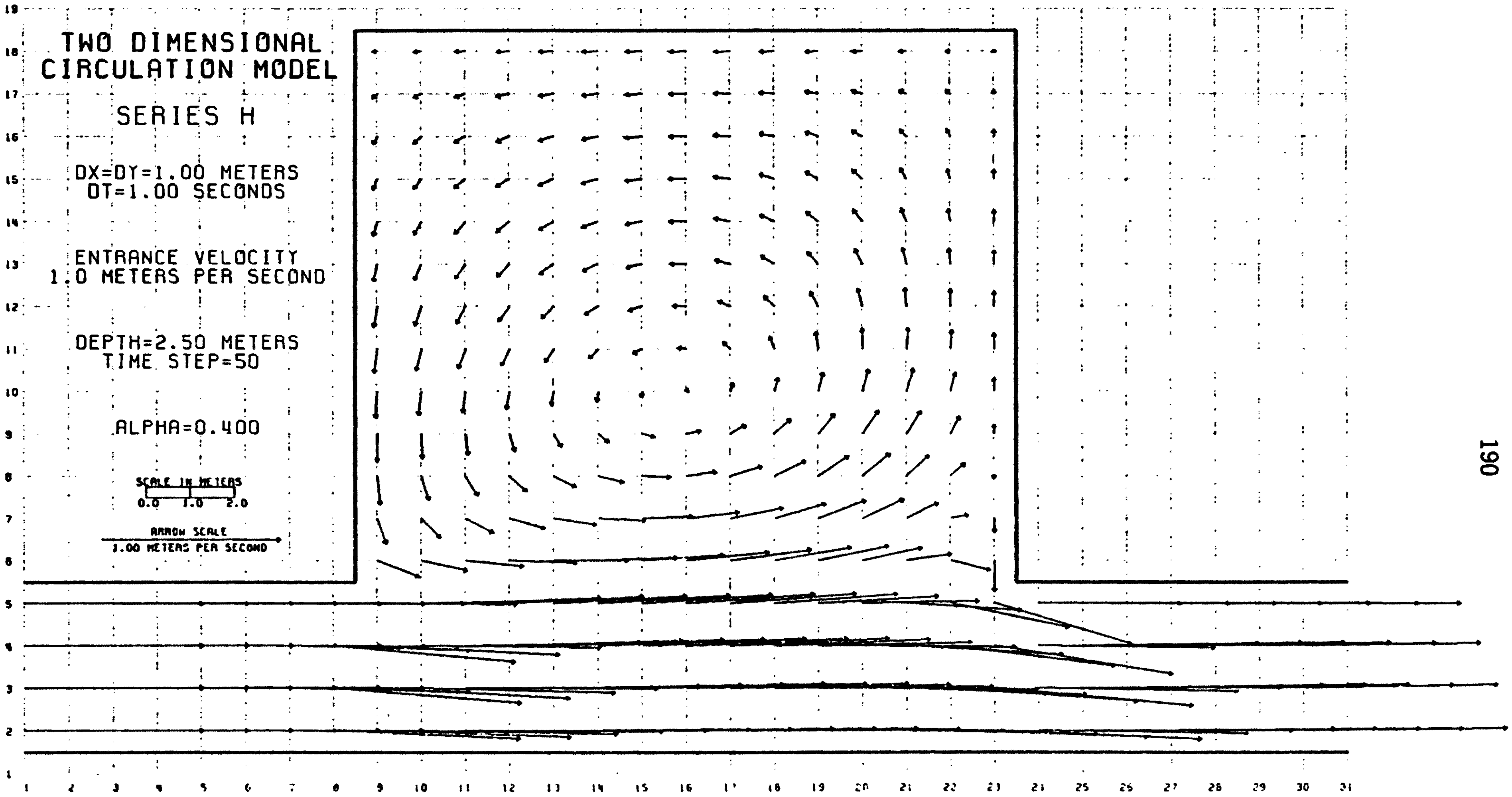

Figure 5.62. U = 1.0 m/s and α = 0.4: time step 50.

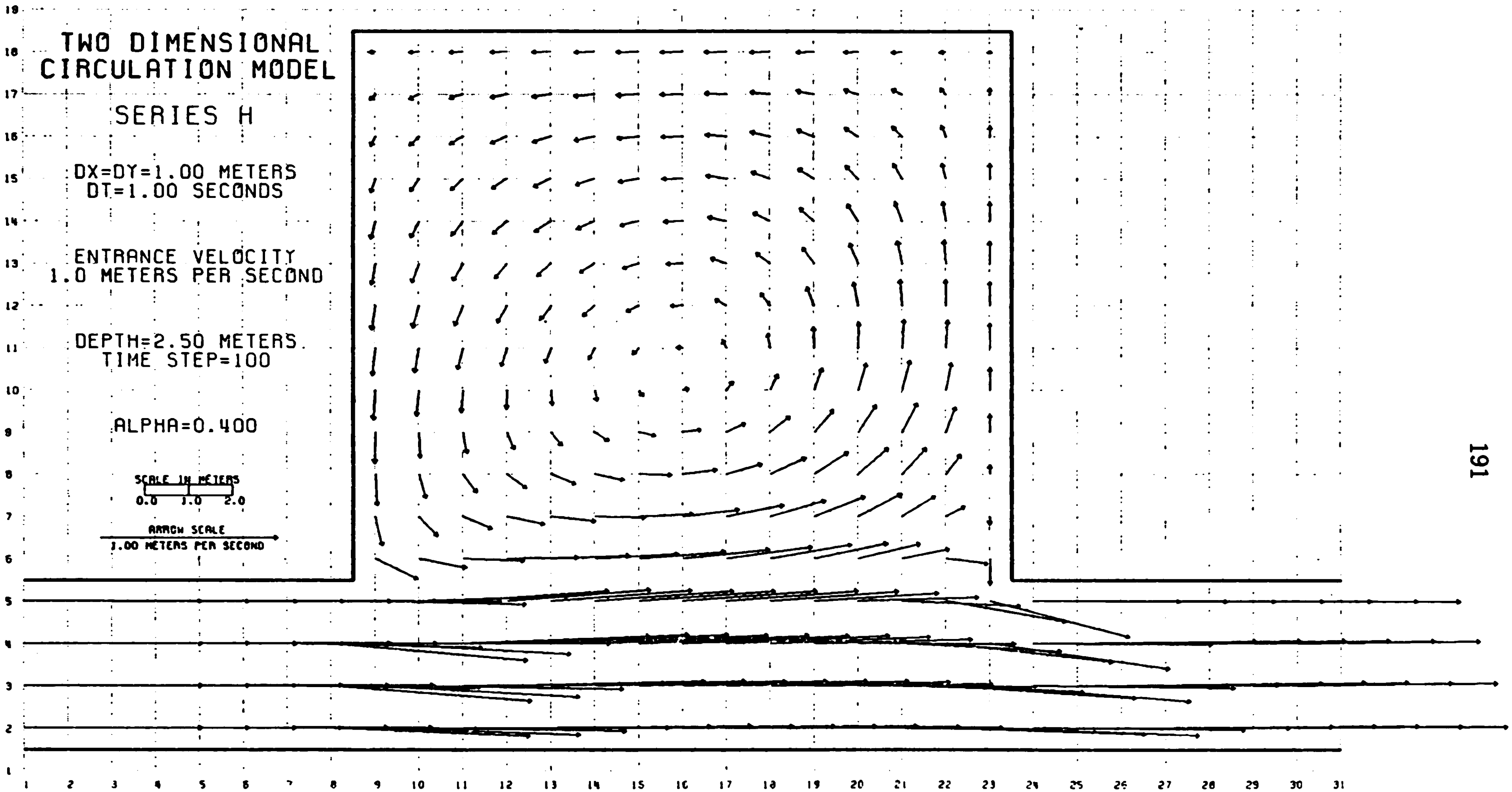

Figure 5.63. U = 1.0 m/s and α = 0.4: time step 100.

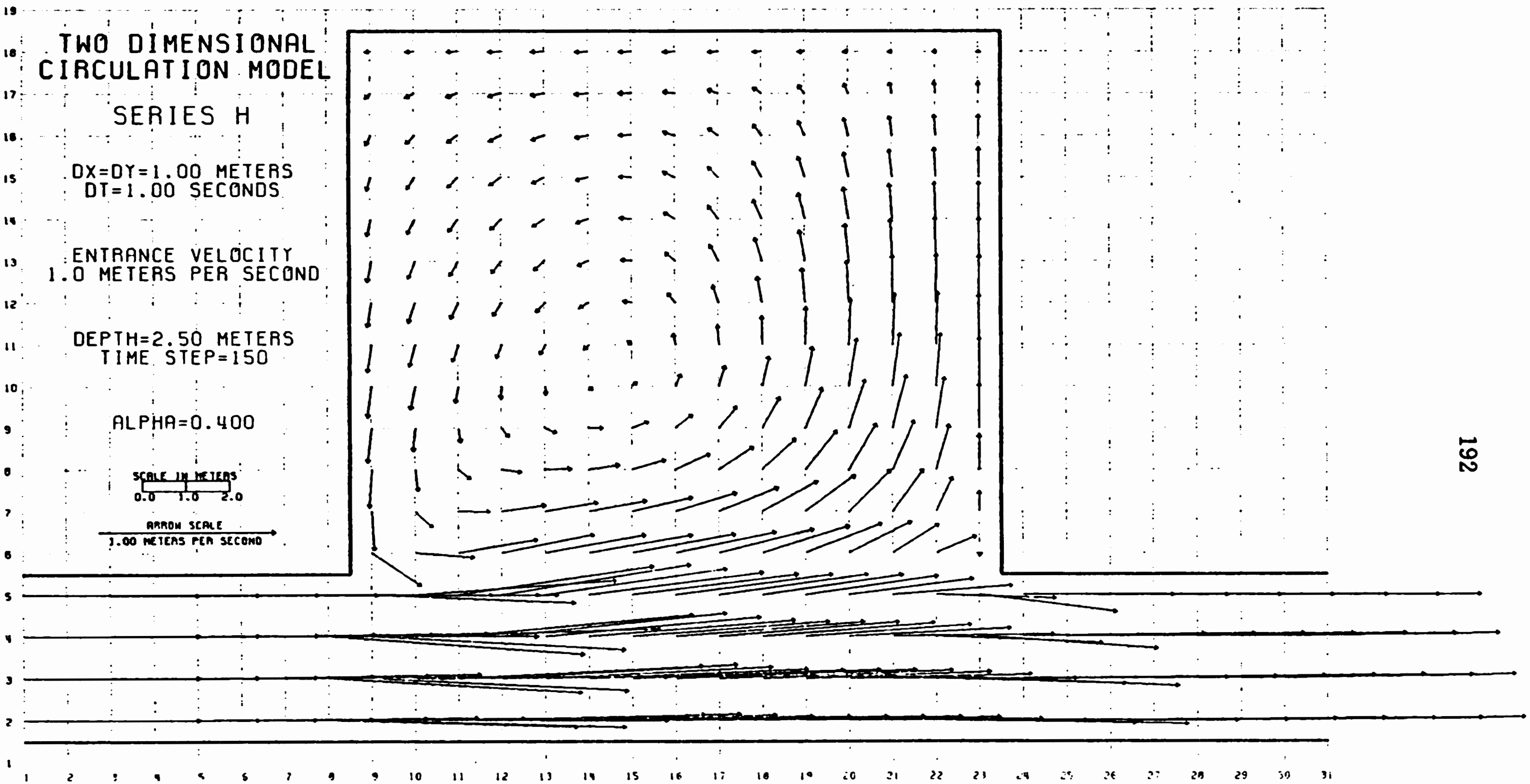

Figure 5.64. U = 1.0 m/s and α = 0.4: time step 150.

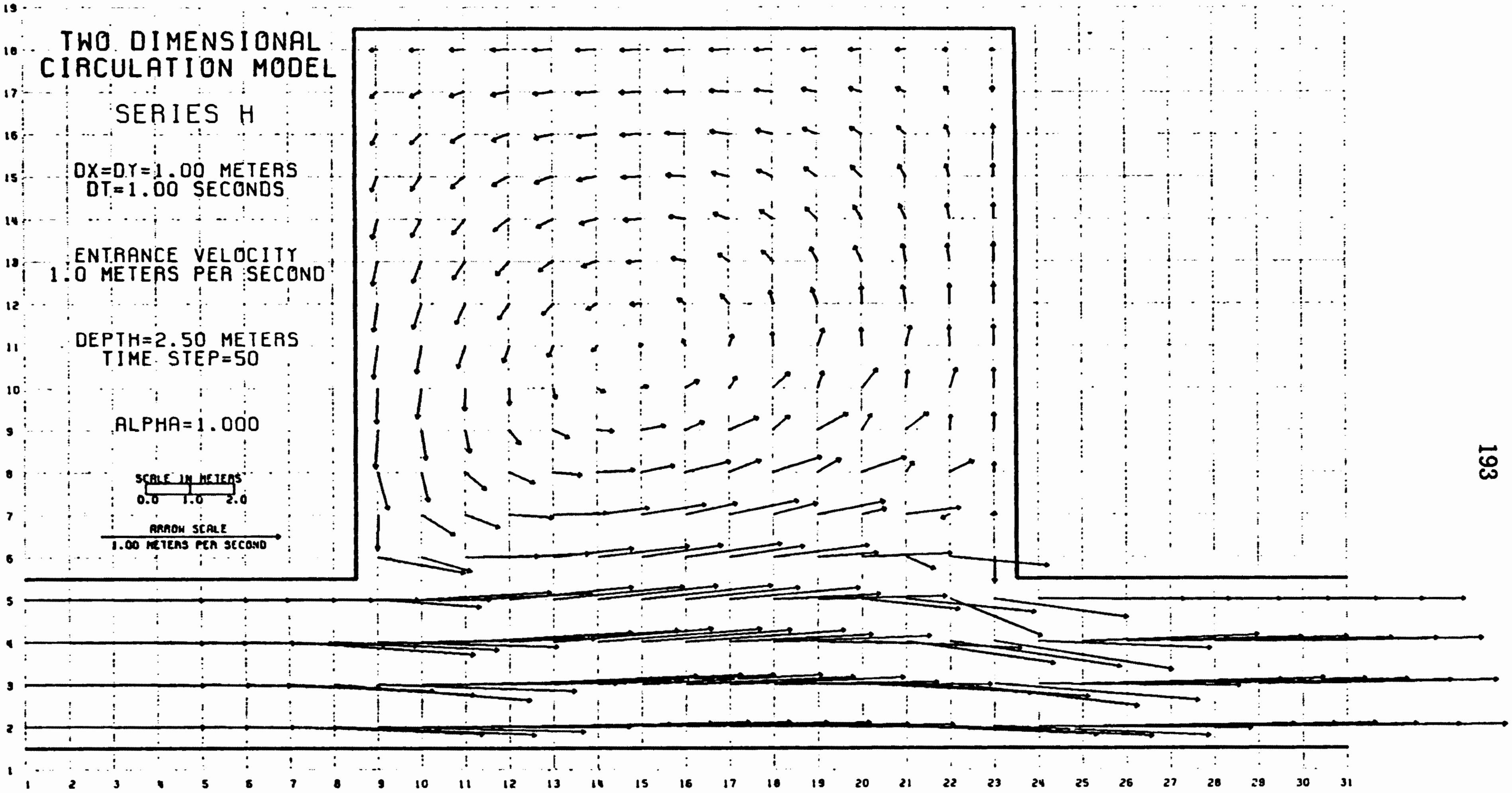

Figure 5.65. U = 1.0 m/s and α = 1.0: time step 50.

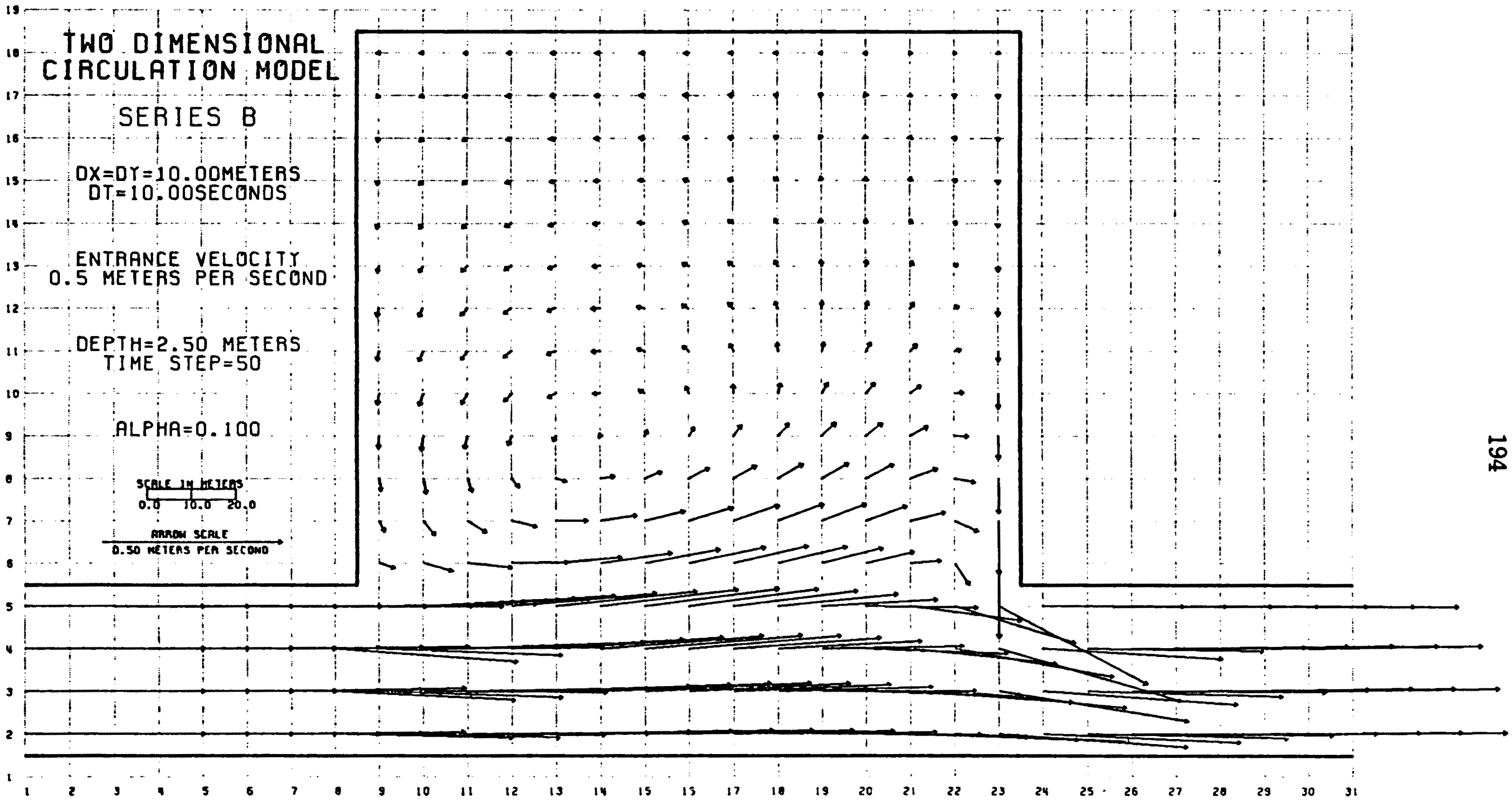

Figure 5.66. Δx = Δy = 10.0 meters and Δt = 10.0 seconds: time step 50.

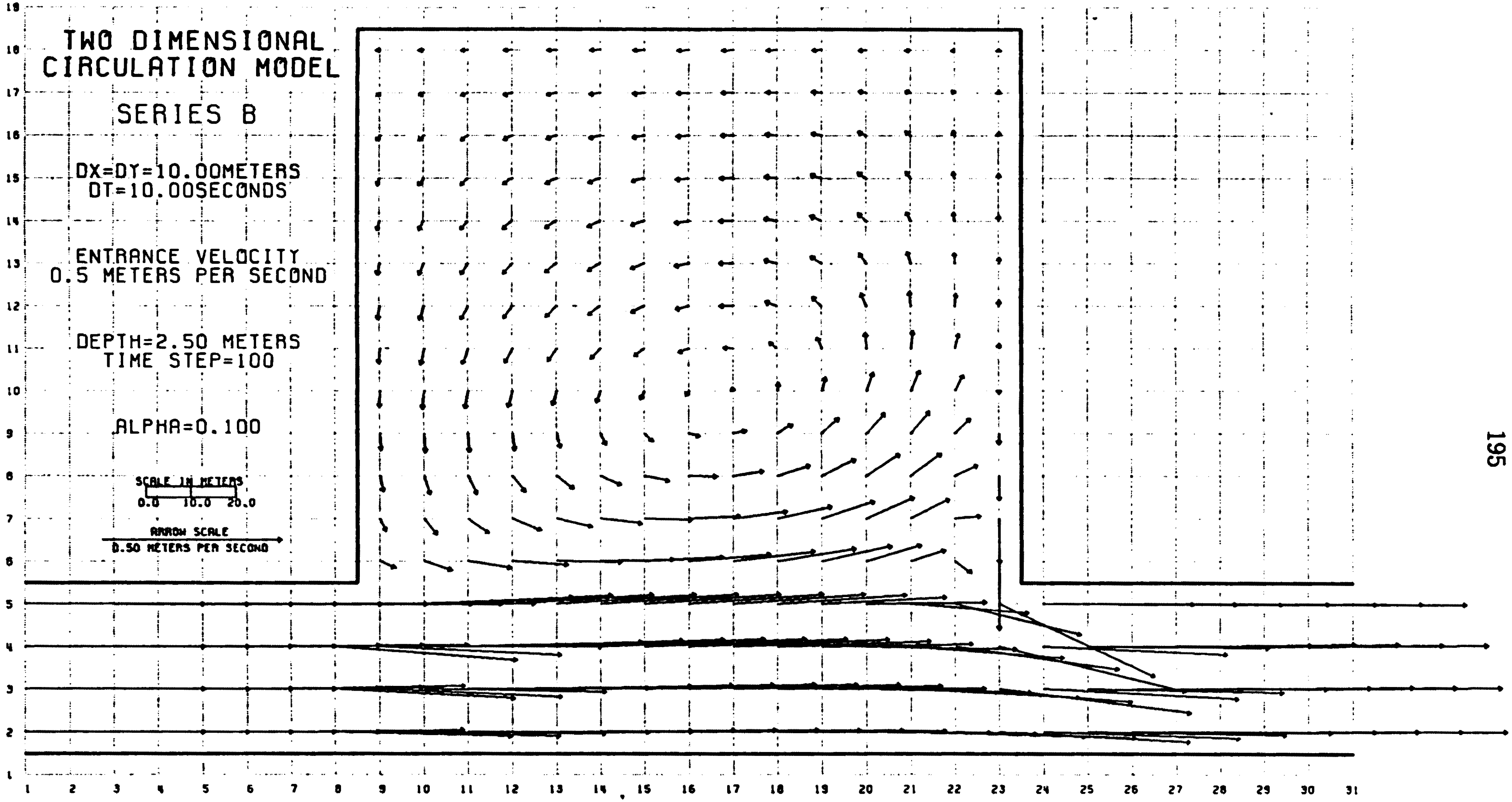

Figure 5.67. Δx = Δy = 10.0 meters and Δt = 10.0 seconds: time step 100.

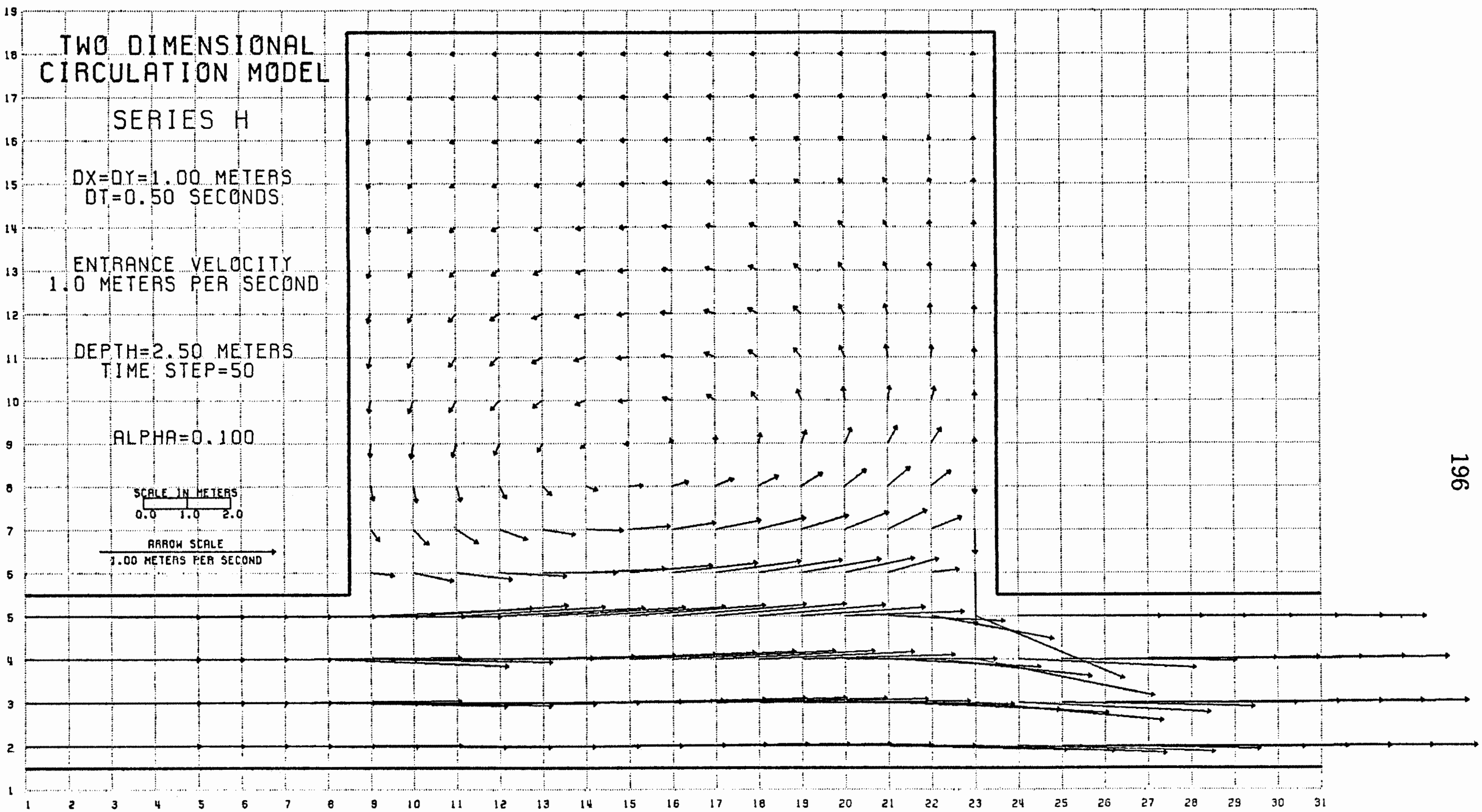

Figure 5.68. U = 1.0 m/s and Δt = 0.5 seconds: time step 50.

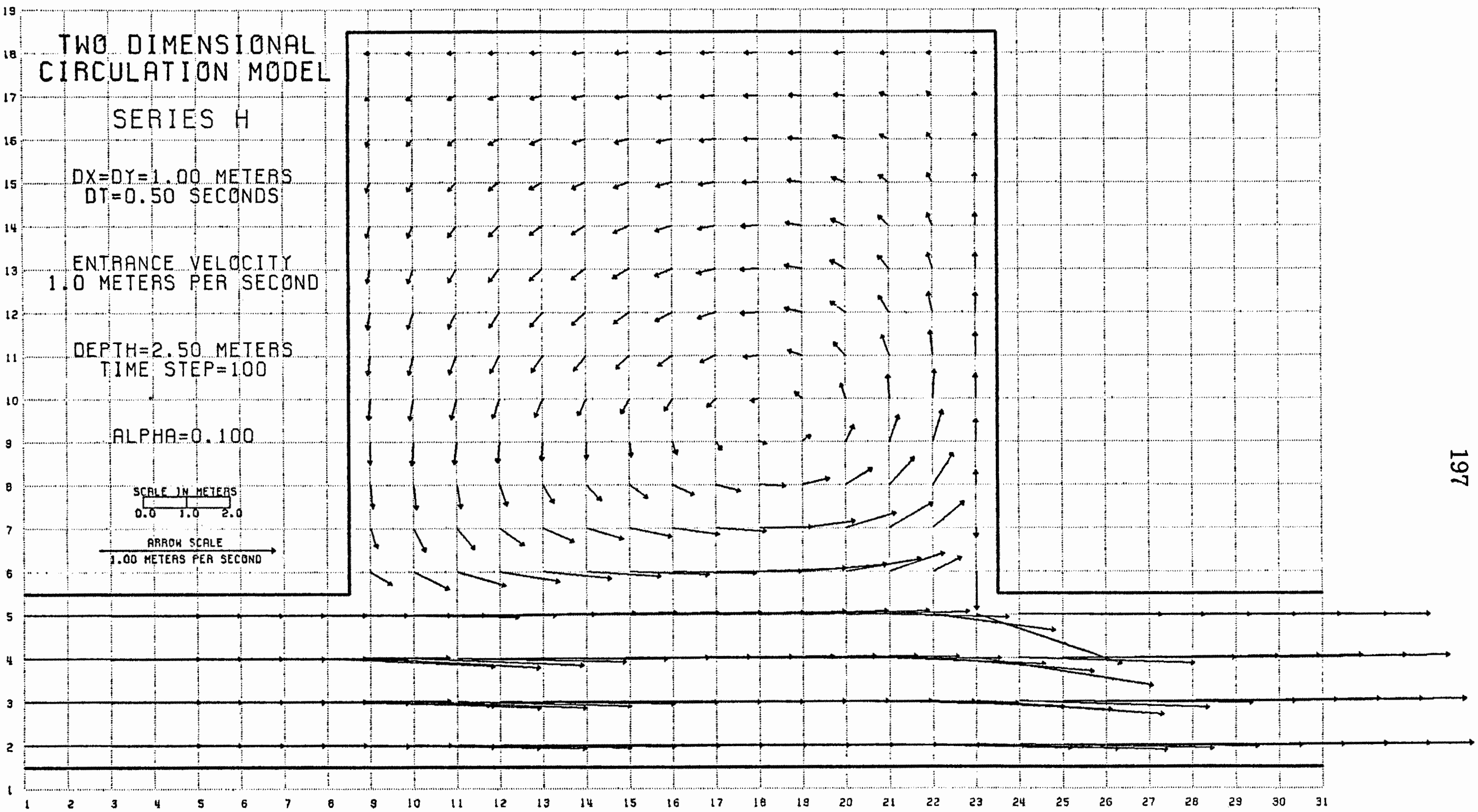

Figure 5.69. U = 1.0 m/s and Δt = 0.5 seconds: time step 100.

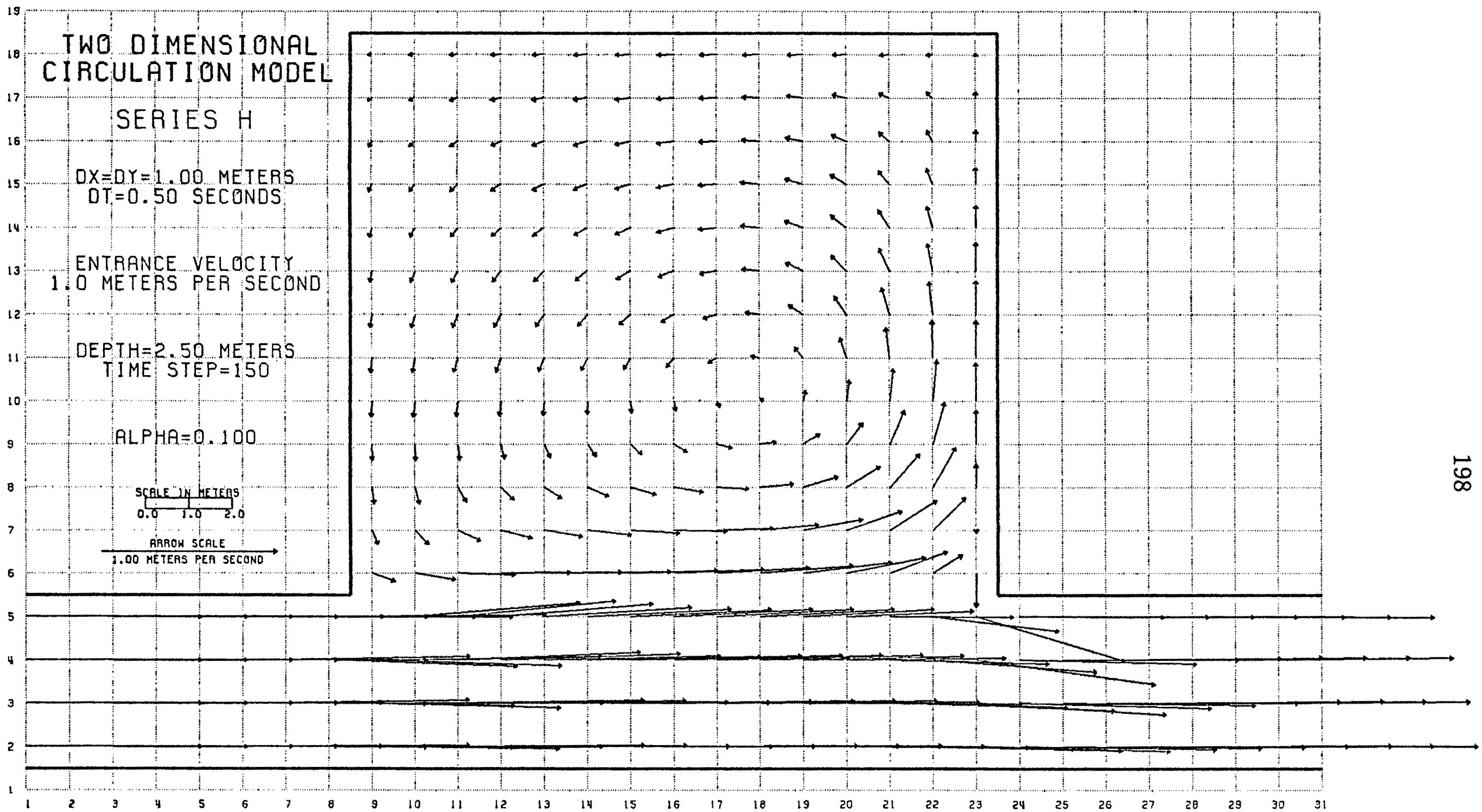

Figure 5.70. U = 1.0 m/s and Δt = 0.5 seconds: time step 150.

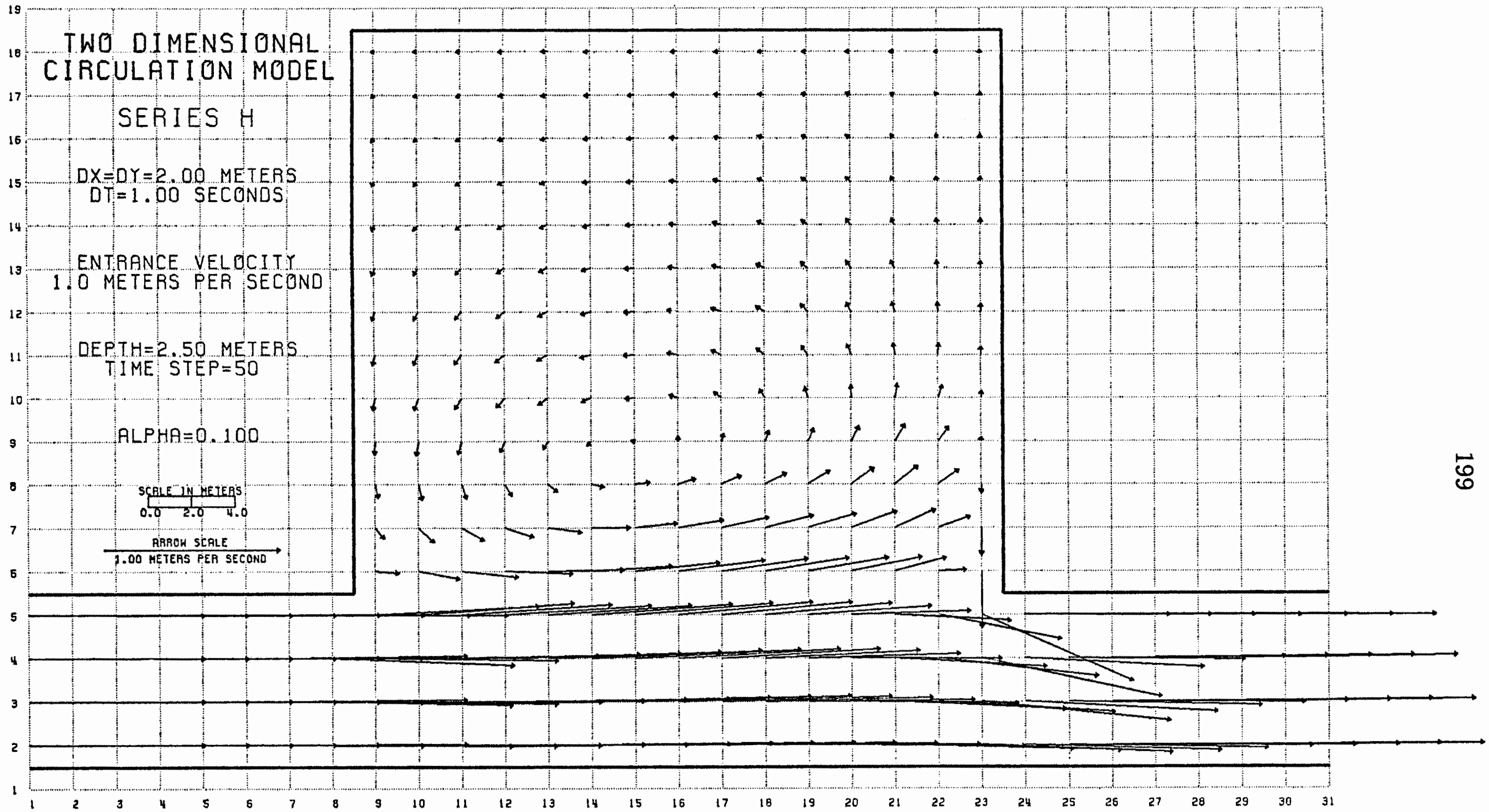

Figure 5.71. U = 1.0 m/s and Δx = Δy = 2.0 meters: time step 50.

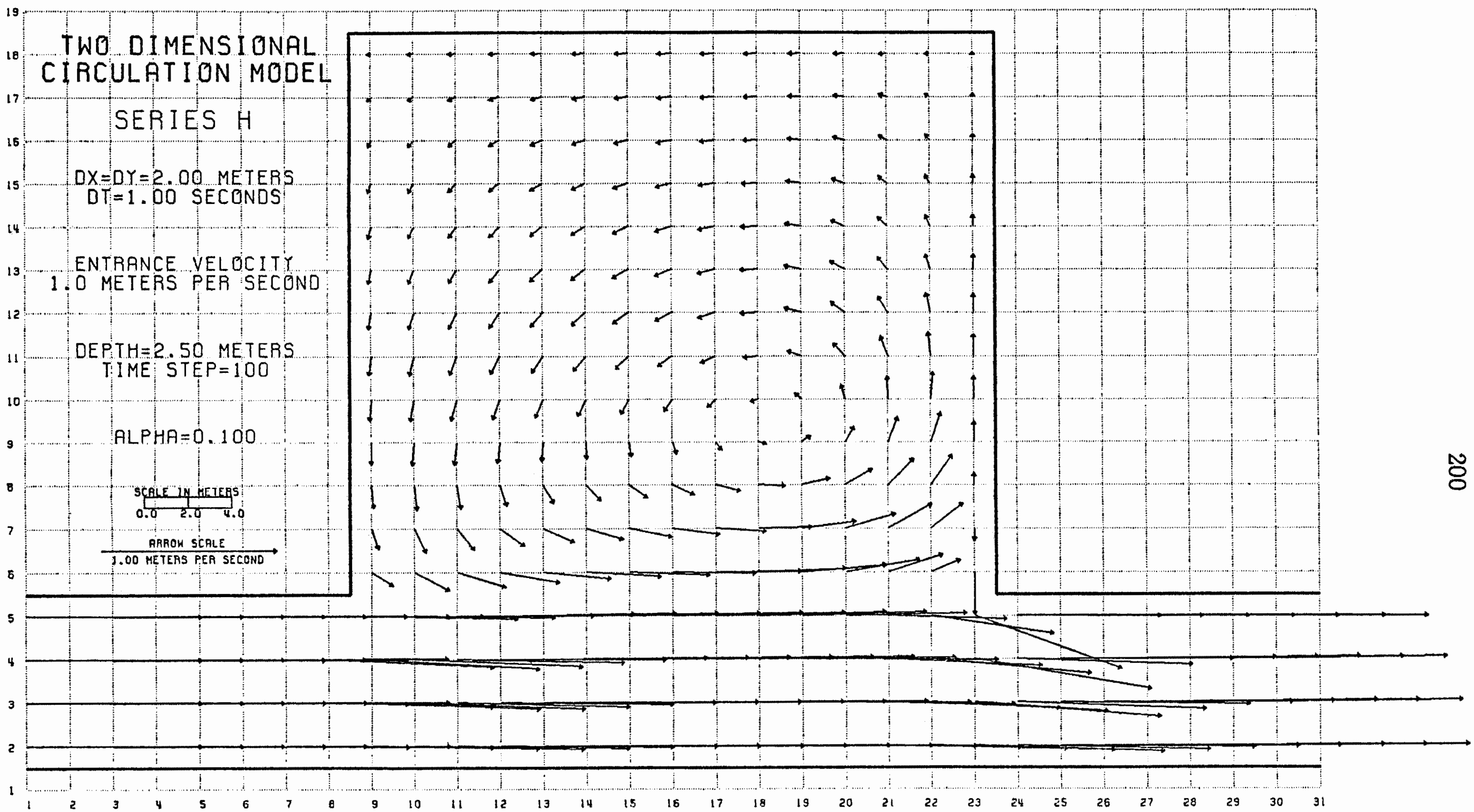

Figure 5.72. U = 1.0 m/s and Δx = Δy = 2.0 meters: time step 100.

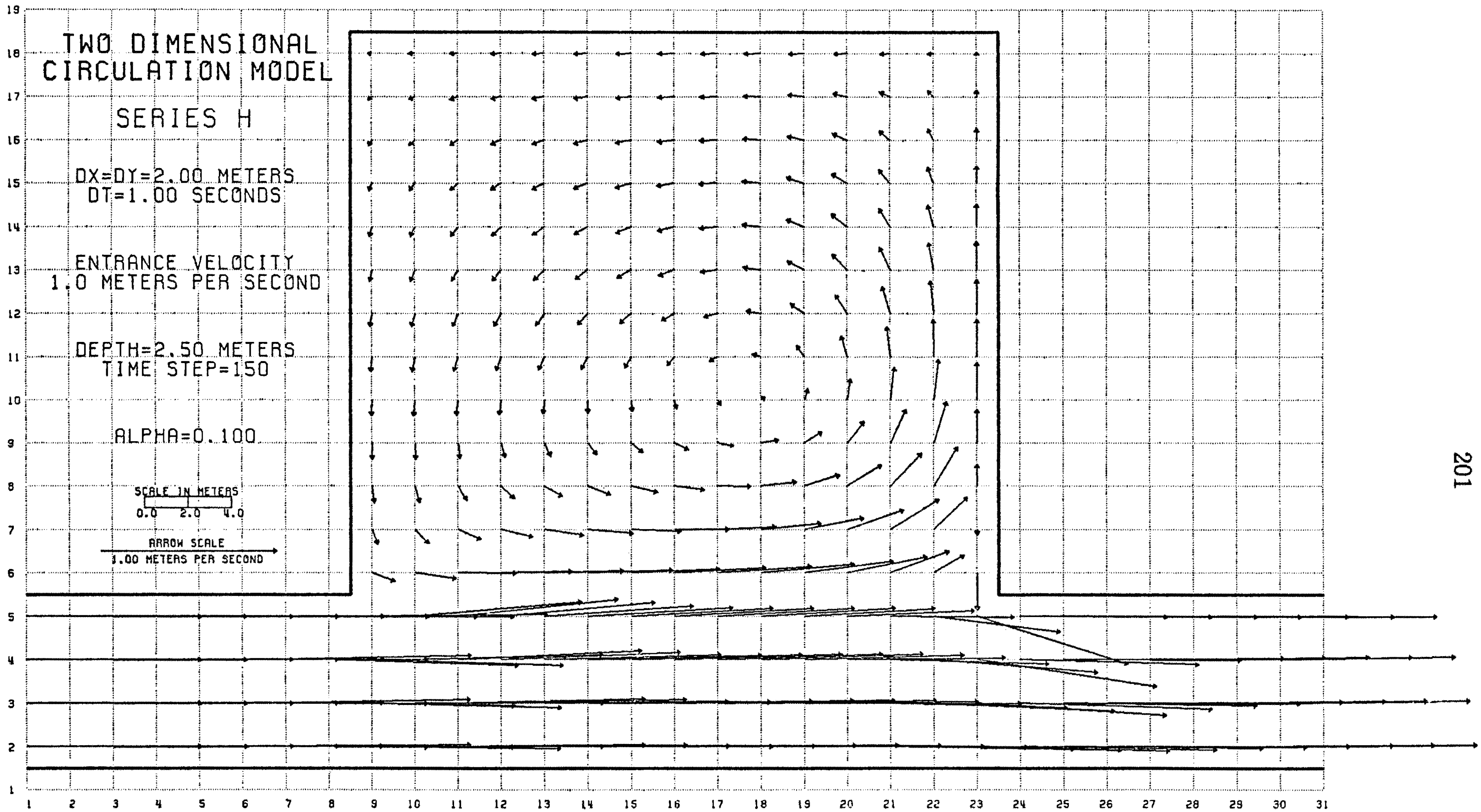

Figure 5.73. U = 1.0 m/s and $\Delta x = \Delta y = 2.0$ meters: time step 150.

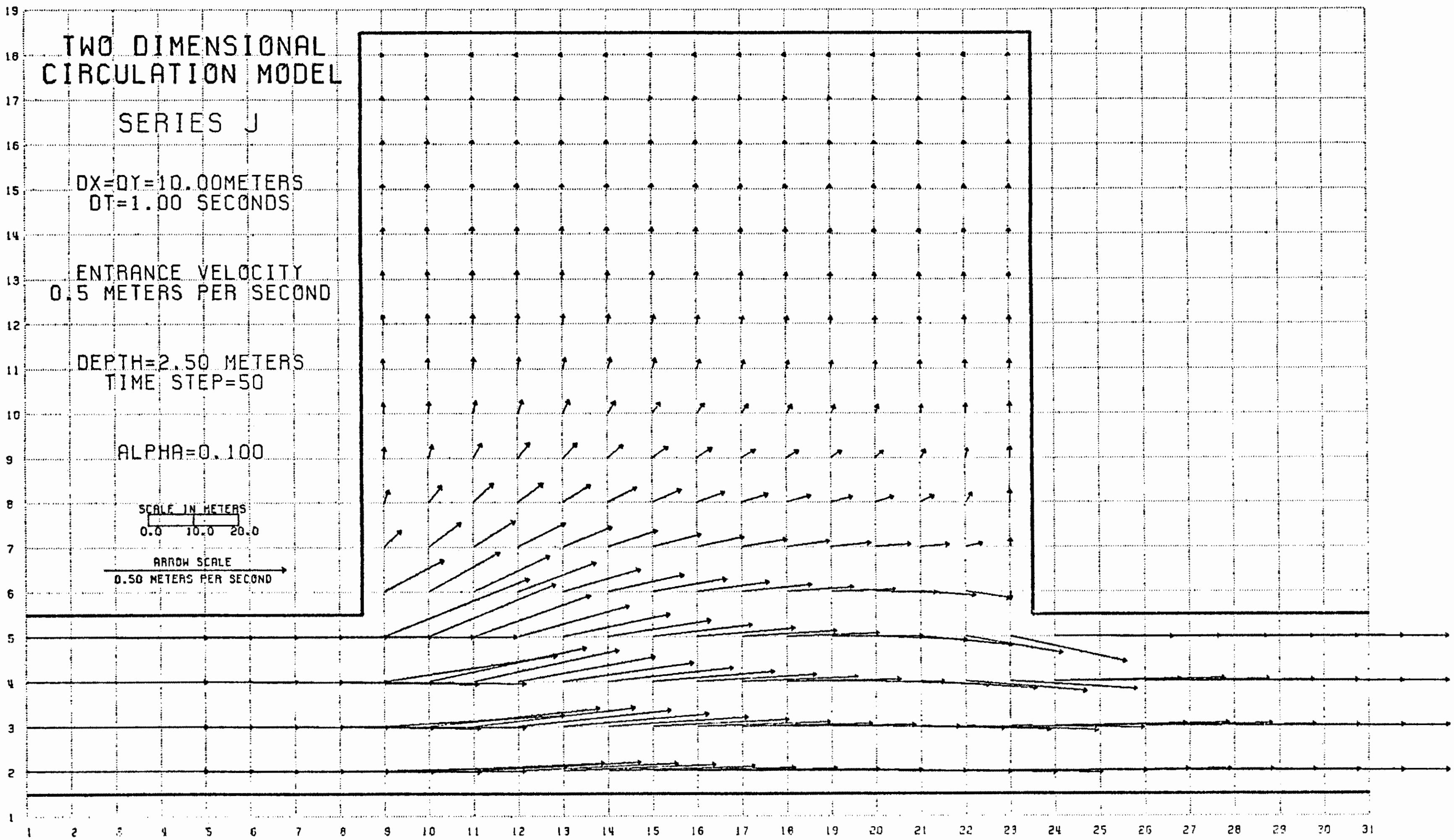

Figure 5.74. $\Delta x = \Delta y = 10.0$ meters and $f_r = 0.04$: time tep 50.

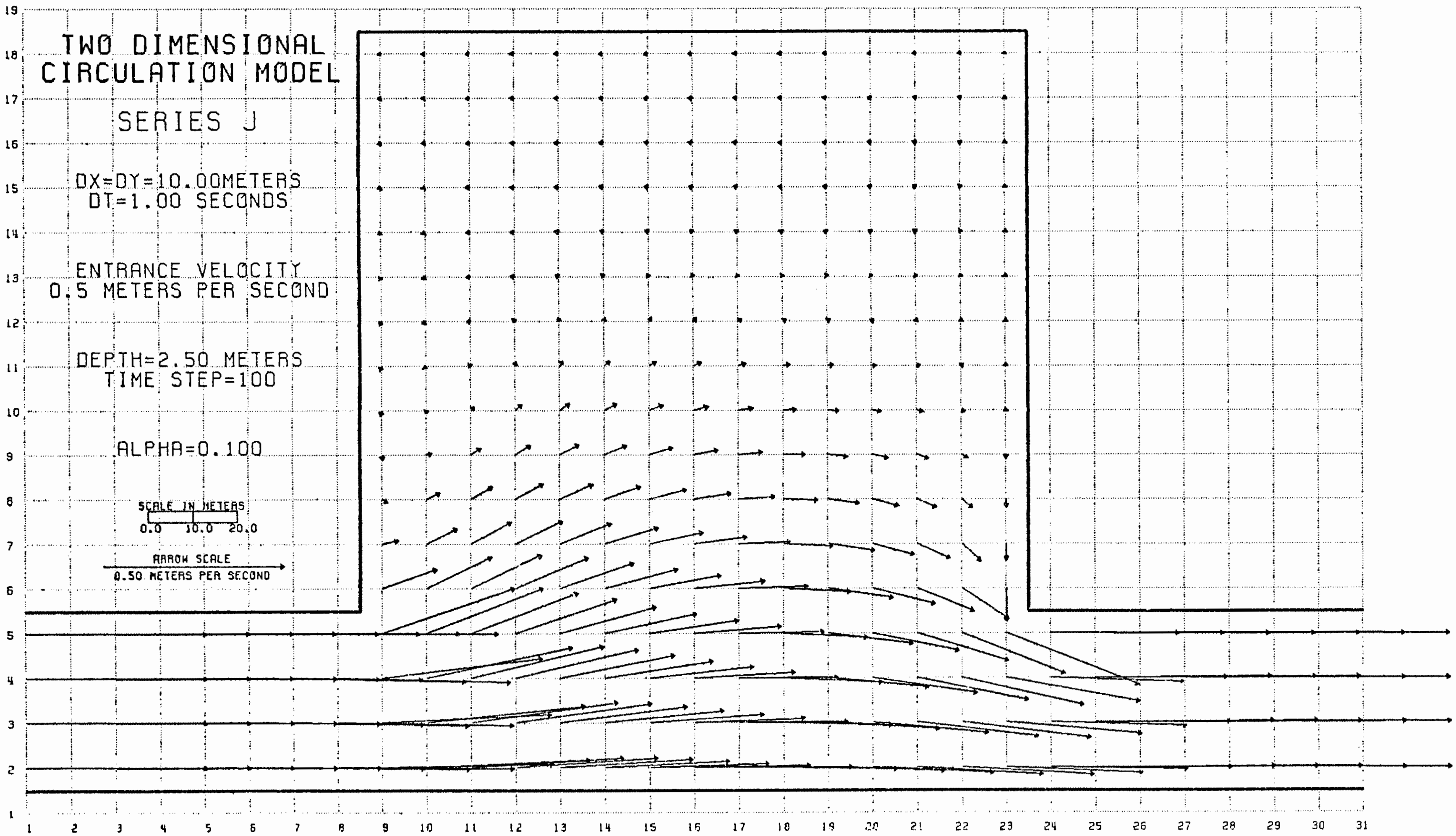

Figure 5.75. $\Delta x = \Delta y = 10.0$ meters and $f_r = 0.4$: time step 100.

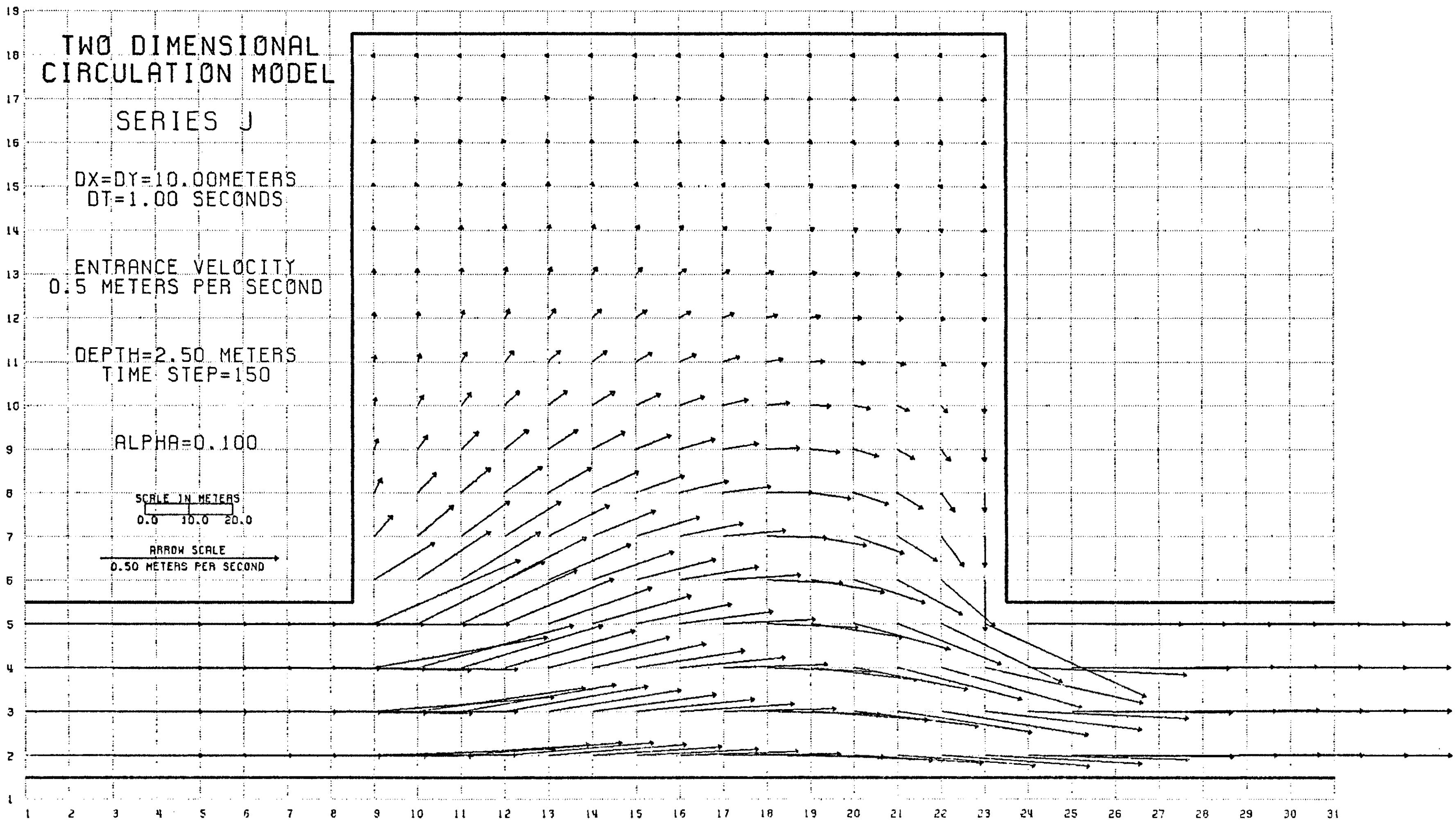

Figure 5.76. $\Delta x = \Delta y = 10.0$ meters and $f_r = 0.04$: time step 150.

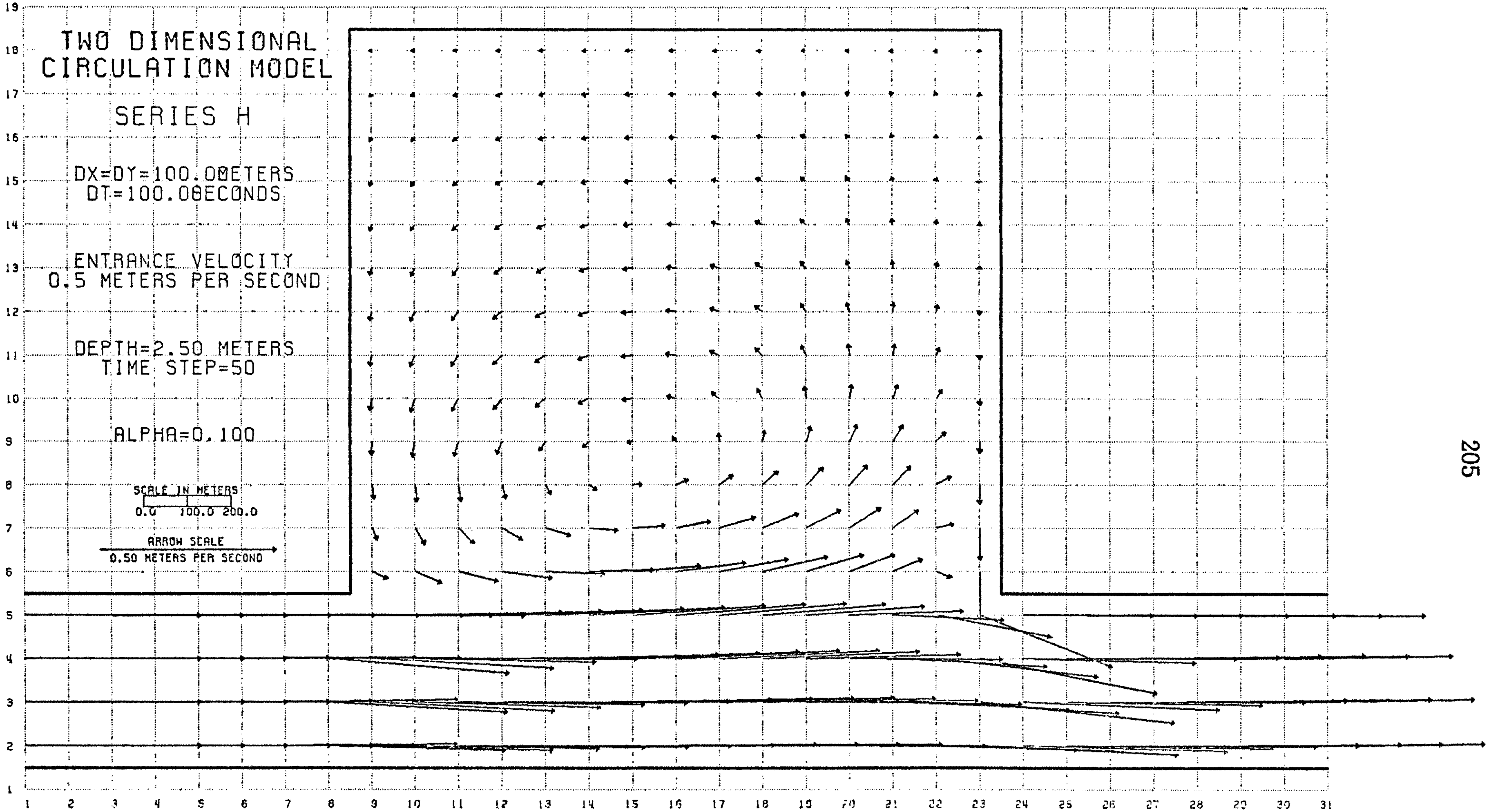

Figure 5.77. $\Delta x = \Delta y = 100.0$ m and $\Delta t = 100.0$ s and $f_r = 0.0$: time step 50.

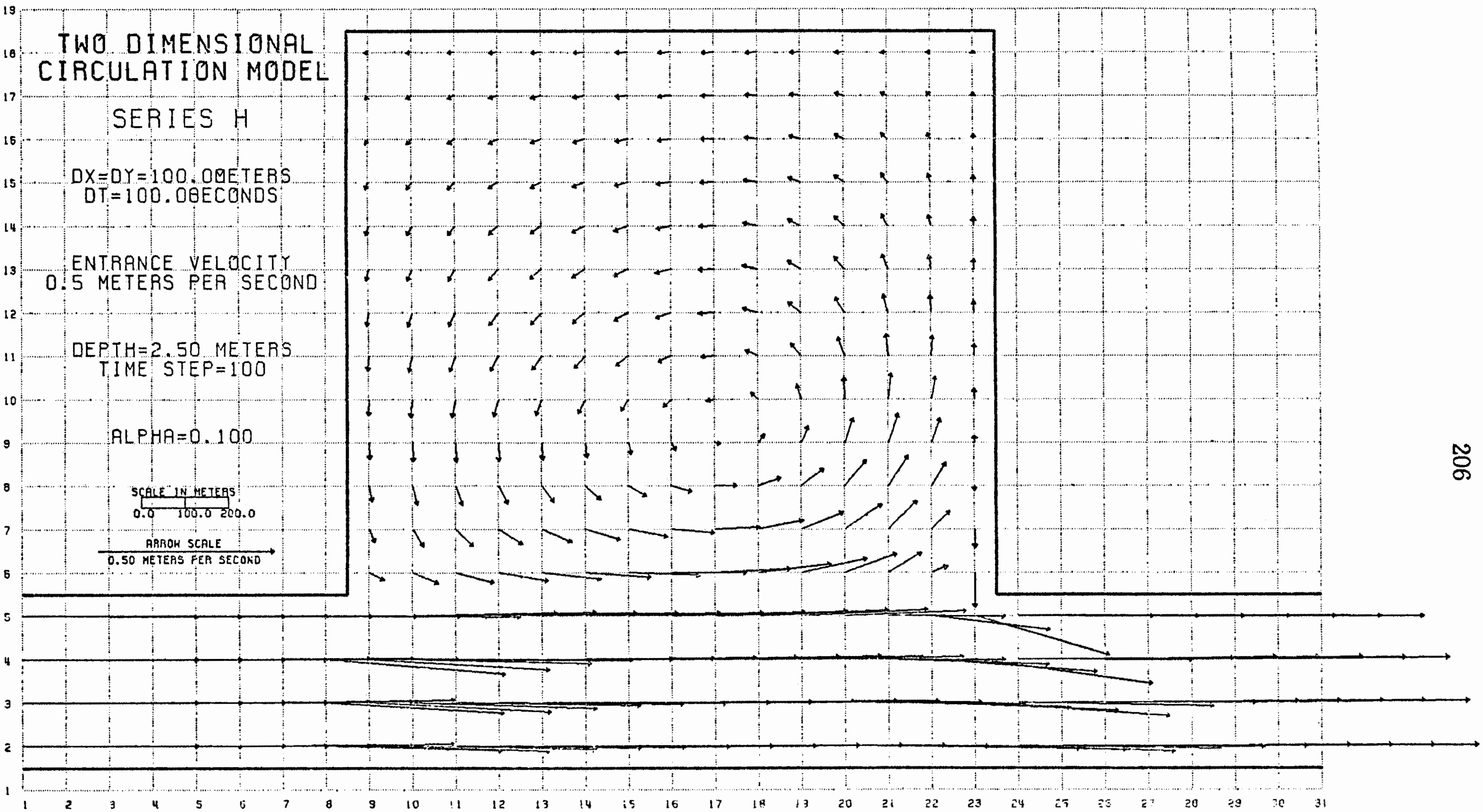

Figure 5.78. $\Delta x = \Delta y = 100.0$ m and $\Delta t = 100.0$ s and $f_r = 0.0$: time step 100.

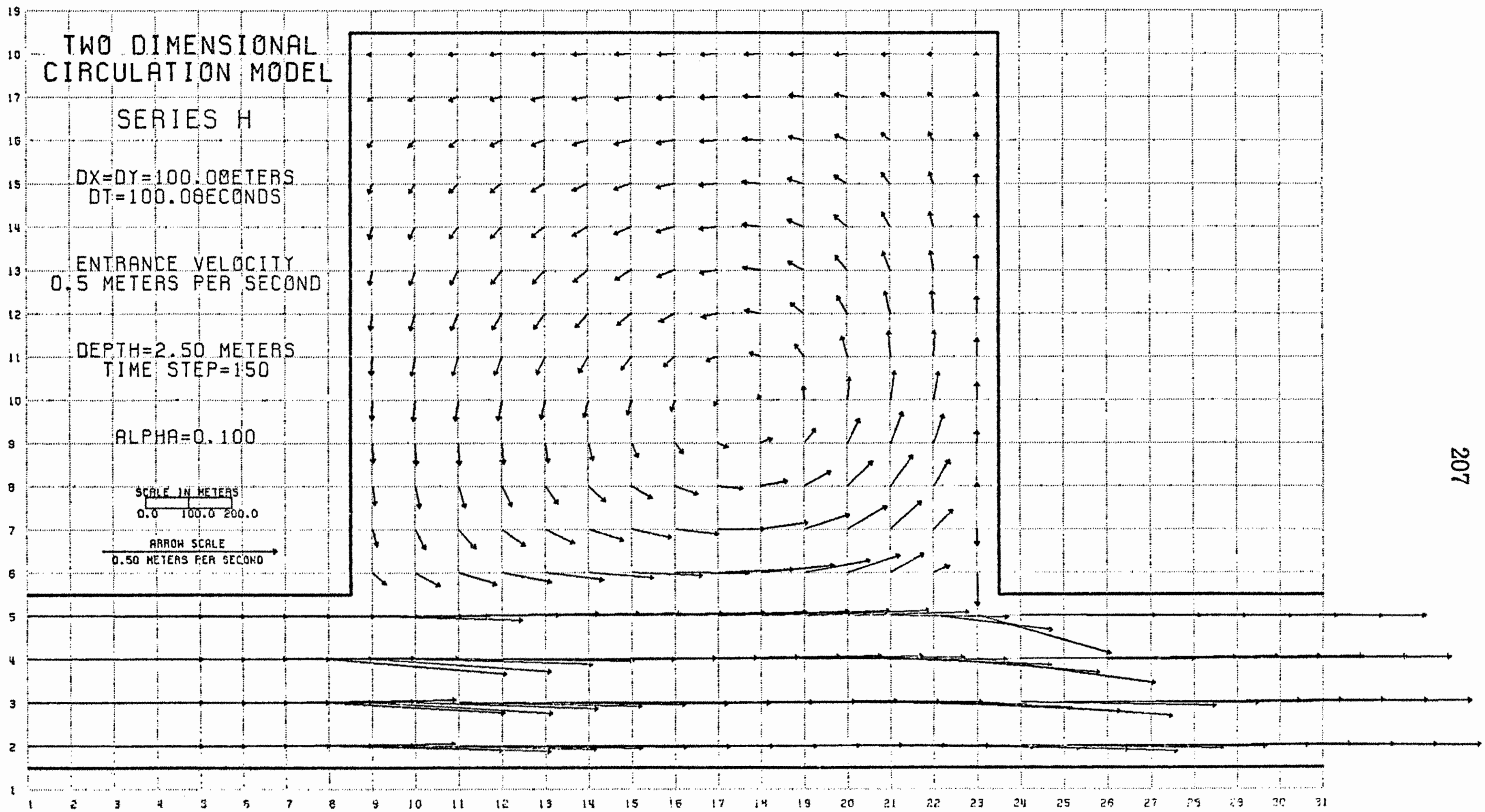

Figure 5.79. $\Delta x = \Delta y = 100.0$ m and $\Delta t = 100.0$ s and $f_r = 0.0$: time step 150.

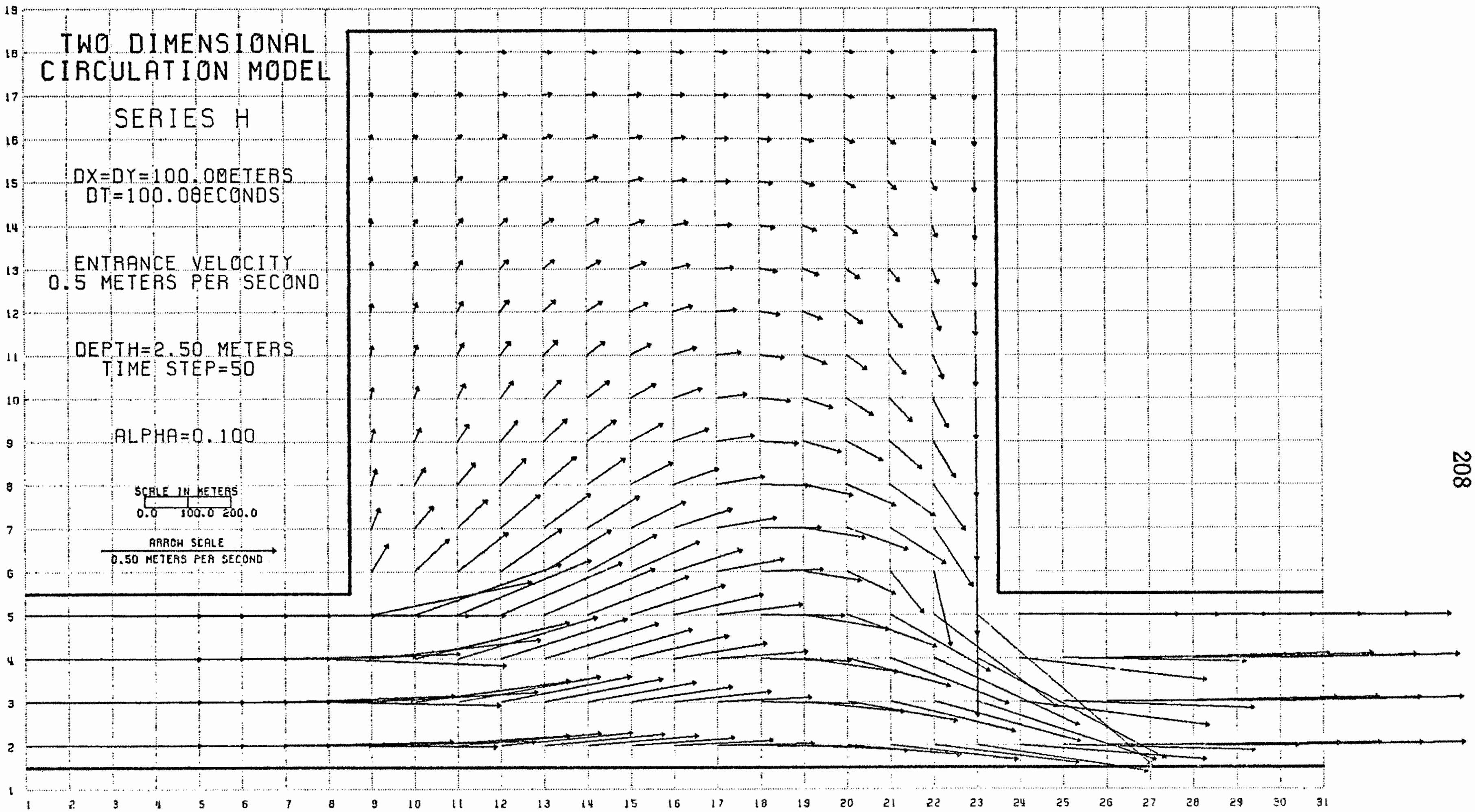

Figure 5.80. Δx = Δy = 100.0 m and Δt = 100.0 s: time step 50.

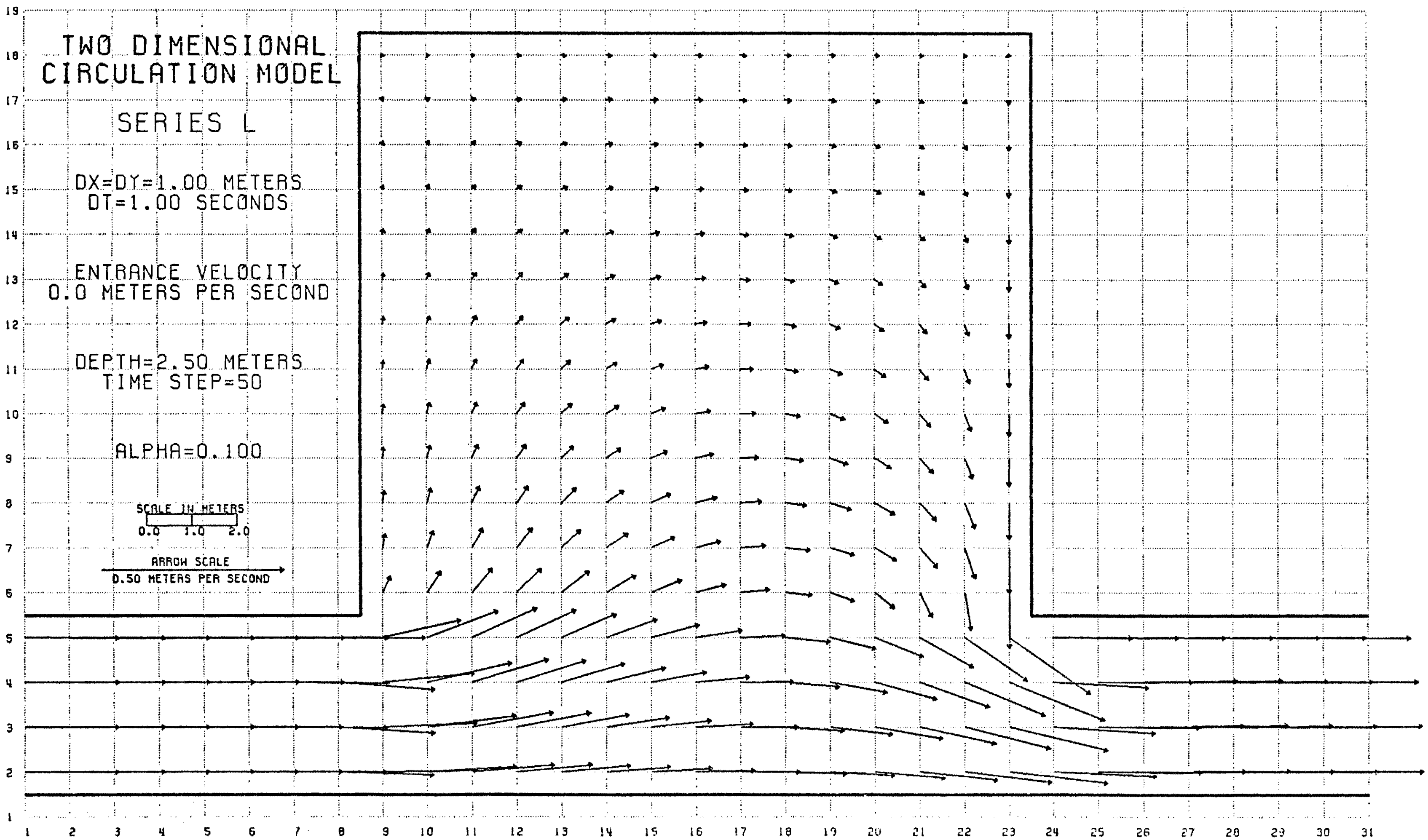

Figure 5.81. Slope-specified baseline: time step 50.

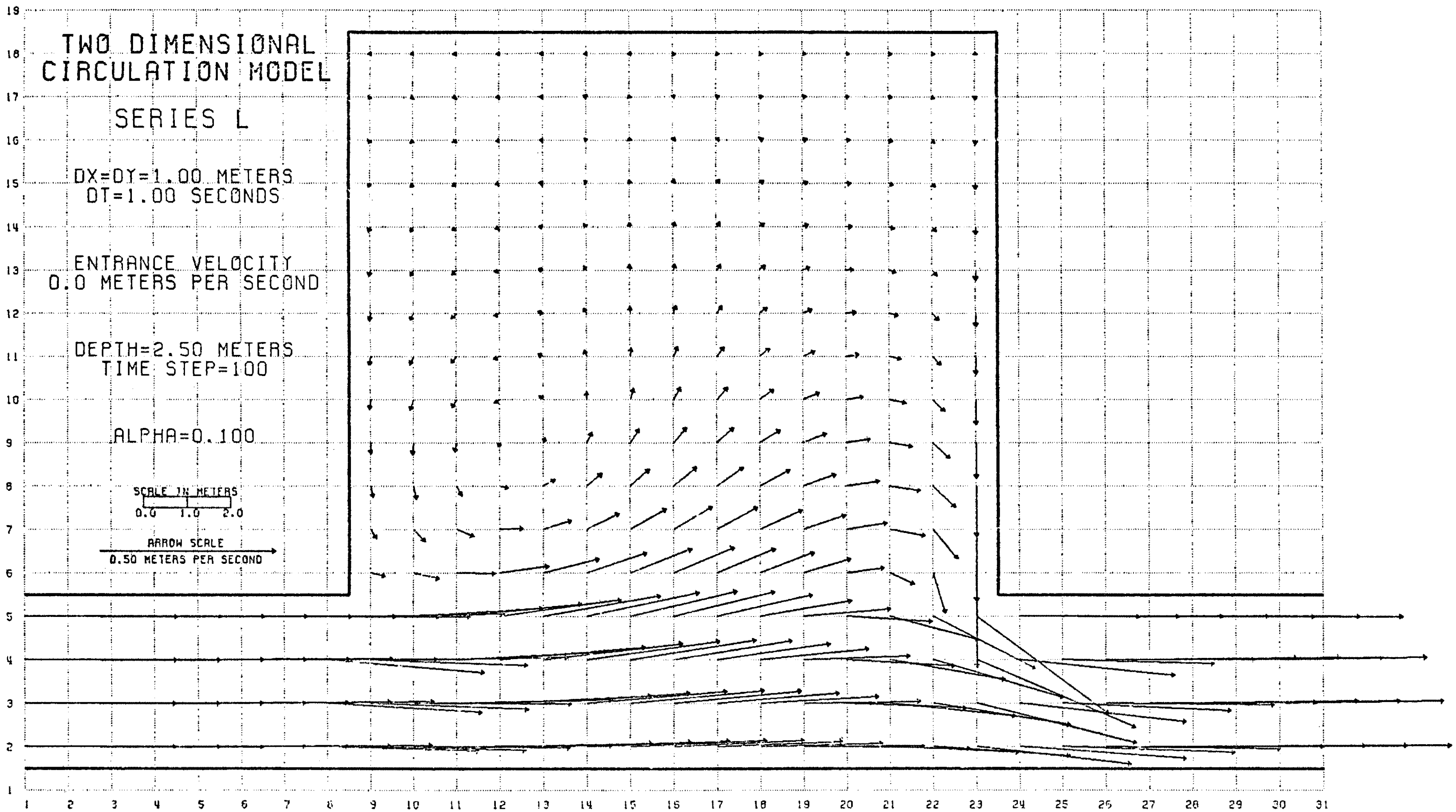

Figure 5.82. Slope-specified baseline: time step 100.

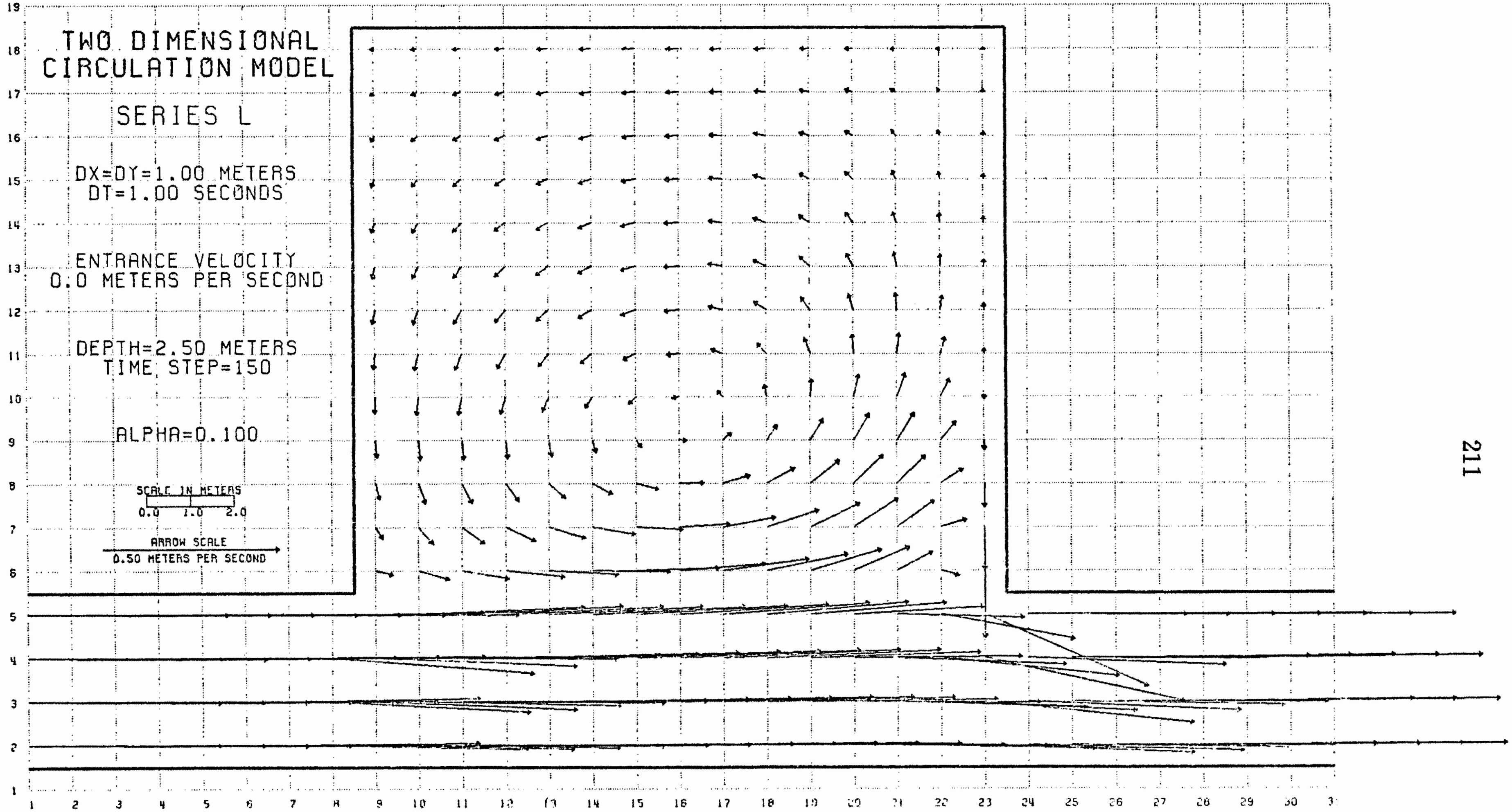

Figure 5.83. Slope-specified baseline: time step 150.

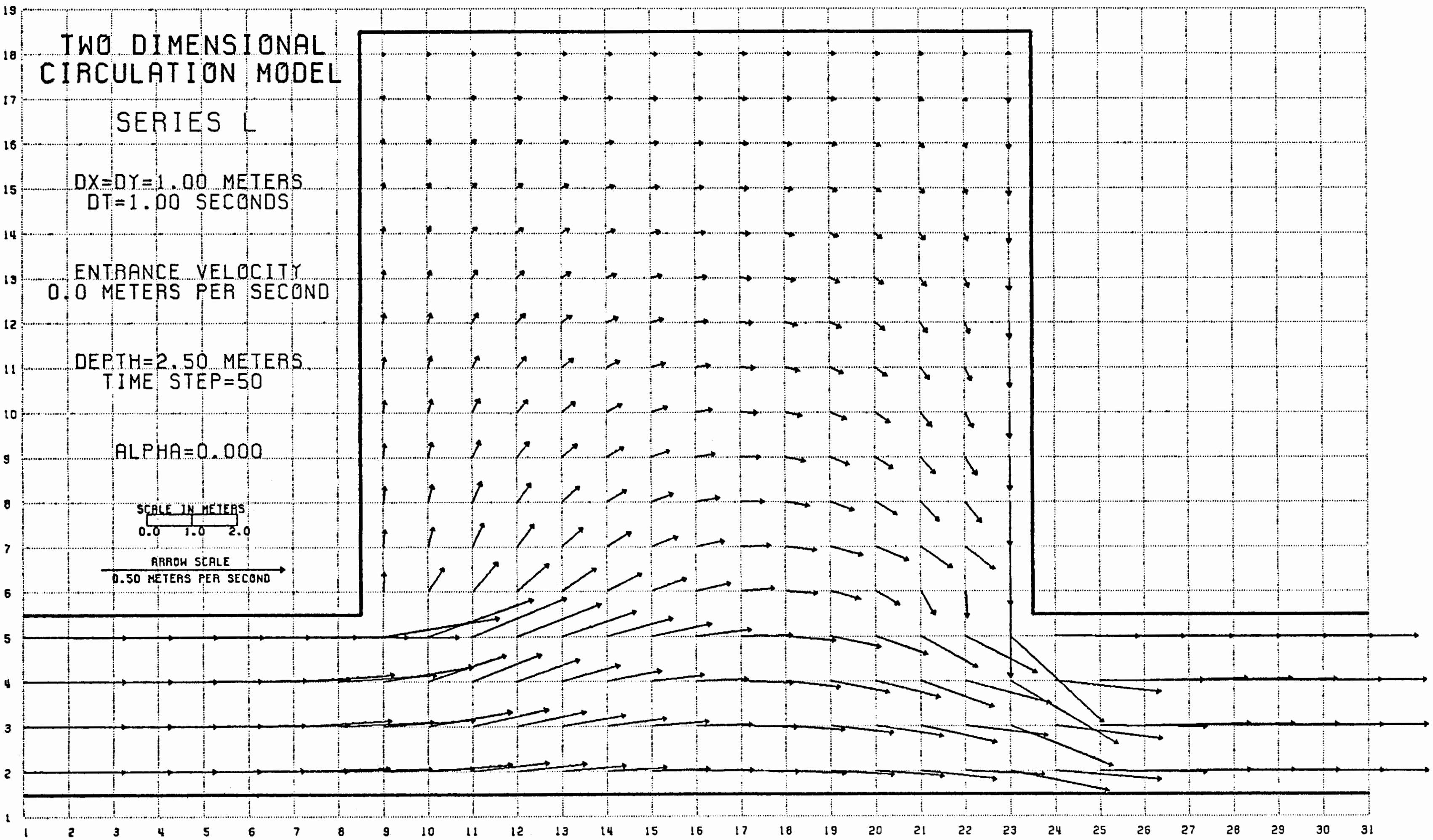

Figure 5.84. Omission of effective stresses: time step 50.

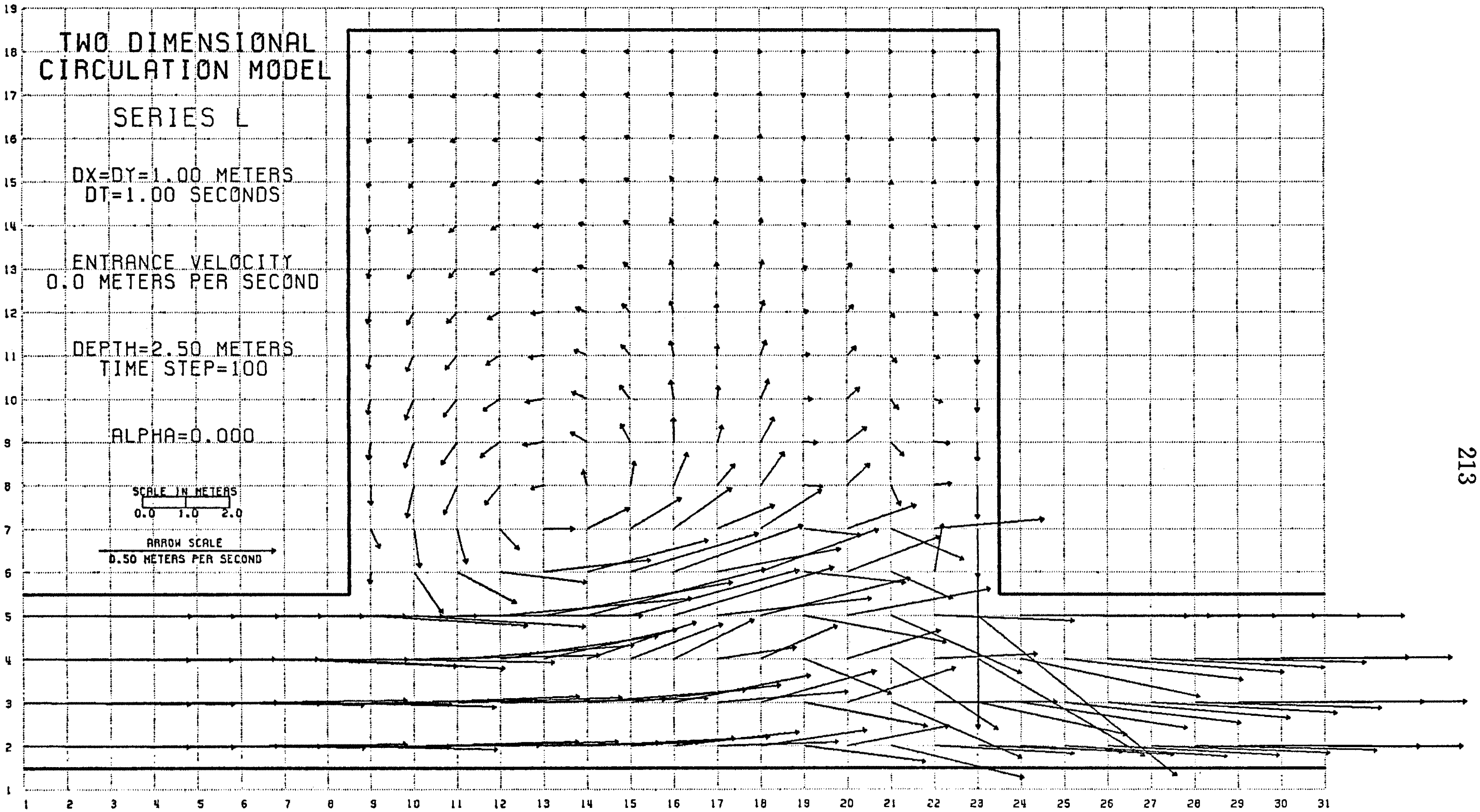

Figure 5.85. Omission of effective stresses: time step 100.

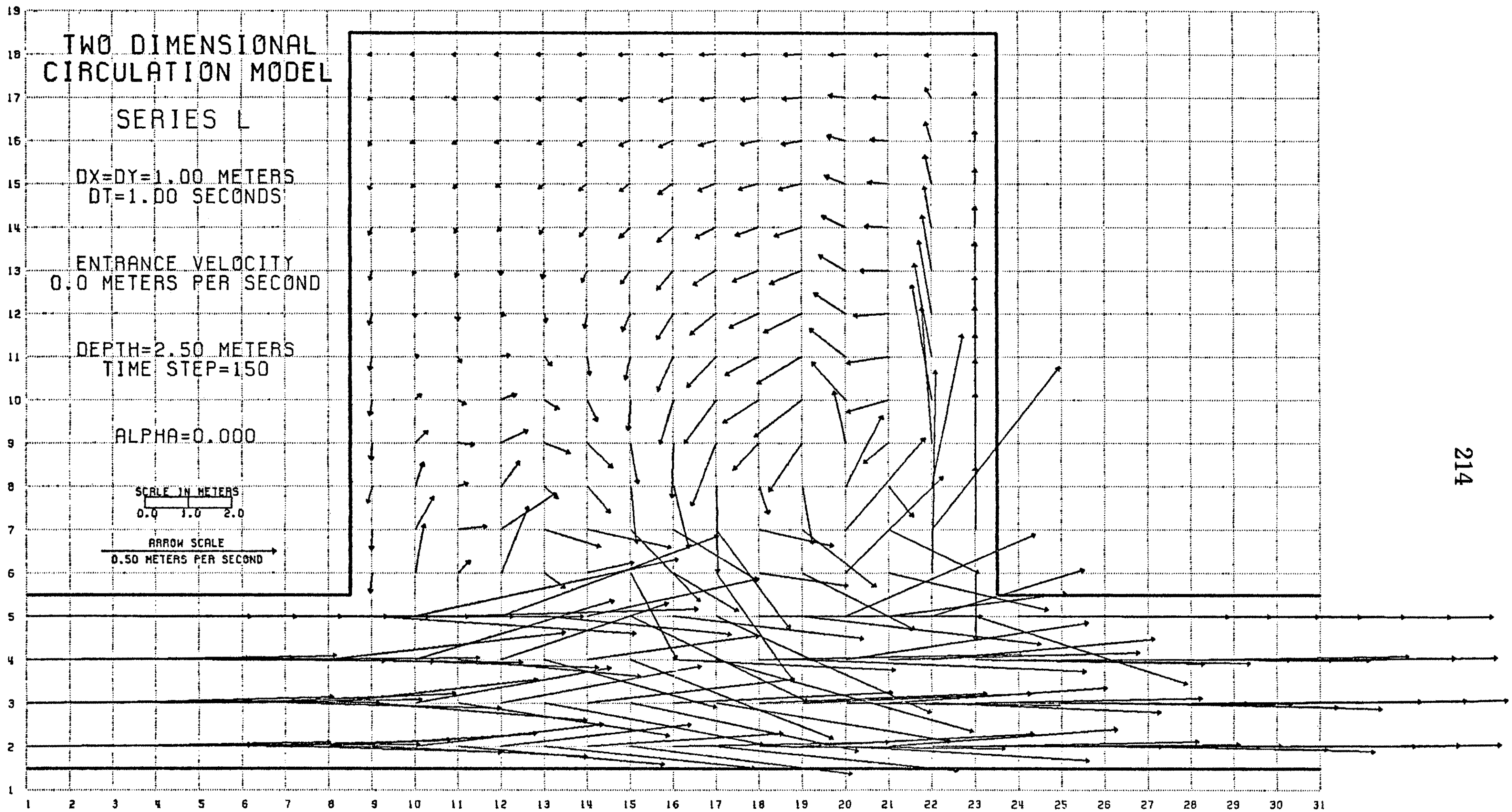

Figure 5.86. Omission of effective stresses: time step 150.

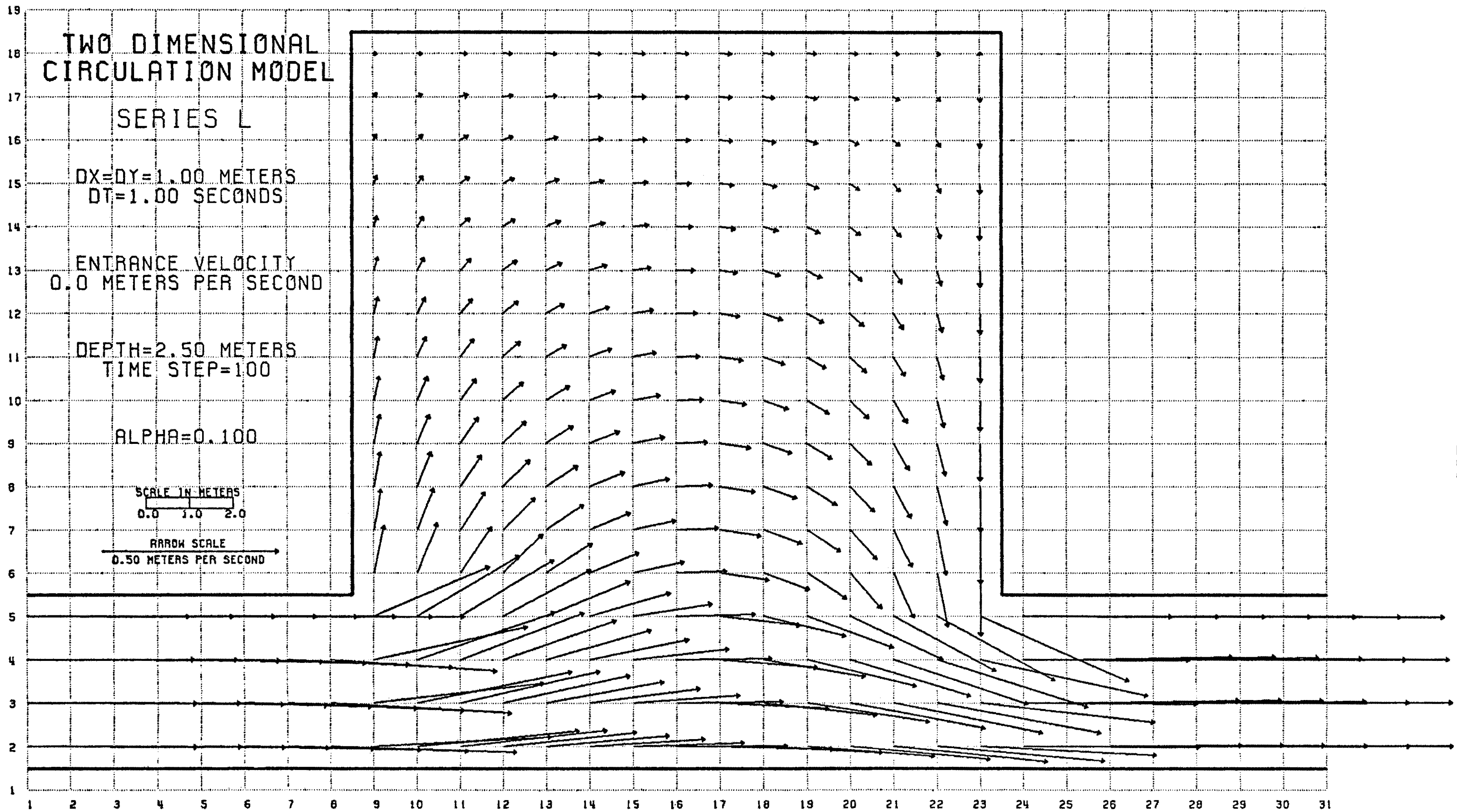

Figure 5.87. Omission of convective inertia: time step 100.

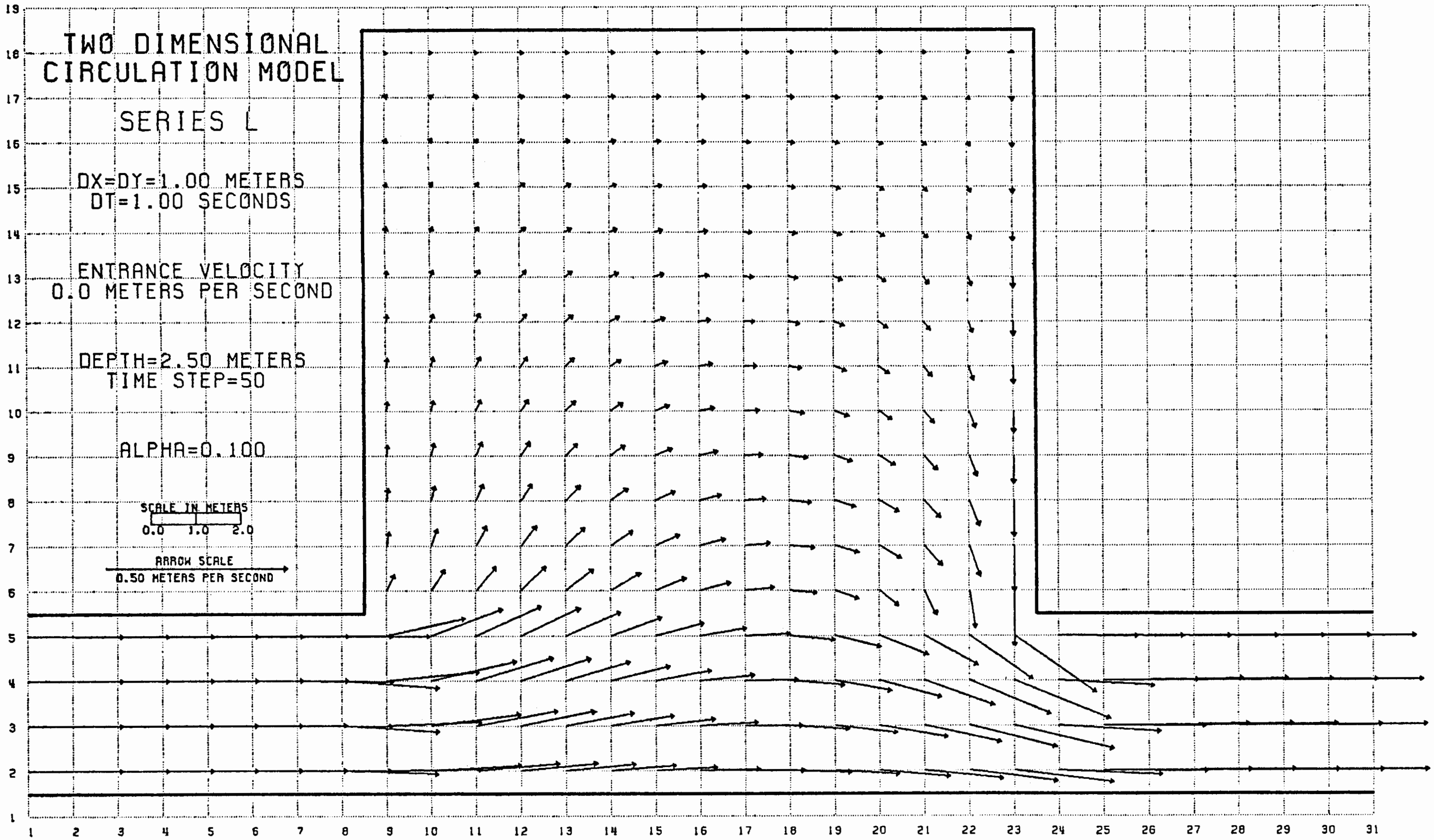

Figure 5.88. Omission of bed resistance: time step 50.

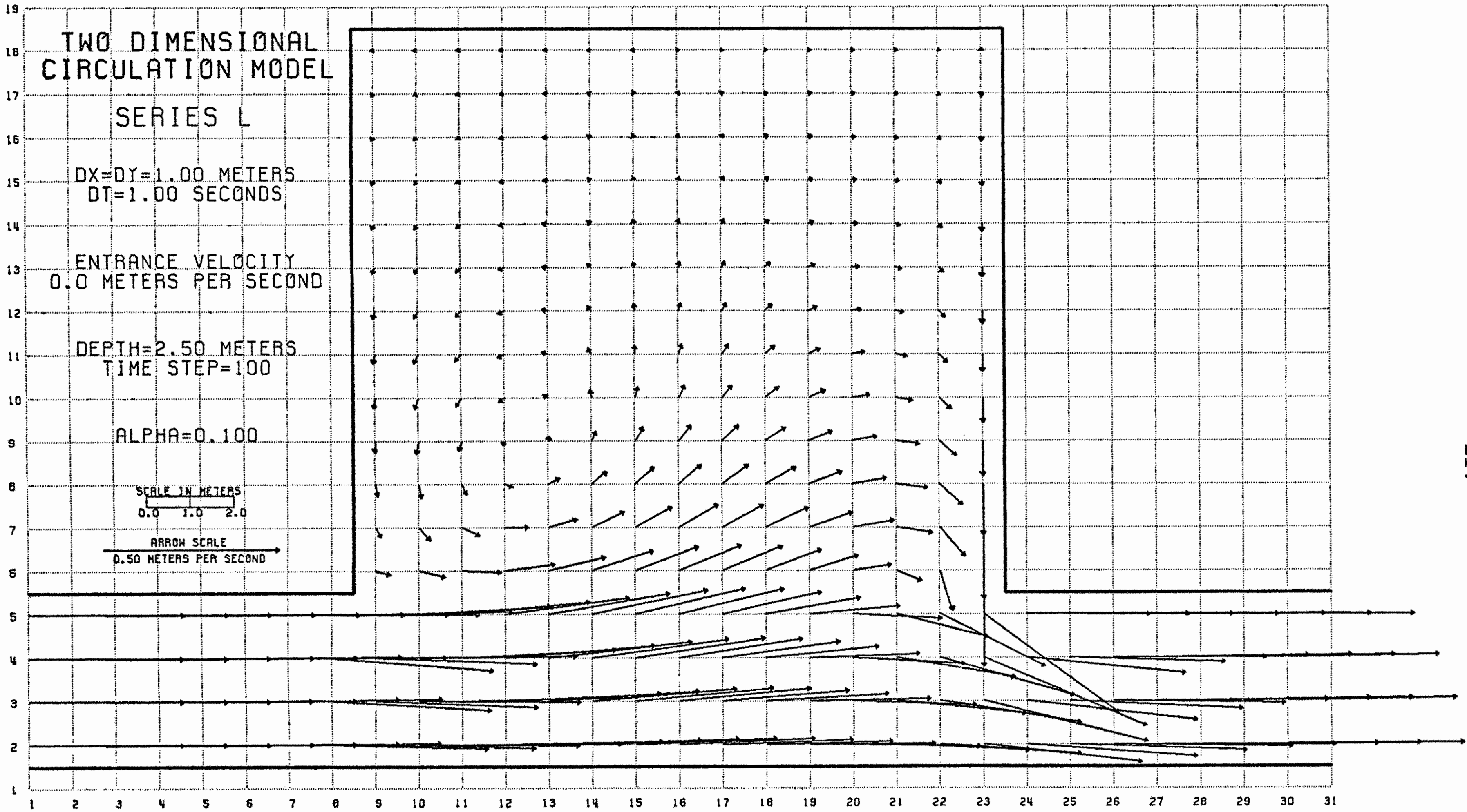

Figure 5.89. Omission of bed resistance: time step 100.

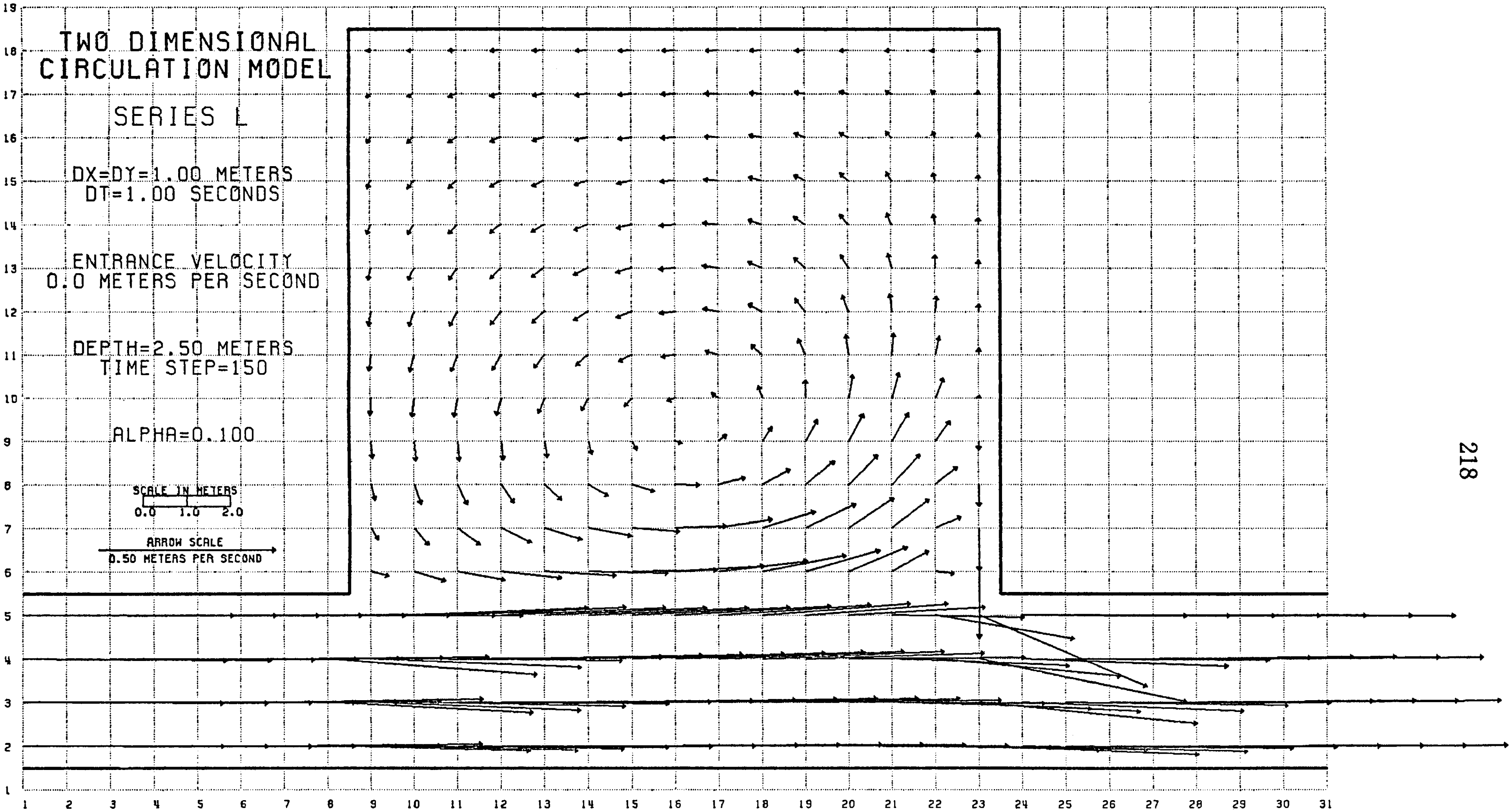

Figure 5.90. Omission of bed resistance: time step 150.

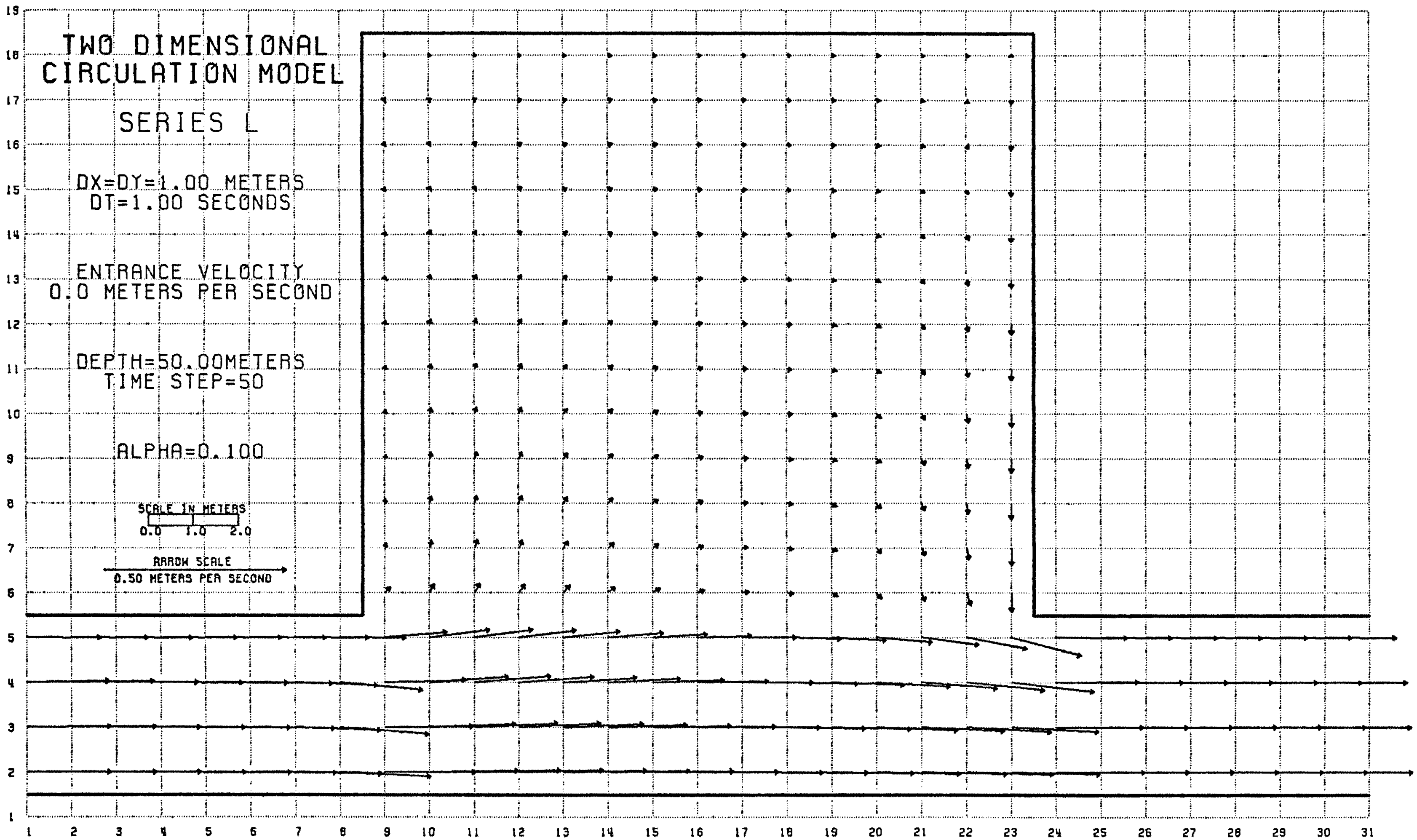

Figure 5.91. Depth, d = 50.0 meters: time step 50.

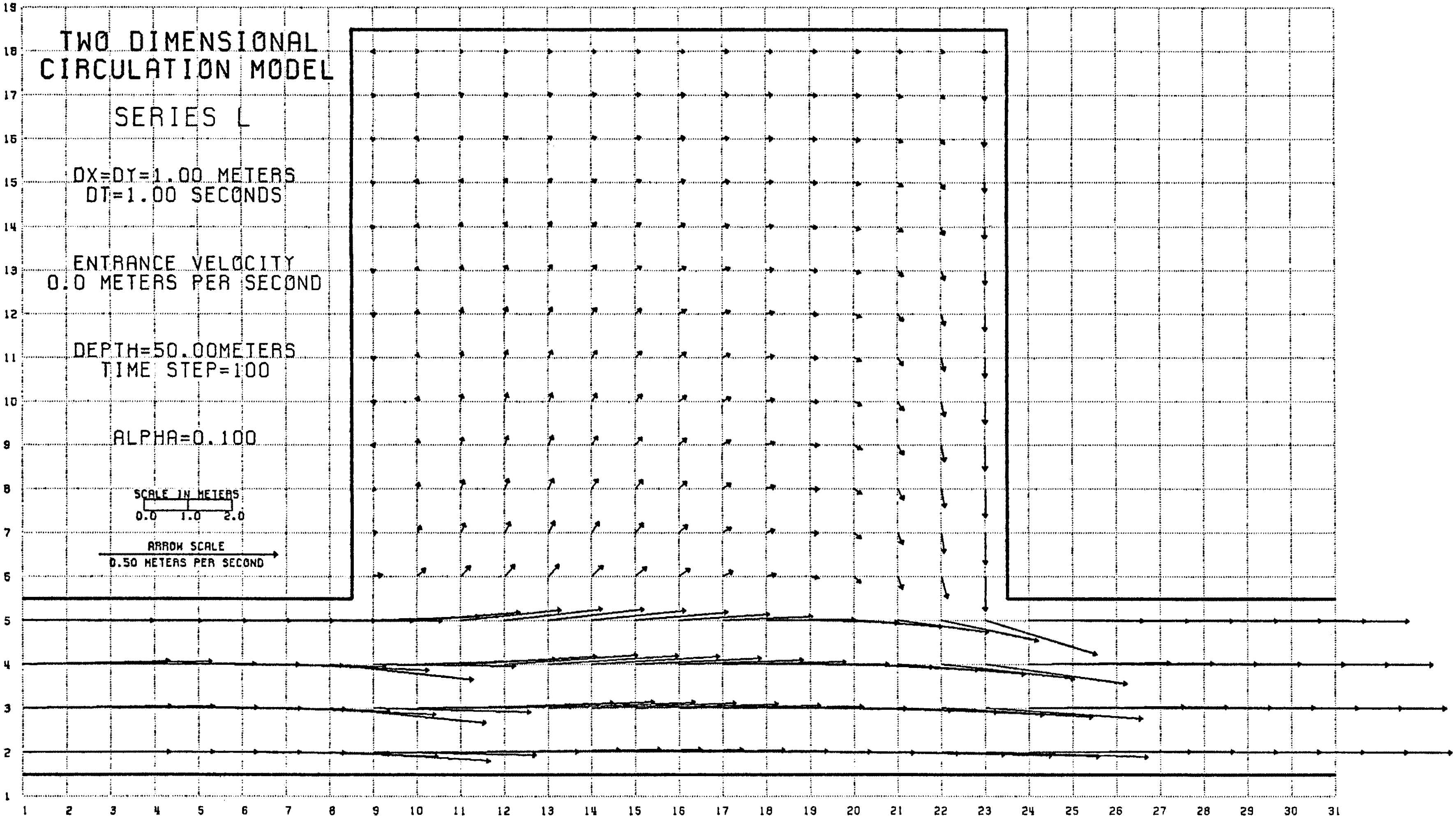

Figure 5.92. Depth, d = 50.0 meters: time step 100.

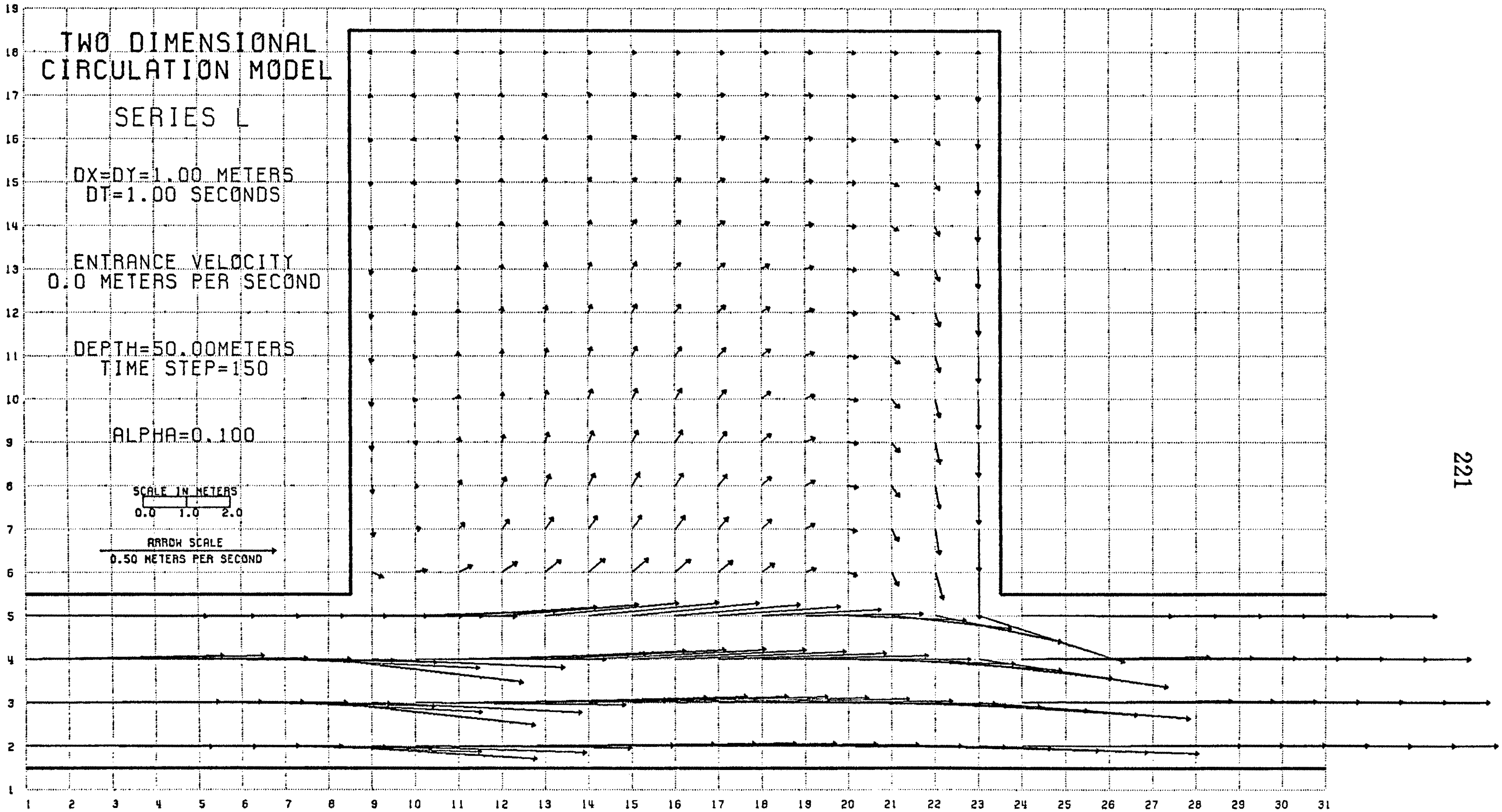

Figure 5.93. Depth, d = 50.0 meters: time step 150.

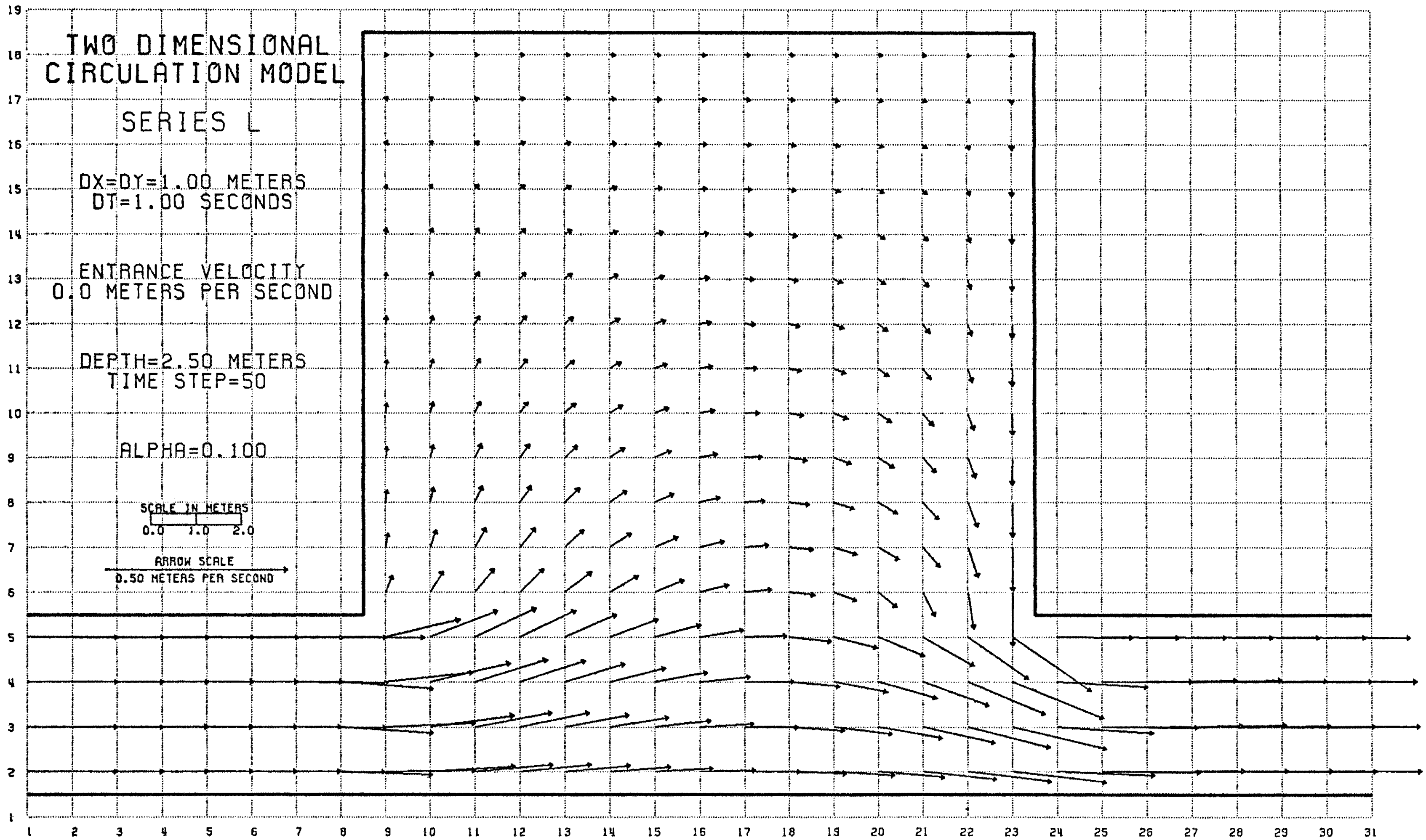

Figure 5.94. Friction factor, f_r = 0.04: time step 50.

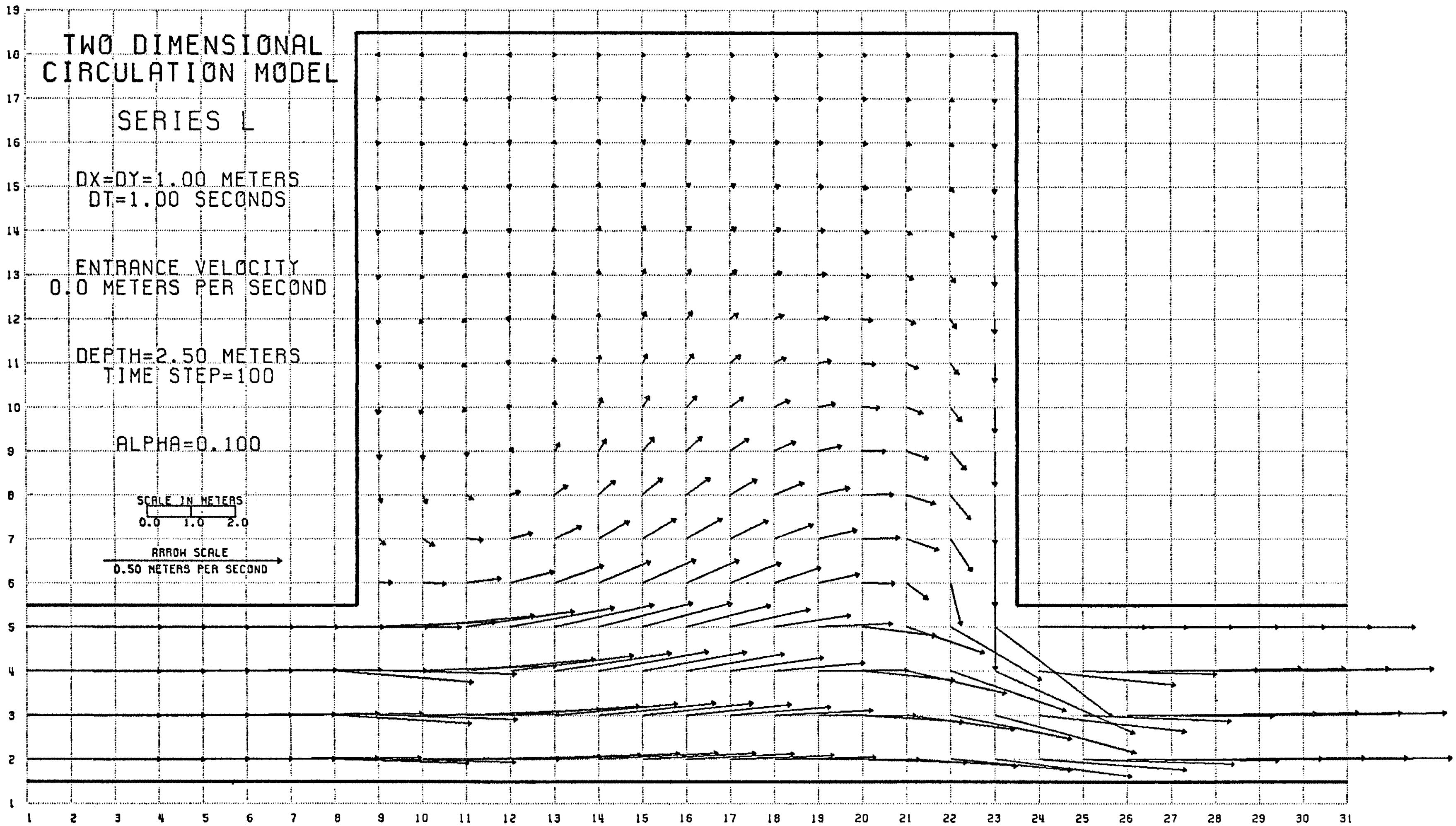

Figure 5.95. Friction factor, f_r = 0.04: time step 100.

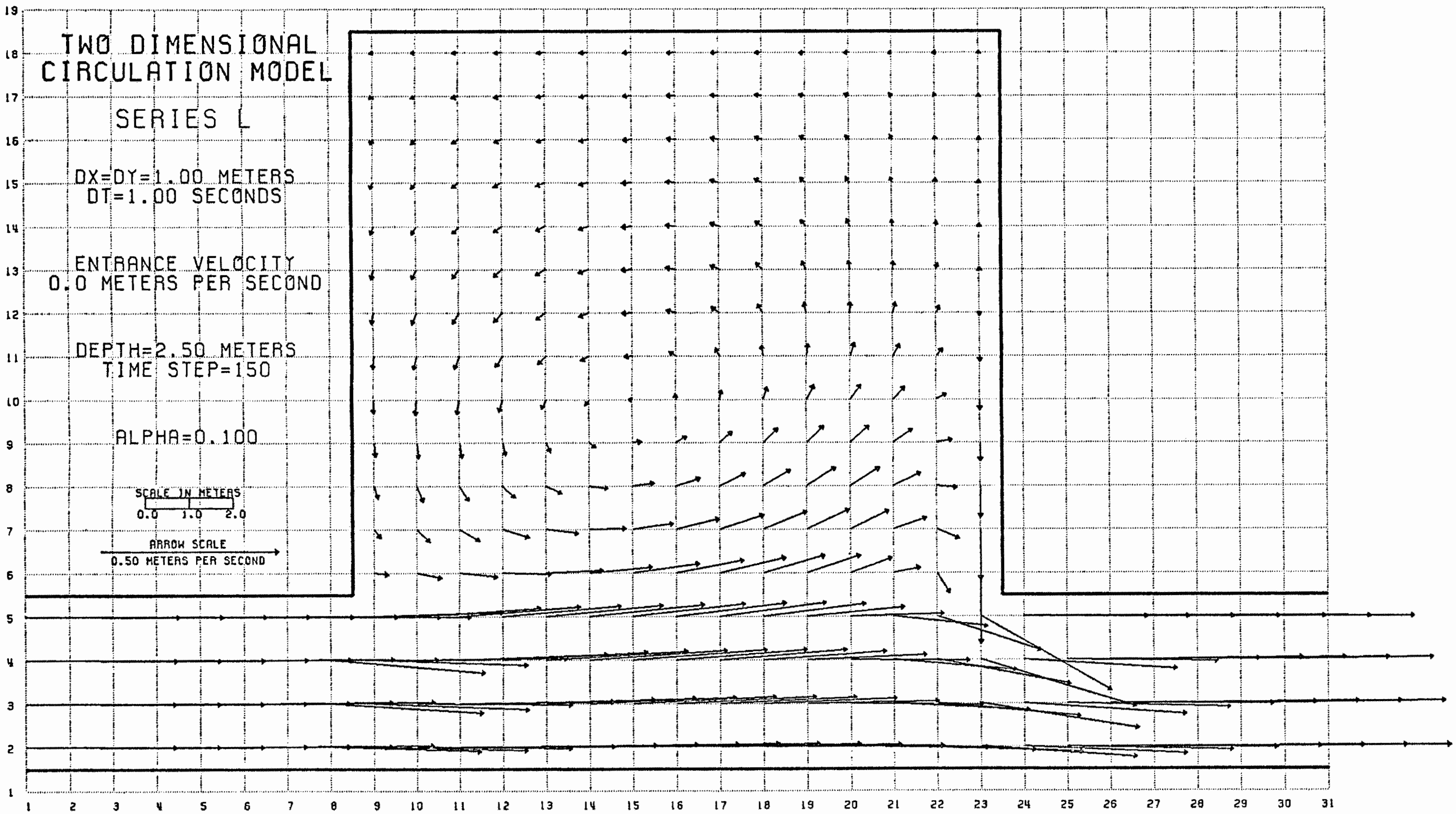

Figure 5.96. Friction factor, f_r = 0.04: time step 150.

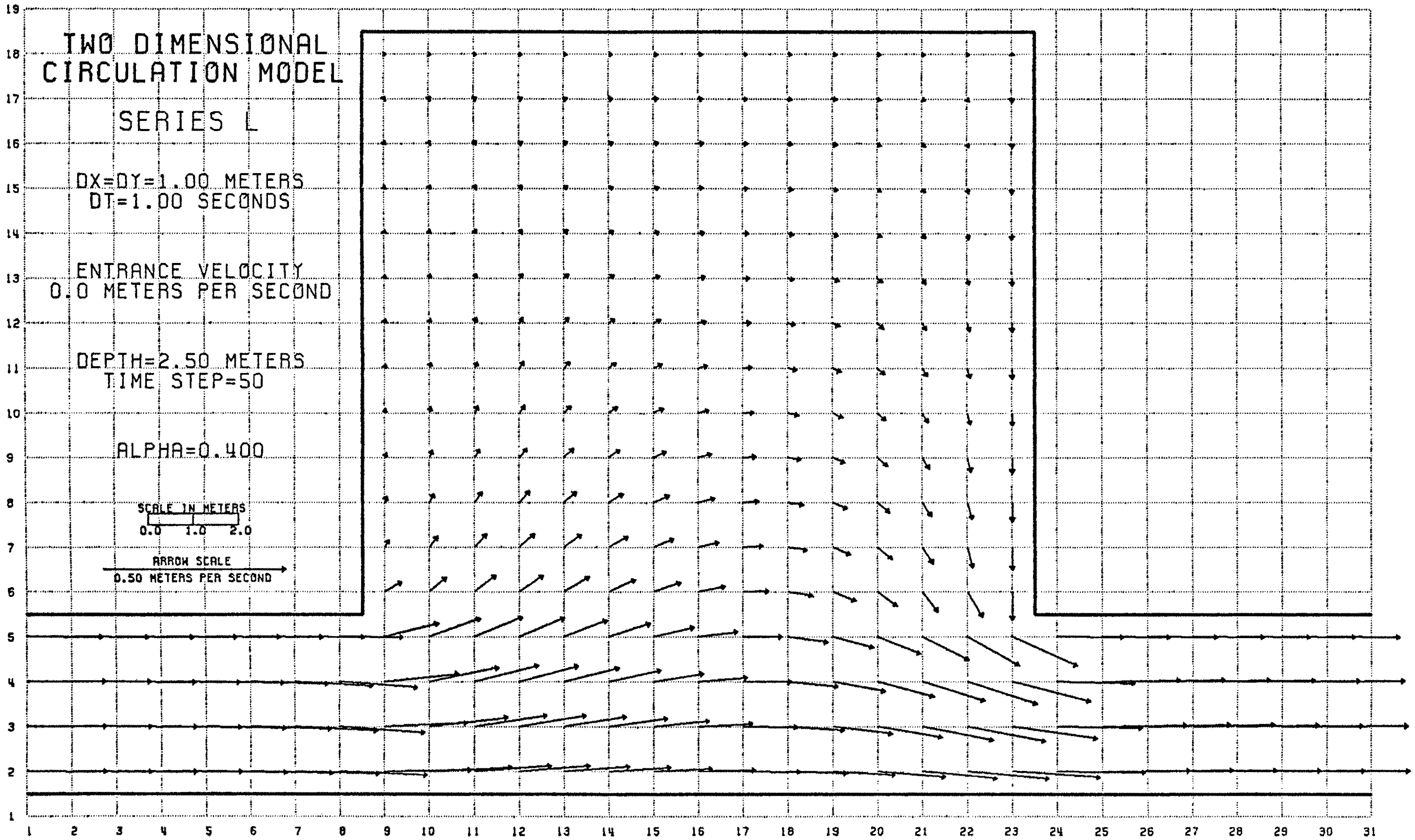

Figure 5.97. Weighting factor, $\alpha = 0.4$: time step 50.

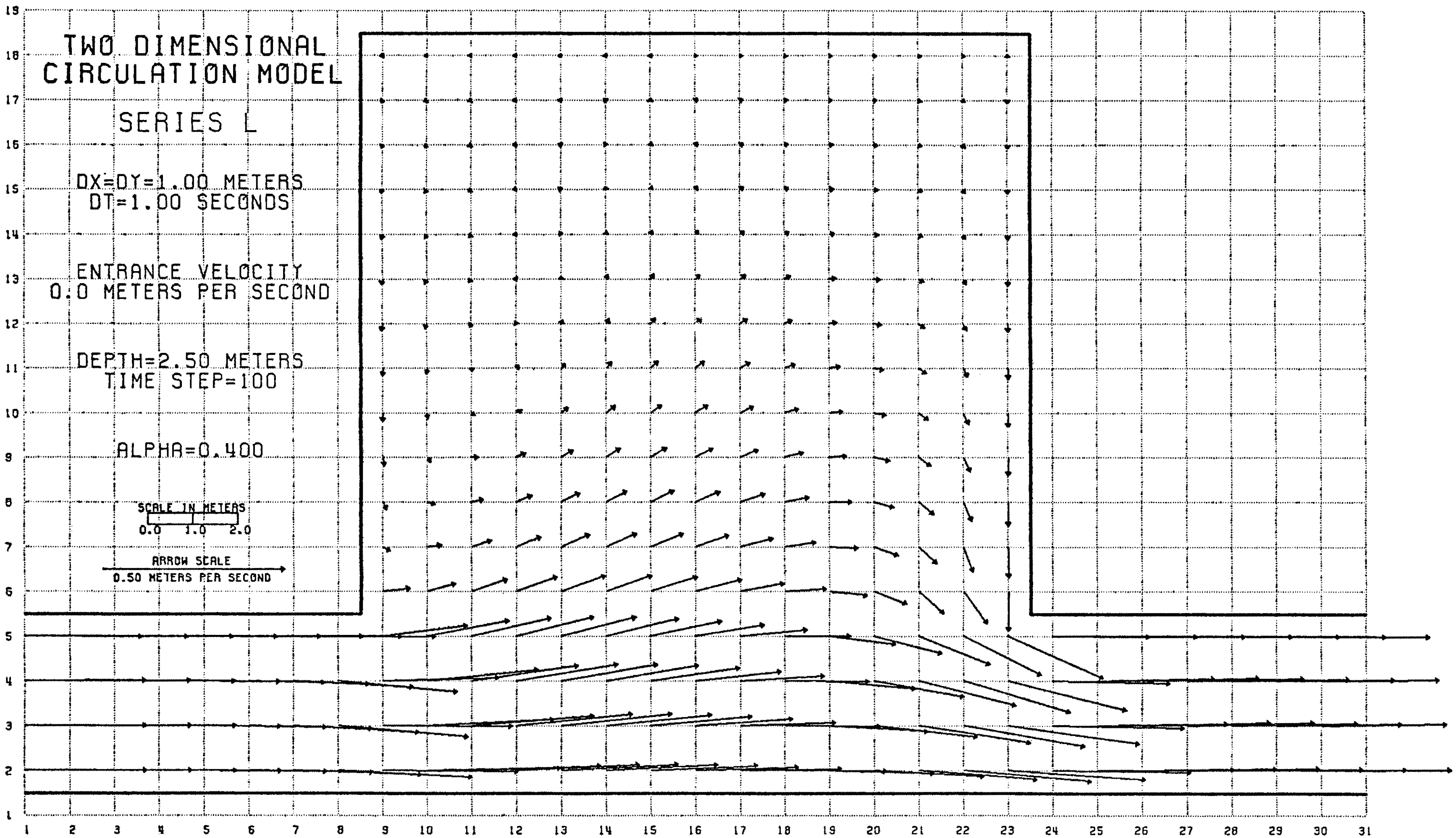

Figure 5.98. Weighting factor, α = 0.4: time step 100.

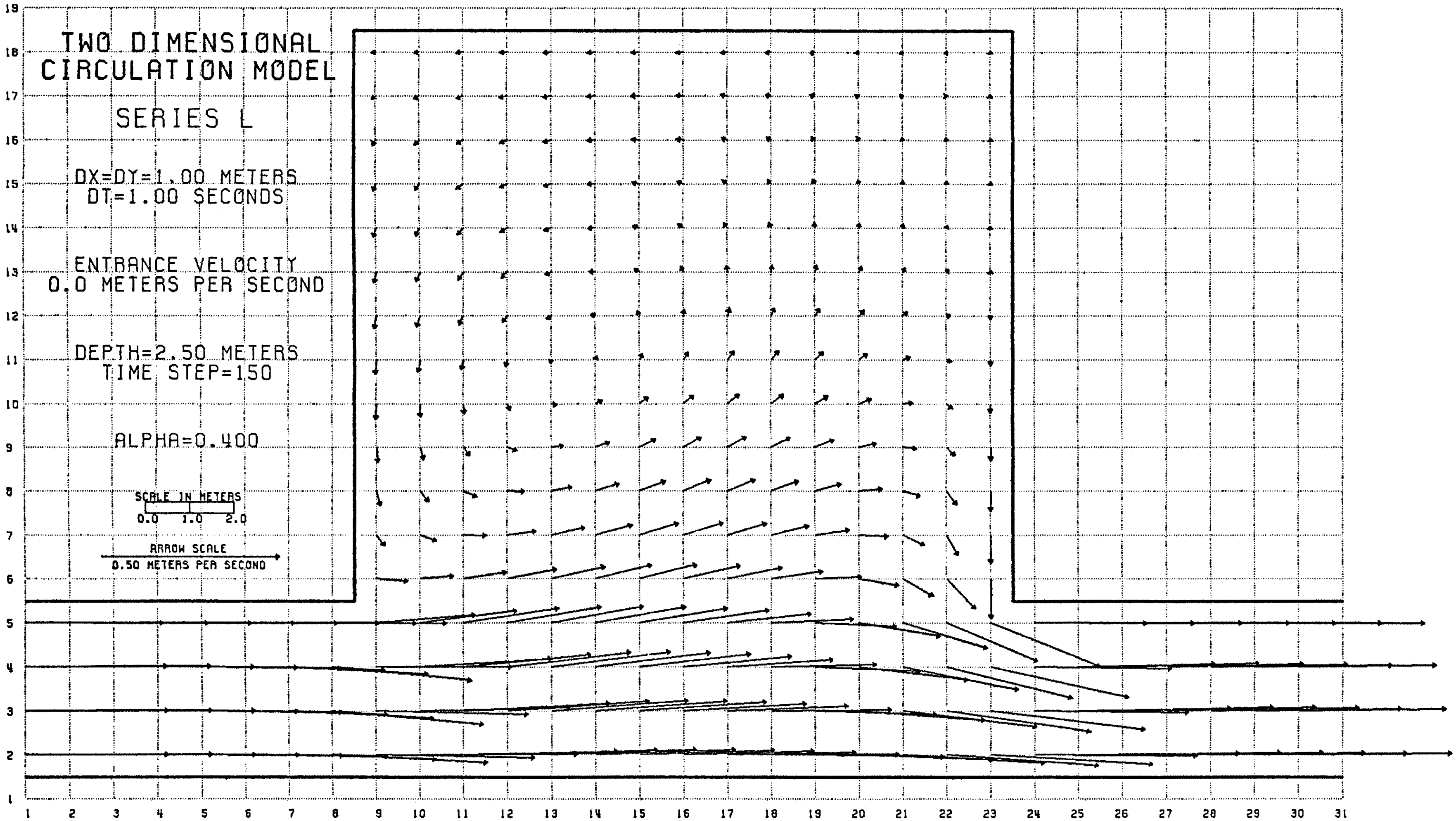

Figure 5.99. Weighting factor, $\alpha = 0.4$: time step 150.

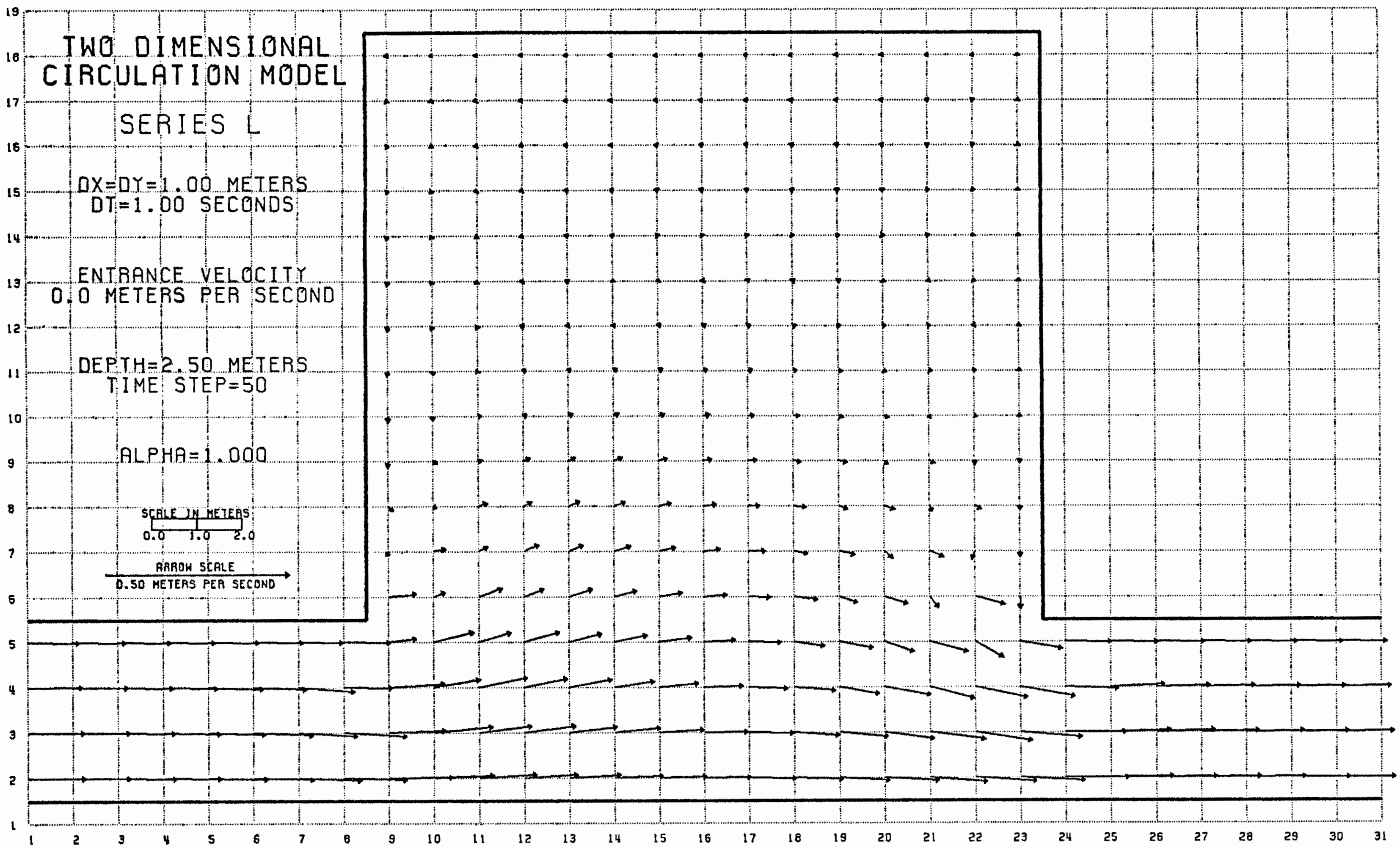

Figure 5.100. Weighting factor, α = 1.0: time step 50.

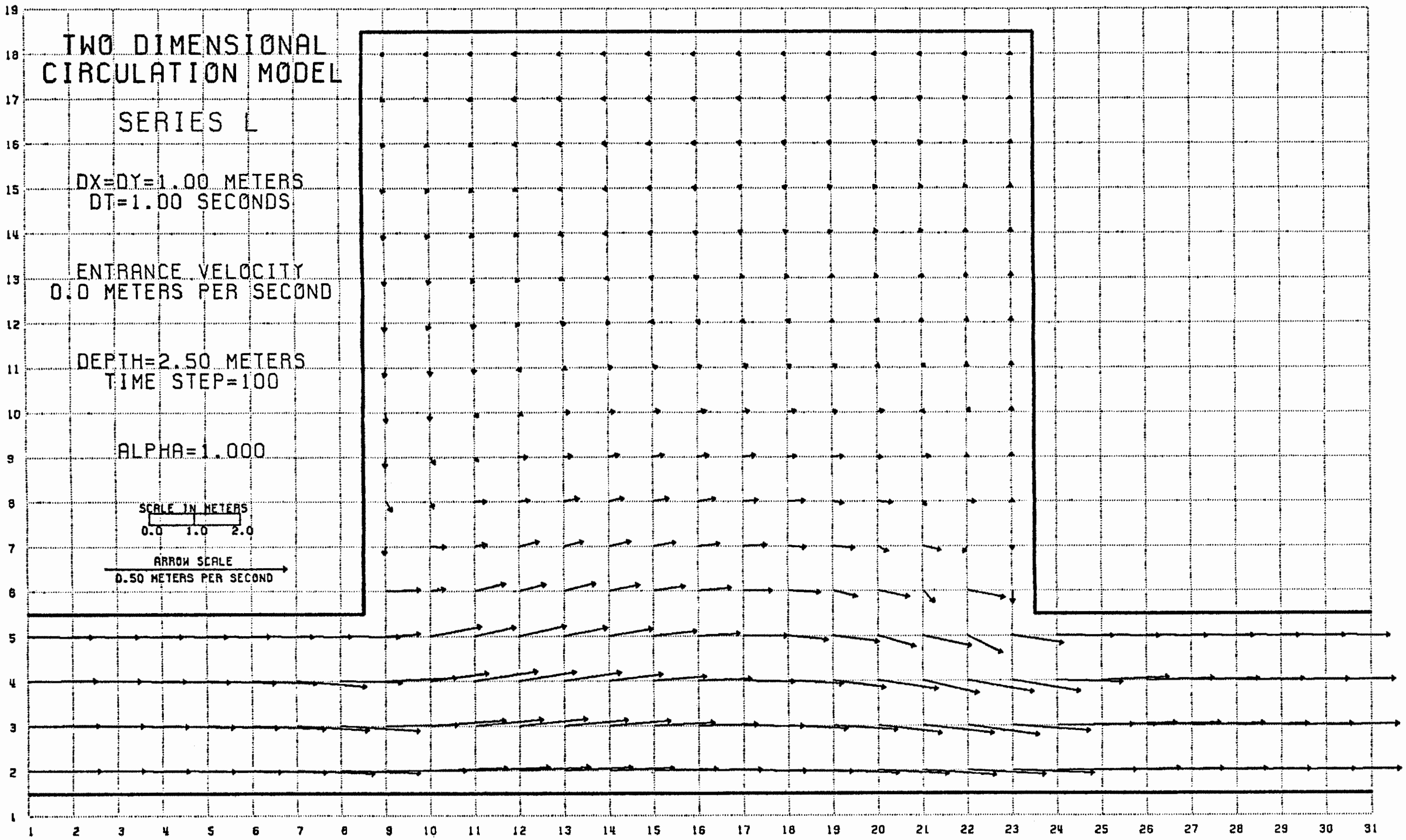

Figure 5.101. Weighting factor, α = 1.0: time step 100.

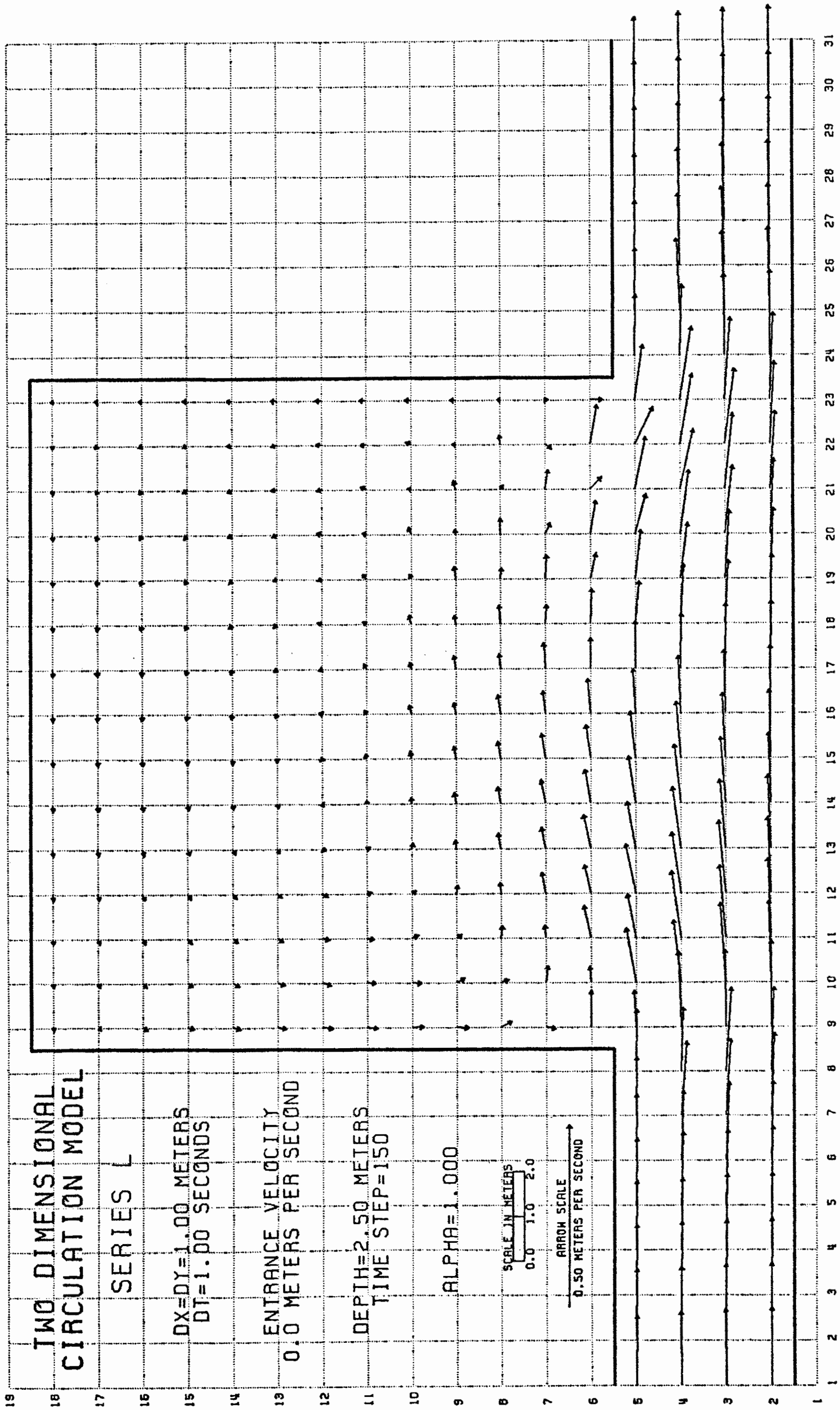

Figure 5.102. Weighting factor, α = 1.0: time step 150.

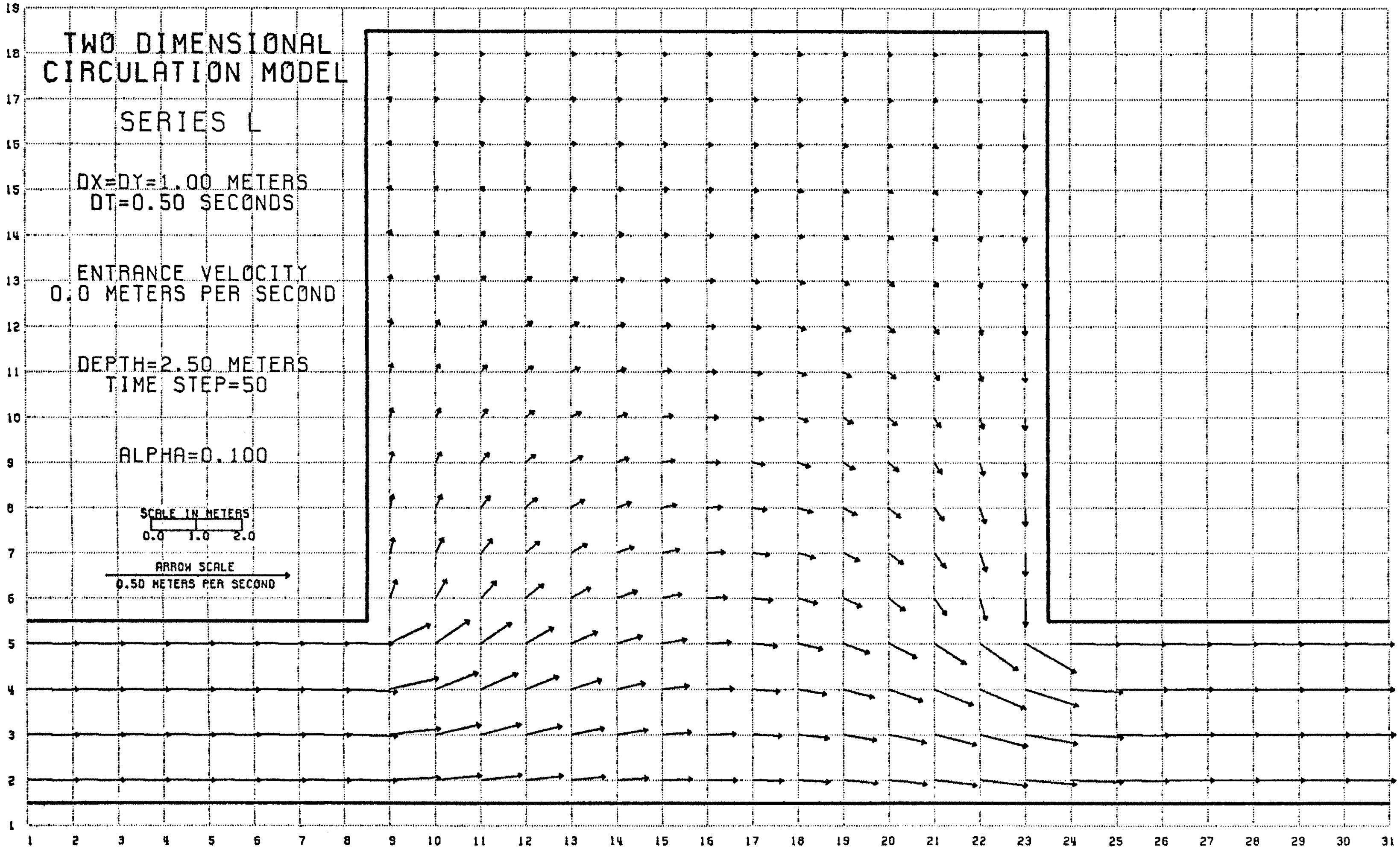

Figure 5.103. Time increment, Δt = 0.5 seconds: time step 50.

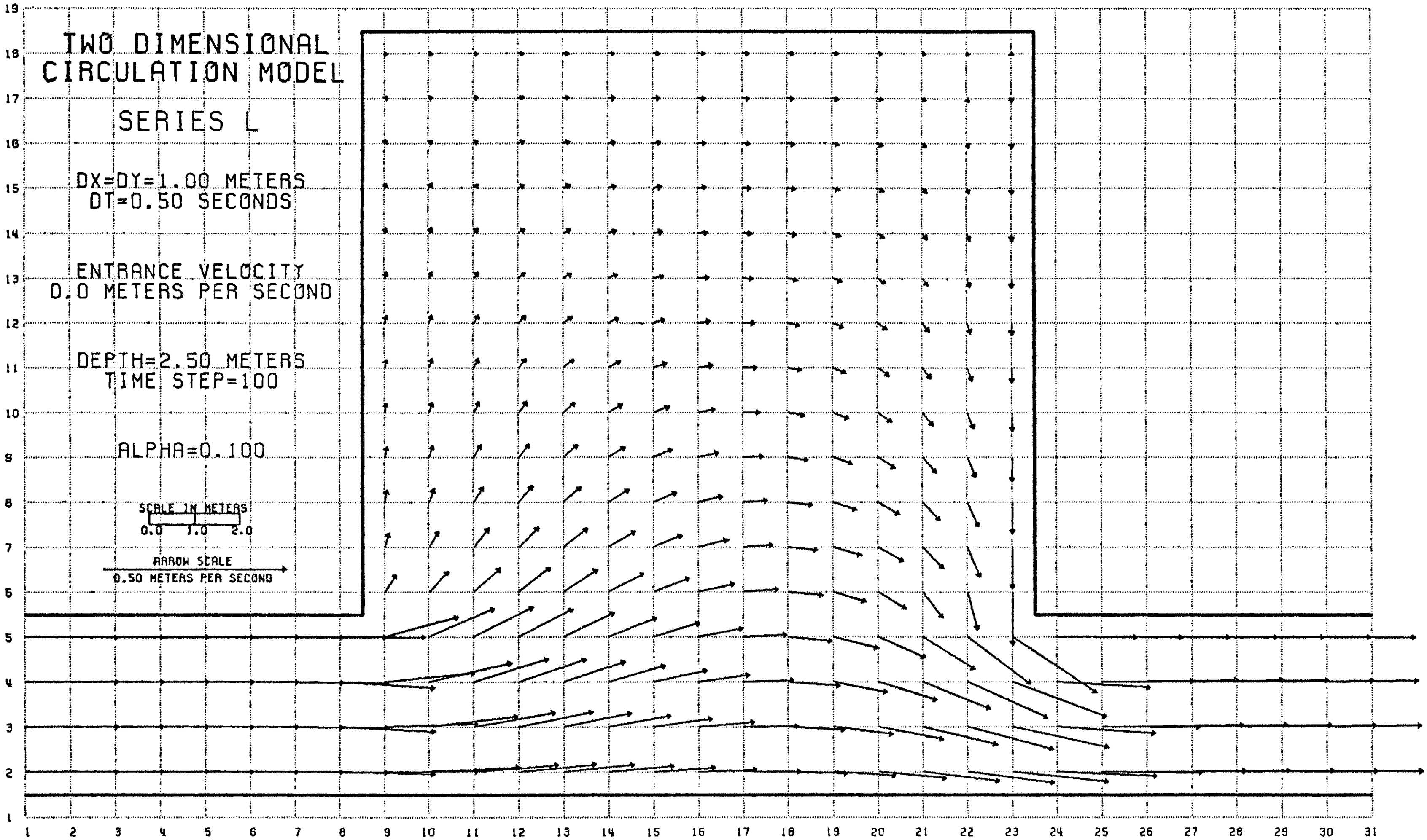

Figure 5.104. Time increment, Δt = 0.5 seconds: time step 100.

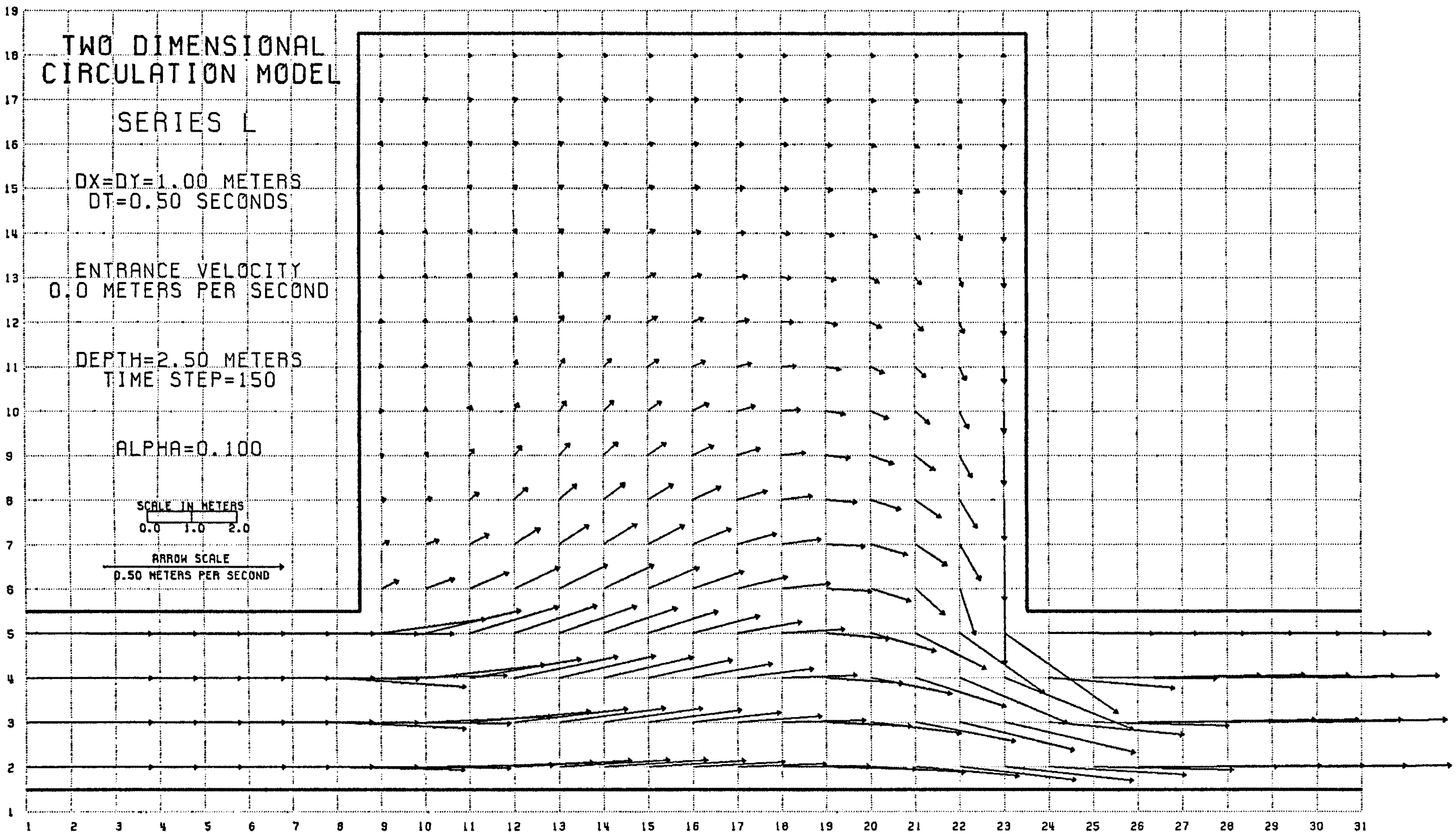

Figure 5.105. Time increment, Δt = 0.5 seconds: time step 150.

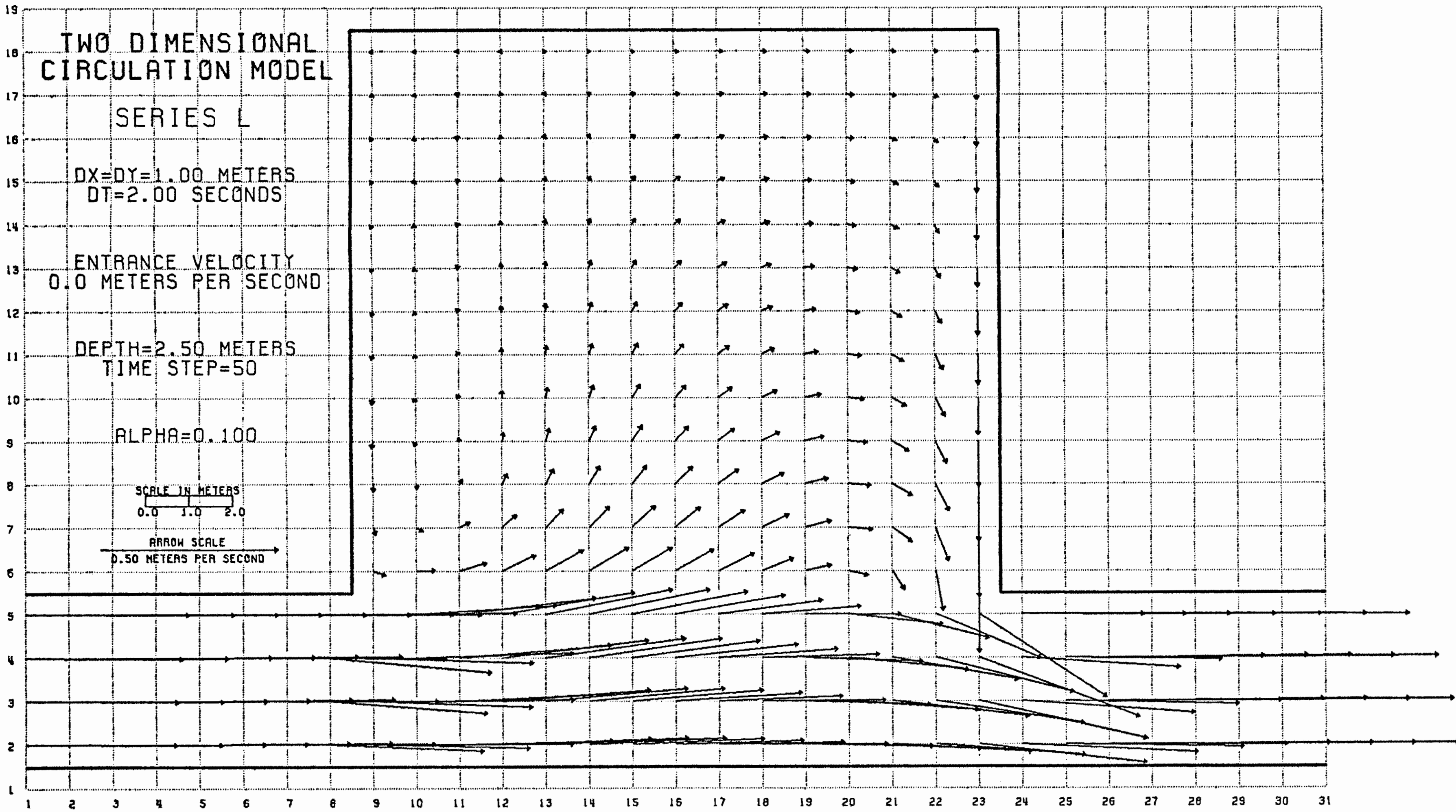

Figure 5.106. Time increment, Δt = 2.0 seconds: time step 50.

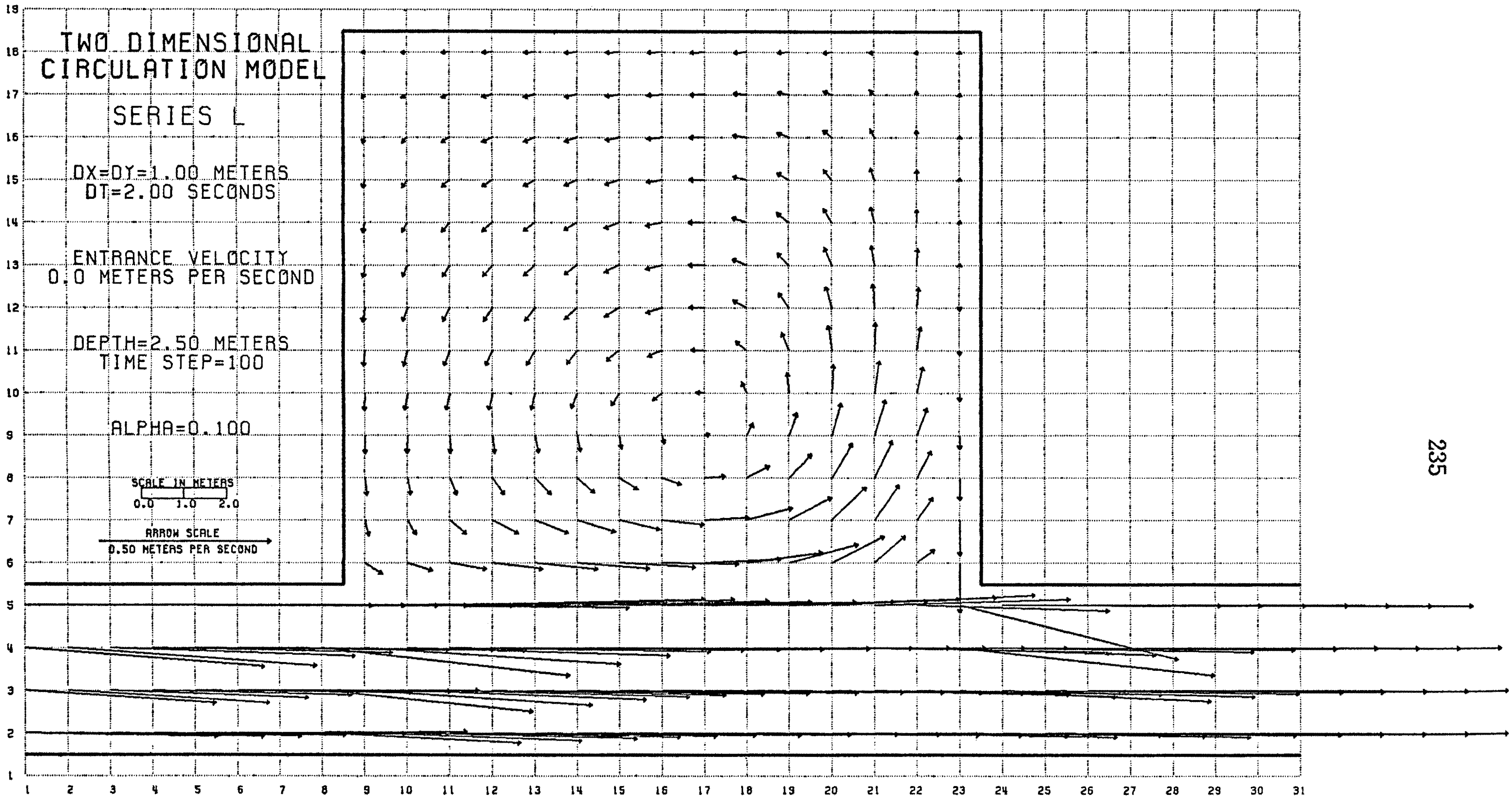

Figure 5.107. Time increment, Δt = 2.0 seconds: time step 100.

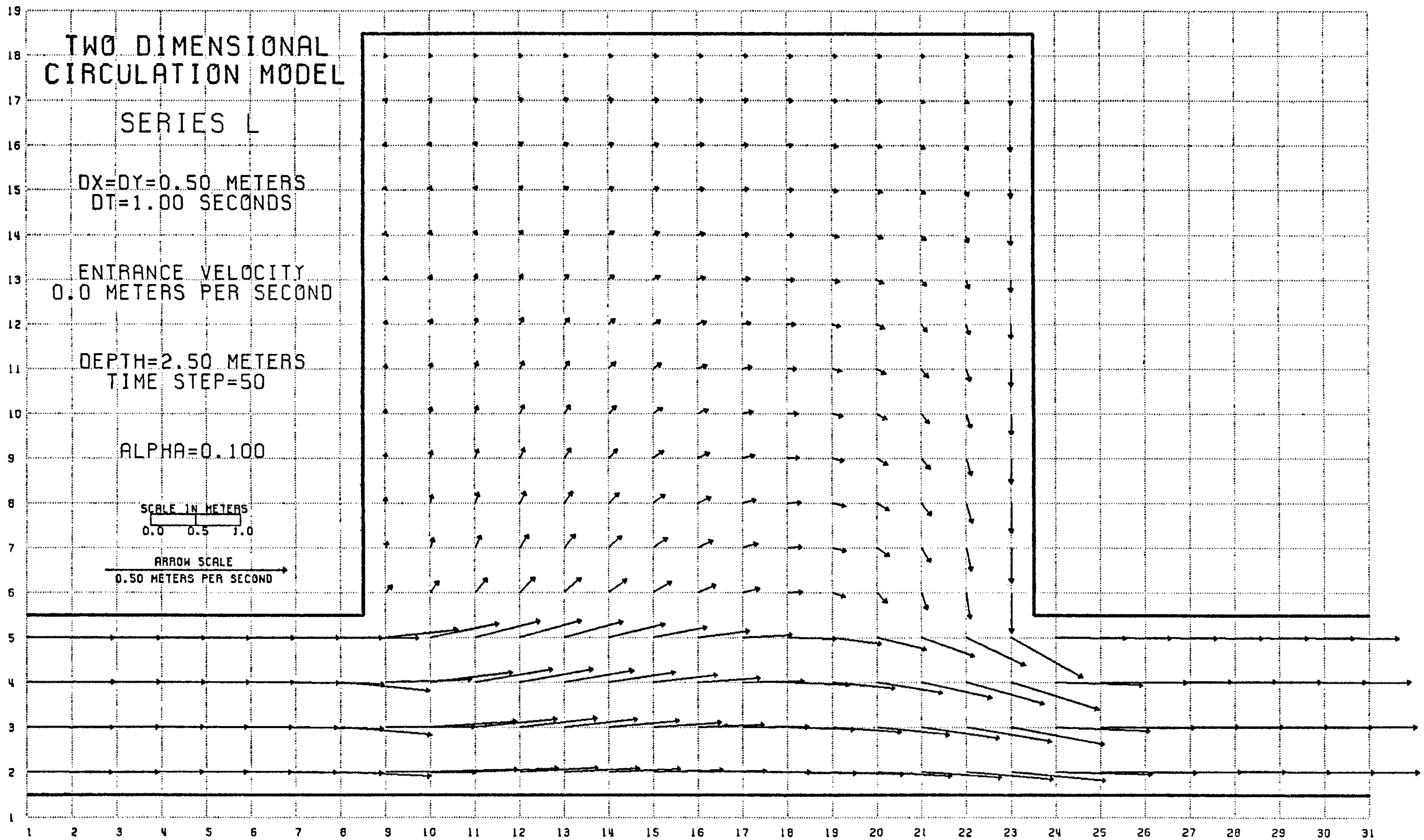

Figure 5.108. Space increment, $\Delta x = \Delta y = 0.5$ meters: time step 50.

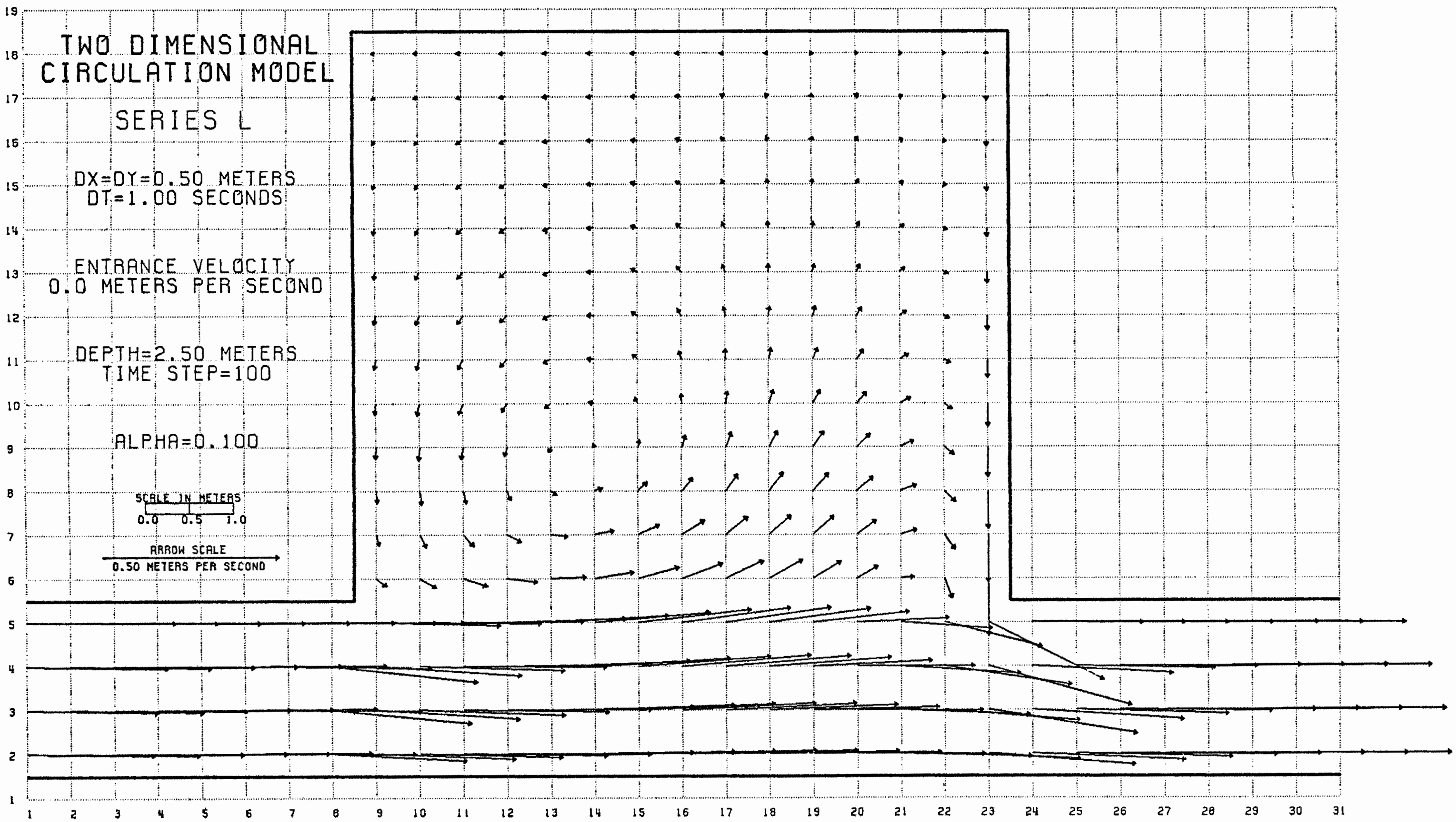

Figure 5.109. Space increment, $\Delta x = \Delta y = 0.5$ meters: time step 100.

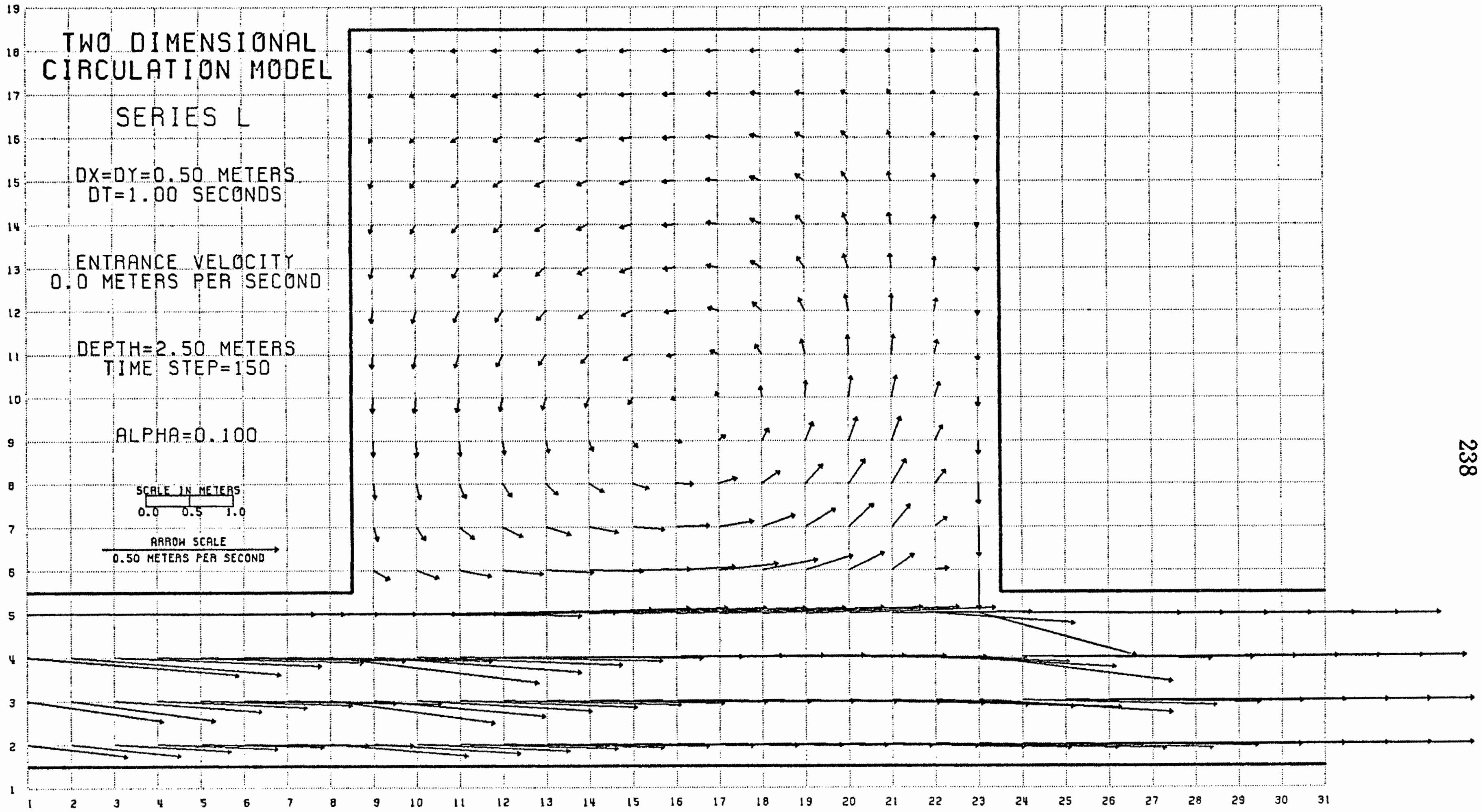

Figure 5.110. Space increment, Δx = Δy = 0.5 meters: time step 150.

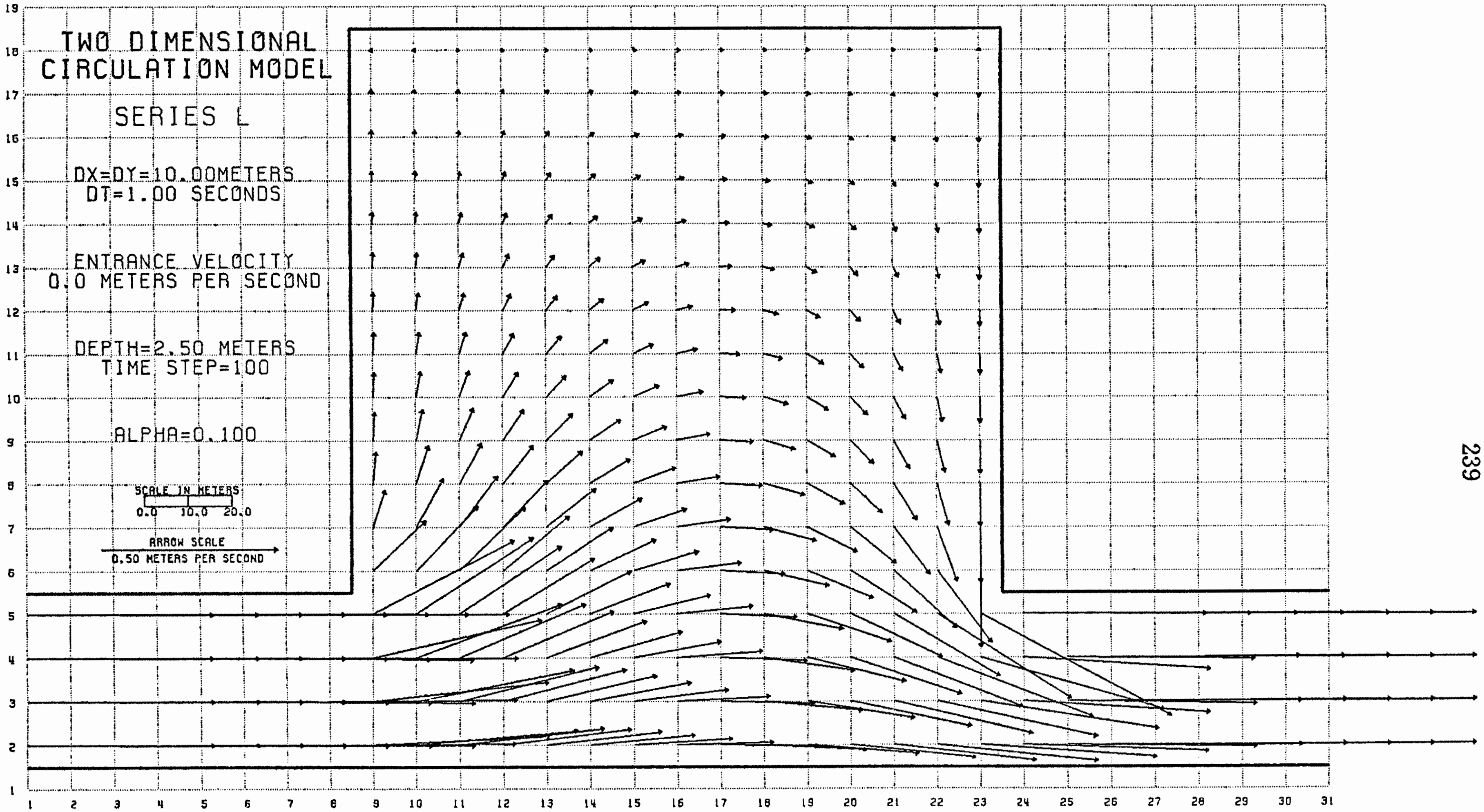

Figure 5.111. Space increment, $\Delta x = \Delta y = 10.0$ meters: time step 100.

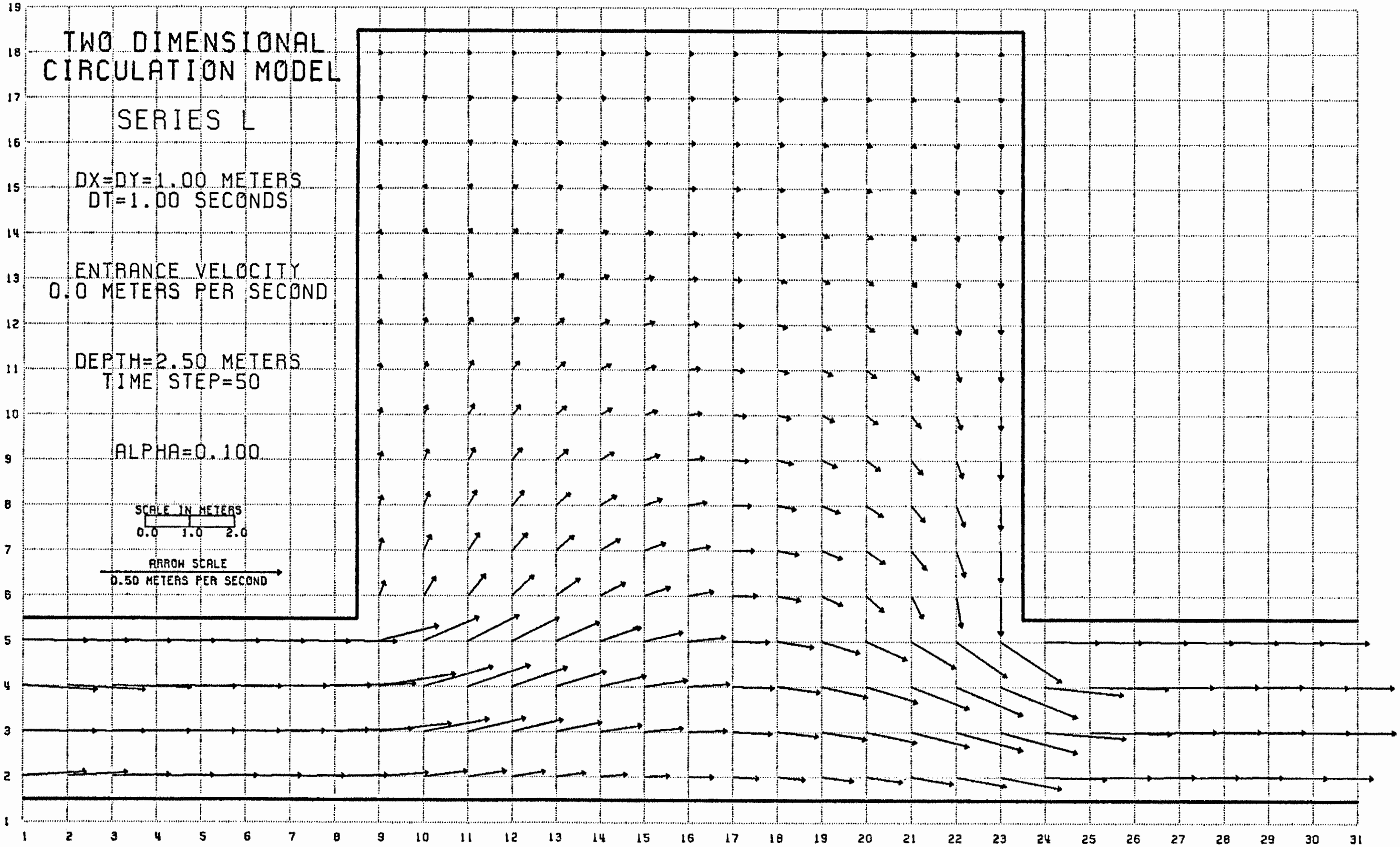

Figure 5.112. No slip condition at the wall: time step 50.

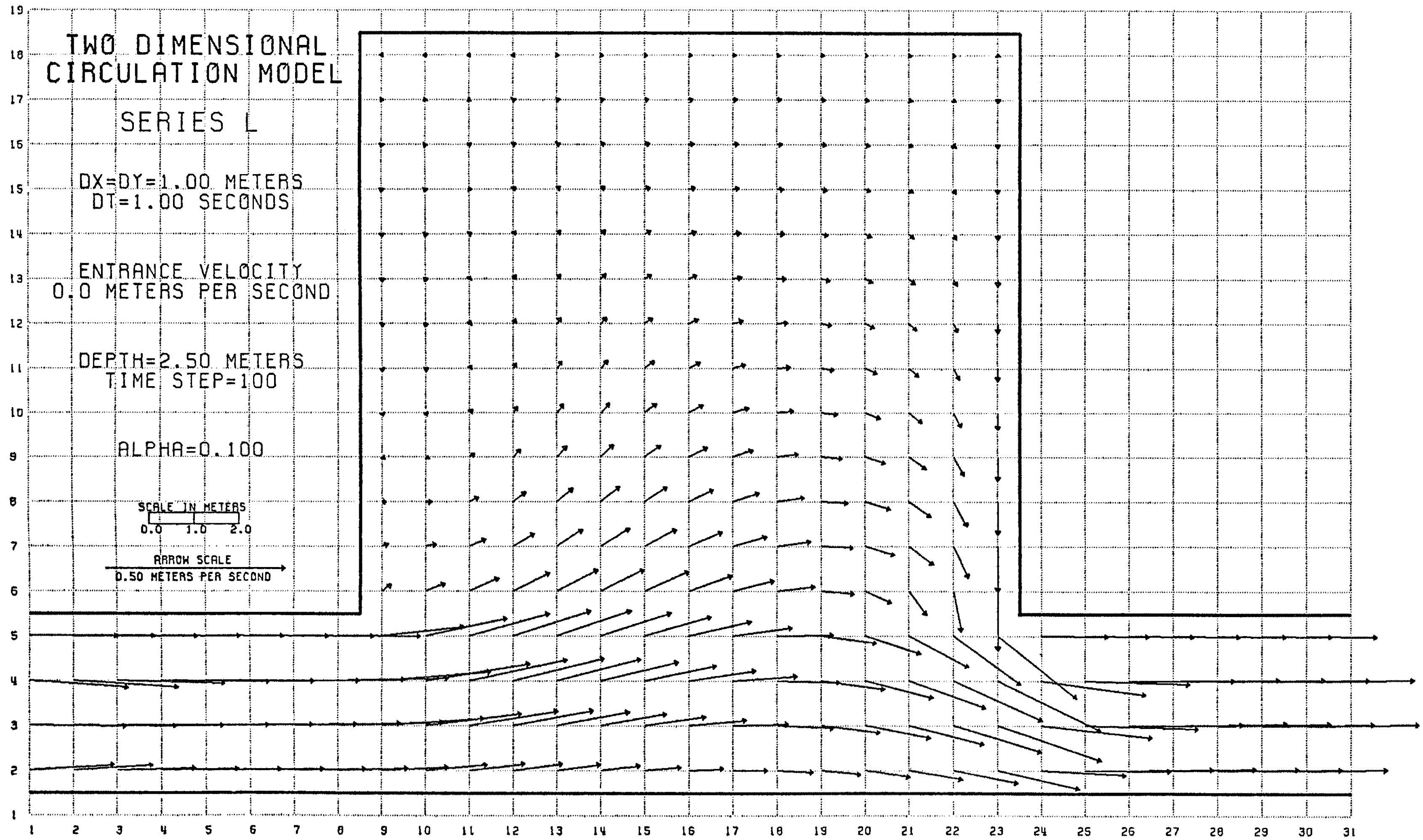

Figure 5.113. No slip condition at the wall: time step 100.

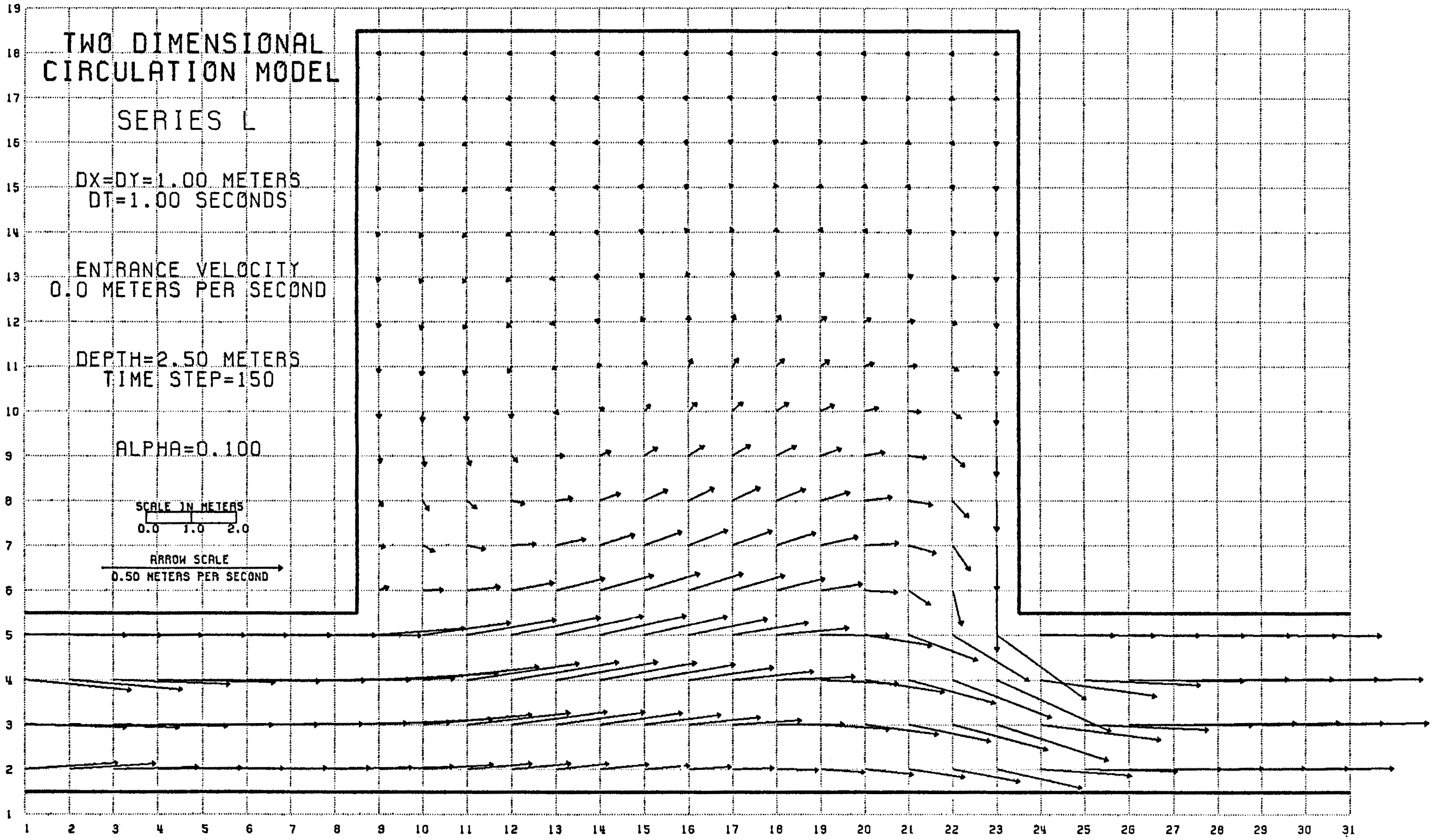

Figure 5.114. No slip condition at the wall: time step 150.

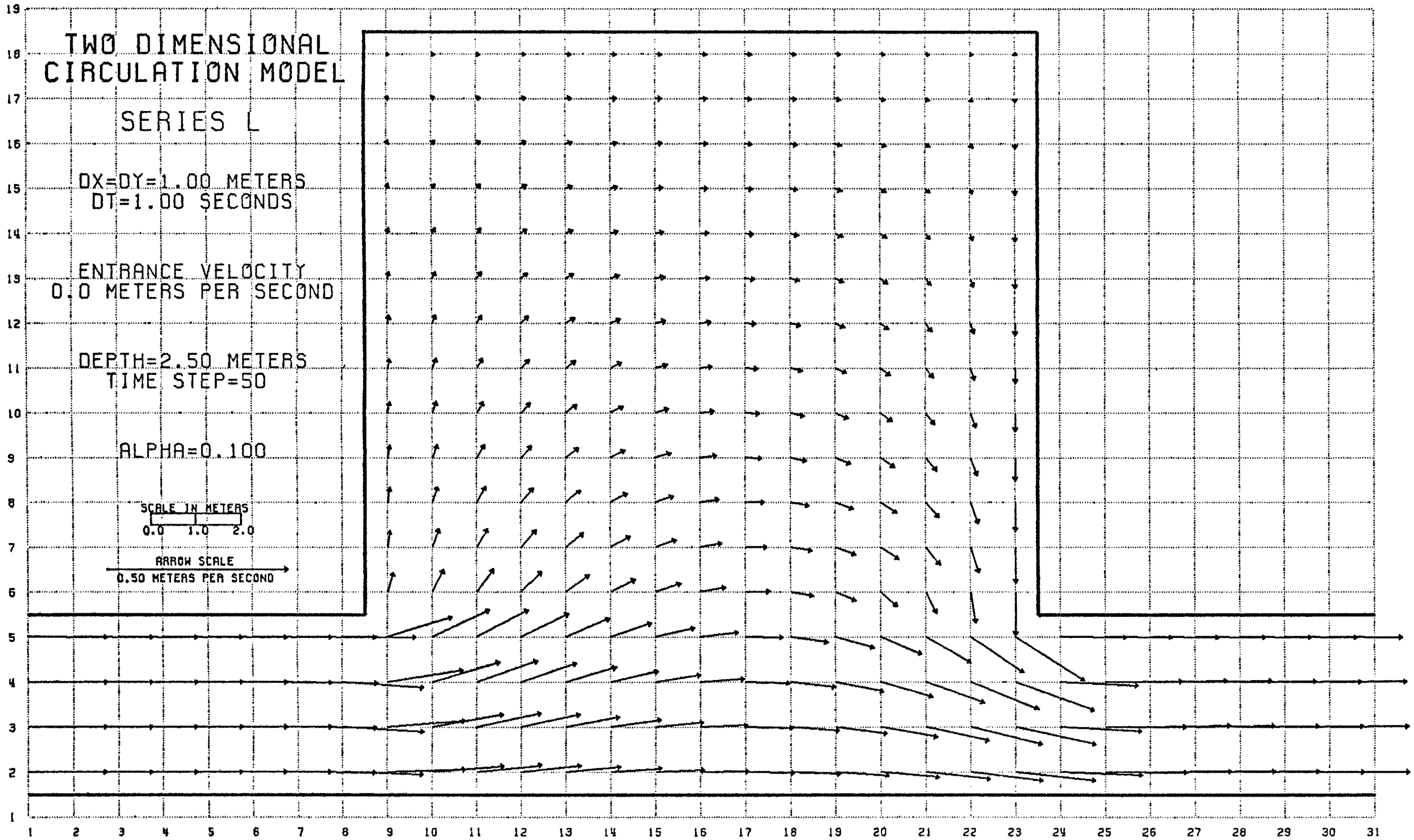

Figure 5.115. Slope-specified cold start baseline: time step 50.

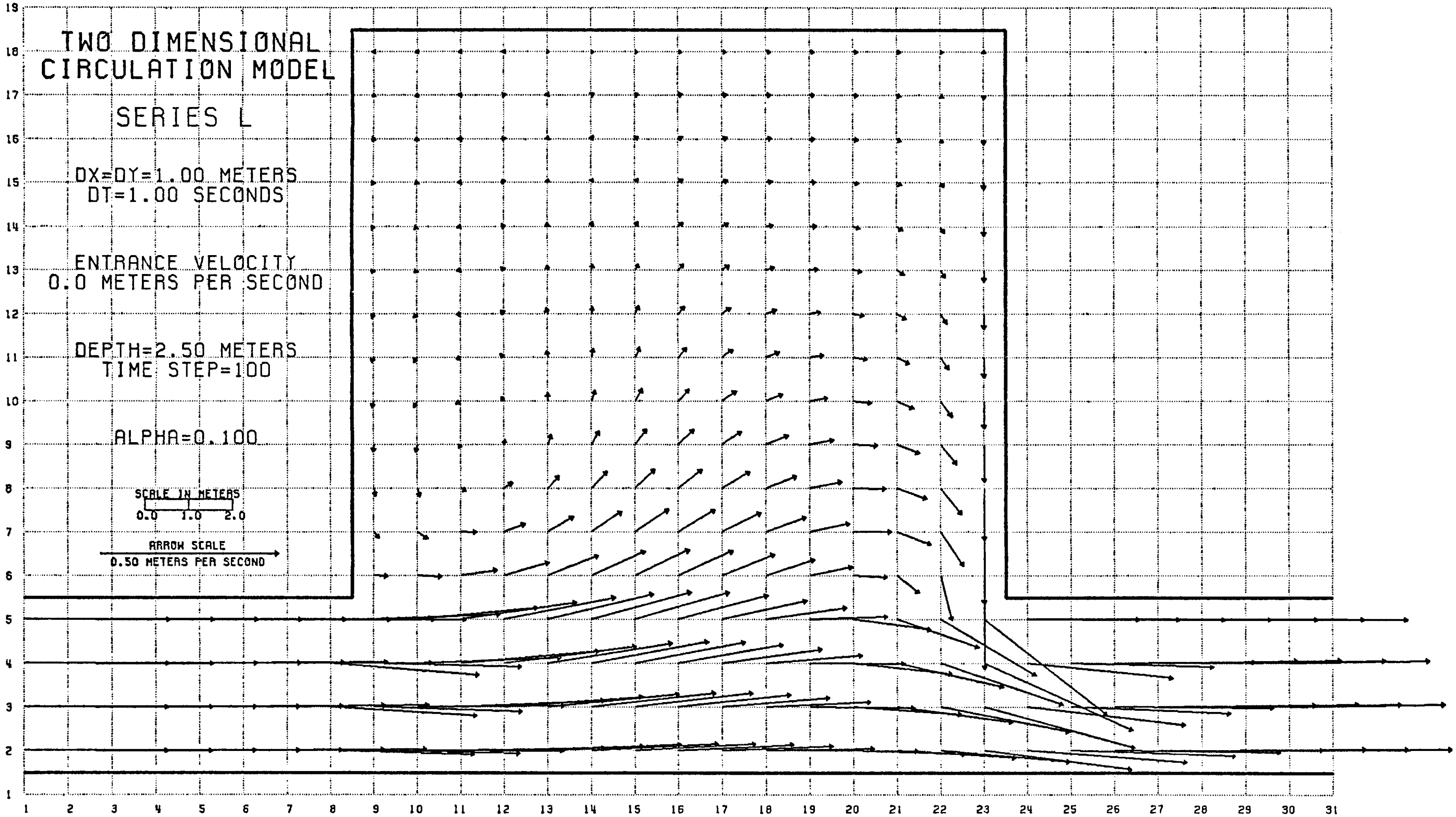

Figure 5.116. Slope-specified cold start baseline: time step 100.

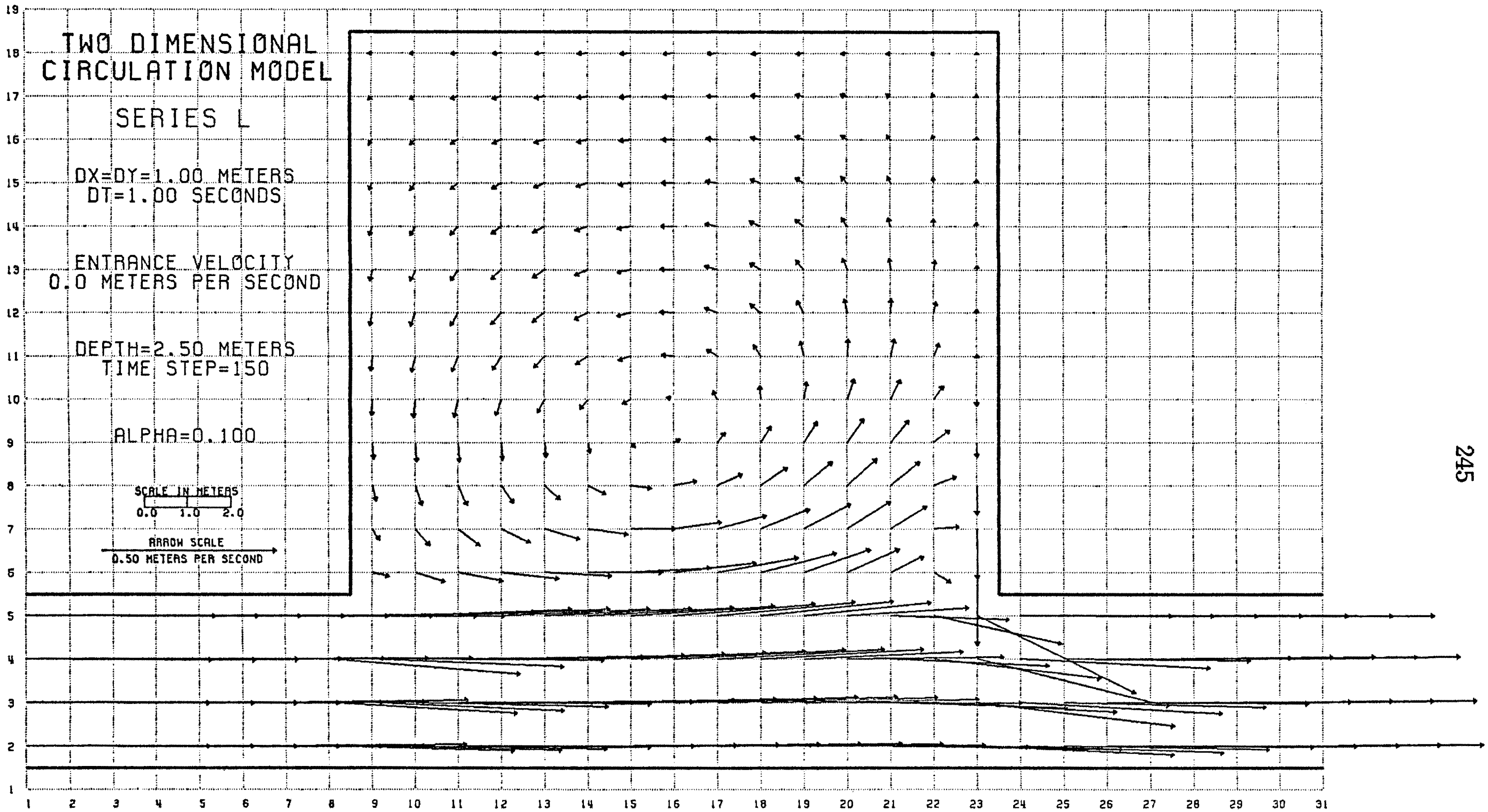

Figure 5.117. Slope-specified cold start baseline: time step 150.

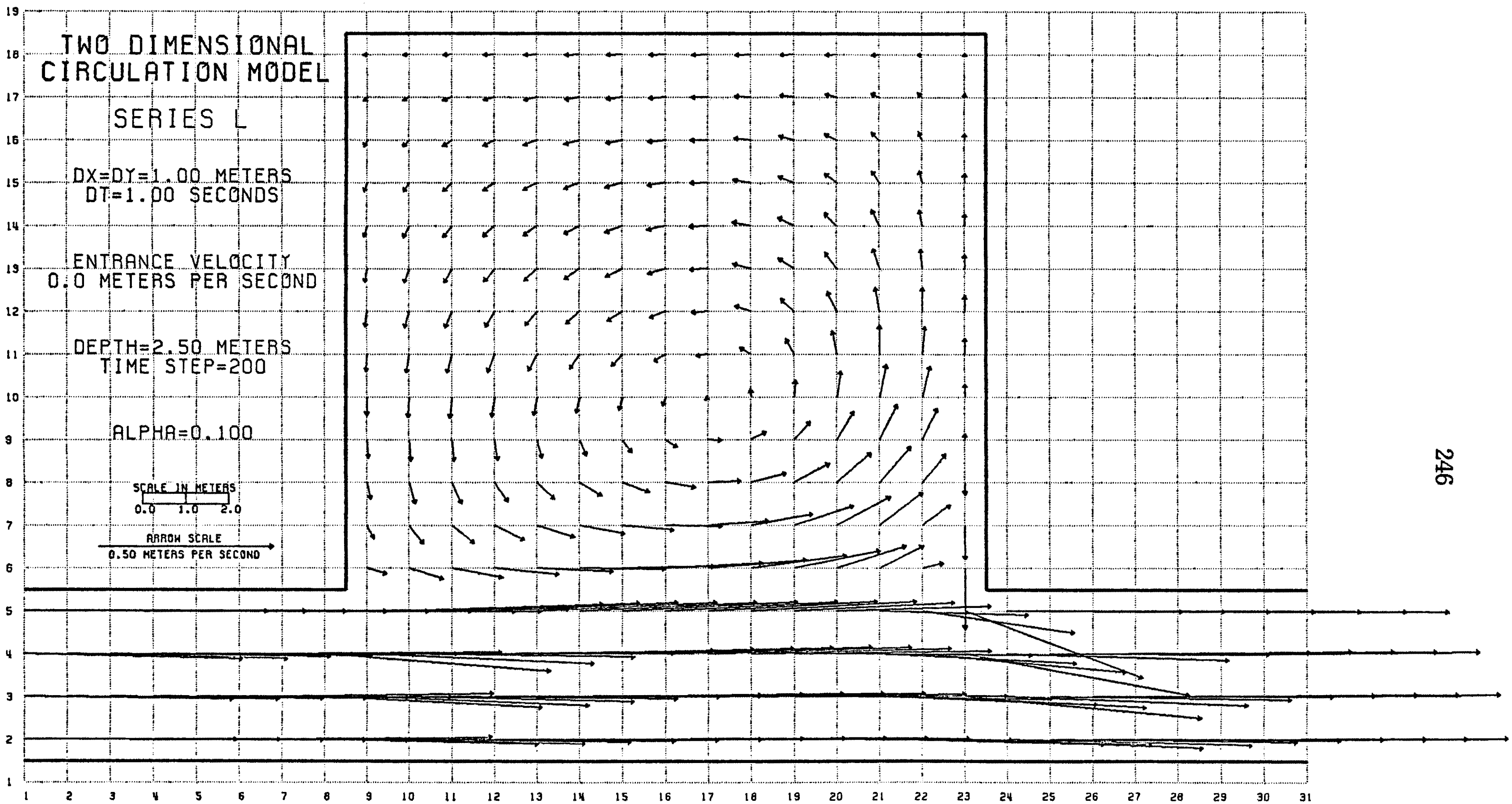

Figure 5.118. Slope-specified cold start baseline: time step 200.

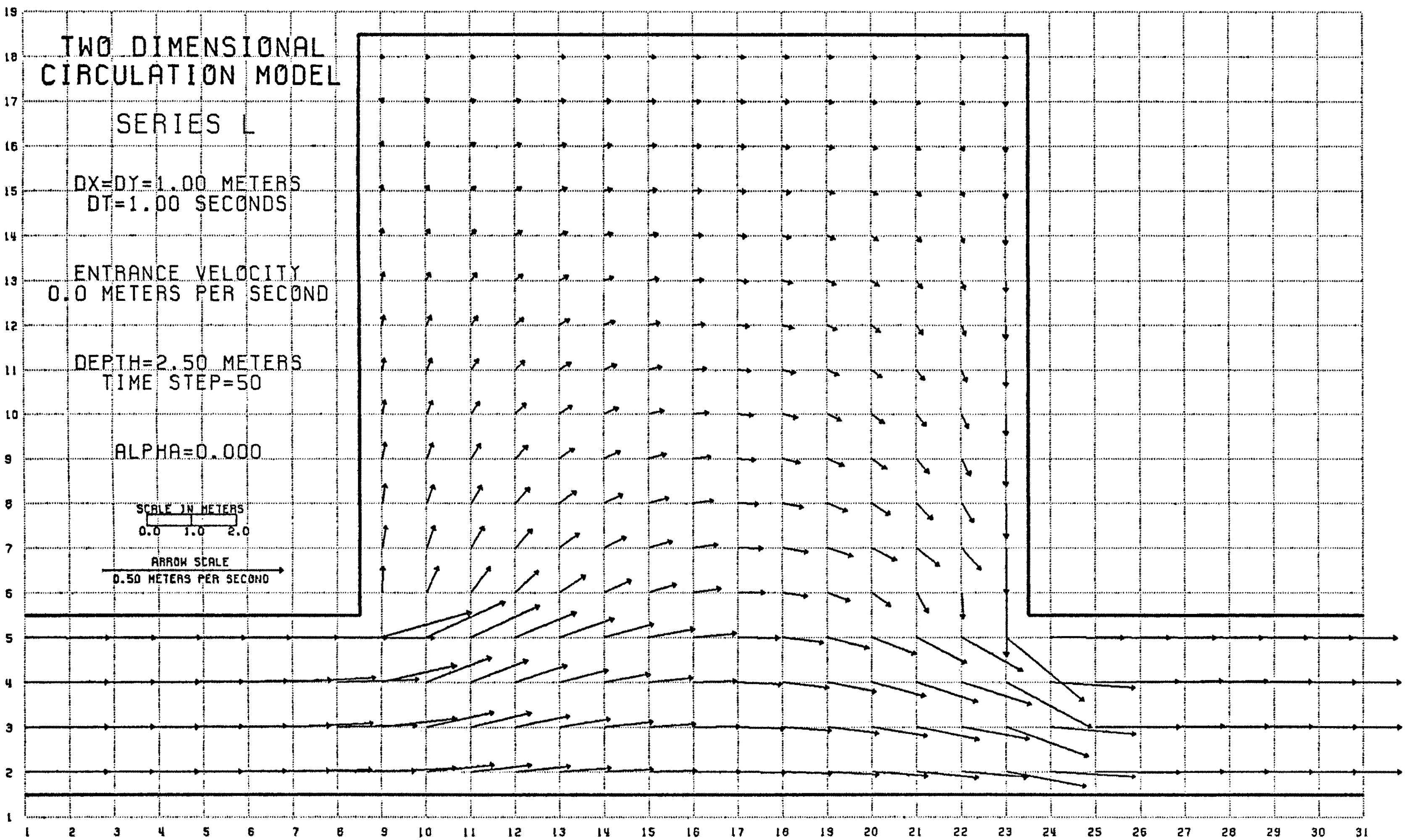

Figure 5.119. Omission of effective stresses: time step 50.

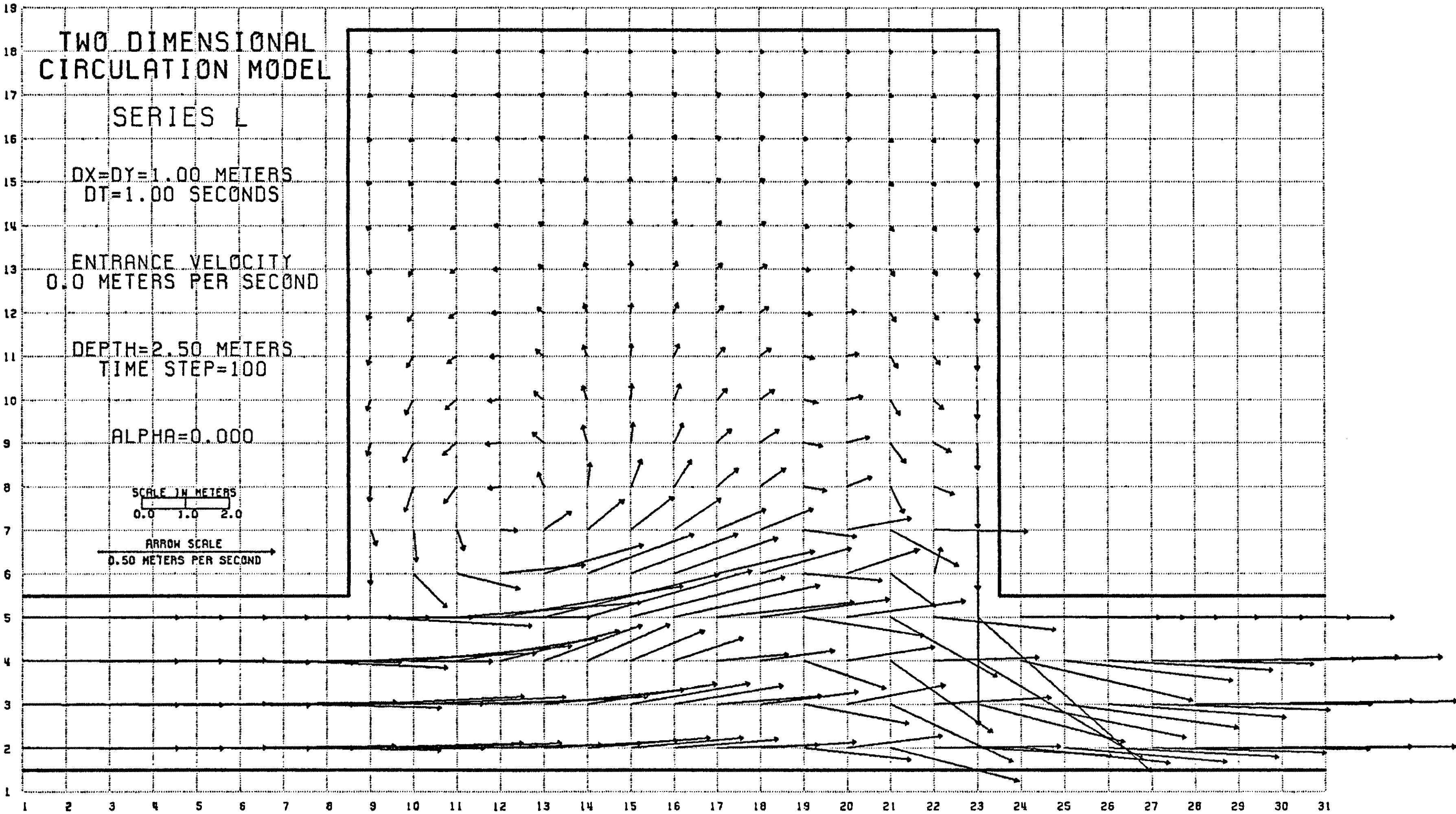

Figure 5.120. Omission of effective stresses: time step 100.

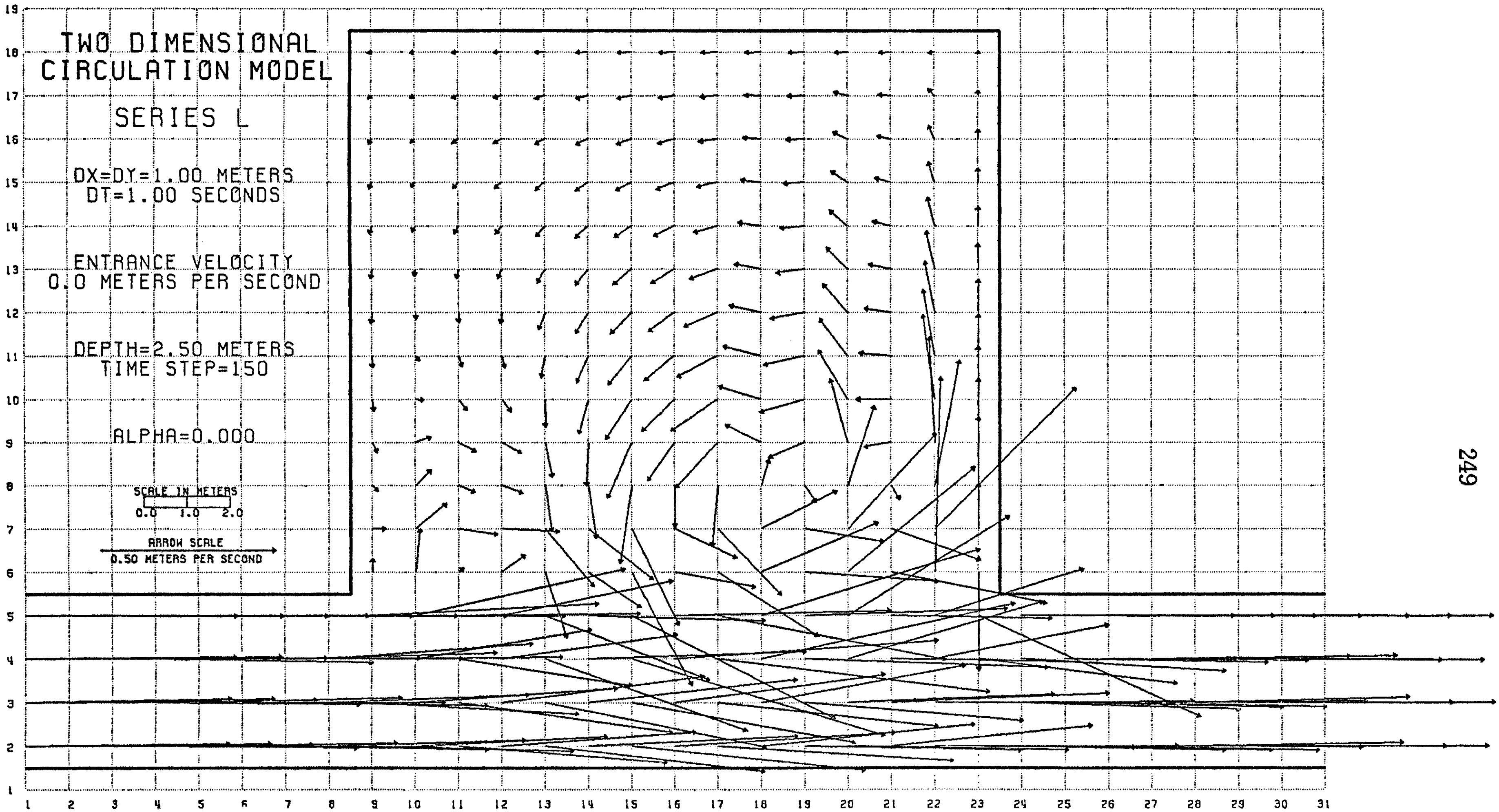

Figure 5.121. Omission of effective stresses: time step 150.

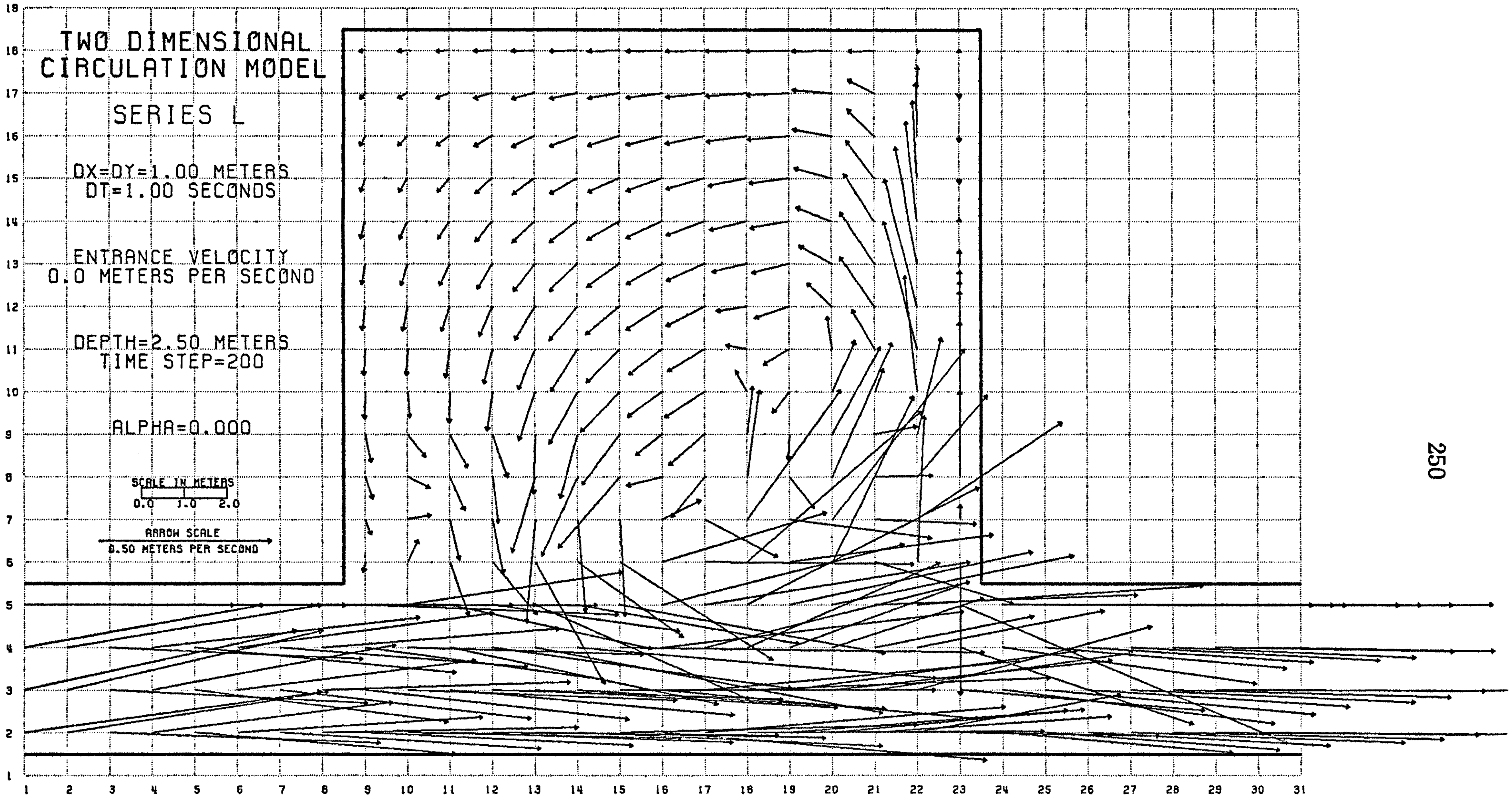

Figure 5.122. Omission of effective stresses: time step 200.

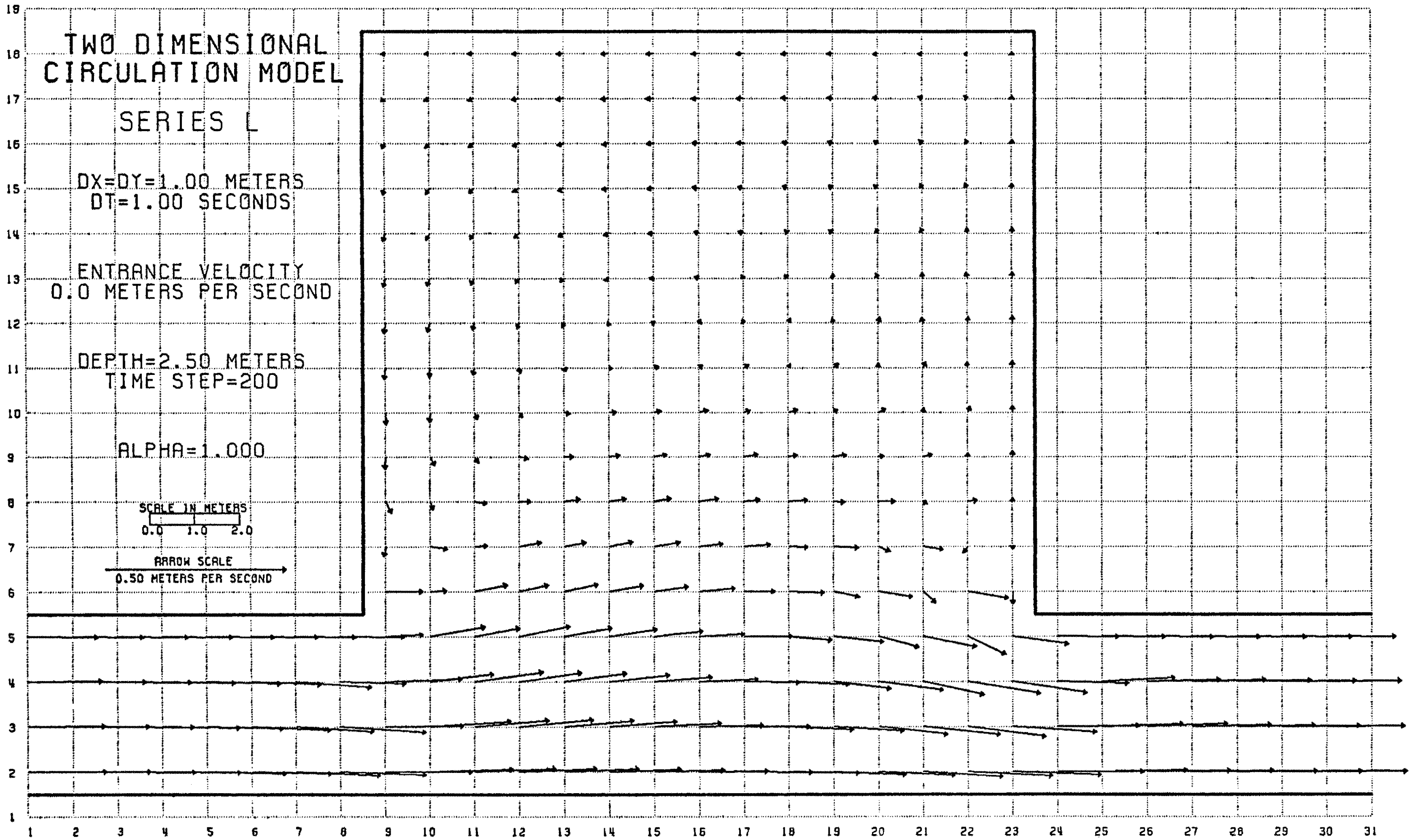

Figure 5.123. Weighting factor, α = 1.0: time step 200.

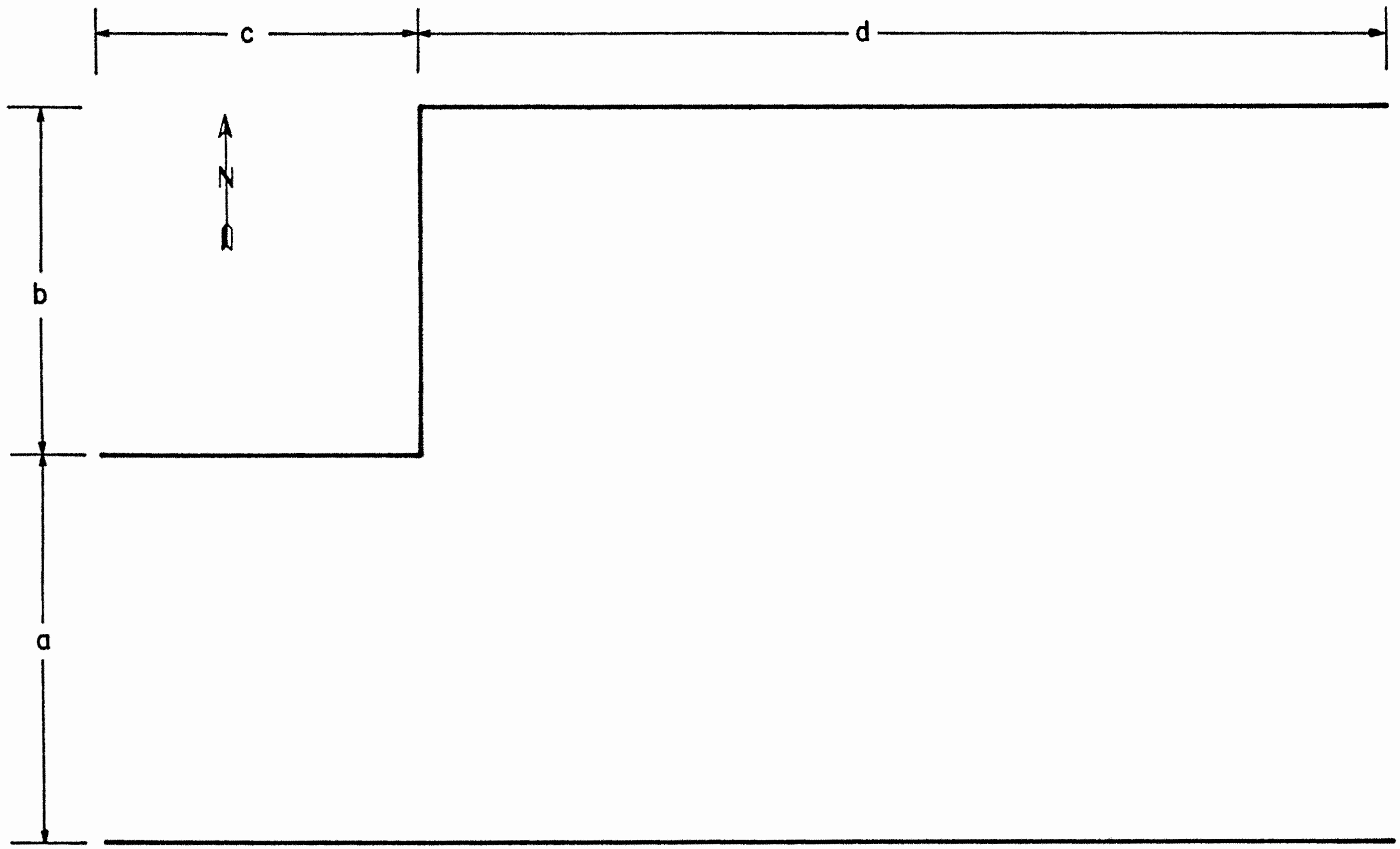

Figure 5.124. Channel expansion configuration.

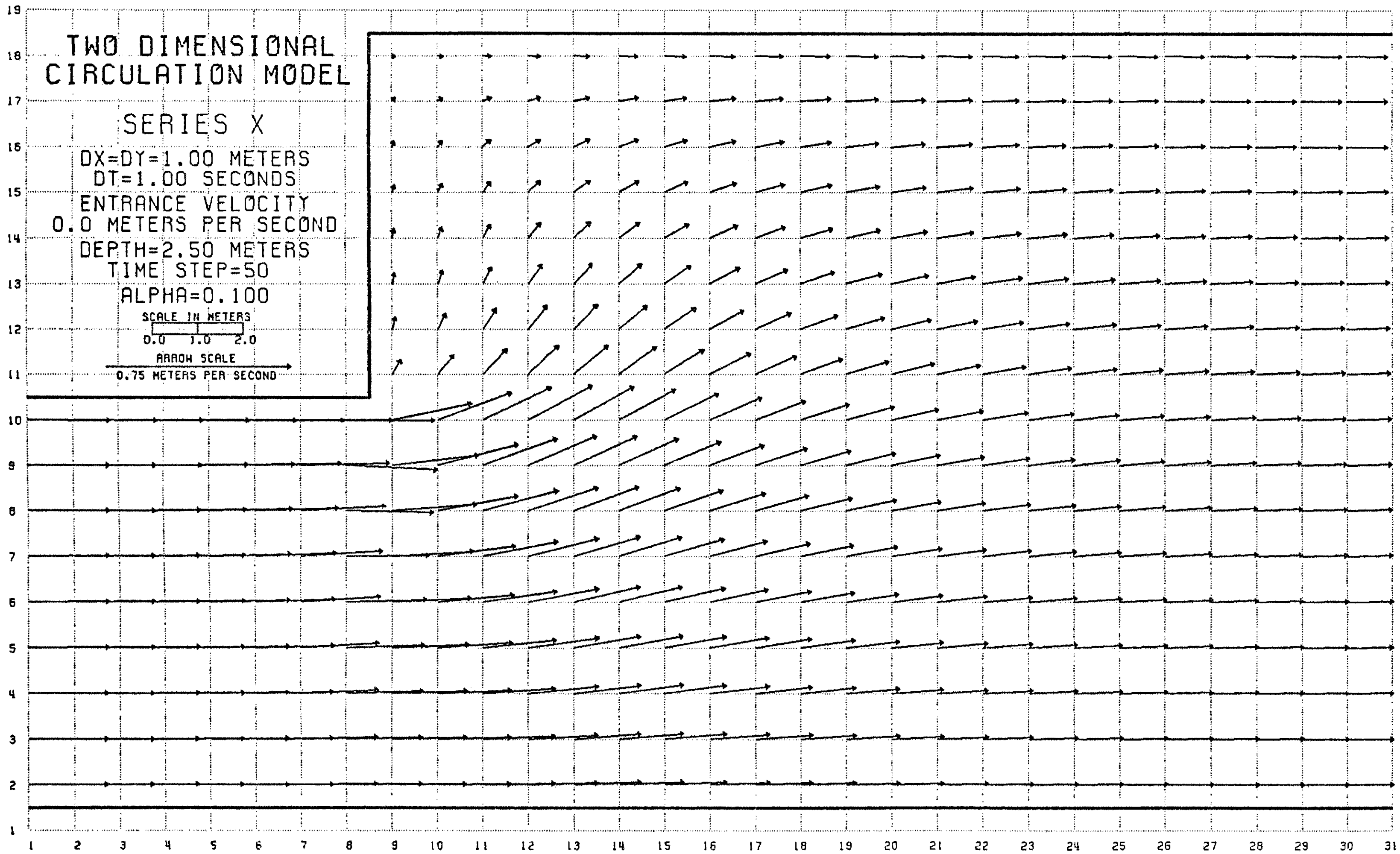

Figure 5.125. Slope-specified baseline: time step 50.

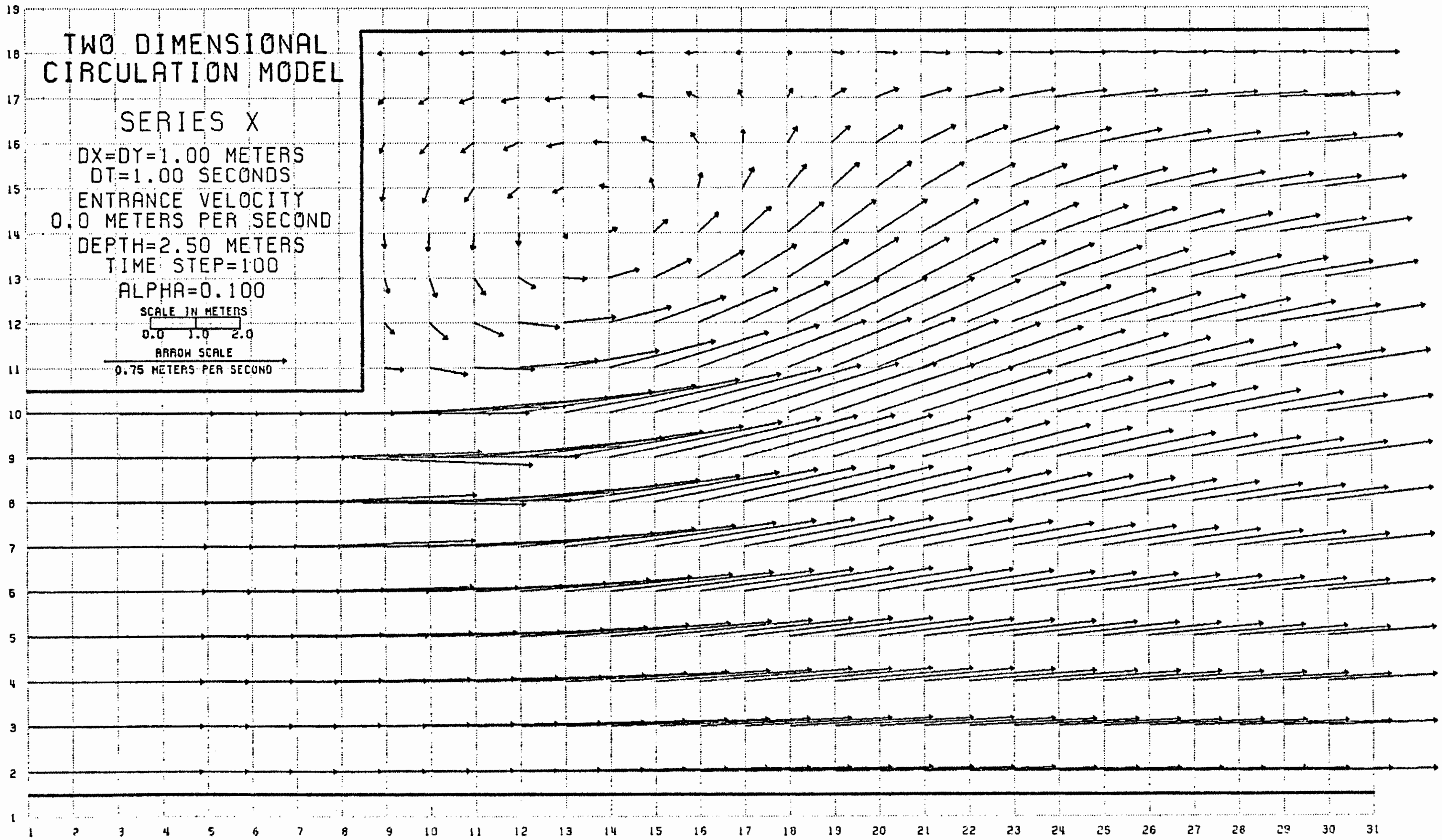

Figure 5.126. Slope-specified baseline: time step 100.

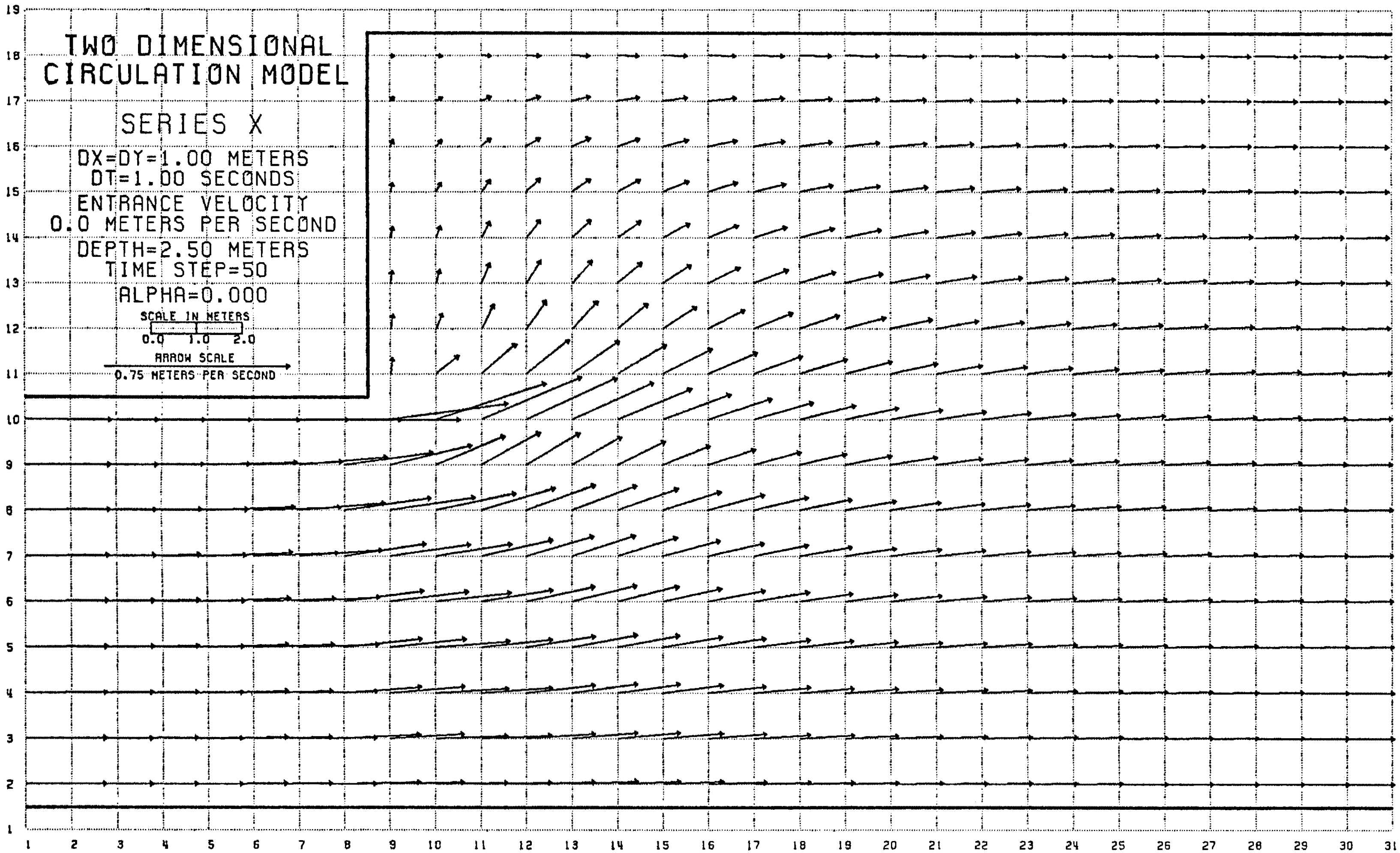

Figure 5.127. Omission of effective stresses: time step 50.

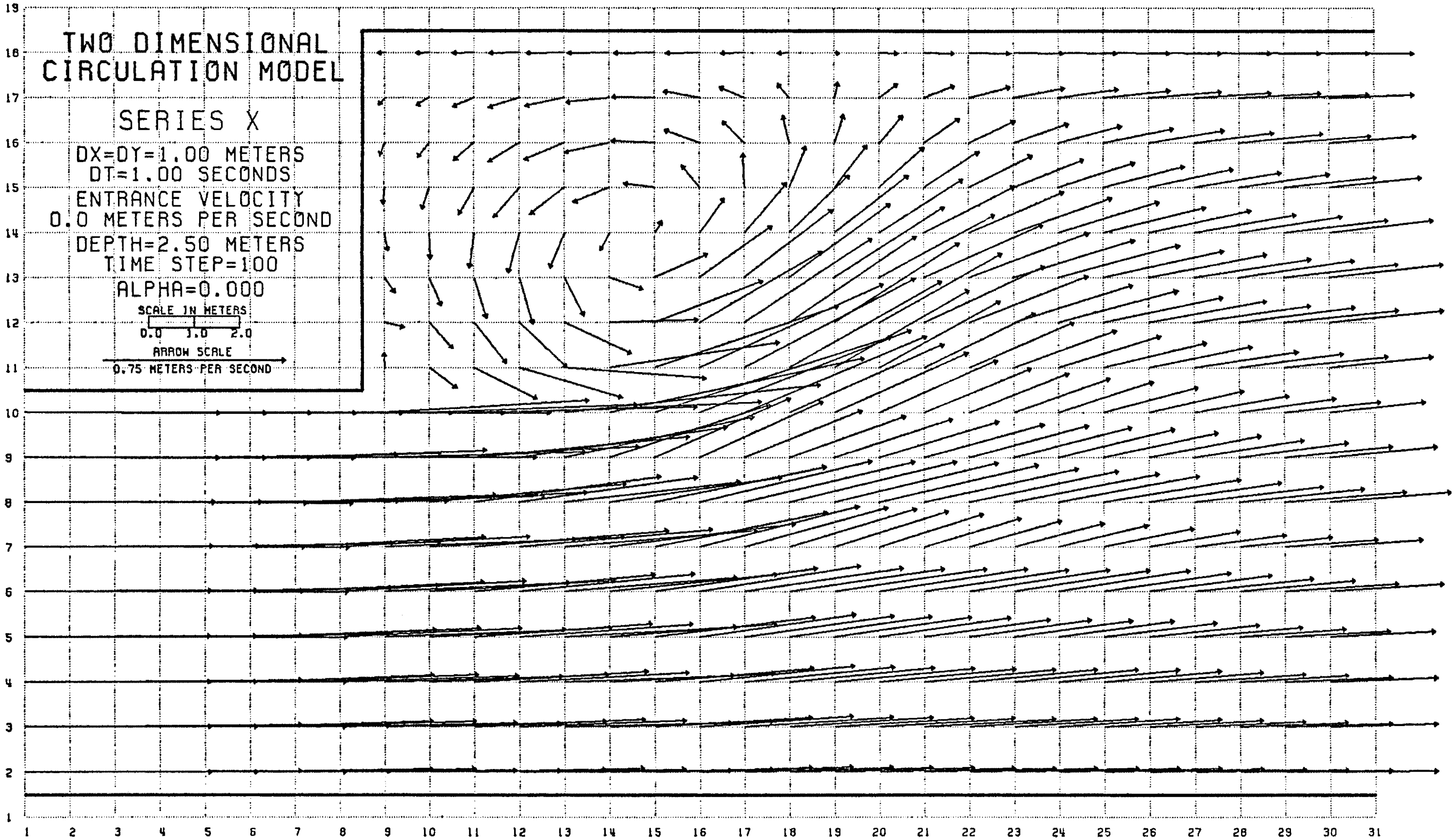

Figure 5.128. Omission of effective stresses: time step 100.

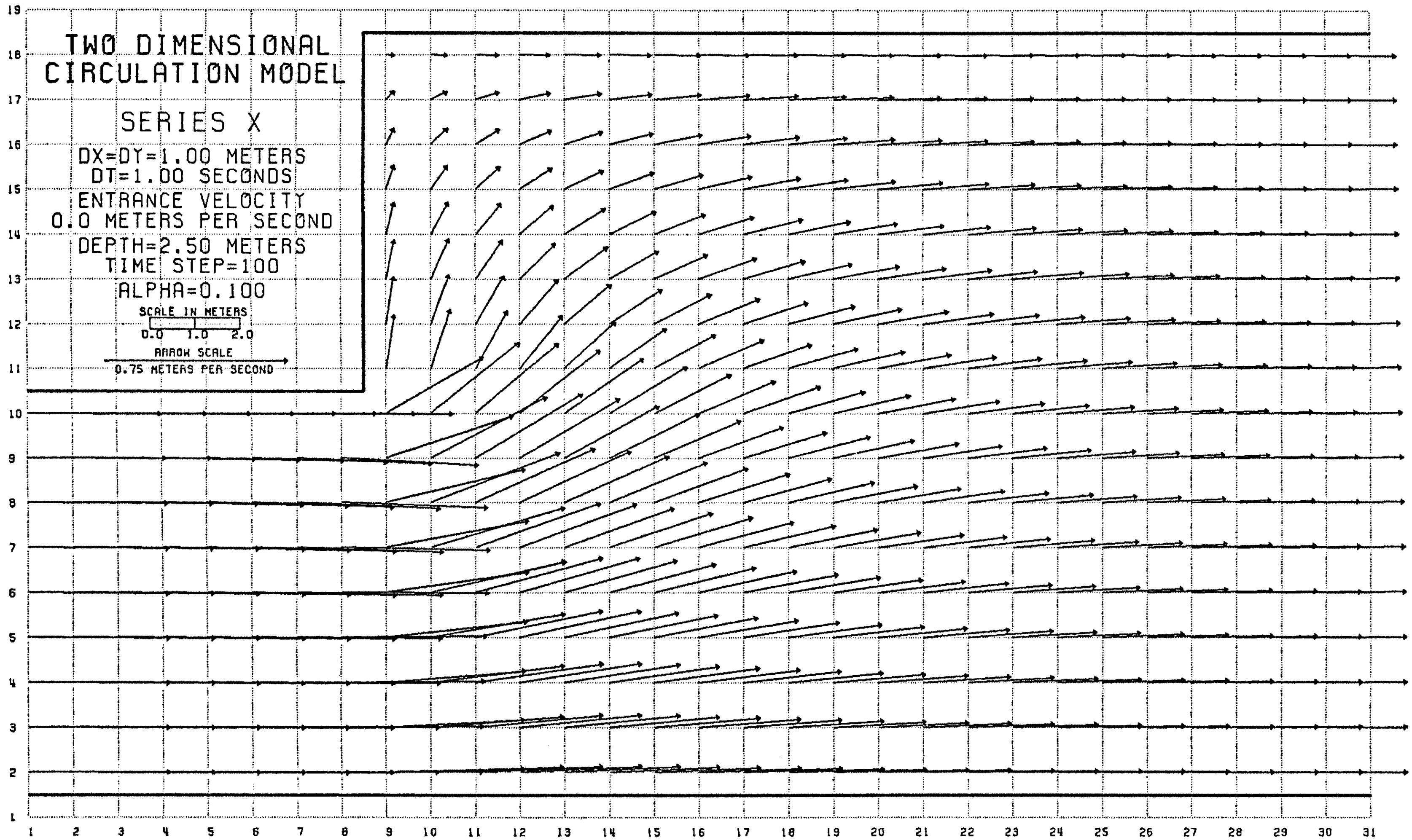

Figure 5.129. Omission of convective inertia: time step 100.

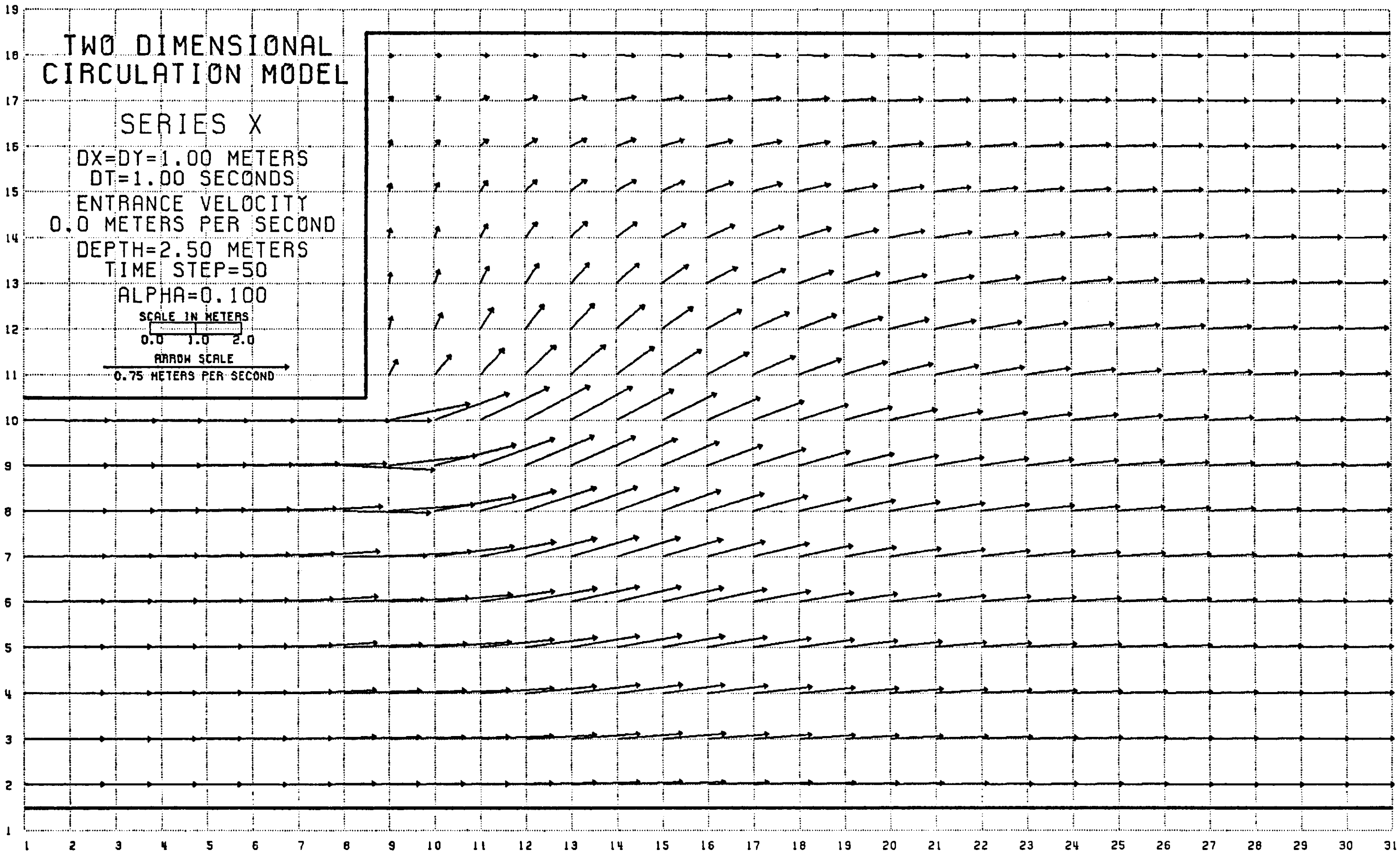

Figure 5.130. Omission of bed resistance: time step 50.

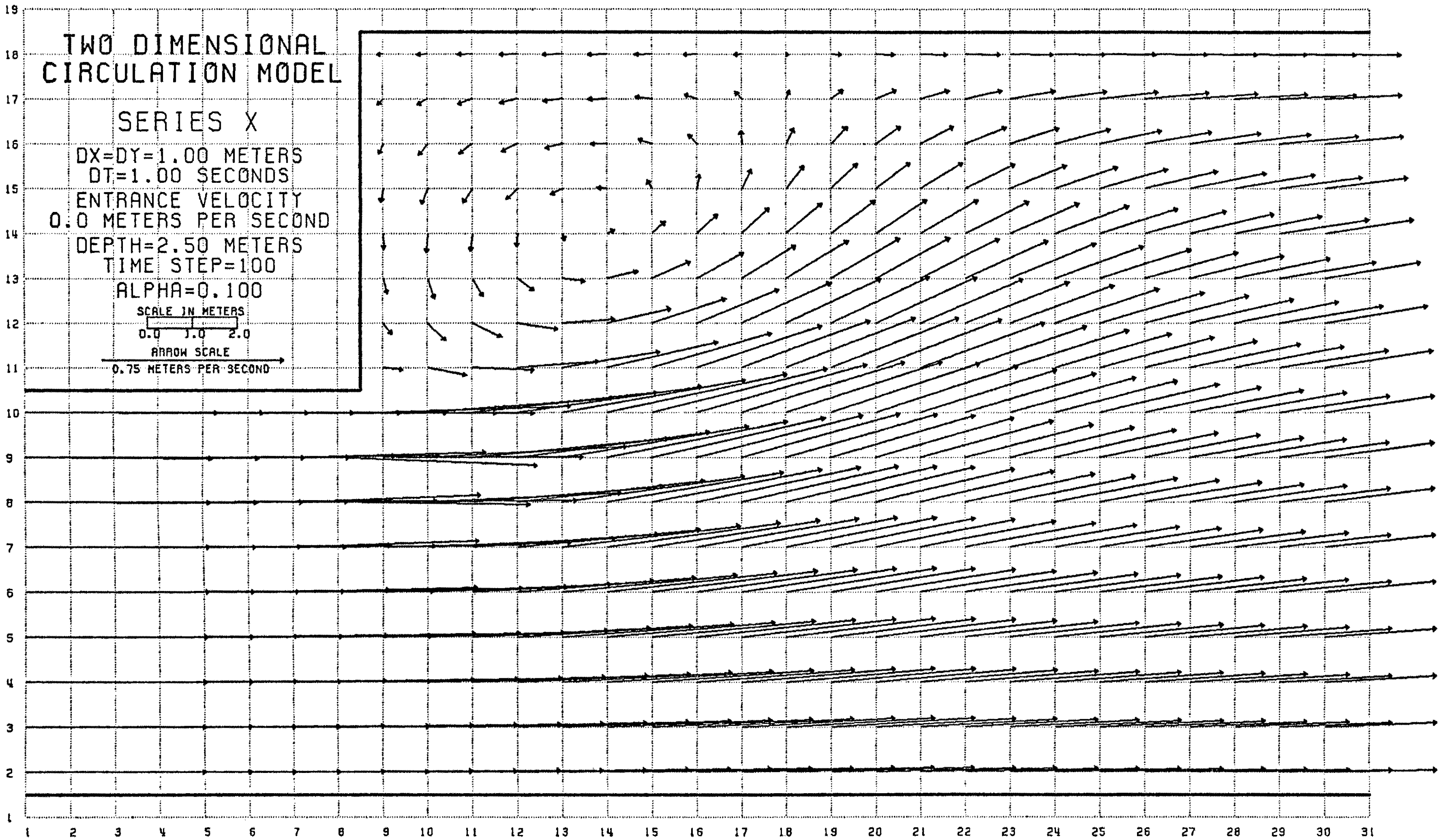

Figure 5.131. Omission of bed resistance: time step 100.

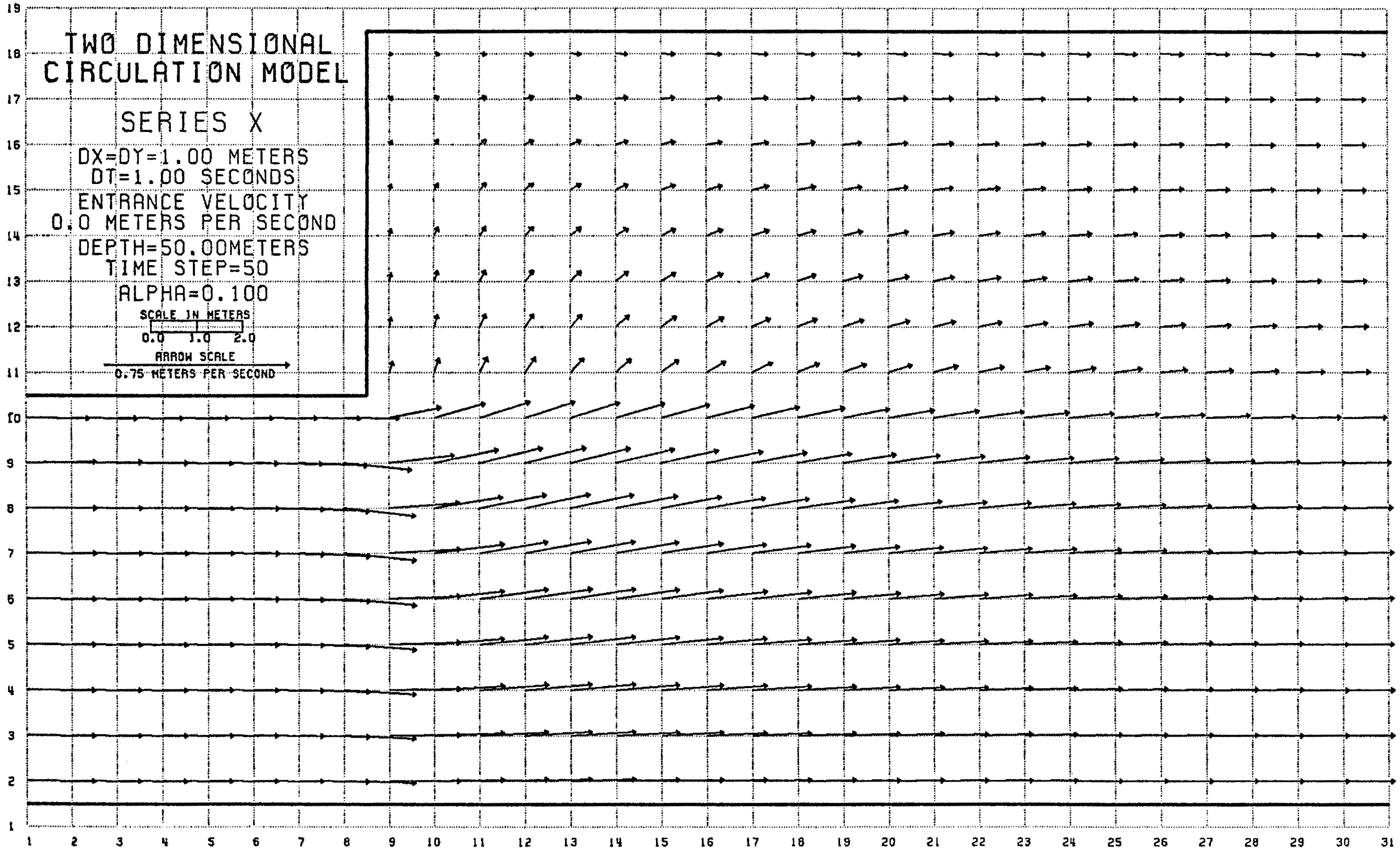

Figure 5.132. Depth, d = 50.0 meters: time step 50.

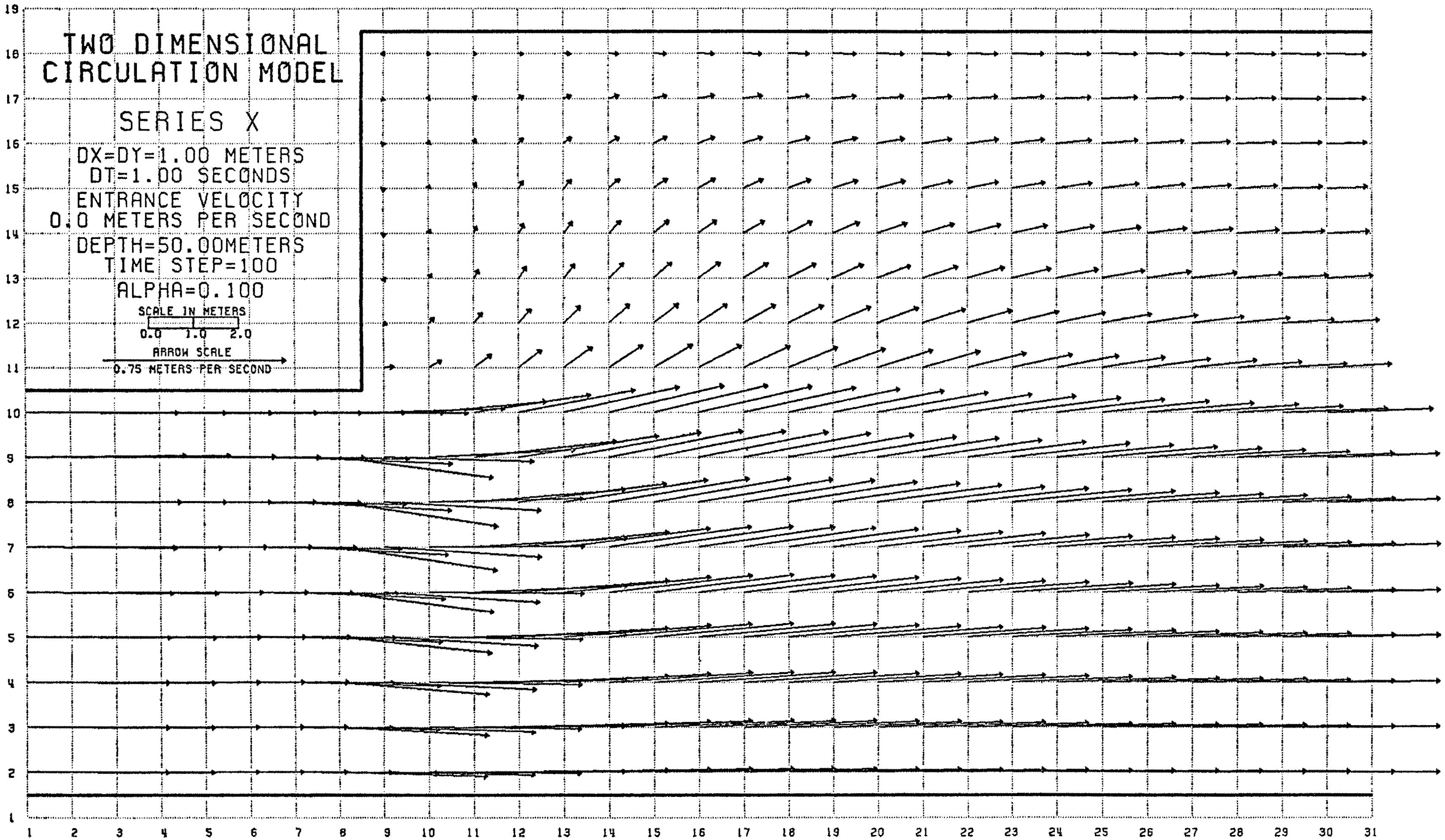

Figure 5.133. Depth, d = 50.0 meters: time step 100.

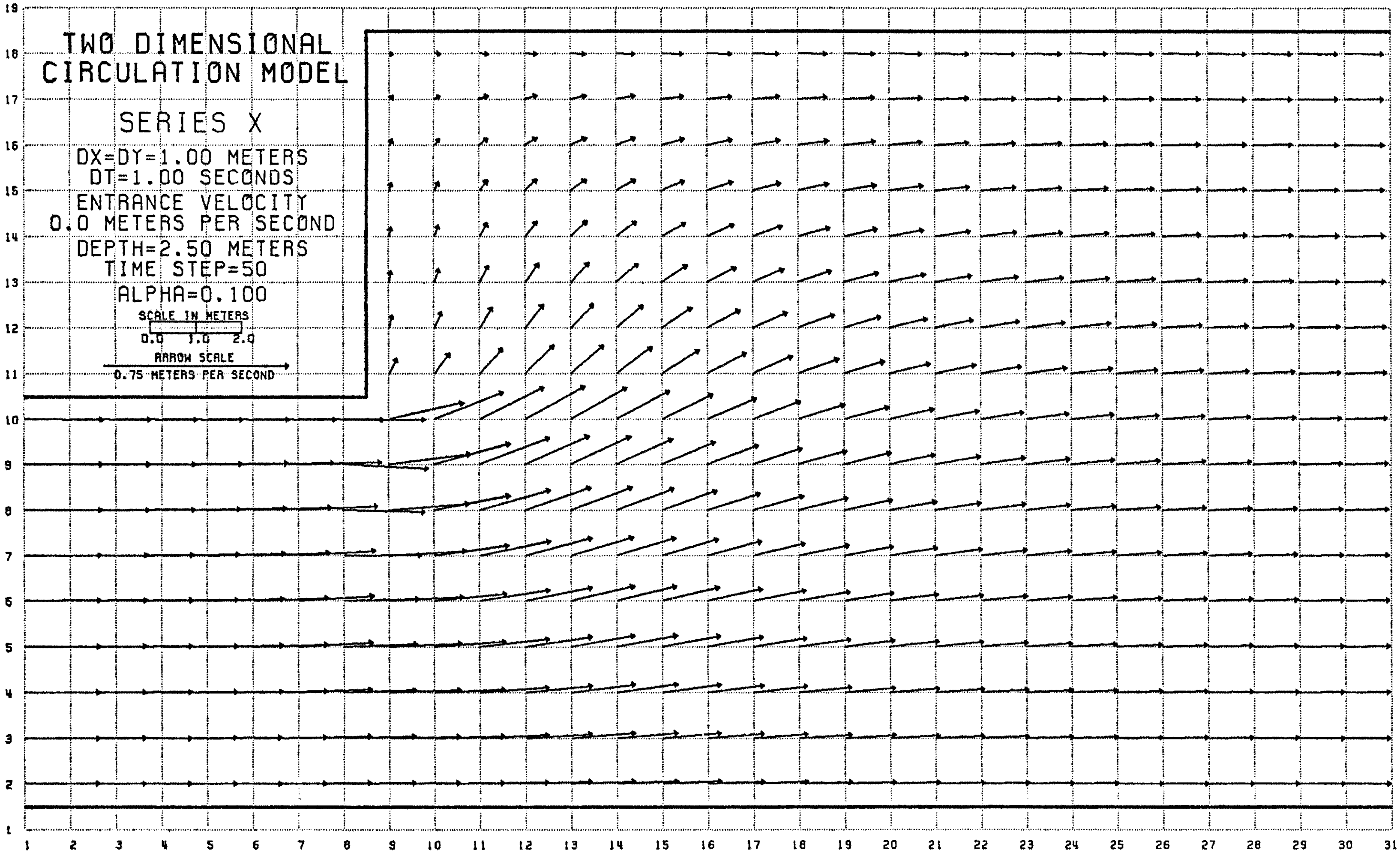

Figure 5.134. Friction factor, f_r = 0.04: time step 50.

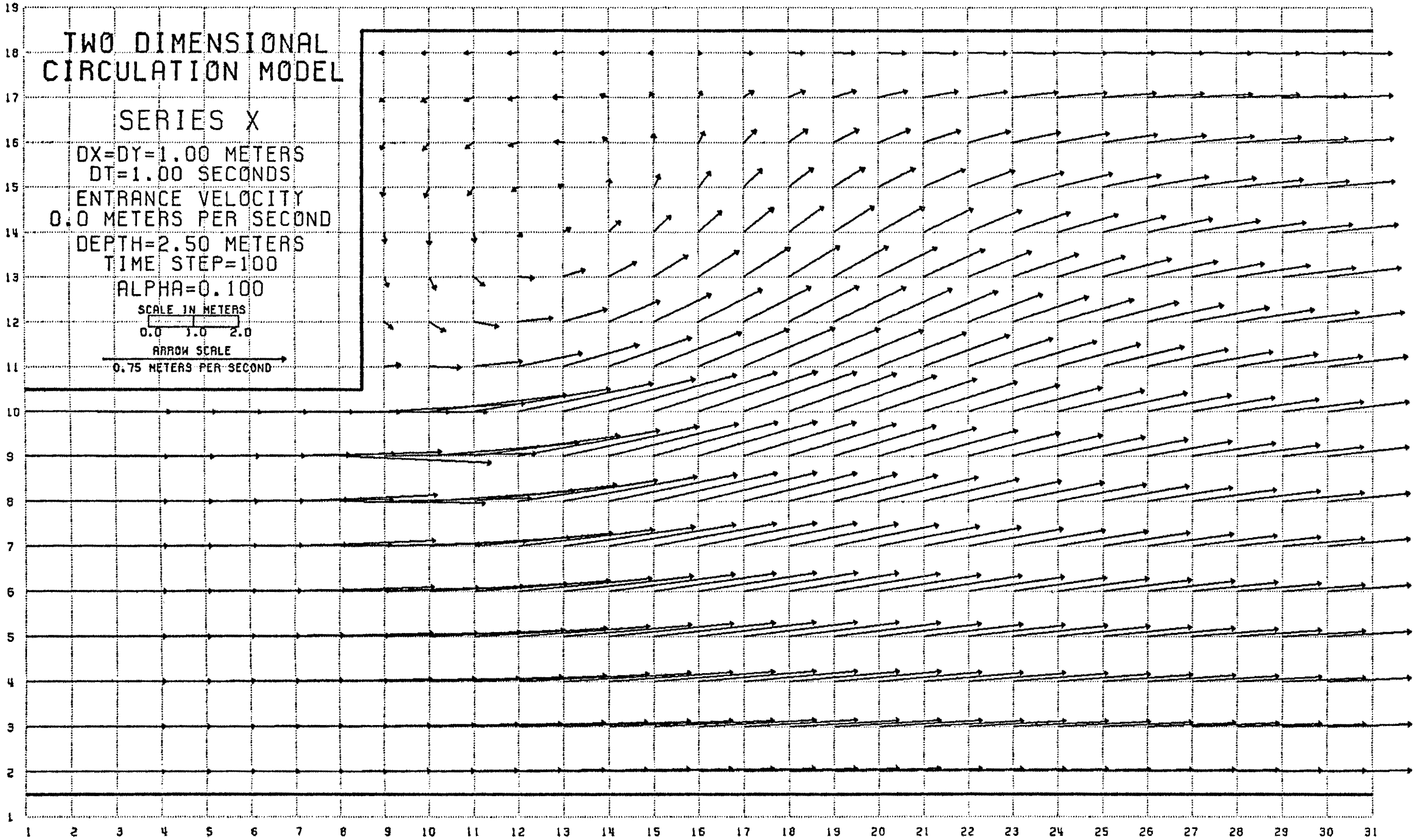

Figure 5.135. Friction factor, f_r = 0.04: time step 100.

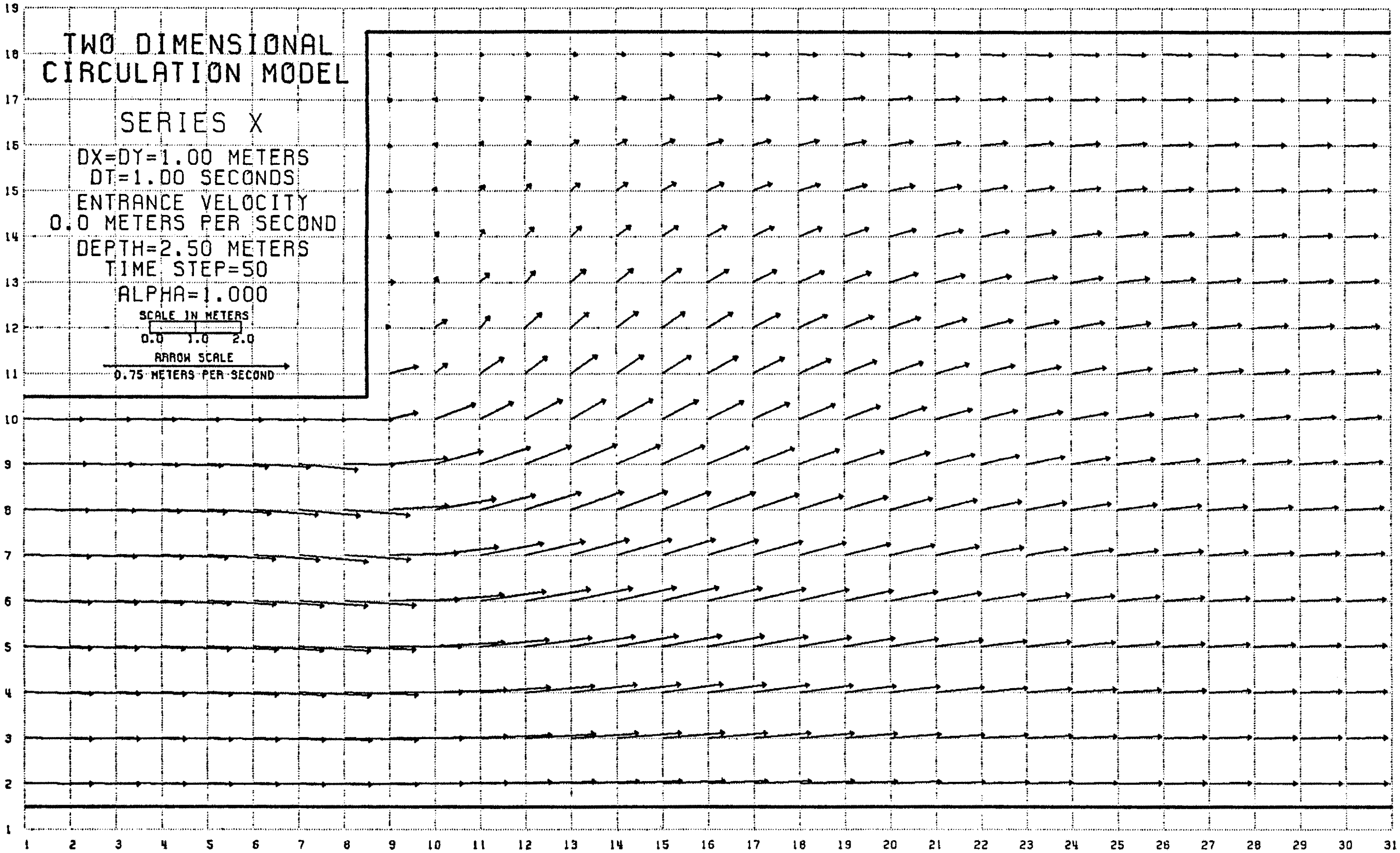

Figure 5.136. Weighting factor, α = 1.0: time step 50.

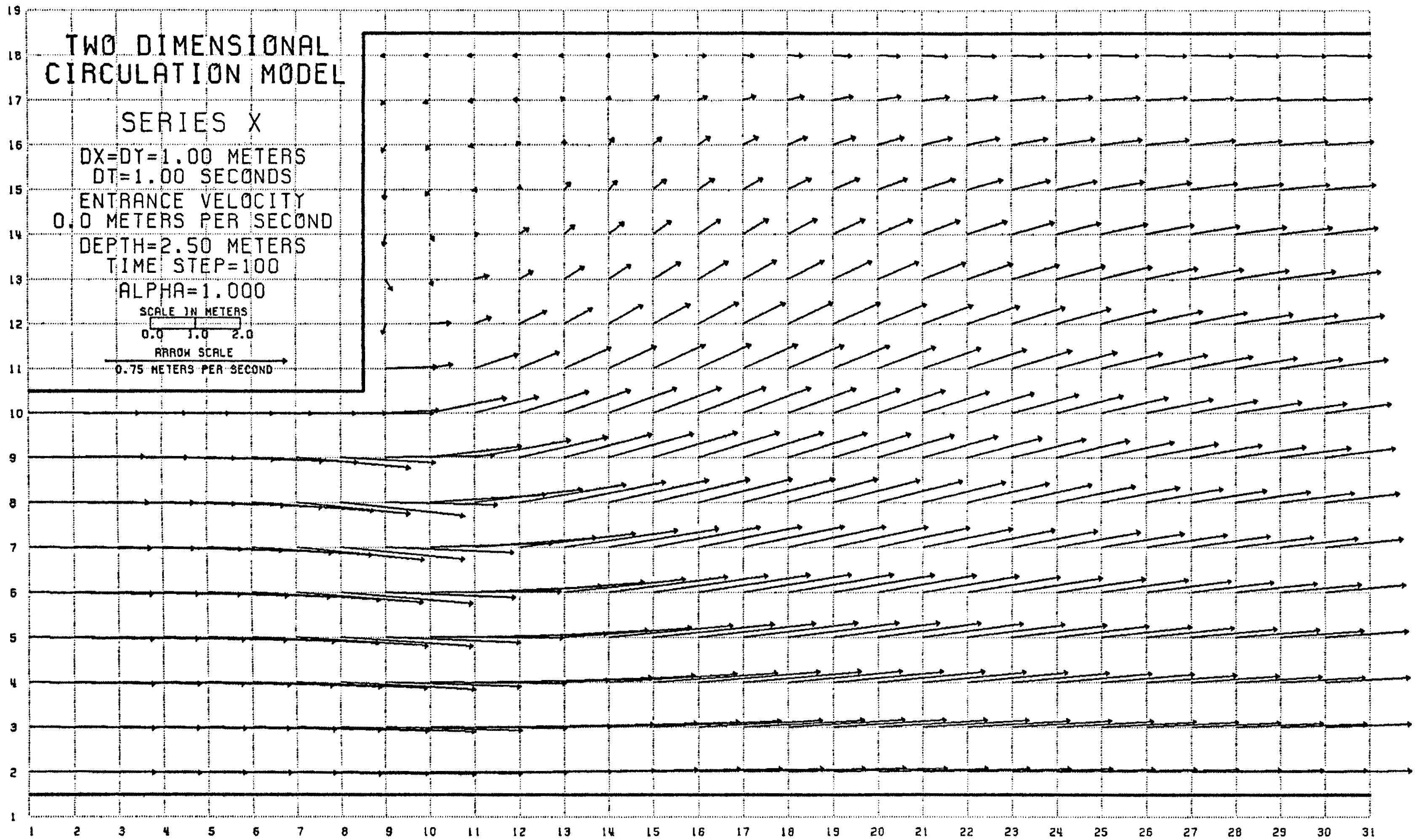

Figure 5.137. Weighting factor, α = 1.0: time step 100.

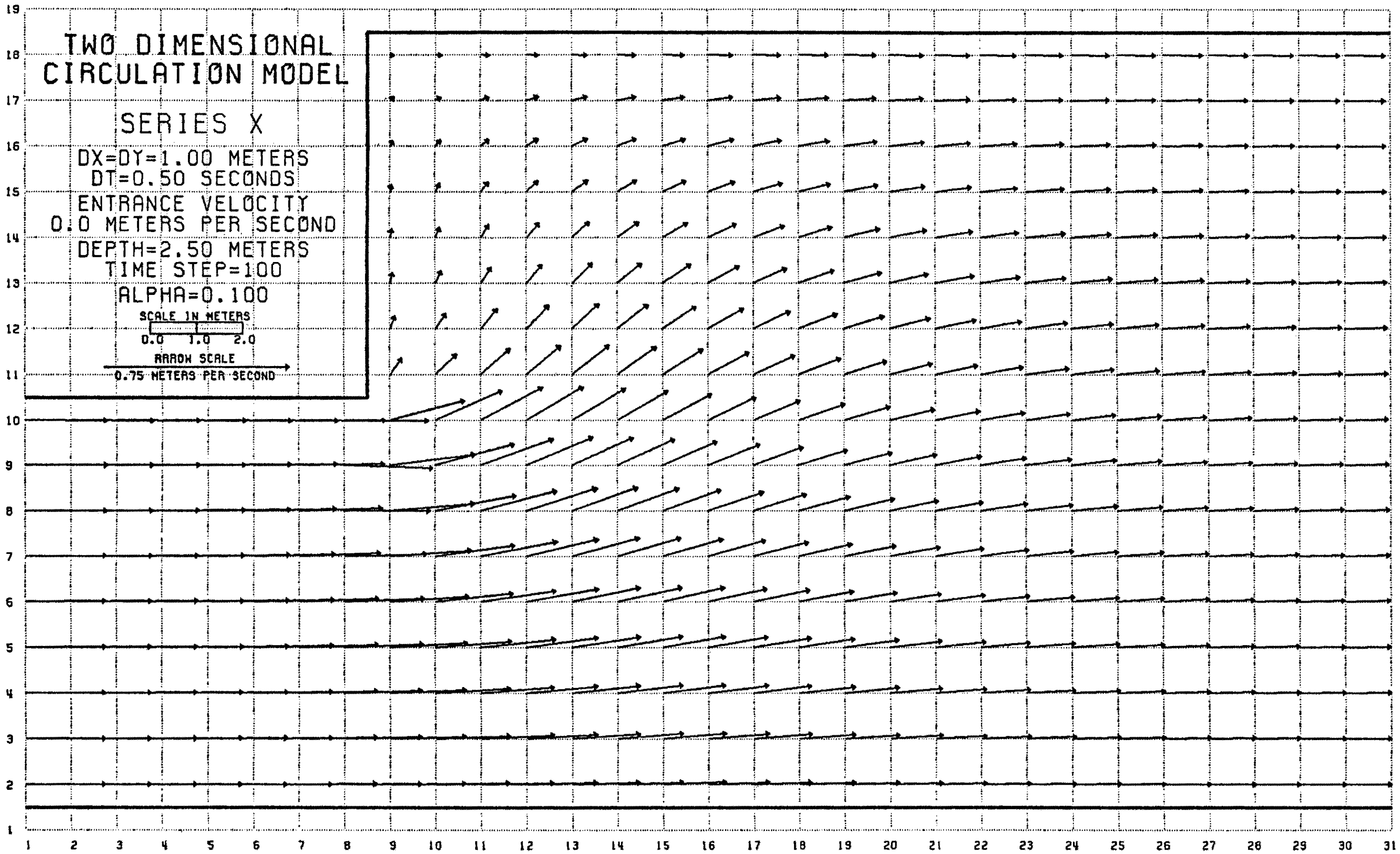

Figure 5.138. Time increment, Δt = 0.5 seconds: time step 100.

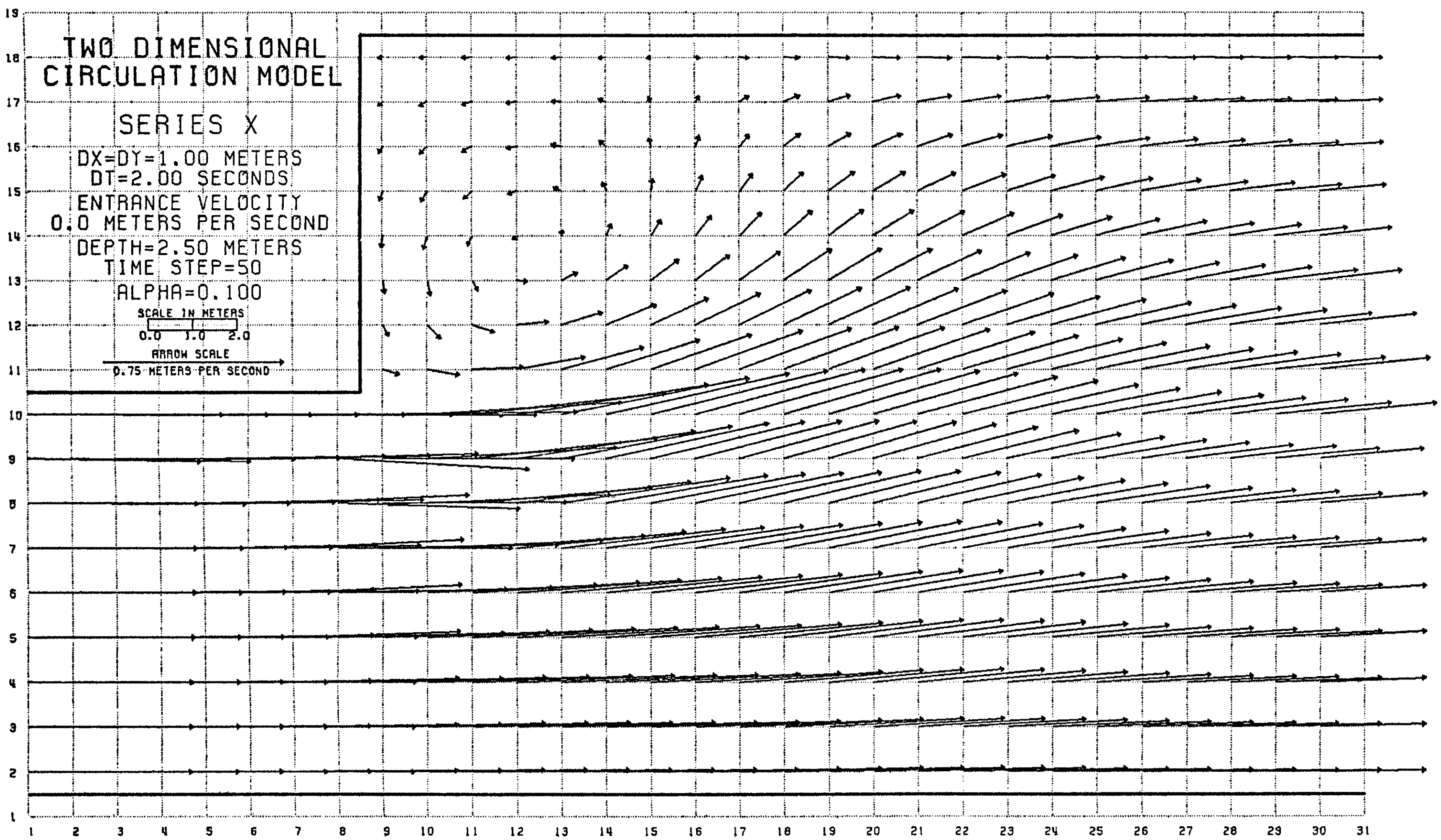

Figure 5.139. Time increment, Δt = 2.0 seconds: time step 50.

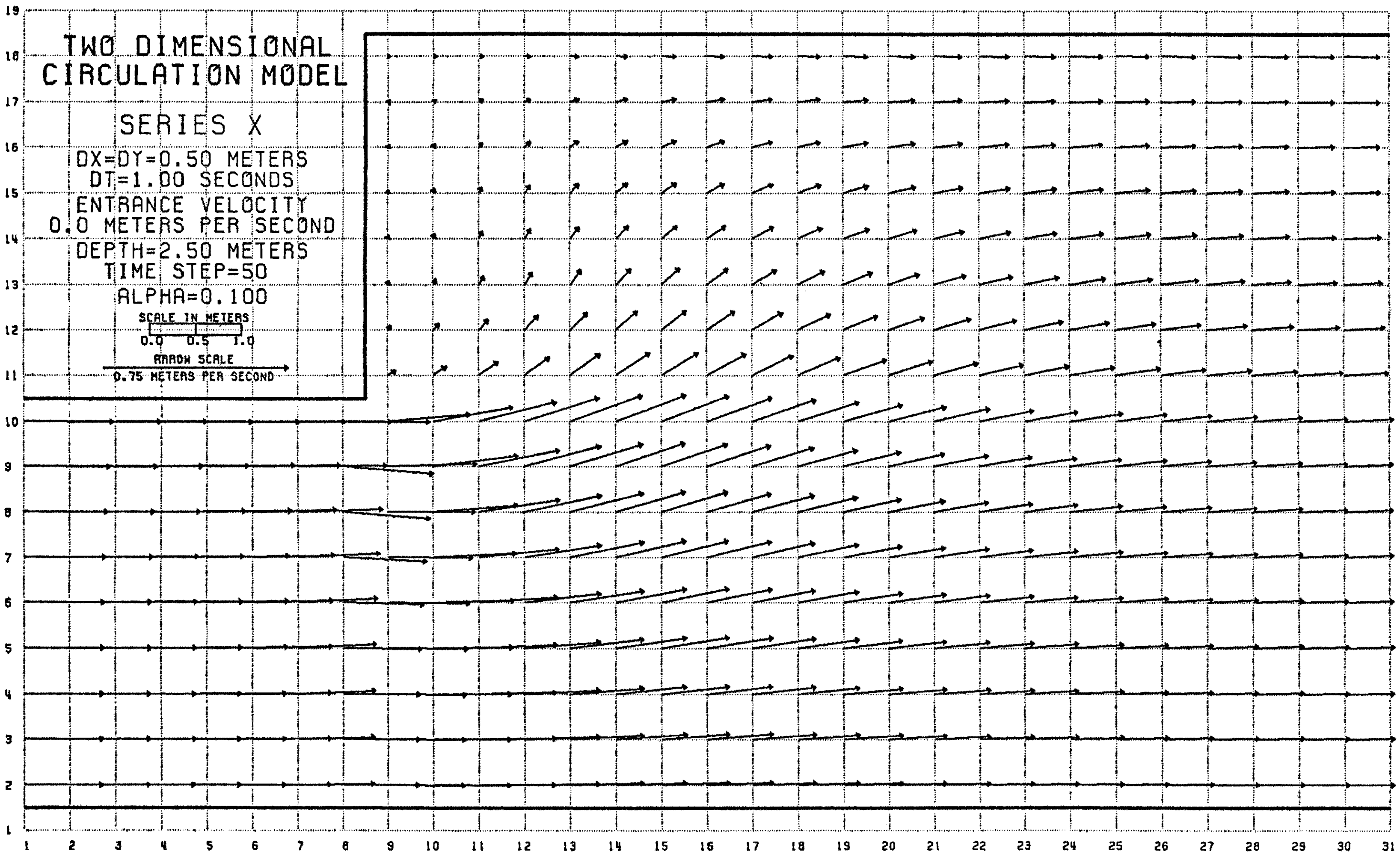

Figure 5.140. Space increment, $\Delta x = \Delta y = 0.5$ meters: time step 50.

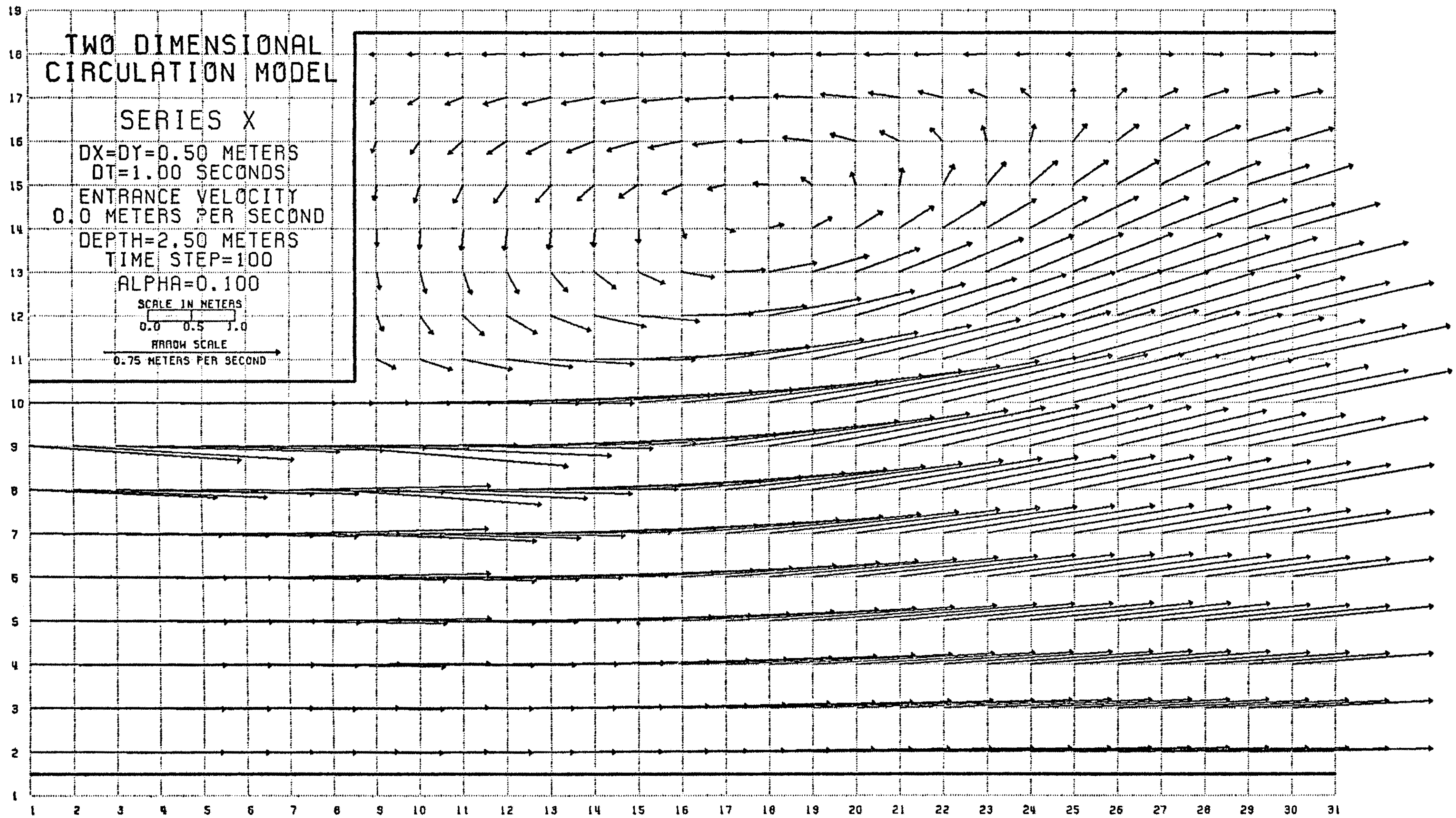

Figure 5.141. Space increment, $\Delta x = \Delta y = 0.5$ meters: time step 100.

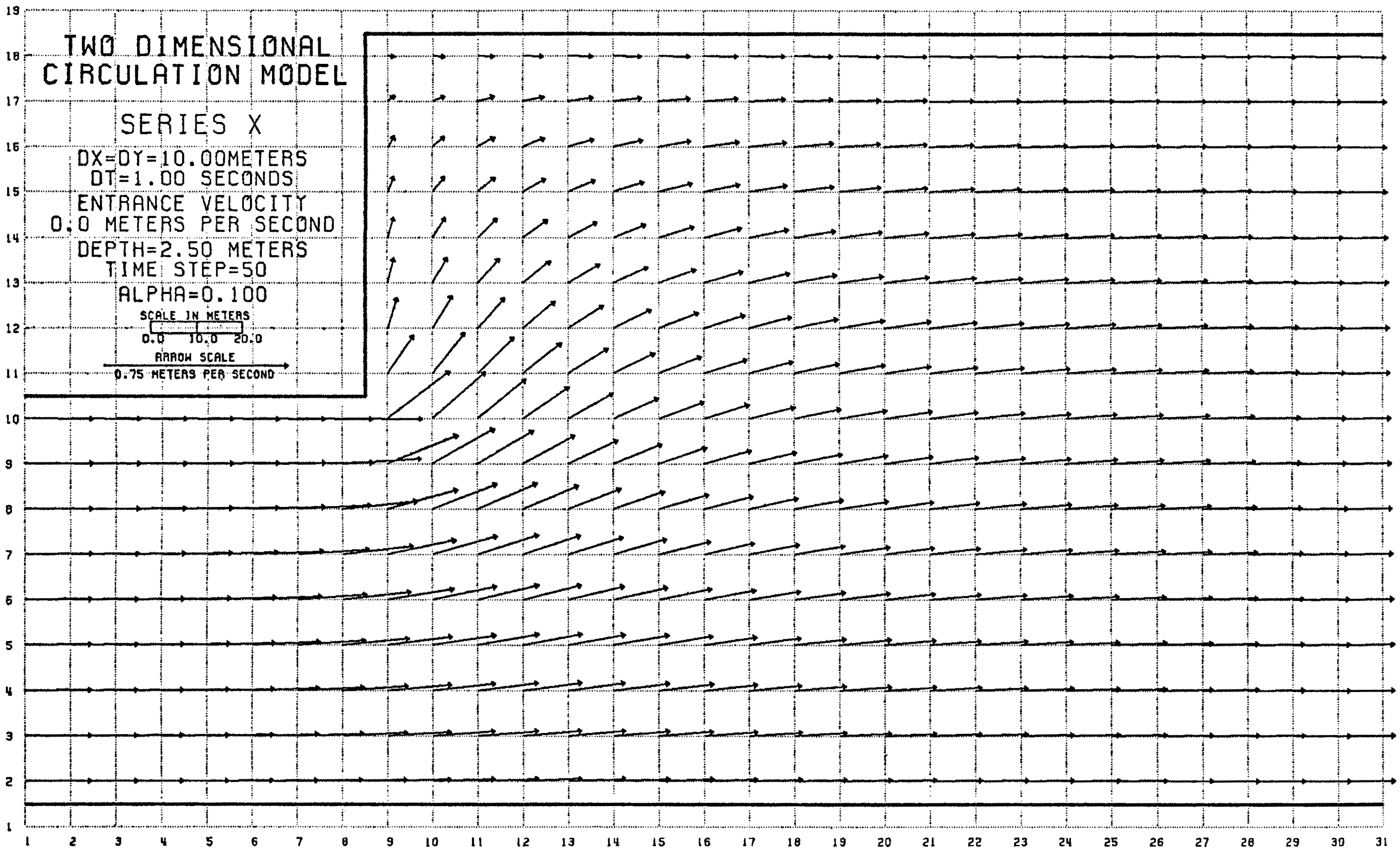

Figure 5.142. Space increment, Δx = Δy = 10.0 meters: time step 50.

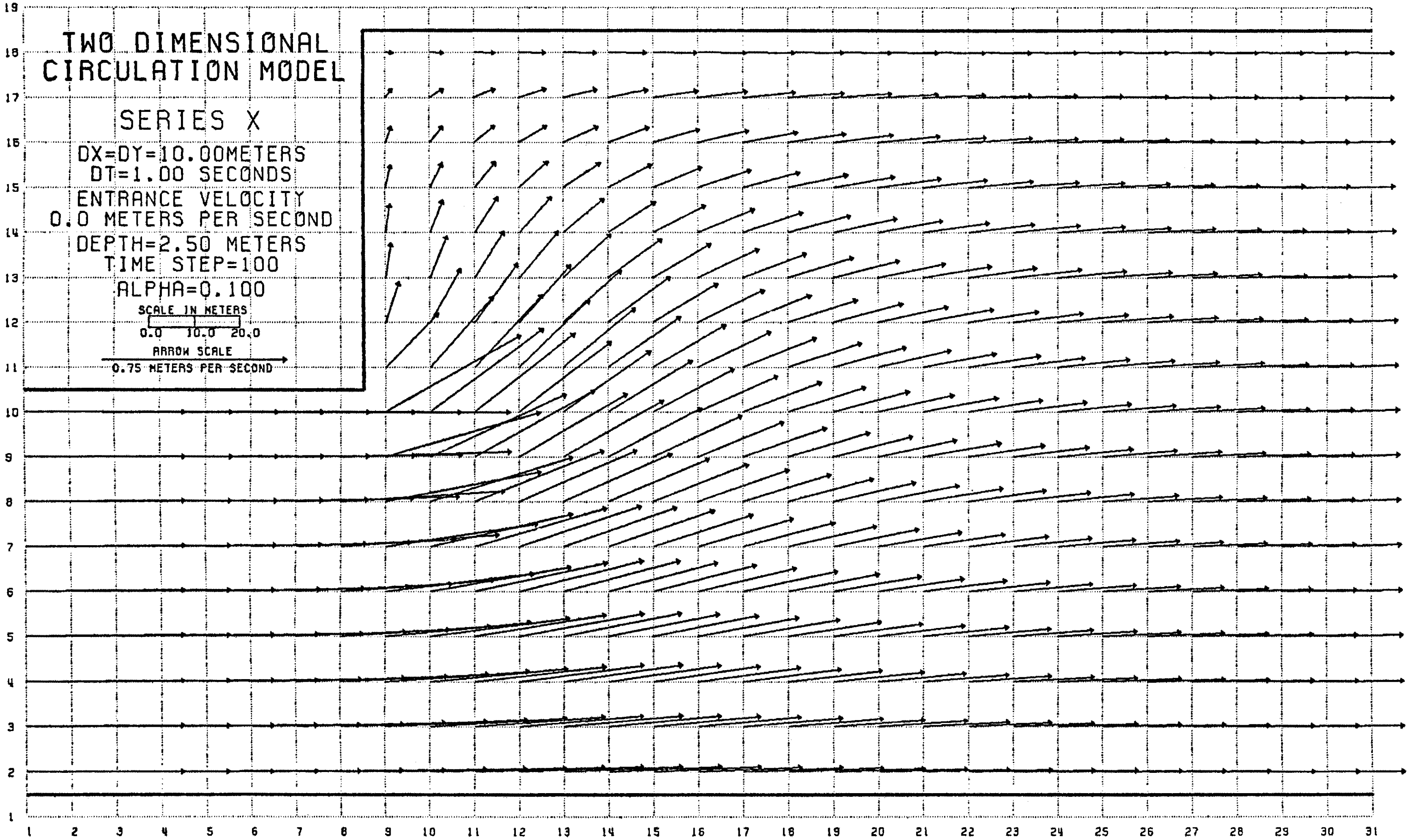

Figure 5.143. Space increment, $\Delta x = \Delta y = 10.0$ meters: time step 100.

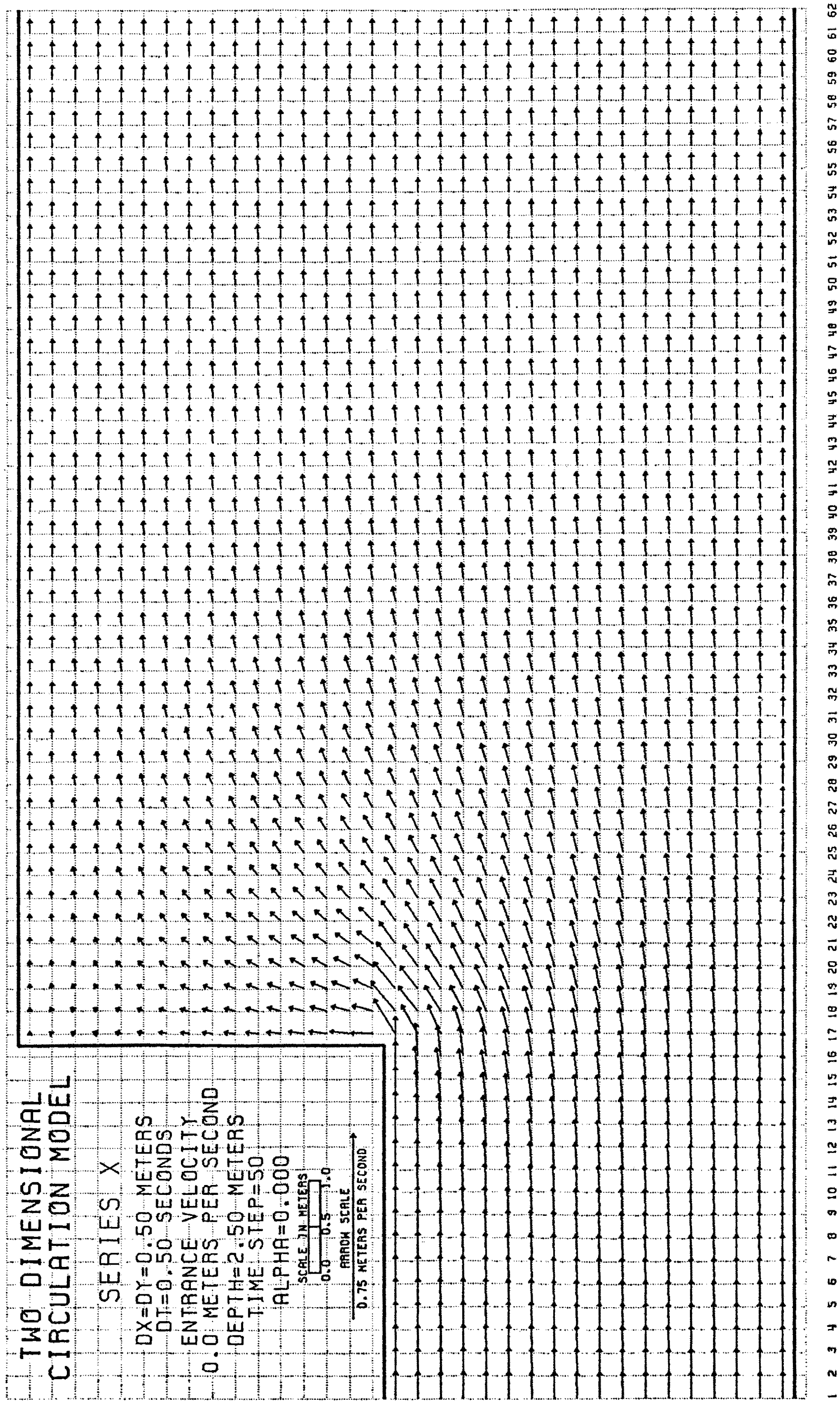

Figure 5.144. Cold start with increased resolution: time step 50.

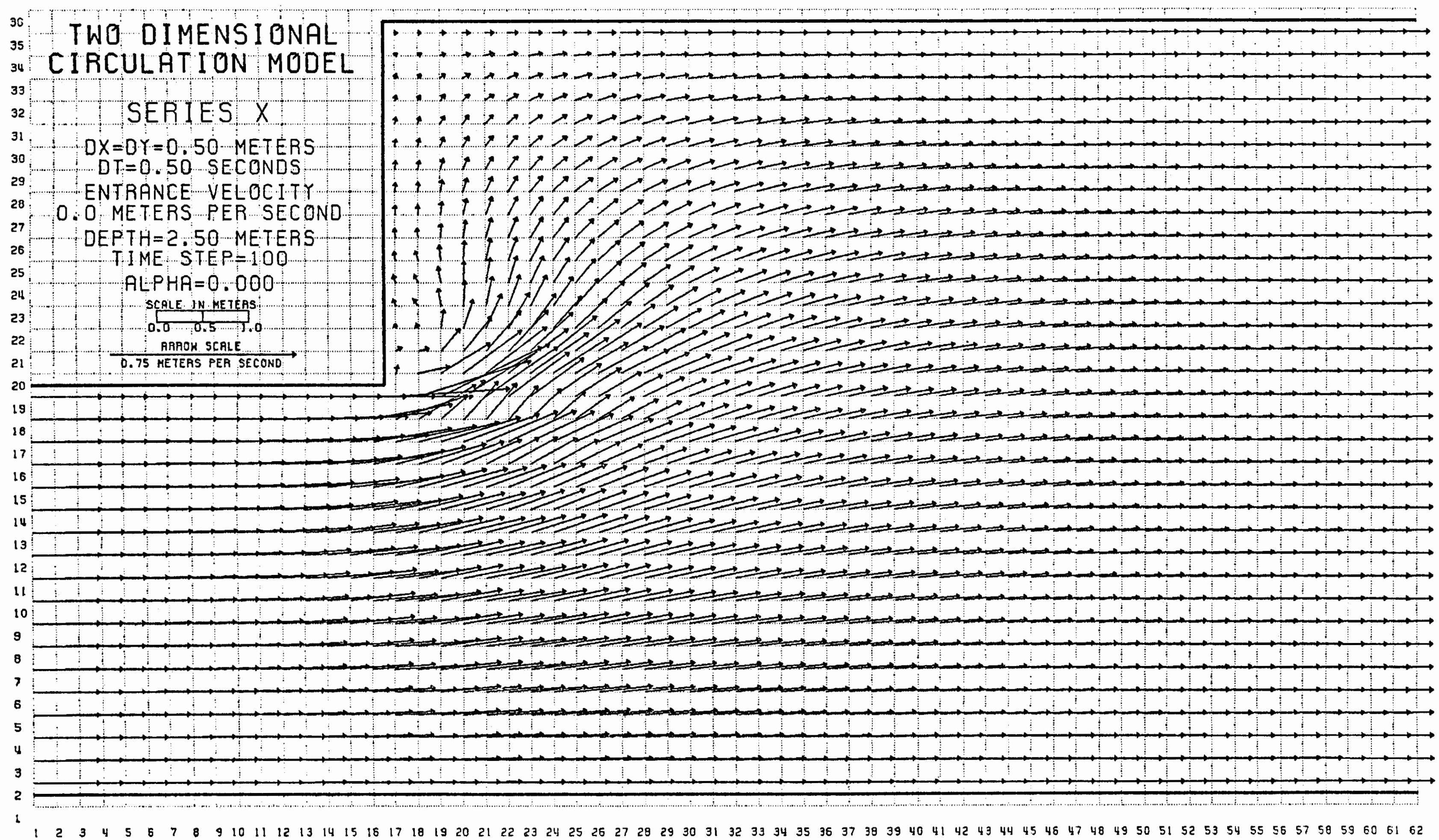

Figure 5.145. Cold start with increased resolution: time step 100.

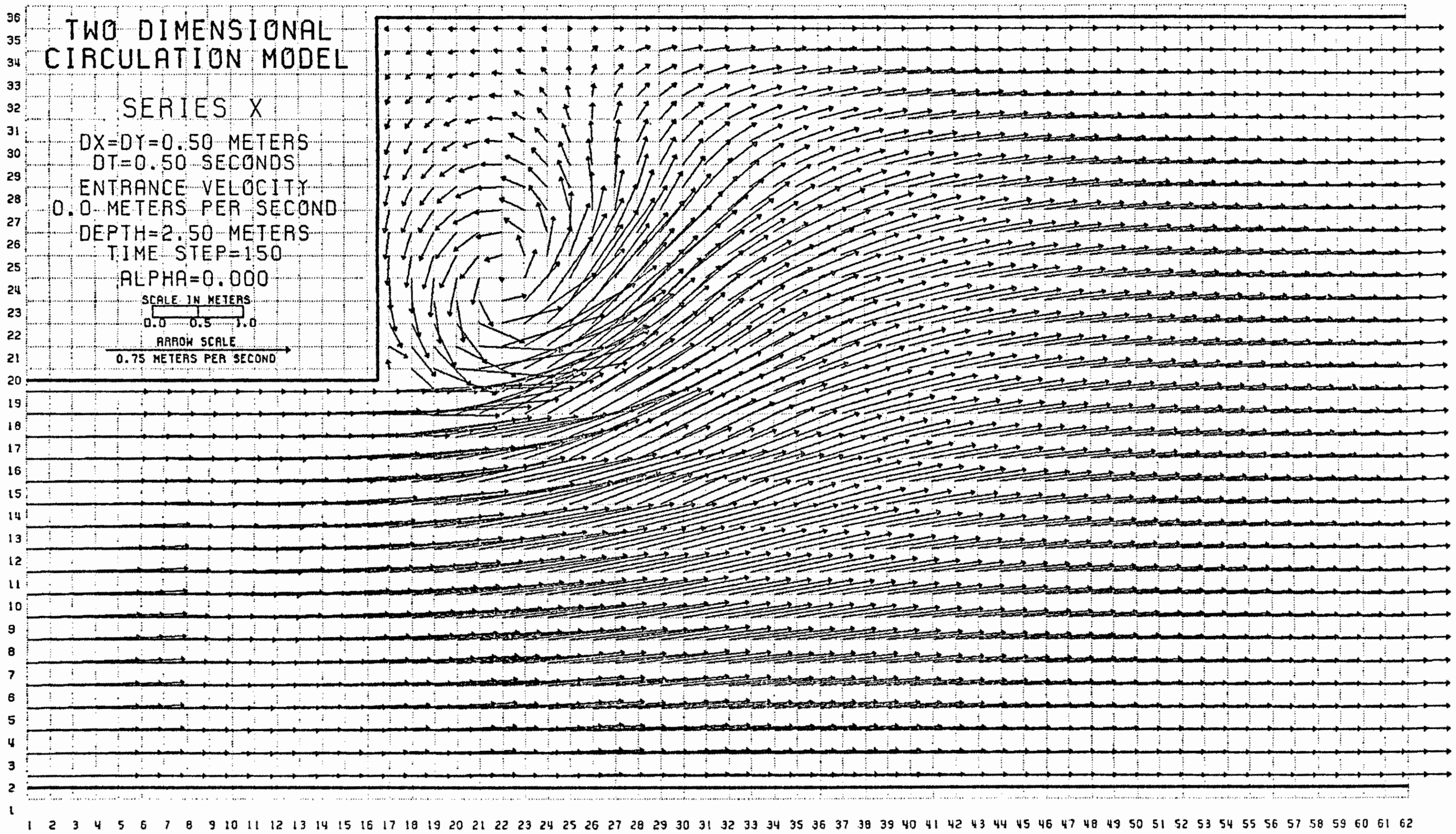

Figure 5.146. Cold start with increased resolution: time step 150.

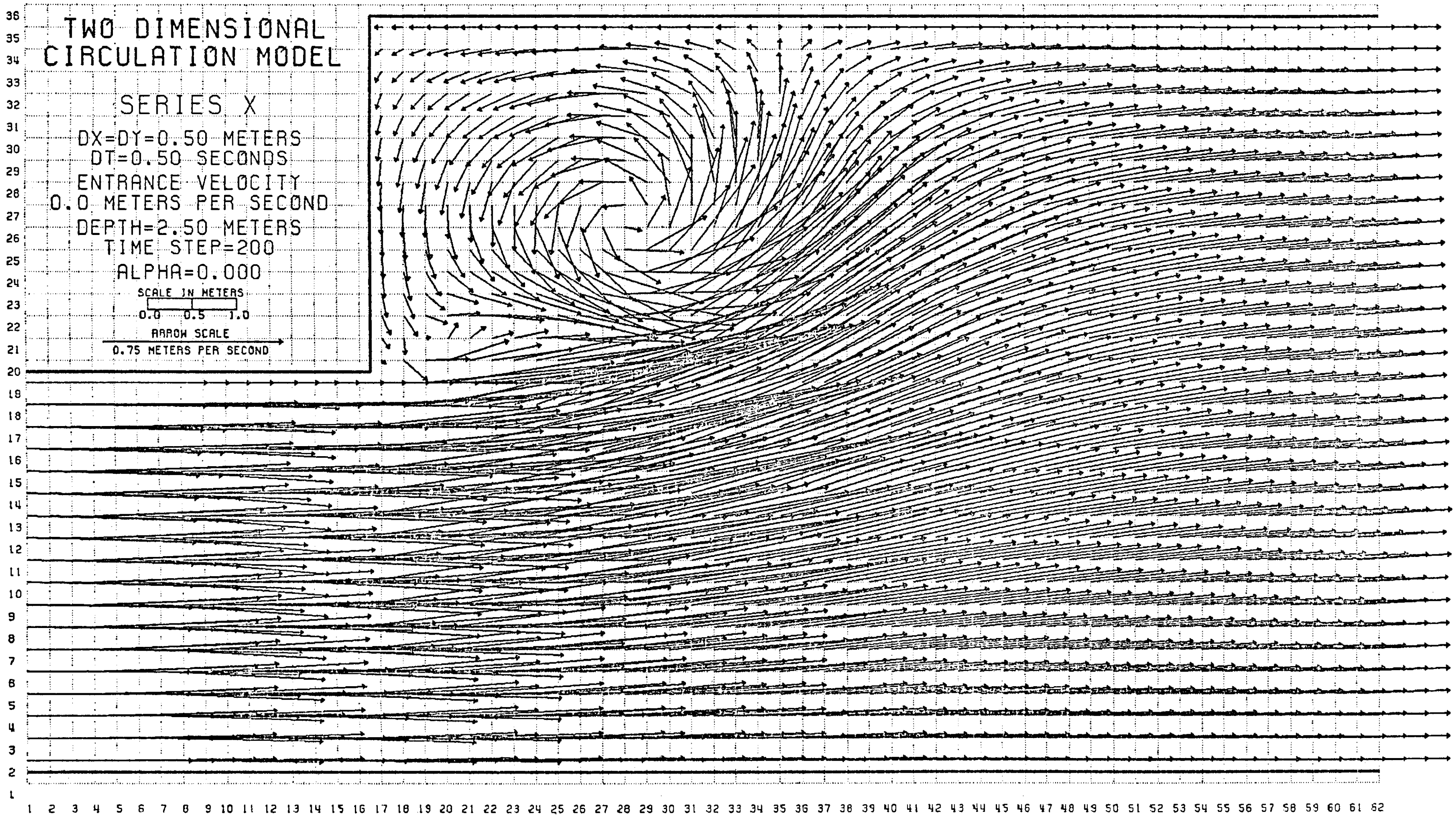

Figure 5.147. Cold start with increased resolution: time step 200.

PROGRAM LISTING

```
      PROGRAM TWOD
C***********************************************************************
C*
C*
C*                             TWOD
C*
C*
C***********************************************************************
C*
C*****DEVELOPED       V. M. PONCE AND S. B. YABUSAKI, COLORADO STATE
C*                    UNIVERSITY,FORT COLLINS,COLORADO 80523
C*
C*****DESCRIPTION     TWOD IS A TWO-DIMENSIONAL OPEN CHANNEL FLOW
C*                    MODEL CAPABLE OF SIMULATING FLOW CIRCULATION.
C*
C***********************************************************************
     1(INPUT,OUTPUT,TAPE5=INPUT,TAPE6=OUTPUT,TAPE7,NPARAM)
      COMMON/A/ U(31,19,2),V(31,19,2),W(31,19,2),Z(31,19)
      COMMON/B/ A(30),B(30),C(30),D(30),E(30)
      COMMON/C/ P(31),Q(31),R(31),S(31)
      COMMON/D/ IW(19),IE(19),IJL(19),IJR(19)
      COMMON/E/ IS(31),IN(31),IKL(31),IKR(31)
      COMMON/P/ GR,NPR,NPL
      COMMON/Q/ JS,KS,JT,KT,NT
      COMMON/R/ DX,DY,DT,T,DT2
      COMMON/S/ IBW,IBE,IBS,IBN,JL,JR,JM,JQ,KL,KR,KM,KQ
      COMMON/T/ ALPHA,UAVE(30,18),VAVE(30,18)
      COMMON/U/ UR,VR,WR,SL,FR,UE
      COMMON/X/ X1(30,17),Y1(30,17),X2(30,17),Y2(30,17),DEGREES(30,17)
      CALL INDA
      CALL IBOU
      CALL INCO
      DO 50 N=1,NT
      DO 10 K=2,KS
      CALL INBX(K,N)
      CALL INDX(K)
      CALL COEX(K,N)
   10 CALL DSPX(K,N)
      CALL BSRX
      CALL EXPX
      CALL BREX
      CALL AVELCTY(N)
      CALL RLOX
      DO 20 J=2,JS
      CALL INBY(J,N)
      CALL INDY(J)
      CALL COEY(J,N)
   20 CALL DSPY(J,N)
      CALL BSRY
      CALL EXPY
      CALL BREY
      CALL AVELCTY(N)
      IF(MOD(N,NPR).EQ.0)CALL PRIN(N)
      CALL RLOX
      IF(MOD(N,NPL).NE.0)GO TO 50
      CALL PLTDATA
      CALL PLOTTER(N)
   50 CONTINUE
      STOP
      END
```

```
C
C*****INPUT OF PROGRAM PARAMETERS
C
      SUBROUTINE INDA
      COMMON/P/ GR,NPR,NPL
      COMMON/Q/ JS,KS,JT,KT,NT
      COMMON/R/ DX,DY,DT,T,DT2
      COMMON/T/ ALPHA,UAVE(30,18),VAVE(30,18)
      COMMON/U/ UR,VR,WR,SL,FR,UE
      WRITE(6,100)
      READ(7,200) DX,DY,DT
      WRITE(6,300)DX,DY,DT
      READ(7,400) JS,KS,NT
      WRITE(6,500)JS,KS,NT
      READ(7,200) UR,VR,WR,SL,FR,UE
      WRITE(6,300)UR,VR,WR,SL,FR,UE
      GR= 9.81
      ALPHA=0.1
      NPR=10
      NPL=50
      JT= JS+1
      KT= KS+1
      T= -0.5*DT*GR/DX
      DT2= 0.5*DT
  100 FORMAT(//* TWOD13, A TWO-DIMENSIONAL IMPLICIT RIVER MODEL*//)
  200 FORMAT(8F10.0)
  300 FORMAT(8E15.6)
  400 FORMAT(8I10)
  500 FORMAT(8I15)
      RETURN
      END
C
C*****INPUT OF BOUNDARIES AND BOUNDARY TYPES
C
      SUBROUTINE IBOU
      COMMON/D/ IW(19),IE(19),IJL(19),IJR(19)
      COMMON/E/ IS(31),IN(31),IKL(31),IKR(31)
      COMMON/Q/ JS,KS,JT,KT,NT
      DO 10 K=1,KT
      READ(7,100) IW(K),IE(K),IJL(K),IJR(K)
      WRITE(6,200)IW(K),IE(K),IJL(K),IJR(K)
   10 CONTINUE
      DO 20 J=1,31
      READ(7,100) IS(J),IN(J),IKL(J),IKR(J)
      WRITE(6,200)IS(J),IN(J),IKL(J),IKR(J)
   20 CONTINUE
  100 FORMAT(4I2)
  200 FORMAT(1X,4I3)
      RETURN
      END
```

```
C
C*****INPUT OF INITIAL CONDITIONS
C
      SUBROUTINE INCO
      COMMON/A/ U(31,19,2),V(31,19,2),W(31,19,2),Z(31,19)
      COMMON/Q/ JS,KS,JT,KT,NT
      COMMON/R/ DX,DY,DT,T,DT2
      COMMON/U/ UR,VR,WR,SL,FR,UE
      DO 5 J=1,31
      DO 5 K=1,19
      U(J,K,2)=9999.
      V(J,K,2)=9999.
      W(J,K,2)=9999.
    5 CONTINUE
      DO 10 K=1,KT
      DO 10 J=1,31
      U(J,K,1)= UR
      V(J,K,1)= VR
      W(J,K,1)= WR
      Z(J,K)=10.0-(J-1)*DX*SL
   10 CONTINUE
      RETURN
      END
C
C*****PRINTING OF VELOCITIES AND ELEVATIONS
C
      SUBROUTINE PRIN(N)
      COMMON/A/ U(31,19,2),V(31,19,2),W(31,19,2),Z(31,19)
      COMMON/Q/ JS,KS,JT,KT,NT
      WRITE(6,200) N
      DO 10 J=1,31
   10 WRITE(6,100)(U(J,K,2),K=1,KT)
      WRITE(6,300) N
      DO 20 J=1,31
   20 WRITE(6,100)(V(J,K,2),K=1,KT)
      WRITE(6,400) N
      DO 30 J=1,31
   30 WRITE(6,100)(W(J,K,2),K=1,KT)
  100 FORMAT(1X,19F7.3)
  200 FORMAT(5X,* VELOCITY U, TIME STEP=*I4)
  300 FORMAT(5X,* VELOCITY V, TIME STEP=*I4)
  400 FORMAT(5X,* WATER SURFACE W, TIME STEP=*I4)
      RETURN
      END
C
C*****BOUNDARY CONDITIONS FOR THE X-DIRECTION
C
      SUBROUTINE INBX(K,N)
      COMMON/A/ U(31,19,2),V(31,19,2),W(31,19,2),Z(31,19)
      COMMON/P/ GR,NPR,NPL
      COMMON/Q/ JS,KS,JT,KT,NT
      COMMON/R/ DX,DY,DT,T,DT2
      COMMON/U/ UR,VR,WR,SL,FR,UE
      IF(K.GT.5)GO TO 5
      W(1,K,2)=WR
      W(JT,K,2)=WR-JS*DX*SL*N/20.
      IF(N.GT.20)W(JT,K,2)=WR-JS*DX*SL
      RETURN
    5 U(8,K,2)=0.
      U(23,K,2)=0.
      RETURN
      END
```

```
C
C*****SET BOUNDARIES FOR X-DIRECTION COMPUTATIONS
C
      SUBROUTINE INDX(K)
      COMMON/D/ IW(19),IE(19),IJL(19),IJR(19)
      COMMON/S/ IBW,IBE,IBS,IBN,JL,JR,JM,JQ,KL,KR,KM,KQ
      IBW=IW(K)
      IBE=IE(K)
      JL= IJL(K)
      JR= IJR(K)
      JM= JL+1
      JQ= JR-1
      RETURN
      END
C
C*****SET BOUNDARIES FOR Y-DIRECTION COMPUTATIONS
C
      SUBROUTINE INDY(J)
      COMMON/E/ IS(31),IN(31),IKL(31),IKR(31)
      COMMON/S/ IBW,IBE,IBS,IBN,JL,JR,JM,JQ,KL,KR,KM,KQ
      IBS=IS(J)
      IBN=IN(J)
      KL= IKL(J)
      KR= IKR(J)
      KM= KL+1
      KQ= KR-1
      RETURN
      END
C
C*****BOUNDARY CONDITIONS FOR THE Y-DIRECTION
C
      SUBROUTINE INBY(J,N)
      COMMON/A/ U(31,19,2),V(31,19,2),W(31,19,2),Z(31,19)
      COMMON/U/ UR,VR,WR,SL,FR,UE
      V(J,1,2)= 0.
      V(J,18,2)=0.
      IF(IABS(16-J).LT.8)RETURN
      V(J,5,2)= 0.
      RETURN
      END
```

```
C
C*****GENERATE COEFFICIENTS FOR X-DIRECTION MATRIX INVERSION
C
      SUBROUTINE COEX(K,N)
      COMMON/A/ U(31,19,2),V(31,19,2),W(31,19,2),Z(31,19)
      COMMON/B/ A(30),B(30),C(30),D(30),E(30)
      COMMON/Q/ JS,KS,JT,KT,NT
      COMMON/R/ DX,DY,DT,T,DT2
      COMMON/S/ IBW,IBE,IBS,IBN,JL,JR,JM,JQ,KL,KR,KM,KQ
      COMMON/U/ UR,VR,WR,SL,FR,UE
      DO 10 J=JM,JQ
      UC= U(J,K,1)
      DCT= (U(J+1,K,1)-U(J-1,K,1))/(2.*DX)
C        DCT=0.0
      VAV= 0.25*(V(J,K,1)+V(J+1,K,1)+V(J+1,K-1,1)+V(J,K-1,1))
      CCT= (U(J,K+1,1)-U(J,K-1,1))/(2.*DY)
C        CCT=0.0
      TEM1= SQRT(UC**2 + VAV**2)
      TEM2= 0.5*(W(J+1,K,1)+W(J,K,1)-Z(J,K)-Z(J,K-1))
      FRT= TEM1/TEM2
      WL= W(J+1,K,1)
      DE= 0.5*(W(J+2,K,1)+W(J+1,K,1)-Z(J+1,K)-Z(J+1,K-1))
      DW= 0.5*(W(J+1,K,1)+W(J,K,1)-Z(J,K)-Z(J,K-1))
      DN= 0.5*(W(J+1,K+1,1)+W(J+1,K,1)-Z(J+1,K)-Z(J,K))
      DS= 0.5*(W(J+1,K,1)+W(J+1,K-1,1)-Z(J+1,K-1)-Z(J,K-1))
      DDV= (DN*V(J+1,K,1)-DS*V(J+1,K-1,1))/DY
      A(J)= 1. + DT2*(DCT+FR*FRT)
      B(J)= UC - DT2*(VAV*CCT)
      C(J)= -DT2*DW/DX
      D(J)=  DT2*DE/DX
      E(J)= WL - DT2*DDV
   10 CONTINUE
      WL= W(JM,K,1)
      DE= 0.5*(W(JM+1,K,1)+W(JM,K,1)-Z(JM,K)-Z(JM,K-1))
      DW= 0.5*(W(JM,K,1)+W(JL,K,1)-Z(JL,K)-Z(JL,K-1))
      DN= 0.5*(W(JM,K+1,1)+W(JM,K,1)-Z(JM,K)-Z(JL,K))
      DS= 0.5*(W(JM,K,1) + W(JM,K-1,1)-Z(JM,K-1)-Z(JL,K-1))
      DDV= (DN*V(JM,K,1)-DS*V(JM,K-1,1))/DY
      C(JL)= -DT2*DW/DX
      D(JL)=  DT2*DE/DX
      E(JL)=  WL - DT2*DDV
      IF(IBW.NE.1)GO TO 50
      DCT=(U(JM,K,1)-U(JL,K,1))/(2.*DX)
C        DCT=0.0
      VAV=0.25*(V(JL,K,1)+V(JM,K,1)+V(JM,K-1,1)+V(JL,K-1,1))
      CCT=(U(JL,K+1,1)-U(JL,K-1,1))/(2.*DY)
C        CCT=0.0
      TEM1=SQRT(U(JL,K,1)**2+VAV**2)
      TEM2=0.5*(W(JM,K,1)+W(JL,K,1)-Z(JL,K)-Z(JL,K-1))
      FRT=TEM1/TEM2
      A(JL)=1.+DT2*(DCT+FR*FRT)
      B(JL)=U(JL,K,1)-DT2*(VAV*CCT)
   50 CONTINUE
      RETURN
      END
```

```
C
C*****GENERATE COEFFICIENTS FOR Y-DIRECTION MATRIX INVERSION
C
      SUBROUTINE COEY(J,N)
      COMMON/A/ U(31,19,2),V(31,19,2),W(31,19,2),Z(31,19)
      COMMON/B/ A(30),B(30),C(30),D(30),E(30)
      COMMON/Q/ JS,KS,JT,KT,NT
      COMMON/R/ DX,DY,DT,T,DT2
      COMMON/S/ IBW,IBE,IBS,IBN,JL,JR,JM,JQ,KL,KR,KM,KQ
      COMMON/U/ UR,VR,WR,SL,FR,UE
      DO 10 K=KM,KQ
      VC= V(J,K,1)
      DCT= (V(J,K+1,1)-V(J,K-1,1))/(2.*DY)
C        DCT=0.0
      UAV= 0.25*(U(J,K,1)+U(J,K+1,1)+U(J-1,K+1,1)+U(J-1,K,1))
      CCT= (V(J+1,K,1)-V(J-1,K,1))/(2.*DX)
C        CCT=0.0
      TEM1= SQRT(VC**2 + UAV**2)
      TEM2= 0.5*(W(J,K+1,1)+W(J,K,1)-Z(J,K)-Z(J-1,K))
      FRT= TEM1/TEM2
      WL= W(J,K+1,1)
      DE= 0.5*(W(J+1,K+1,1)+W(J,K+1,1)-Z(J,K+1)-Z(J,K))
      DW= 0.5*(W(J,K+1,1)+W(J-1,K+1,1)-Z(J-1,K+1)-Z(J-1,K))
      DN= 0.5*(W(J,K+2,1)+W(J,K+1,1)-Z(J,K+1)-Z(J-1,K+1))
      DS= 0.5*(W(J,K+1,1)+W(J,K)-Z(J,K)-Z(J-1,K))
      DDU= (DE*U(J,K+1,1)-DW*U(J-1,K+1,1))/DX
      A(K)= 1. + DT2*(DCT+FR*FRT)
      B(K)= VC - DT2*(UAV*CCT)
      C(K)=  -DT2*DS/DY
      D(K)=  DT2*DN/DY
      E(K)= WL- DT2*DDU
   10 CONTINUE
      WL= W(J,KM,1)
      DE= 0.5*(W(J+1,KM,1)+W(J,KM,1)-Z(J,KM)-Z(J,KL))
      DW= 0.5*(W(J,KM,1)+W(J-1,KM,1)-Z(J-1,KM)-Z(J-1,KL))
      DN= 0.5*(W(J,KM+1,1)+W(J,KM,1)-Z(J,KM)-Z(J-1,KM))
      DS= 0.5*(W(J,KM,1)+W(J,KL,1)-Z(J,KL)-Z(J-1,KL))
      DDU=  (DE*U(J,KM,1)-DW*U(J-1,KM,1))/DX
      C(KL)= -DT2*DS/DY
      D(KL)=  DT2*DN/DY
      E(KL)=  WL - DT2*DDU
      RETURN
      END
```

```
C
C*****X-DIRECTION DOUBLE SWEEP MATRIX INVERSION
C
      SUBROUTINE DSPX(K,N)
      COMMON/A/ U(31,19,2),V(31,19,2),W(31,19,2),Z(31,19)
      COMMON/B/ A(30),B(30),C(30),D(30),E(30)
      COMMON/C/ P(31),Q(31),R(31),S(31)
      COMMON/Q/ JS,KS,JT,KT,NT
      COMMON/R/ DX,DY,DT,T,DT2
      COMMON/S/ IBW,IBE,IBS,IBN,JL,JR,JM,JQ,KL,KR,KM,KQ
      P(JL)= 0.
      IF(IBW.EQ.1)GO TO 20
      Q(JL)= 0.
      R(JL)= 0.
      S(JL)= U(JL,K,2)
      GO TO 30
   20 Q(JL)=W(JL,K,2)
      R(JL)=T/(T*P(JL)+A(JL))
      S(JL)=(B(JL)-T*Q(JL))/(T*P(JL)+A(JL))
   30 CONTINUE
      DO 40 J= JM,JQ
      JX= J-1
      PQ= 1./(C(JX)*R(JX) + 1.)
      P(J)= -PQ*D(JX)
      Q(J)=  PQ*(E(JX)- C(JX)*S(JX))
      RS= 1./(T*P(J) + A(J))
      R(J)=  RS*T
      S(J)=  RS*(B(J)- T*Q(J))
   40 CONTINUE
      IF(IBE.EQ.1)GO TO 50
      PQ=1./(C(JQ)*R(JQ) + 1.)
      P(JR)=-PQ*D(JQ)
      Q(JR)= PQ*(E(JQ)-C(JQ)*S(JQ))
      W(JR,K,2)=P(JR)*U(JR,K,2)+Q(JR)
   50 CONTINUE
      DO 60 J=JL,JQ
      L= JL+JQ-J
      U(L,K,2)= R(L)*W(L+1,K,2) + S(L)
      W(L,K,2)= P(L)*U(L,K,2) + Q(L)
   60 CONTINUE
      RETURN
      END
```

```
C
C*****Y-DIRECTION DOUBLE SWEEP MATRIX INVERSION
C
      SUBROUTINE DSPY(J,N)
      COMMON/A/ U(31,19,2),V(31,19,2),W(31,19,2),Z(31,19)
      COMMON/B/ A(30),B(30),C(30),D(30),E(30)
      COMMON/C/ P(31),Q(31),R(31),S(31)
      COMMON/Q/ JS,KS,JT,KT,NT
      COMMON/R/ DX,DY,DT,T,DT2
      COMMON/S/ IBW,IBE,IBS,IBN,JL,JR,JM,JQ,KL,KR,KM,KQ
      P(KL)= 0.
      Q(KL)= 0.
      R(KL)= 0.
      S(KL)= V(J,KL,2)
      DO 40 K=KM,KQ
      KY= K-1
      PQ= 1./(C(KY)*R(KY) +1.)
      P(K)= -PQ*D(KY)
      Q(K)=  PQ*(E(KY)- C(KY)*S(KY))
      RS= 1./(T*P(K)+A(K))
      R(K)= RS*T
      S(K)= RS*(B(K)  - T*Q(K))
   40 CONTINUE
      IF(IBN.EQ.1)GO TO 5
      PQ=1./(C(KQ)*R(KQ)  + 1.)
      P(KR)=-PQ*D(KQ)
      Q(KR)= PQ*(E(KQ)-C(KQ)*S(KQ))
      W(J,KR,2)=P(KR)*V(J,KR,2)+Q(KR)
    5 CONTINUE
      DO 60 K=KL,KQ
      L= KL+KQ-K
      V(J,L,2)= R(L)*W(J,L+1,2)  + S(L)
      W(J,L,2)= P(L)*V(J,L,2)  + Q(L)
   60 CONTINUE
      RETURN
      END
C
C*****BOUNDARY RELOCATION NECESSARY FOR X-DIRECTION EXPLICIT COMPUTATION
C
      SUBROUTINE BSRX
      COMMON/A/ U(31,19,2),V(31,19,2),W(31,19,2),Z(31,19)
      COMMON/P/ GR,NPR,NPL
      DO 10 K=2,18
      IF(K.GT.5)GO TO 5
      U(30,K,2)=U(29,K,2)
      GO TO 10
    5 W(8,K,2)=W(9,K,2)
      W(24,K,2)=W(23,K,2)
   10 CONTINUE
      DO 20 J=1,30
      U(J,1,2)=U(J,2,2)
      W(J,1,2)=W(J,2,2)
      IF(IABS(16-J).LT.8)GO TO 15
      W(J,6,2)=W(J,5,2)
      U(J,6,2)=U(J,5,2)
   15 CONTINUE
      IF(J.LE.7.OR.J.GE.24)GO TO 20
      U(J,19,2)=U(J,18,2)
      W(J,19,2)=W(J,18,2)
   20 CONTINUE
      U(8,6,2)=U(9,6,2)
      U(23,6,2)=U(22,6,2)
      RETURN
      END
```

```
C
C*****BOUNDARY RELOCATION NECESSARY FOR Y-DIRECTION EXPLICIT COMPUTATION
C
      SUBROUTINE BSRY
      COMMON/A/ U(31,19,2),V(31,19,2),W(31,19,2),Z(31,19)
      DO 10 K=1,18
      IF(K.GT.5)GO TO 5
      V(1,K,2)=V(2,K,2)
      V(31,K,2)=V(30,K,2)=V(29,K,2)
      GO TO 10
    5 W(8,K,2)=W(9,K,2)
      V(8,K,2)=V(9,K,2)
      V(24,K,2)=V(23,K,2)
      W(24,K,2)=W(23,K,2)
   10 CONTINUE
      DO 20 J=1,30
      IF(IABS(16-J).LT.8)GO TO 15
      W(J,6,2)=W(J,5,2)
   15 W(J,1,2)=W(J,2,2)
      IF(J.GE.8.AND.J.LE.24)W(J,19,2)=W(J,18,2)
   20 CONTINUE
      RETURN
      END
C
C*****X-DIRECTION EXPLICIT COMPUTATIONS
C
      SUBROUTINE EXPX
      COMMON/A/ U(31,19,2),V(31,19,2),W(31,19,2),Z(31,19)
      COMMON/D/ IW(19),IE(19),IJL(19),IJR(19)
      COMMON/P/ GR,NPR,NPL
      COMMON/Q/ JS,KS,JT,KT,NT
      COMMON/R/ DX,DY,DT,T,DT2
      COMMON/U/ UR,VR,WR,SL,FR,UE
      DO 50 K= 2,17
      KY=K
      IF(K.EQ.5)KY=K+1
      JM=IJL(KY)+1
      JR=IJR(KY)
      DO 50 J= JM,JR
      CCT= (U(J,K,2)+U(J,K+1,2)+U(J-1,K+1,2)+U(J-1,K,2))*
     $        (V(J+1,K,1)-V(J-1,K,1))/(8.*DX)
C        CCT=0.0
      DCT= (V(J,K+1,1)-V(J,K-1,1))/(2.*DY)
C        DCT=0.0
      PRT= GR*(W(J,K+1,1)-W(J,K,1))/DY
      TEMP1= FR
      TEMP2= 0.25*(U(J,K,1)+U(J,K+1,1)+U(J-1,K+1,1)+U(J-1,K,1))
      TEMP3= 0.5*(W(J,K+1,2)+W(J,K,2)-Z(J,K)-Z(J-1,K))
      TEMP4= SQRT(V(J,K,1)**2 + TEMP2**2)
      FRT= TEMP1*TEMP4/TEMP3
      V(J,K,2)= (V(J,K,1) - DT2*(CCT+PRT))/(1.+ DT2*(DCT+FRT))
   50 CONTINUE
      RETURN
      END
C
C*****BOUNDARY RELOCATION NECESSARY FOR Y-DIRECTION IMPLICIT COMPUTATION
C
      SUBROUTINE BREX
      COMMON/A/ U(31,19,2),V(31,19,2),W(31,19,2),Z(31,19)
      DO 10 J=1,30
      IF(IABS(16-J).GE.8)V(J,5,2)=0.
      V(J,18,2)=0.0
   10 V(J,1,2)=0.
      DO 20 K=1,18
      IF(K.GT.5)GO TO 5
      V(1,K,2)=V(2,K,2)
      GO TO 20
    5 V(8,K,2)=V(9,K,2)
      V(24,K,2)=V(23,K,2)
   20 CONTINUE
      RETURN
      END
```

```
C
C*****Y-DIRECTION EXPLICIT COMPUTATIONS
C
      SUBROUTINE EXPY
      COMMON/A/ U(31,19,2),V(31,19,2),W(31,19,2),Z(31,19)
      COMMON/E/ IS(31),IN(31),IKL(31),IKR(31)
      COMMON/P/ GR,NPR,NPL
      COMMON/Q/ JS,KS,JT,KT,NT
      COMMON/R/ DX,DY,DT,T,DT2
      COMMON/U/ UR,VR,WR,SL,FR,UE
      DO 50 J= 2,JS
      JX=J
      IF(J.EQ.23)JX=J+1
      KM=IKL(JX)+1
      KR=IKR(JX)
      DO 50 K= KM,KR
      CCT= (V(J,K,2)+V(J+1,K,2)+V(J+1,K-1,2)+V(J,K-1,2))*(U(J,K+1,1)-
     $        U(J,K-1,1))/(8.*DY)
C           CCT=0.0
      DCT= (U(J+1,K,1)-U(J-1,K,1))/(2.*DX)
C           DCT=0.0
      PRT= GR*(W(J+1,K,1)-W(J,K,1))/DX
      TEMP1= FR
      TEMP2= 0.25*(V(J,K,1)+V(J+1,K,1)+V(J+1,K-1,1)+V(J,K-1,1))
      TEMP3= 0.5*(W(J+1,K,2)+W(J,K,2)-Z(J,K)-Z(J,K-1))
      TEMP4= SQRT(U(J,K,1)**2 + TEMP2**2)
      FRT= TEMP1*TEMP4/TEMP3
      U(J,K,2)= (U(J,K,1)- DT2*(CCT+PRT))/(1.+ DT2*(DCT+FRT))
   50 CONTINUE
      RETURN
      END
C
C*****BOUNDARY RELOCATION NECESSARY FOR X-DIRECTION IMPLICIT COMPUTATION
C
      SUBROUTINE BREY
      COMMON/A/ U(31,19,2),V(31,19,2),W(31,19,2),Z(31,19)
      COMMON/P/ GR,NPR,NPL
      DO 10 K=2,18
      IF(K.GT.5)GO TO 5
      U(30,K,2)=U(29,K,2)
      W(31,K,2)=W(30,K,2)
      GO TO 10
    5 U(8,K,2)=0.0
      U(23,K,2)=0.0
   10 CONTINUE
      DO 20 J=1,30
      IF(J.GE.8.AND.J.LE.23)U(J,19,2)=U(J,18,2)
      IF(J.LE.8.OR.J.GE.23)U(J,6,2)=U(J,5,2)
      U(J,1,2)=U(J,2,2)
   20 CONTINUE
      RETURN
      END
C
C*****RELOCATION OF COMPUTED VALUES TO LOWEST TIME LEVEL
C
      SUBROUTINE RLOX
      COMMON/A/ U(31,19,2),V(31,19,2),W(31,19,2),Z(31,19)
      COMMON/D/ IW(19),IE(19),IJL(19),IJR(19)
      COMMON/Q/ JS,KS,JT,KT,NT
      DO 10 K= 1,KT
      JL=IJL(K)
      JR=IJR(K)+1
      IF(K.NE.6)GO TO 5
      JL=IJL(K-1)
      JR=IJR(K-1)+1
    5 CONTINUE
      DO 10 J= JL,JR
      U(J,K,1)= U(J,K,2)
      V(J,K,1)= V(J,K,2)
      W(J,K,1)= W(J,K,2)
   10 CONTINUE
      RETURN
      END
```

```
C
C*****GENERATION OF PLOT DATA
C
      SUBROUTINE PLTDATA
      COMMON/A/ U(31,19,2),V(31,19,2),W(31,19,2),Z(31,19)
      COMMON/U/ UR,VR,WR,SL,FR,UE
      COMMON/X/ X1(30,17),Y1(30,17),X2(30,17),Y2(30,17),DEGREES(30,17)
      UEX=UE
      IF(UE.EQ.0.)UEX=0.5
      U(23,6,2)=0.0
      DO 10 J=1,30
      KM=4
      IF(J.GT.8.AND.J.LT.24)KM=17
      DO 10 K=1,KM
      X1(J,K)=(J-1)*0.5
      Y1(J,K)=0.25+(K-1)*0.5
      X2(J,K)=2.0/UEX*U(J,K+1,2)+X1(J,K)
      Y2(J,K)=2.0/UEX*V(J,K+1,2)+Y1(J,K)
      IF(U(J,K+1,2).NE.0.0.OR.V(J,K+1,2).NE.0.)GO TO 5
      DEGREES(J,K)=0.0
      GO TO 15
    5 CONTINUE
      DEGREES(J,K)=270.+ATAN2(V(J,K+1,2),U(J,K+1,2))*180./3.14159265359
      IF(DEGREES(J,K).GT.360.)DEGREES(J,K)=DEGREES(J,K)-360.
   15 CONTINUE
  100 FORMAT(5F20.6)
   10 CONTINUE
      RETURN
      END
```

```
C
C*****PLOTTING OF VELOCITY VECTORS
C
      SUBROUTINE PLOTTER(N)
      COMMON/A/ U(31,19,2),V(31,19,2),W(31,19,2),Z(31,19)
      DIMENSION XX(7),YY(7)
      COMMON/Q/ JS,KS,JT,KT,NT
      COMMON/R/ DX,DY,DT,T,DT2
      COMMON/T/ ALPHA,UAVE(30,18),VAVE(30,18)
      COMMON/U/ UR,VR,WR,SL,FR,UE
      COMMON/X/ X1(30,17),Y1(30,17),X2(30,17),Y2(30,17),DEGREES(30,17)
      CALL PLOTS(0,0,0)
      CALL SETMSG(0)
      CALL NEWPEN(5)
      CALL PLOT(1.0,1.0,-3)
      CALL PLOT(0.0,0.0,3)
      CALL PLOT(15.0,0.0,2)
      CALL PLOT(0.0,2.0,3)
      CALL PLOT(3.75,2.0,2)
      CALL PLOT(3.75,8.5,2)
      CALL PLOT(11.25,8.5,2)
      CALL PLOT(11.25,2.0,2)
      CALL PLOT(15.0,2.0,2)
      CALL NEWPEN(1)
      CALL GRID(0.0,-0.25,30,0.5,18,0.5,
     1          04210421042104210421B)
      DO 20 J=1,31
      XJ=J
      X=(J-1)*0.5
      IF(J.GT.9)X=X-0.08
      CALL NUMBER(X,-0.45,0.08,XJ,0.0,-1)
   20 CONTINUE
      DO 30 K=1,19
      YK=K
      Y=(K-1)*0.5-0.29
      CALL NUMBER(-0.2,Y,0.08,YK,0.0,-1)
   30 CONTINUE
      CALL NEWPEN(2)
      DO 10 J=1,30
      KM=4
      IF(J.GT.8.AND.J.LT.24)KM=17
      DO 10 K=1,KM
      CALL PLOT(X1(J,K),Y1(J,K),3)
      CALL SYMBOL(X2(J,K),Y2(J,K),0.05,2,DEGREES(J,K),-2)
   10 CONTINUE
      XN=N
      DEPTH=WR-Z(1,1)
      CALL NEWPEN(4)
      CALL SYMBOL(0.445,8.26,0.2,15HTWO DIMENSIONAL,0.0,15)
      CALL SYMBOL(0.225,7.95,0.2,17HCIRCULATION MODEL,0.0,17)
      CALL NEWPEN(2)
      CALL SYMBOL(1.075,7.4,0.2,8HSERIES L,0.0,8)
      CALL SYMBOL(0.6,6.76,0.15,17HDX=DY=     METERS,0.0,17)
      CALL SYMBOL(0.75,6.535,0.15,15HDT=     SECONDS,0.0,15)
      CALL SYMBOL(0.6,5.76,0.15,17HENTRANCE VELOCITY,0.0,17)
      CALL SYMBOL(0.3,5.535,0.15,21H    METERS PER SECOND,0.0,21)
      CALL SYMBOL(0.6,4.76,0.15,17HDEPTH=     METERS,0.0,17)
      CALL SYMBOL(0.9,4.535,0.15,10HTIME STEP=,0.0,10)
      CALL SYMBOL(1.05,3.76,0.15,11HALPHA=     ,0.0,11)
      CALL NUMBER(1.5,6.76,0.15,DX,0.0,2)
      CALL NUMBER(1.2,6.535,0.15,DT,0.0,2)
      CALL NUMBER(0.3,5.535,0.15,UE,0.0,1)
      CALL NUMBER(1.50,4.76,0.15,DEPTH,0.0,2)
      CALL NUMBER(2.4,4.535,0.15,XN,0.0,-1)
      CALL NUMBER(1.95,3.76,0.15,ALPHA,0.0,3)
      XX(1)=XX(2)=XX(7)=1.875
      XX(3)=XX(4)=2.375
      XX(5)=XX(6)=1.375
      YY(1)=YY(5)=YY(4)=3.125
      YY(2)=YY(6)=YY(3)=YY(7)=3.00
```

```
      CALL PLOT(XX(1),YY(1),3)
      DO 40 J=2,7
      CALL PLOT(XX(J),YY(J),2)
   40 CONTINUE
      DO 50 J=1,3
      XJ=(J-1)*DX
      JJ=J
      IF(J.EQ.1)JJ=6
      XX(JJ)=XX(JJ)-0.08
      CALL NUMBER(XX(JJ),2.90,0.08,XJ,0.0,1)
   50 CONTINUE
      CALL SYMBOL(1.275,3.15,0.08,15HSCALE IN METERS,0.0,15)
      CALL PLOT(0.875,2.5,3)
      CALL SYMBOL(2.875,2.5,0.05,2,270.,-2)
      CALL SYMBOL(1.435,2.555,0.08,11HARROW SCALE,0.0,11)
      CALL SYMBOL(0.995,2.365,0.08,22H      METERS PER SECOND,0.0,22)
      UEX=UE
      IF(UE.EQ.0.)UEX=0.5
      CALL NUMBER(0.995,2.365,0.08,UEX,0.0,2)
      CALL PLOT(0.,0.,-999)
      IF(N.EQ.NT)CALL PLOT(0.,0.,999)
      RETURN
      END
C
C*****VELOCITY AVERAGING
C
      SUBROUTINE AVELCTY(N)
      COMMON/A/ U(31,19,2),V(31,19,2),W(31,19,2),Z(31,19)
      COMMON/E/ IS(31),IN(31),IKL(31),IKR(31)
      COMMON/Q/ JS,KS,JT,KT,NT
      COMMON/T/ ALPHA,UAVE(30,18),VAVE(30,18)
      DO 10 J=2,JS
      KR=IKR(J)
      DO 10 K=2,KR
      IF(J.EQ.23)GO TO 5
      UAVE(J,K)=(1.-ALPHA)*U(J,K,2)+ALPHA*0.25*(U(J-1,K,2)+U(J+1,K,2)
     1          +U(J,K+1,2)+U(J,K-1,2))
    5 CONTINUE
      IF(K.EQ.KR)GO TO 10
      VAVE(J,K)=(1.-ALPHA)*V(J,K,2)+ALPHA*0.25*(V(J-1,K,2)+V(J+1,K,2)
     1          +V(J,K+1,2)+V(J,K-1,2))
   10 CONTINUE
      DO 20 J=2,JS
      KR=IKR(J)
      DO 20 K=2,KR
      IF(J.EQ.23)GO TO 15
      U(J,K,2)=UAVE(J,K)
   15 CONTINUE
      IF(K.EQ.KR)GO TO 20
      V(J,K,2)=VAVE(J,K)
   20 CONTINUE
      RETURN
      END
```